UNIVERSITÀ DEGLI STUDI DI PADOVA

DIPARTIMENTO DI FISICA E ASTRONOMIA
Corso di Dottorato in Fisica 29º Ciclo

Energy and angular resolution of a new concept nano-satellite MeV telescope

Supervisors: **prof. Denis Bastieri**
prof. Fan Junhui

Candidato:
Donaggio Barbara

Anno Accademico 2018/2019

Ai miei genitori, a mio zio Gianni, a Nina e Leon

"Anni passati ad inseguire nell'ombra una verità che si intuisce senza riuscire ad esprimerla, l'ansia di arrivare, e l'alternarsi di fiducia e di dubbi finché ad un tratto sopraggiunge la chiarezza e la comprensione: tutto questo può capire solo chi l'abbia vissuto"

Albert Einstein 1933

Contents

Abstract

The electromagnetic spectrum in the high-energy band is object of observation by both space and ground-based telescopes, but at energies around about 1 MeV we unfortunately have only the contribution that the COMPTEL detector left us. The detector was onboard the Compton Gamma-Ray Observatory (CGRO) which has been deorbited in the year 2000 after 9 years of observations. In this energy band, between 0.1 and 10 MeV, the dominant interaction is the Compton scattering. The time-scale for the realization of a new Compton telescope is about 10 years and a cost of about half a billion Euros, but on a much shorter time-scale (about 18 months) and with a much lower cost, equal to about half a million Euro, it is possible to send a nano-satellite MeV telescope into orbit. Of course, this satellite will have lower capabilities than a larger telescope, but it will be a source of considerable information and a test bench for algorithms and technologies for future larger missions.

Chapter 1

Science at MeV energies

Science at MeV energies is quite diverse, as many different astrophysical objects emit radiation in this energy range. The main broad division is between galactic and extra-galactic sources.

1.1 Galactic sources

1.1.1 Isolated Neutron Star and Pulsars

Neutron stars form a special class of compact objects which are the end product of stellar evolution (remnants of supernova explosions) with masses between one and several Sun masses and diameters of only tens of kilometers across.

Pulsars are rapidly-rotating, highly-magnetized neutron stars (the huge surface magnetic fields B reach up to ≈ 10^{14}G) emitting radiation across the electromagnetic spectrum (Abdo et al. 2009). The first pulsar was observed half a century ago (see Hewish et al. 1968). The Fermi Large Area Telescope (LAT) is sensitive to photon energies from 20 MeV to over 300 GeV and has detected more than 200 γ-ray pulsar. The spectral shapes of most pulsars exhibit exponential cut-off in the GeV range. It is thought that the high-energy (HE) emission take places in vacuum gaps along the last closed field lines in the outer magnetosphere, in the so-called outer gaps model (Cheng et al. 1986 and 2000) or in the pulsar magnetosphere near (or starting near) the magnetic pole, in the so-called polar cap model (Ruderman et al. 1975; Harding et al. 2008). Outer gaps are charge-deficient regions with a strong electric field along the magnetic field near the null charges surface $\Omega \bullet B$, where Ω is

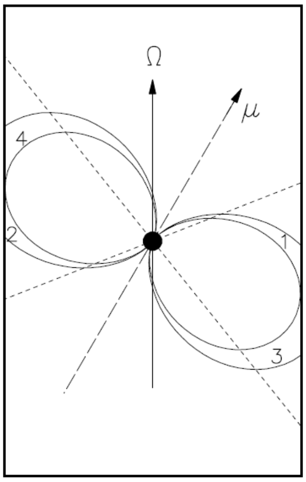

Figure 1: *Schematic illustration of the outer gaps of a pulsar. The outer gap extends from the null charge surface (dashed lines) to the light cilinder (Cheng et al. 2000).*

the stellar angular velocity and B is the local magnetic field (Cheng et al. 2000).

Among γ-ray pulsars the so-called soft γ-ray pulsar (only 18 have been detected above 20 keV and belong to this class), a population still partially understood, given the limited sample of objects. The soft γ-ray pulsar are all fast rotators with spin period between 16.1 ms and 324 ms. They tend to be a young population with characteristic ages range from 1,23 kyr (PSR B0531+21) up to 43 kyr (PSR J1813-1246) and very luminous with spin-down powers ($L_{Sd} = 4\pi^2 I\nu\dot{\nu}$ I is the moment of inertia of the neutron star assumed to be $10^{45}\,\mathrm{g\cdot cm^2}$) above $4\times10^{36}\,\mathrm{erg/s}$. Most of the soft γ-ray pulsar (11 members) have broad, structured single pulse profiles, and six have double or even multiple (PSRJ0835-4510; Vela pulsar) pulses. They typically show hard power-low spectra in the hard X-ray band, reaching their maximun luminosities in the MeV range (spectral turnover appears around 10 MeV). Most of the soft γ-ray pulsar are not seen at GeV energy by Fermi. According to a model proposed by Wang et al. (2013) (Wang et al. 2013; Wang et al. 2014) a possible explanation can be that the charges of the pair created in the outer gap move in opposite directions due to the electric field: one in the inflow directions, towards the surface of the neutron star, and another in the outflow direction. For the soft γ-ray pulsar the Earth viewing angle measured from the rotation axis is smaller (or close to) the inclination angle of the magnetic axis so we can see only the inward emission which interact with the high magnetic field and are converted into pairs, which them emit lower energy synchrotron radiation. A satellite that can also measure the polarization characteristics of γ-rays could discriminate between the various models, because the polarization signature is sensitive to the electromagnetic geometry (the location of the emitting zones; Cerutti et al. 2016).

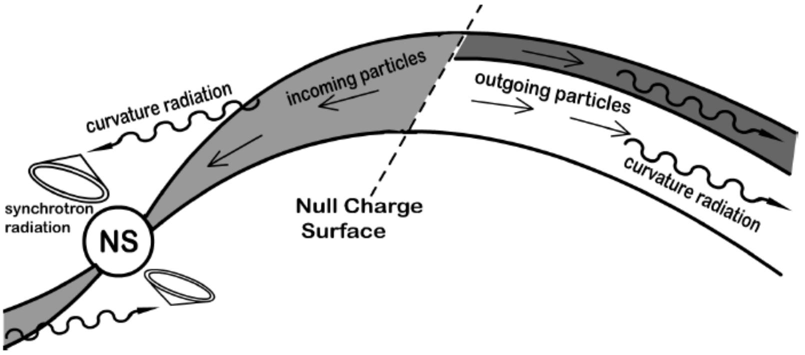

Figure 2: *Schematic view of the structure of the outer gap (Wang et al. 2013; Wang et al. 2014).*

Neutron stars (NS) magnetospheres are very rich of charged particles which is immersed in strong gravitational and electromagnetic fields. The plasma is pulled out from the star by the strong electric fields that are produced by the fast rotation of the stellar magnetic field. There are large-scale currents coming out from the stellar polar regions and return back to them in a thin sheet. This sheet flow along the separatrix between the open and closed magnetic field lines and in the case where the magnetic dipole is inclined with respect to the rotation axis the thin sheet ondulates around the star. The undulating current sheet structure is stable up to at least to distances of 10 light cylinder radius (the co-rotating part of the magnetosphere) (Kalapotharakos et al. I 2012). From the analysis of the spectral energy distribution (SED) and cut-offs at HE, we can infer that the sharp γ-ray pulses, observed in the pulsar, are produced in thin accelerators in the outer magnetosphere. Then we deduce that most of the open magnetosphere is filled with a dense plasma. This plasma is able to screen the electric fields and tend to be force free. Despite the advanced Magnetohydrodynamics (MHD) (Kalapotharakos et al. D 2012; Li et al.2012) and particle-in-cell (PIC) (Philippov et al. 2014; Cerutti et al. 2016; Kalapotharakos et al. 2017) simulations there are still open questions about the structure of the pulsar magnetosphere and where are the potential acceleration sites. Other questions relate to how specific regions can retain large electric fields along the magnetc field lines to accelerate primary particle to TeV energies, and which is the origin of the large space density of charges that support the magnetospheric currents.

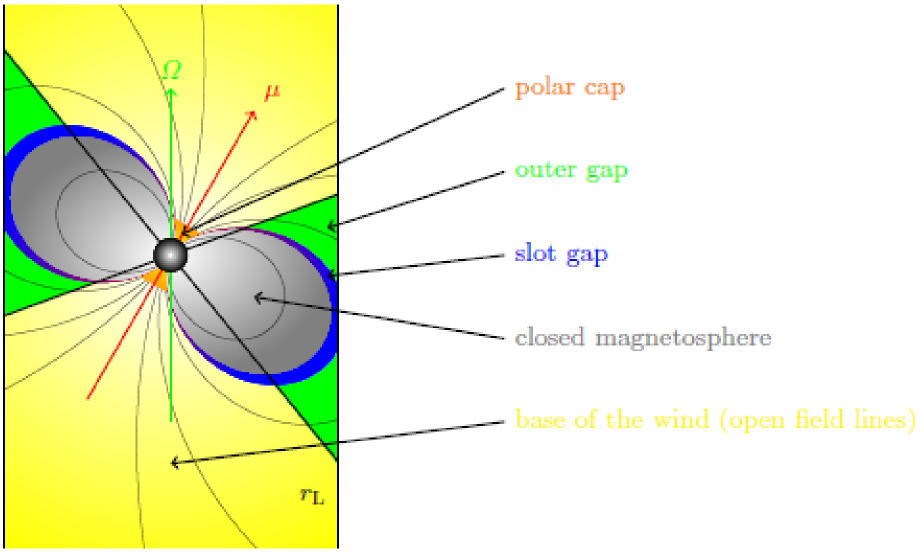

Figure 3: *Schematic view of the magnetosphere within the light cylinder.*

From the Fermi LAT data we can see that pulsar with largest spin-down powers or largest magnetic field strenghts are very soft and their SED peak in the 100 keV ÷ 100 MeV band. The peak energy of the SED is linked to the maximum energy of the pairs in the cascades. The SED of the pulsed synchrotron radiation at MeV energies allows to deduce the spectrum and number density of the bulk of the cascading pairs. The peak energy, E_{pk}, of the synchrotron component seen at MeV energies, which scales as $\gamma_{\pm}^2 B_{\pm}$, where $B_{\pm}$ is the ambient magnetic fields, and $\gamma_{\pm}$ is the maximum Lorentz factor, provides useful information about the origin of the cascade pairs. Joint observations at MeV end GeV energies could shed light on where the cascades take place, and on what are the dominant radiation mechanisms for the primary and secondary particles. Even if we assume that the GeV emission is generated by particles accelerated in the current sheet near or beyond the light cylinder, while the pulsed emission in the MeV band could be related to "polar" pairs produced at varius altitudes above the polar caps where the primary particles are accelerated.

Primary particles can produce pairs in cascades which lose their momentum perpendicular to the magnetic field to synchrotron radiation near the polar caps and acquire pitch angle as they stream into the outer magnetosphere through resonant absorption of radio emission (Harding et al. 2015). In this case, we can see that the neutron star surface magnetic field, B_{NS}, is related to the maximun energy of the pairs and so the SED peak energy should scale as $E_{pk} \propto B_{NS} B_{LC}$ (where, B_{LC}, is the magnetic field at the light cylinder). If the pair are produced in the outer-gap regions (Harding et al. 2015) the SED peak energy should scale as $E_{pk} \propto B_{LC}^{7/2}$. For this reason, it would be important to be able to compare the MeV peak energy for a large sample of pulsar so as to be able find the origin of the pair cascade in the in the open magnetosphere and to discriminate between the various models. The MeV data inform us how the magnetosphere manages to be near force free and massively produce the outward currents.

Polarization data are essential to identify which radiation process (synchrotron, Curvature or Inverse-Compton) is responsible for the pulsed emission (in the current sheet and in the open magnetosphere).

Comparing MeV and GeV information for pulsar with different magnetic fields near the polar caps, different spin-down power and different viewing inclination and magnetic obliquities, is very important for understanding the relative geometries of the primary accelerators and secondary cascades and the beam widths of their respective radiations. Mev luminosity is related to the multiplicity of secondary pairs in the cascade and so we can know the amount of plasma that eventually flows into the pulsar wind and termination shock.

An energetic pulsar produces a confined magnetic wind of particles (electrons and positrons) that creates a Pulsar wind nebulae (PWNe). The spin-down luminosity of the pulsar is dissipated by the outward flow of electron-positron pairs produced in cascades in the magnetosphere and accelerated near or in the termination shock. This is the reverse shock that reacts to the contact outer discontinuity of the nebula with the interstellar medium through pressure balance (Rees et al.1974). The Crab Nebula is the best-known PWN and is the brightest and most powerful. Like the others PWNe its spectrum consists of two components: synchrotron in soft γ-ray extending to 100 MeV and inverse Compton at higher energies extendind to at least 50 TeV. But for the Crab Nebula the IC enission is synchrotron-self Compton and the pairs are continuosly accelerated to a PeV (De Jager et al. 1992). While the inverse Compton emission in other PWNe is instead produced by up-scattering of the ambient photon fields. It is important to note that the Fermi sensitivity is right between the two components (SR and IC) for the PWNe where SR components extends to lower energies. An important question concerns what is the maximum energy of particles accelerated in PWNe and how does it depend on properties of the pulsar. Flares from the Crab PWN are observed by Fermi and AGILE (De Jager et al. 1992; Beuhler et al. 2014) while flux variations on year timescale probably due to GeV flares are observed by the Fermi GBM and Swift (Wilson-Hodge et al. 2016). Flares from PWNe with SR cut-offs in the MeV band could be detected by a satellite with a wide field of view. Also flux variations in the Crab PWN could be observed. We could then understand if the GeV flares produces variability at energies below 100 MeV and have information about the flare location and geometry from the timescale. The voltage across the open field lines determines the maximum steady-state (non-flaring) for particle accelerated in a PWN. This voltage is expressed by the formula:

$$V_{open} = 6\times10^{12} B_{12} P^{-2} \text{ eV}$$

where B_{12} is the pulsar surface magnetic field strength and P is the period. For most of the middle-aged PWNe the maximum of the SR spectrum is given by

$$\varepsilon_{SR} \propto V_{open}^{2} B_{s} \approx 0.14 \text{ MeV } L_{36}^{6/5} [\sigma/(1+\sigma)]^{1/2} \tau_{kyr}^{-3/10}$$

where B_s is the field strength at the termination shoch, L_{36} is the pulsar spin-down luminosity in units of 10^{36} erg s^{-1}, σ is the wind magnetization and τ_{kyr} is the pulsar age in kyr. Therefore, a satellite that is also sensitive in the MeV range should be able to see the SR cut-offs of the PWNe. This satellite could collaborate with Athena and CTA and give important information about the transfer of the pulsar spin-down power to the wind and how the radiating electron-positron pairs diffuse into the ISM (this mechanism can explain the observed cosmic-ray positron excess; Accardo et al.2014). We could also understand which is the maximum particle energy and increase the number of PWN detection at γ-ray energies.

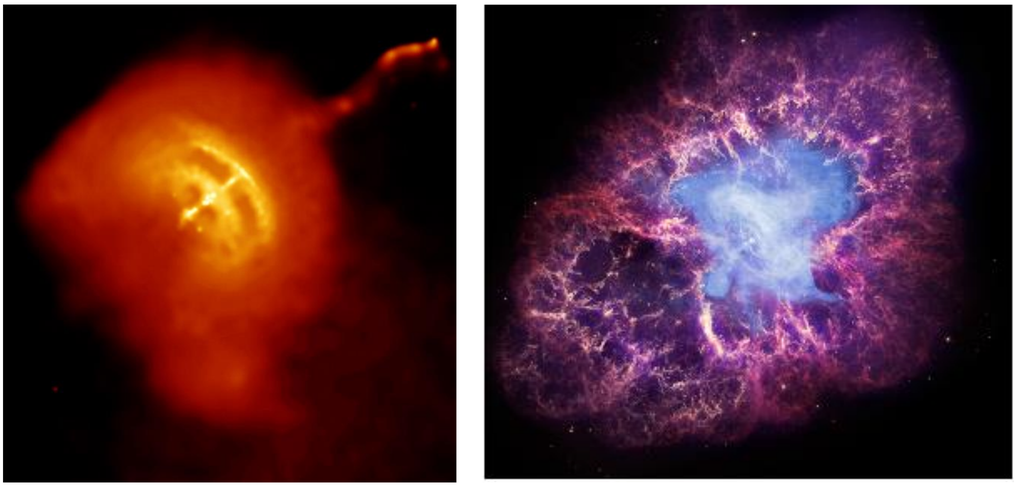

Figure 4: On the left: *The Vela Pulsar (centre) and its surrounding pulsar wind nebula.* **On the right***: image of Crab Nebula with X-ray emission (blue) from Chandra, optical emission (red and yellow) from HST, and IR emission (purple) from Spitzer* [**Slane, P. O. 2017, arXiv:1703.09311v1]**

1.1.2 Magnetars

Ultra-magnetized neutrons stars (or magnetars) form a subclass of the Radio Quiet Neutrons Stars (RQNSs). Among the RQNSs there are two groups: Soft Gamma Repeaters (SGRs) and Anomalous X-Ray Pulsars (AXPs), which display observational similarities:

- the X-ray luminosities of both of them are often larger than the values expected from tapping their rotational power reservoir ($\dot{E}_{rot} = I\Omega\dot{\Omega} \ll L_X$);
- they show no evidence for a companion star that could power their emission via accretion;
- both appear to be young, given their location within Supernova Remnants (SNRs) and star forming regions;
- They have similar timing properties with rotational periods 2 ÷ 12 s, and period derivatives $10^{-13} \div 10^{-11}$ s s^{-1}, that point to a magnetic field of $\sim 10^{14} \div 10^{15}$ G close, or stronger than, the electron critical magnetic field at which the cyclotron energy equal the rest mass energy:

  $$B_{crit} = \frac{m_e^2 c^3}{e\hbar} \approx 4.4\times 10^{13} G.$$

  Indeed, assuming that the spin-down torque is due to magnetic dipole radiation, the characteristic age (or "Spin Down Age") of the source and surface magnetic field can be estimated from the measured spin period P and its derivative $\dot{P}$

  $$t_{SDA} = \frac{P}{2\dot{P}}$$

  $$B = \left(\frac{3Ic^3 P\dot{P}}{8\pi^2 R^6}\right)^{1/2} \approx 3.2\times 10^{19} \left(P\dot{P}\right)^{1/2} \quad G.$$

  these equations can be obtained from the magneto-dipole formula (Pacini, 1967)

  $$\frac{dI\Omega}{dt} = -\frac{B_{pol}^2 R^6 \Omega^3}{6c^3} \sin^2 \alpha$$

  where α is the angle between the spin and magnetic axes, $\Omega = 2\pi/P$, is the spin frequency and $I \cong 10^{45}$ g cm^2 is the NS moment of inertia;
- The X-ray spectra are often well fit by a two-component model, a blackbody (BB; $kT \approx 0.5$ keV) plus a high-energy power-law (PL; photon index $\Gamma \approx 1.5 \div 3$) (e.g. Rea et al. 2008), or two thermal components ($kT_1 \sim 0.3$ keV and $kT_2 \sim 0.7$ keV) (e.g. Gotthelf & Halpern 2007; Tiengo, Esposito & Mereghetti 2008);
- The integral satellite detected their persistent emission from IR /optical range up to the hard X-rays ($\approx$200 keV). Only upper limits at higher energies, $\approx 1 \div 10$ MeV, are avaiable (CGRO Comptel observation);

This striking similarity motivated the suggestion that SGRs and AXPs share a common energy source. In fact, their behaviour is well described by the so-called "magnetar model" which is currently believed to be the most successful in explaining the peculiar emission properties of the SGRs and AXPs. These objects are thought to be strongly magnetized (isolated) neutron stars emitting across all wavelengths via the decay and the instabilities of their ultra B-fields (Thompson & Duncan 1993). Pons et al. (2007) found a strong correlation between the inferred magnetic field, and the surface temperature for a wide range of magnetic field (from magnetars to ordinary pulsars). In fact the presence of a magnetic field in the crust of a relatively young NS affected the transport properties of all plasma components (especially the electrons), and causes an anisotropic heat transport in the NSs envelope governed by the field geometry.

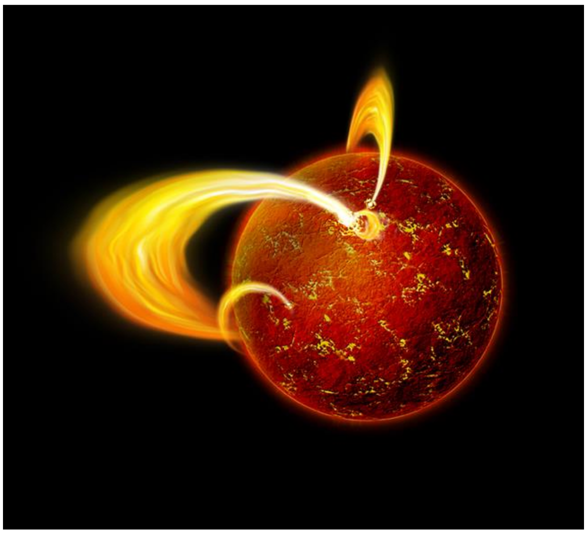

Figure 5: *Artistic impression of a magnetar.*

Since the evolving crustal magnetic field may also affects on the rotational evolution of the NS (see Pons et al. 2007), in order to deeper comprehend the NS evolution, a better understanding of the basic processes related to the NS thermal and magneto-rotational evolution is necessary.

Among the different behaviors there is the spectrum at high energy ($\approx 10 \div 100$ keV): the SGRs spectrum steepens while the AXPs spectrum exhibit a spectral upturn.

Through the reprocessing of thermal photons emitteted by the star surface with resonant Compton scattering (RCS) onto charges, moving in a "twisted" magnetosphere, we have the high energy magnetar emission (Nobili et al.2008; Thompson et al. 2002). However, the model still has unclear points that require a greater understanding such as the distribution of the scattering particles in the velocity space, or the geometry of the region where current flow (the "j-bundle"; Beloborodov et al. 2013). Furthermore, curvature radiation from ultra relativistic charges accelerated in the external magnetosphere could be responsible for the hard X-ray emission. This problem could be solved by a satellite with high sensitivity in the MeV range. In fact, according to the assumed velocity distribution of the charges, the geometry of the twisted region and the viewing angle, the theoretical predictions based on the RCS scenario are different above ~ 0.5 MeV. Moreover, polarization studies would be important for magnetars in the 0.3 ÷1 MeV range.

1.1.3 Gamma-ray emission from X-ray binaries

The γ-ray emission from X-ray binaries can be either powered by accretion onto a compact object or by collisions between winds from the binary components (Dubus 2013 and 2015). They are subdivided in High-Mass X-Ray Binaries (HMXBs), Intermediate-mass X-ray binaries (IMXBs) and Low-Mass X-ray binaries (LMXBs). It is interesting to observe that no HE γ-ray have been detected from LMXB in which there is a black–holes, except for V404 Cyg (Loh et al. 2016) where there is a hint of transient emission.

Millisecond pulsars (MSPs) are thought to be old, rapidly rotating (with a rotational period in the range of about 1÷10 milliseconds) neutron stars which have been spun up or "recycled" by the transfer of mass and angular momentum from a companion star in a close binary system.

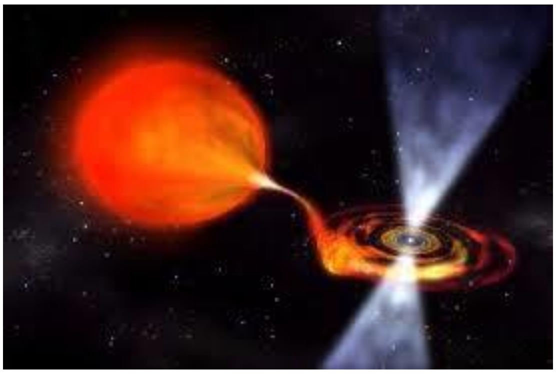

Figure 6: *An artist's impression of a millisecond pulsar and its companion*

In support of this scenario ms pulsations have been detected in accretion-powered LMXBs (Wijnands et al. 1998). These three transitional millisecond pulsars (tMSPs) belong to the “redbacks” class, systems with orbital periods less than 1 d and with low mass (~ 0.2 to 0.5 M_{Sun}) companions (typically G-type stars). Radio pulsation were detected in the LMXB state with a drastic increase in high-energy emission – more than an order of magnitude in X-rays and a factor of a few in gamma rays – and the appearance of a disk around the pulsar. The apparence of this strong variable radio flux, in the LMXB state, with a spectral index ~ 0 (Hill et al. 2011; Deller et al. 2015) is the tipical behaviour of microquasar (see later) suggesting that both γ-ray and radio emission originate in a jet. X-ray coherent pulsations are detected out to 100 keV with no high or low energy cut-off (Papitto et al. 2014).

There are several models that explain the enhanced high-energy emission, in all of them is important whether or not the disk penetrates the pulsar magnetosphere. If it does, we have a pulsar in propeller state and energized electrons emit synchrotron X-rays that them interact with the same electrons to create synchrotron self Compton (SSC) >100 MeV gamma rays (Papitto et al. 2014). If it does not there is the interaction of the acretion disk with the pulsar wind (Takata et al.2014) and we have synchrotron X-ray and inverse Compton (IC) off UV disk photons >100 MeV (Takata et al.2014).

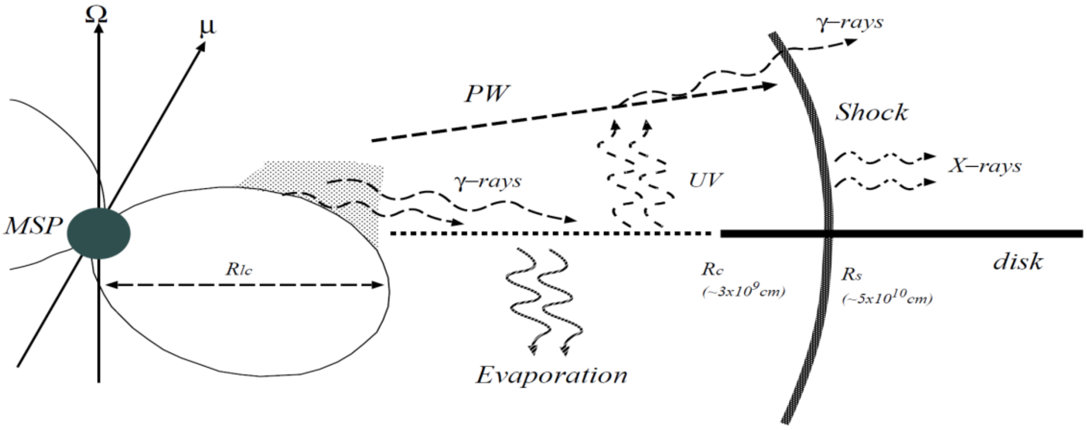

Figure 7: *Schematic vie of the enhanced high-energy emission from J 1023 system after 2013 late-June. Below the critical distance (R_C) the gamma rays evaporate the disk matter (Takata et al.2014).*

From measurements of the shape of the spectrum in the MeV range we could discriminate between the several models and constrain the physics and conditions in the binary system.

Gamma-ray binaries are composed of a massive star and a compact object and where γ-rays dominate the (SED), peaking above 1 MeV. In addition, from the COMPTEL data gamma-ray binaries are poweful MeV emitters. There are two dominant radiation mechanisms: synchrotron emission, from radio to X-rays/ soft γ-rays, and inverse Compton (IC) scattering of stellar photon, dominant in the high-energy and the very high-energy range (Bosch-Ramon and Khangulyan 2009). Gamma-ray binaries have been detected from radio up to TeV gamma-rays. For PSR B1259-63 it was possible to detect radio pulsations (Johnston et al. 1992) which leads us to think that the compact object is a rotation-powered pulsar and the γ-rays, emitted close to periastron, are due to the interaction of the relativistic wind from a young pulsar with the wind from its stellar companion (Dubus 2006). PSR J2032+4127 is a new γ-ray binary detected by Fermi-LAT. This source is a pulsar with a Be binary companion star and a long period system (~ 40 years). It is assumed that the gamma ray emission in this source is produced in the star-pulsar wind colliding region but observations in the MeV range are needed to fully characterize the γ-ray spectrum of the source. LS

5039, the best studied γ-ray bynary, is a γ-ray source at TeV energies but also there is a very strong MeV radiation, modulated along the orbit, that follow a synchrotron component coming from ≤1 keV and peaking around 30 MeV. Also here the observations in the MeV range would be necessary for explaining both the spectra and the orbital modulation. Furthermore, the MeV-GeV spectral range is situated between the synchrotron and the IC ranges (Paredes et al. 2006) and therefore essential to understand the physics originating the synchrotron and IC emmission from these objects. On the other hand, is also linked to the gamma-ray absorption and reprocessing on the spectrum. The observing window below ~ 100 MeV is important to understand which of the two mechanisms is dominant. If synchrotron emission is dominant and can exceed the 100 MeV limit (see the Crab Nebula) we have important physical information about highly relativistic motion, extreme particle acceleration and possible contamination by a different radiation component. Instead, if IC is dominant, we have information on how non-thermal particles propagate away from the stellar companion and observing IC orbital modulation we probe the geometry of the source.

For powerful pulsar with winds with a Lorents factor of about $10^5 \div 10^6$, the MeV photons can interact with the pulsar wind and produce electromagnetic cascade in the wind with strong γ-ray and lower energy radiation which modify the wind nature (Derishev and Aharonian 2012).

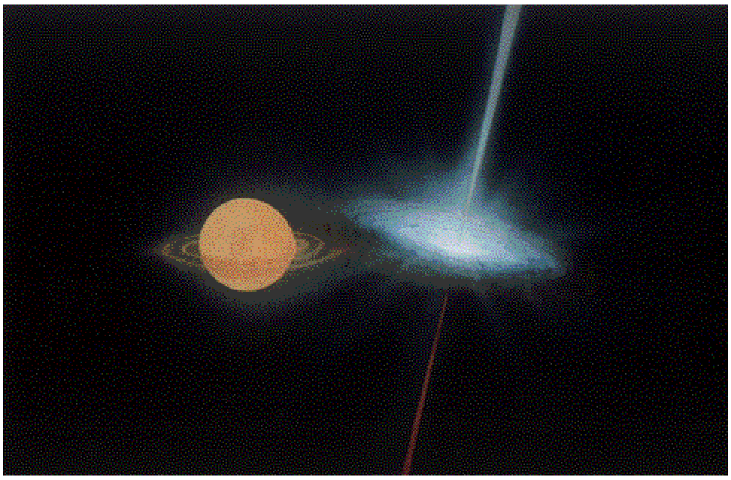

Figure 8: *Artist'simpression of a black-hole binary system with a relativistic jet, commonly termed a ``microquasar'' (credit: NASA/GSFC).*

Now, we consider the gamma-ray emission from accretion-powered X-ray binaries usually called microquasar, i.e. systems featuring jets. Among this object there are Cyg X-3 (Fermi LAT Collaboration, 2009) and Cyg X-1 (Zanin et al. 2016; Zdziarski et al. 2017), two HMXB, where we can see HE γ-rays. In Cyg X-3 we can obsserve γ-rays in its soft spectral state with a strong orbitally modulation which are interpreted according to a model proposed by Dubus et al. (2010)

and Zdziarski et al. (2012) as Compton scattering of the blackbody emission of the donor in the jet. But this model can not be verified due to the lack of accurate observations at the MeV range. We can see strong orbital modulation also in X-rays up to ~ 100 keV with the minimum around the superior conjunction (Zdziarski et al. 2012). Instead in Cyg X-1, an archetypical black-hole binary, we can see HE γ-rays in the hard spectral state where a compact radio jet is also detected. There is also an excess of emmission below 100 MeV in both hard and soft spectral states, appearing to connect to the HE tails observed in γ-rays (Zdziarski et al. 2017). Another important observation in Cyg X-1 is the presence of a strong polarized emission around 1 MeV (Jourdain et al. 2012; Rodriguez et al. 2015) which could be explained with synchrotron emission from the jet. If the MeV tail is thought to be linked to polarized jet synchrotron emission, in this case an intersection between the synchrotron and the compton components is expected below 100 MeV (Zdziarski et al. 2014). If instead the tails is due to Compton scattering by nonthermal electrons in the accretion flow, we have an intersection between the accretion and the jet emission. A detailed analysis of the MeV emission allows us to provide important information about the emission mechanisms and to investigate disk-jet interactions in accretion powered binaries. In fact, with observation below 100 MeV we are able to discriminate between the jet and the accretion components and to test several models in which the tail beyond the accretion-disc blackbody peak in the soft states of X-ray binaries is due to jet synchrotron emission. Then, through the observations of the γ-ray orbital modulation below 100 MeV (due to IC scattering of stellar blackbody photons) we could determine the γ-ray source along the jet and the jet orientation.

1.1.4 Globular clusters as γ-ray emitters

Globular clusters (GCs) are composed by luminous collections (~$10^5 \div 10^6$) of ancient low-mass stars (neutron stars, white dwarfs) packed in a symmetrical, somewhat spherical form.

Fermi LAT discovered recently several GCs emitting GeV γ-rays (Abdo et al. 2009 and 2010; Kong et al. 2010; Tam et al. 2011). Ter 5 is a particolar GC that emit γ-rays at TeV energies but also non termal diffusive radiation in the 1÷7 keV. This GeV emission is probally due to a cumulative emission produced in the inner MPS magnetosphere (Eger et al. 2010; Clapson et al. 2011). In fact, γ-rays pulsations are observed from two MPSs (B1821 (Freire et al. 2011) and J1823-3021 (Johnson et al. 2013)) within GCs. Another possible scenario for the GeV (TeV) emission is represented by the inverse Compton scattering process of electron-positron pairs injected from MSP magnetospheres into a dense low energy radiation field present within (and around) GCs (Bednarek and Sitarek 2007; Kopp et al. 2013; Cheng et al. 2010). The MPSs in the galactic field are very different from those observed inside GCs (Cheng et al. 2010). These MPSs in

GCs are probally captured by low-mass star and then their inner magnetic field could be different and produce a low energy electron-positron plasma. Gamma-rays and probally diffusive synchrotron radiation are produce by electron-positron pairs from MPSs which must cross a dense radiation field produced by the GCs, the nearby galactic disk and the microwave background radiation (Cheng et al. 2010). Enhanced GeV emission is observed in the MPSs while they are in the accretor tansition state. The electron-positron pairs, which can termalize in the atmosphere of the companion stars and/or their winds, could annihilate producing the narrow line ~ 0.5 MeV. The observation of this line gives information about the injection rate of the electron-positron plasma from the MPSs inside GCs.

Figure 9: *The Messier 80 globular cluster in the constellation Scorpius.*

1.1.5 Galactic sources as sites of cosmic rays acceleration

The understanding of different galactic processes (how Fermi acceleration works in various environments, the feed-back between cosmic ray acceleration, Galactic magnetic fiels and the dynamics of the interstellar medium) is important to identify the different contributors to cosmic rays acceleration.

A significant fraction of primary cosmic rays originate from the supernova explosions of stars. In fact shocks of supernova remnants (SNRs) accelerates a Galactic component of cosmic rays (Ginzburg and Syrovatsky 1961). From the γ-ray emission spectra of the middle-aged SNRs there is the evidence of hadronic cosmic rays. Even if a fraction of these cosmic rays is probably re-accelerated. Gamma-ray emission below ~ 200 MeV has been observed by AGILE and Fermi coming from two bright SNRs, W44 and IC443 (Giuliani et al. 2011; Ackermann et al. 2013; Cardillo et al. 2014). It is important to identify the so-called “pion bump”, the measurement of the specific shape of the hadronic γ-ray spectrum, in young SNRs sources to have direct evidence of directly accelerated (and not re-accelerated) cosmic ray in SNR shocks. Though the theoretical hadronic γ-ray spectra from SNRs are far from those obtained from the cosmic ray spectra (Malkov et al.2011). The spectra of cosmic rays released over the entire lifetime of the remnant are related with the instantaneous particle spectra (Hanusch et al. 2017). In fact the "pion bump" has been confirmed in two middle-aged SNRs ($t_{age} > 10^4$ yrs) with slow shocks $v_{sh} \approx 100$ km/s (Reach & Rho 2000) and then low cosmic ray acceleration efficiency. The study of the quantity of re-accelerated Galactic cosmic rays is important to understand how they modify the required source abundances and their impact on the propagation history of cosmic rays in the Galaxy. To do that, we need an excellent angular resolution and high continuum sensitivity. Re-acceleration of galactic cosmic rays dominates over acceleration of low-energy particles (Uchiyama et al. 2010; Lee et al. 2015; Cardillo et al. 2016) in old SNRs while is a secondary process in young SNRs where instead primary particles dominate (Telezhinsky et al. 2012; Telezhinsky et al. 2013; Pohl et al. 2015) and there are high velocity shocks. Them in young SNRs the observation below 200 MeV cames from freshly accelerated cosmic rays. We must also identify the nuclear de-excitation lines to infer the elemental composition of cosmic ray and where is the most conducive acceleration site in the supernova enviroment. The lines induced by the Ne-Fe group dominate in the 1÷3 MeV band while while those due to C and O in the 4÷6 MeV band. The study of nuclear de-excitation lines needs a satellite with high energy resolution (in particulary in low energy range).

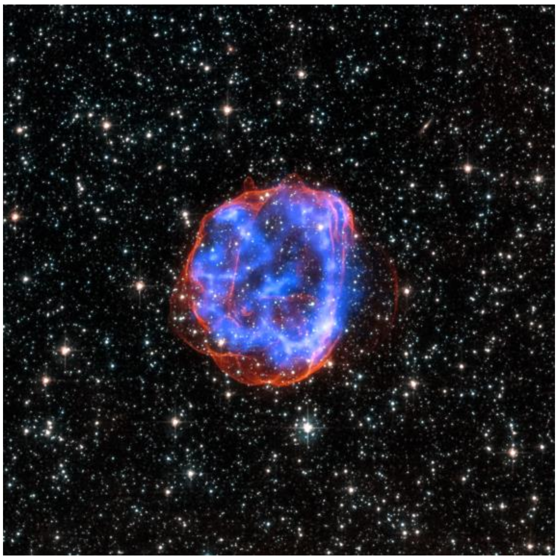

Figure 10*: A supernova remnant in the Great Magellanic Cloud, image that combines x-ray and visible light. (NASA)*

Furthermore we must determine the enviromental parameters (for example the level of the magnetic field amplification driven by cosmic rays) related to the correlation between the measurement of the non-thermal bremsstrahlung flux below 200 MeV from energetic primary electrons (which is decisive in determing the separation of leptonic and hadronic contributions to γ-ray emission) and radio synchrotron emission of the same electrons. This comparison provides a direct measure of the strenght of the turbulently amplified magnetic fiels (Cowsik & Sarkar 1980) which is very important in particle acceleration theory (Blandford & Eichler 1987). Finally, we must measure the impact on the elemental composition of cosmic rays at Earth created by the re-acceleration of Galactic cosmic rays at the shock fronts of SNRs. The acceleration efficiency and the time-dependent spectrum of the escaping particles are two vital parameters for the cosmic ray acceleration study in supernova remnants, but despite the efforts are still little known.

Another source of cosmic rays acceleration consists in the stellar winds. For example we could consider the system η Carinae (the most luminous massive binary systems of our Galaxy) It is composed by one of the most massive stars known (η Car A, the primary star with a mass ≥ 90 M_{SUN} and a radius of 0.5 AU) and of a companion (η Car B) believed to be an O supergiant or a WR star. The relative separation of the two stars varies by a factor ~ 20 with its minimum of a few AU to the periastron.

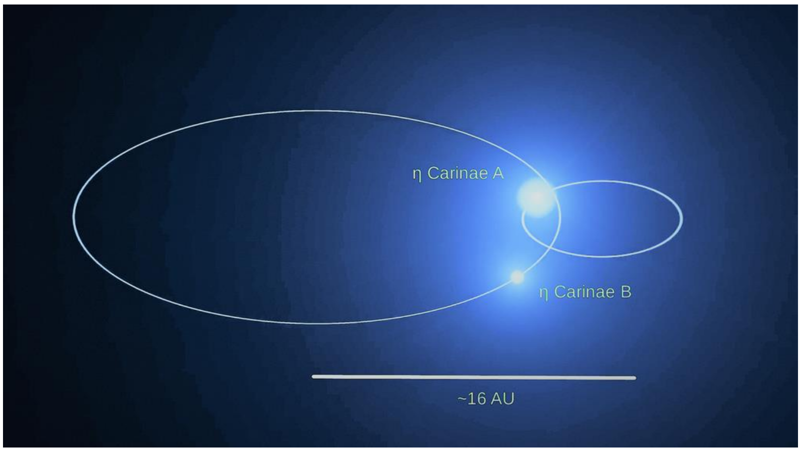

Figure 11: *Eta Carinae orbit.*

A colliding region of hot shocked gas is formed from the interaction of their supersonic winds. In this region charged particles accelerate via diffusive shocks acceleration up to high energies. The measurement of the maximun energy, that the electrons and hadrons reach in every cells of the hydrodynamic simulations presented by (Parkin et al. 2011), has been calculated by Balbo and Walter (Balbo and Walter 2017) with a dipolar magnetic field at the surface of the primary star. Particles in η Carinae could accelerate close to the knee of the cosmic ray spectrum. There are two types of model which explain the γ-ray emission of η Carinae the lepto-hadronic and the hadronic models (see Ohm et al. 2015).

The obscured molecular clouds, that actively form stars in our Galaxy, have been the subject of multi-wavelength studies. In star-forming region there is a particular relationship between stars, gas and cosmic rays. From these studies we have a lot of information about the physics of star formation and the radiation impact of massive stars on their parent cloud. However, the production of cosmic rays in star-forming region and their diffusion in those turbolent sites is still little known. In particular we must deepen the imprint (in spectrum and in composition) of star forming region on the cosmic ray distribution in the Milky Way. In the Cygnus X superbubble, where there are many OB stars, a cocoon of freshly accelerated hard cosmic rays has been observed by Fermi LAT (Ackermann et al. 2011). From the Advanced Composition Explorer (ACE) observations we know that the 20% of the local comic rays came from massive star outflow and ejecta. While the remaining 80% has been accelerated to cosmic-ray energies by supernova shocks (Murphy et al. 2016).

Figure 12: *The entire Orion Nebula in a composite image of visible light and infrared*

Massive stars and their massive supersonic winds are clustered in space and time. Therefore, it is interesting to ask ourselves if the cosmic rays after freshly escaping from their accelerators are confined for some time and potentially re-accelerated in the highly turbulent medium of star-forming regions. The supernova source of the recent detection of radioactive ^{60}Fe observed in the local cosmic rays must be located within 1 kpc (Binns et al. 2017). We deduced only locally the diffusion properties of the Galactic cosmic rays observing the Local Bubble and the Gould Belt which is characterized by its numerous OB associations (Grenier 2000). The favorable sites of cosmic ray acceleration in rich stellar clusters are multiple powerful winds of early-type stars and supernova remnants (Cesarsky and Montmerle 1983; Bykov 2014) which create the superbubbles, filled with hot X-ray emitting gas, over a time scale of ~ 10^7 years. In these superbubbles we have 10% efficiency of the ensemble of MHD shocks to transfer kinetic power to (re-)accelerate cosmic rays with a substantial temporal evolution of the cosmic ray spectra over 10 Myr. The main radiation mechanism consists of inelastic collisions of cosmic ray nuclei in the ambient gas and to the production of pions and γ-rays. The only means to measure cosmic ray nuclei are γ-ray observations because the detection of diffuse non-thermal X rays is difficult in these hot and complex regions. The maximum cosmic ray energy and the acceleration efficiency can be calculated using GeV-TeV observations. While from observations below 1 GeV we have information about the bulk of the cosmic ray population in the bubble and their diffusion lengths inside the bubble. The extended Cygnus X (far away 14 kps; Rygl et al. 2012) contains several thousand OB stars and is important for understanding the high-energy activity of superbubbles. The hard cocoon emits a flux in the 1÷100 GeV band of $(5.8 \pm 0.9) \times 10^{-8}\ \gamma \mathrm{cm}^{-2} \mathrm{s}^{-1}$ that corresponds to a luminosity of $(9 \pm 2) \times 10^{34} (D / 1.4\mathrm{pc})^2\ \mathrm{erg\ s}^{-1}$. It would be possible, with a satellite with high angular resolution, to separate the diffuse cocoon emission from other sources like pulsar PSR J2032 + 4127 with its wind nebula and the γCygni supernova remnant with its pulsar PSR J2021 + 4026.

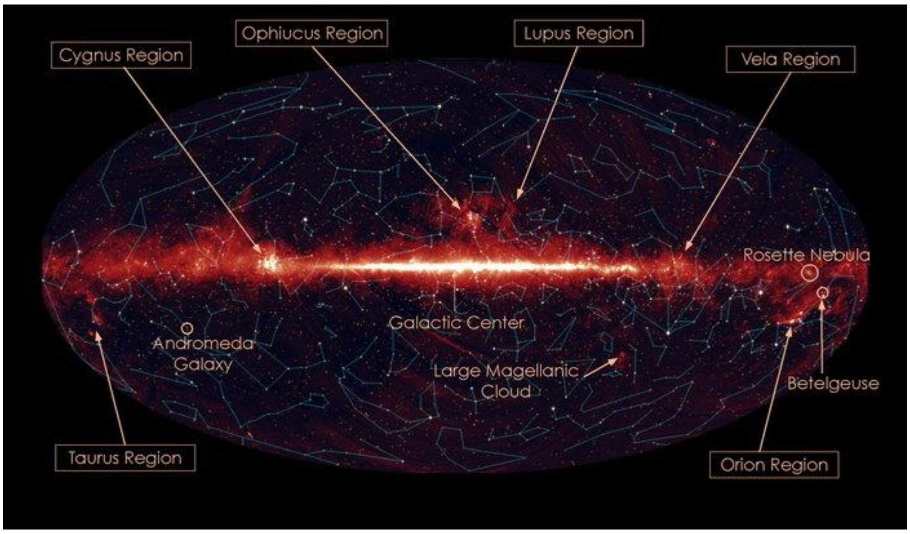

Figure 13: *All-sky map in infrared light with constellation and star forming regions (NASA).*

With a new satellite, we should be able to observe the cocoon below 1 GeV in order to deduce the energy distribution of the bulk of the cosmic ray nuclei and the cosmic ray pressure inside the bubble, to separate the emissions from cosmic ray electrons and nuclei and to search for spectral variations across the bubble with which to test possible acceleration scenarios by individual sources or by the collective action of wind and supernova shock waves. Recently, there is a a possible new γ-ray detection from a star-forming region in the Milky Way (Katsuta et al. 2017) observed by

Fermi LAT but severe confusion limits the identicationof the origin of the extended emission, even here the new satellite could provide new insights for study. The young OB associations NGC 2244 in the Rosette nebula and NGC 1976 in the Orion nebula, that can impart a fraction of the kinetic energy of their strong supersonic stellar winds to cosmic ray acceleration, will be visible from the new satellite below 3 GeV if a few per cent of the stellar-wind powers are supplied to cosmic rays. The observation in the MeV and in the TeV of active star-forming regions in different stages of evolution and for different cluster masses will extend our knowledge on the high-energy activity of turbulent bubbles blown by stellar clusters.

Finally, as the last possible source of cosmic rays, we analyze the Fermi bubbles (FBs). These were discovered by Fermi LAT (Su et al. 2010; Ackermann et al. 2014) and consist of two large structures (see in Fig.14), in the gamma-ray sky extending to 55º above and below the Galactic center. The FBs can be formed by emission of a jet from the supermassive black hole at the centers of the galaxy (AGN scenario)(Guo & Mathews 2012; Guo et al. 2012; Yang et al. 2012), by a spherical out-flow from the black hole (Zubovas et al. 2011), by a sequence of shocks from several accretion events onto the black hole (Cheng et al. 2011), or by a period of starburst activity with wind from supernova explosions (starbust scenario)(Sharp and Bland-Hawthorn 2010; Crocker & Aharonian 2011). With the γ-ray emission from the FBs, predictions of computer simulations of the evolution of jets from supermassive black holes (Guo and Mathews 2012; Yang et al. 2012), winds from supernova explosions, or cosmic ray driven winds (Wiener et al. 2017) can be tested to discover the properties and the origin of the bubbles.

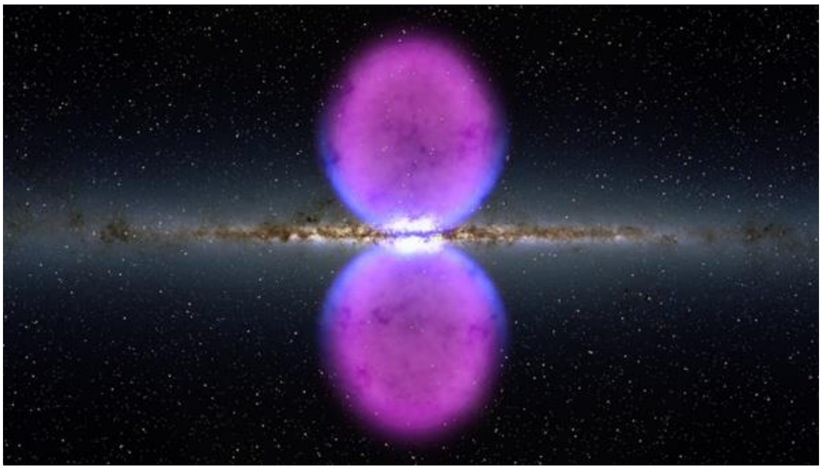

Figure 14: *The Fermi Bubbles of the Milky Way.*

We know that the emission of gamma rays above a few tens of GeV is mainly due to two emmission processes: inverse Compton (IC) scattering (leptonic scenario) or interactions of hadronic cosmic rays with gas (hadronic scenario). To distinguish the two scenarios at energy below 100 MeV, we can go to observe the characteristic cutoff in the hadronic gamma-ray spectrum due to non-zero mass of the π^0 meson. But this cutoff is not present in the FBs (Ackermann et al. 2014) as the spectrum below 100 MeV is dominated by secondary IC. To separate the two scenarios then we can use indirect signatures. The leptonic scenario is supported by the observed microwave haze emission coming from the FBs (Su et al. 2010; Ackermann et al. 2014). While the hadronic scenario is supported by the absence of a softening of the gamma-ray emission as a function of latitudes (although re-acceleration of electrons could explain a hard spectrum of gamma rays in the leptonic scenario; Mertsch and Sarkar 2011). The two scenarios would be distinguishable below 10 MeV but currently in this energy range there is no satellite with adequate sensitivity.

1.2 Multimessenger

1.2.1 Cosmic rays

Cosmic Rays (CRs) are very high-energy particles, mainly protons and atomic nuclei (99%) and solitary electrons (1%). Their energy spectrum is extended up to E ~ 10^{20} eV. The galactic CR are likely produced through Fermi acceleration processed in Supernova Remnant (SRN) shocks and in other exotic sources. The large number of photons observed in the Milky Way are due to both leptonic (bremsstrahlung and inverse Compton scattering) and hadronic (pion decay) interaction of cosmic rays (CRs) with the gas in the interstellar medium and the interstellar radiation field. Propagation models and direct CR measurements are often compared with this gamma-ray interstellar emission (see Acero et al. 2016). The CRs may be responsible for the driving of Galactic winds, which are the basis of the formation and evolution of the Milky Way. The process of star formation is strongly influenced by low-energy cosmic rays (LECRs), with kinetic energies $\leq 1\text{GeV}$ nucleon $^{-1}$, in fact they heat the dense star-forming clouds and they ionize the gas and initiate a rich network of chemical reactions (and production of gas coolants). The LECRs are seen as a primary source of ionization of dense molecular clouds and of coupling of the gas with the ambient magnetic field in these regions. The LECRs, also, contribute:

- to hold molecular cores in equilibrium against gravitational forces;
- to iniate a rich ion-neutral chemistry within the cold neutral medium of the interstellar medium (ISM);
- to drive large-scale magnetohydrodynamic turbulence and cause amplification of magnetic field in the ISM;
- to provide critical pressure support in starburst regions to launch Galactic winds into the halo (Grenier et al. 2015) and to regulate the gas transfer in and out of a galaxy (Zweibel 2013; Pakmor et al. 2016).

The LECRs are probally a fondamental component of the ISM but they are poorly know in composition and flux and less abundant in the local ISM. This has been demonstrated by the Voyager 1 spacecraft, that measured the local interstellar energy spectra of Galactic CR nuclei down to 3 MeV nucleon^{-1} and electrons down to 2.7 MeV nucleon^{-1}, beyond the eliopause (Stone et al. 2013) to avoid the solar modulation effect. From the data of the H_3^+ in diffuse molecular clouds, the density of LECRs is probally higher near a site of CR acceleration (for example SNRs) (Indriolo et al. 2010; Indriolo & McCall 2012). The LECRs can be produced by SNRs, OB associations (Montmerle 1979; Parizot et al. 2004), microquasars (Heinz & Sunyaev 2002) and normal stars producing astropheric anomalous CRs (Scherer et al. 2008). From the Be abundances in stellar atmospheres we know that a significant component of LECR nuclei in the Galaxy exists together with the standard CRs probally produced by diffusive shock acceleration in SNRs (Tatischeff & Kiener 2011). With the MeV gamma-ray astronomy we can study the various effects of sub-GeV hadronic CRs in the ISM. In fact π^0-decay γ-rays (from the interaction of CR nuclei with interstellar matter) dominate the diffuse galactic emission in the GeV range. Fermi LAT data above 100 MeV allow to set limits on the CR origin and propagation (Ackermann et al. 2011; Ackermann et al. 2012a; Ackermann et al 2012b; Casandjian 2015). An alternative system to be able to analyze hadronic CRs below the kinetic energy threshold for the production of neutral pions could be to go to observe the gamma-ray lines generated by nuclear collisions of CRs with interstellar matter in the 0.1÷10 MeV range. The most intense lines would be those of the ^{12}C, ^{16}O, ^{20}Ne, ^{24}Mg, ^{28}Si, and ^{56}Fe (Ramaty et al. 1979).

The nuclear line emission is composed of both narrow lines from excitation of heavy nuclei in the ISM and from broad lines generated by interaction of CR heavy ions with H and He, as well as thousands of weaker lines that together form a quasi-continuum in the range 0.1÷10 MeV (Benhabiles-Mezhoud et al. 2013). Some lines generated from interaction with interstellar dust grains can be very narrow, because some of the excited nuclei can stop in solid materials before emitting γ-rays (Tatischeff & Kiener 2004). Among these we have lines from ^{56}Fe, ^{24}Mg, ^{28}Si, and ^{16}O. In Fig. 15 We can see the predicted gamma-ray emission due to nuclear interactions of CRs in the inner Galaxy. The low-energy component in Fig. 15, responsible for observing the mean ionization rate of diffuse molecular clouds, is an important factor to deduce the composition, the spectral and spatial distribution of the LECR component in the Galaxy. From Galaxy formation simulation (Pakmor et al. 2016), we know that in the case where the cosmic rays diffuse isotropically in the disk we have these quickly diffuse out of the disk while with an anisotropic diffusion most CRs remain in the disk and therefore influence the dynamics of the gas in the disk. Fermi LAT and AGILE have collected a lot of data on CRs and and on the induced interstellar gamma-ray emission but for a deeper understanding of different emission processes and of the many model-dependent structures still unclear (such as Fermi bubbles, Loop I, outer Galaxy, the Galactic center excess) that show up as excesses over the adopted models (Su et al. 2010; Barkov & Bosch-Ramon 2014; Ackermann et al. 2014; Ajello et al. 2016; Acero et al. 2016), we need a satellite with a better angular resolution for gamma-ray and a broader energy coverage.

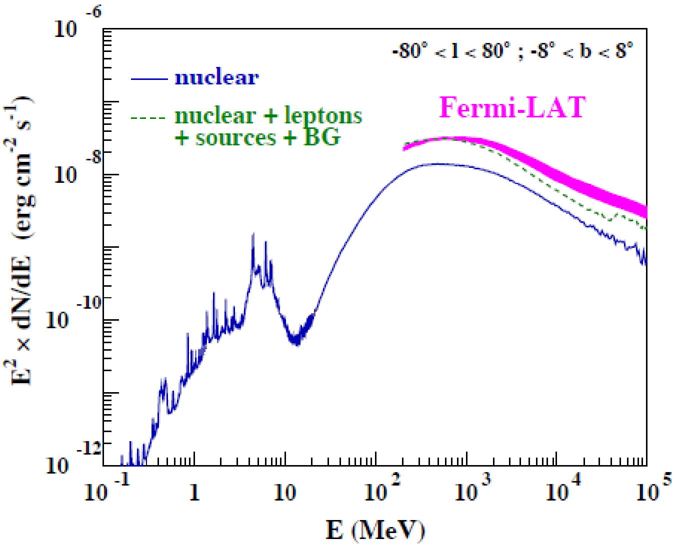

Figure 15: *Predicted gamma-ray emission due to nuclear interactions of CRs in the inner Galaxy (longitude -80º < l<80º and latitude -80º < l<80º). The gamma-ray line emission below 10 MeV is due to LECRs, whose properties in the ISM have been adjusted such that the mean CR ionization rate deduced from* H_3^+ *observations and the Fermi-LAT data (magenta band) at 1 GeV are simultaneously reproduced (adapted from Benhabiles-Mezhoud et al. (2013)). The dashed green line shows the total calculated emission when adding leptonic contributions, point sources and extragalactic gamma-ray background that were taken from Ackermann et al. (2012b).*

The new satellite will have to analyze the distribution of CR sources and their propagation in the Galaxy describing their density and spectral variation over the Galaxy. However, despite of the limited angular resolution of Fermi LAT and AGILE it has been possible to observe a large propagation halo size, additional gas in the outer Galaxy, and / or a CR source distribution (Ackermann et al. 2011; Ackermann et al. 2014). Observations of the interstellar emission in gamma rays allow to observe the large-scale distribution and spectrum of CRS and to deduce CR propagation and interactions in the Galaxy. Unfortunately our knowledge of the diffuse emission from the Galaxy at the MeV energies is very limited (Orlando et al. 2017). From hard-X-ray spectrum up to MeV ranges measured from SPI on board INTEGRAL mission and COMPTEL, we know that the measured diffuse intensity of the Galactic ridge is a factor of 5 above the baseline inverse Compton models, but this may be due to diffuse inverse Compton emission from an increased electron density or an interstellar radiation field. Or there can be contamination from point-like sources that can not be resolved with current satellites. Hadronic gas-related emission peaks at GeV energies, while below 100 MeV the interstellar emission is produced by both inverse Compton scattering of CR electrons on the interstellar radiation field and cosmic microwave background and by bremsstrahlung emission due by CR electrons interactions with gas. Moreover, the inverse Compton emission should dominate interstellar diffuse component below few tens of MeV. A satellite in the MeV range (ie well below the peak of the hadronic pion-decay at 67.5 MeV) will allow us to observe the full pion-decay signature, as well as to understand CR protons, Helium and leptons. Some γ-rays come from CR nuclei in inelastic collisions with gas nuclei. This satellite can separate the different components that are degenerate with the inverse Compton component (such as the extragalactic diffuse emission and the dark matter emission in the Galactic center). Moreover, down to the below GeV energies we could have from the bremsstrahlung and the inverse Compton emission the distribution of the CR electrons in the Galaxy. From interstellar radio synchrotron emission produced by the same electrons that produce inverse Compton at MeV energies we would obtain model constraints on the leptonic component and CR electrons (Strong et al. 2011; Su et al. 2010). The latter are particularly interesting to study as they often remain close to their sources (they have more energy losses than protons and heavy nuclei) and can therefore better describe the inhomogeneities. The new satellite will have high PSF so it will be able to provide high-quality images that will allow us to derive essential information on CRs and their propagation in the Galaxy.

We need observational constraints on the degree of anisotropy of CR diffusion, on their properties on the scales of star-forming regions, on their penetration inside the dense gas and their feedback on the multi-phase structure of clouds. It is important to study the gas mass of ISM at all scales and in several phases to have detailed information about the galaxy evolution and in connecting the mass distributions of stars and of their parental clouds. The full γ-rays census of the gas mass give information on the use of other gas tracers. Most of the mass consist of neutral gas at medium densities ($0.1\text{-}10^3$ cm^{-3}), in atomic and molecular forms that are commonly traced by HI (21 cm) and CO (2.6 mm) lines. There are three problem, the first is to analyze the “dark” neutral medium (DNM) in the H-H_2 interface. Gathering optically-thick HI and CO-dark H_2, the DNM easily escapes the observations (Grenier et al. 2005; Planck Collaboration, Fermi Collaboration, 2015; Pineda et al. 2013). The second is to estimate H_2 masses because cold H_2 molecules can not be detected directly. The integrated CO line intensities and the H_2 column densities are linked to the X_{CO} factor. Then the X_{CO} ratio must be evaluated in a variety of molecular clouds more or less susceptible to UV radiation (Smith et al. 2014). The third is to determine dust grains evolution in the gas phase. The grains emission cross section and the their specific reddening change with increasing gas density (Remy et al. 2017; Remy et al. 2017 submitted to A&A). Through infrared dust emission is possible to determine the existence of gas in distant galaxies. Therefore, evaluating the changes in dust properties allows to understand the galaxy evolution. CR electrons with lowest energy (below the pion bump) heat and ionize the gas, while the bulk of the CRs with higher-energy provide pressure support. It is possible to trace the gas with the CRs starting from the hypothesis that there is a uniform CR flux through the phases of a given cloud complex, and that there are measurements of the gamma-ray emissivity spectrum for nucleon gas in the atomic envelope assuming that gas mass can be measured by HI line emission. We know that the concentration or exclusion processes in the cloud are important at momenta below 1 GeV (Schlickeiser et al. 2016) for this, CR nuclei with higher energies, above the pion bump, can serve to estimate X_{CO} ratios, to reveal DNM envelopes of clouds, and to measure dust properties for nucleon gas. This system is strongly supported by the large CR diffusion lengths in the ISM (Zweibel 2013) and the uniformity of the GeV gamma-ray spectra that have been detected in the gas phases of nearby clouds (Grenier et al. 2015). With a satellite that can observe bremsstrahlung intensity below 50 MeV we could have accurate derivations of the spectrum of CR nuclei at low momenta. With greater sensitivity we could observe the CRs content in faint cirrus clouds and compare it with that of more massive clouds with strong and entangled magnetic fields. The estimate of X_{CO} gradients across molecular clouds requires a greater sensitivity and spatial separation of the different gas phases. This estimate will allow to measure the relative efficiency of the formation and photodissociation of CO molecules as the H_2 gas becomes denser (Bertram et al. 2016). With better angular resolution we could see dust evolution for gas nucleon to the densest, coldest molecular cores where grain evolution is strongest.

1.2.2 Neutrinos

Neutrinos allow to study high-energy cosmic sources. Neutrinos are neither deflected by the magnetic fields nor absorbed like photons in pair production via γγ interactions. Neutrinos at TeV-PeV energies are produced by the decay of charged pions produced in inelastic photo-hadronic ($p\gamma$) or hadronuclear (pp) processes. In these processes, protons are about 20 times more energetic than the resulting neutrinos. There is a kinematical threshold in the photoproduction of υs (and photons) via pion decay. Photoproduction occurs through Δ^+ the resonance slightly above this threshold: $p\gamma \rightarrow \Delta^+ \rightarrow N\gamma$. In this case we have that the proton energy must be $E_P \geq 350\ \mathrm{PeV}/\varepsilon$ (for UV photons emitted in AGN jets, $E_P \geq 10\ \mathrm{PeV}$ i.e. above the knee), where ε is the target photon energy in eV. Ultra high energy cosmic rays (UHECRs) are probably accelerated during the photoproduction of neutrinos on optical/UV photons. IceCube has detected a diffuse flux of cosmic neutrinos but the sources are still unknown. The signal observed by IceCube could come from like star-forming and / or start-burst galaxies, GRBs, or AGNs. Microquasars are also possible candidates. Ahlers et al. have done a review on neutrino source candidates and multi-messenger connections (Ahlers et al. 2015). The neutrino emission in GRBs is probably in temporal coincidence with the prompt γ-ray emission. GRBs could generate highest energy cosmic rays and neutrinos only if the central engine is surrounded by dense material envelope, like the chocked jets proposed in (Senno et al. 2016). Approximately 27% of the observed IceCube intensity probably comes from blazars. However, we must consider that neutrinos can be generated in flaring events for this reason we must keep neutrino and gamma-ray signals under observation. For example, the long-lasting gamma-ray (0.1 ÷ 300 GeV) outburst of the blazar PKS B1424-418 occured in temporal and positional coincidence with the third PeV-energy neutrino event (IC 35) detected by IceCube with a small a posteriori chance coincidence probability of ~ 5% (Kadler et al. 2016). Also on September 2017 the Fermi-LAT has detected an enhanced gamma-ray emission from a blazar associable with the neutrino IC170922A (GCN IceCube EHE 50579430 130033; Tanaka et al. 2017). It is important to detect excesses of events due to astrophysical sources by differentiating the directional, energy and time information from the signal emission from the background. Unfortunately, so far the observation of very high-energy (VHE) gamma-rays counterparts of high-energy IceCube events was unsuccessful (Santander et al. 2017; the MAGIC Collaboration, 2017) probably because gamma-rays emitted in association with neutrinos are absorbed, perhaps in the sources themselves or during propagation over large redshifts. The ANTARES and IceCube neutrino telescopes (Ageron et al. 2011; Abbasi et al. 2009) are inserted into an alert system and when an interesting neutrino event is detected, this allows a real-time multiwavelength follow-up (Ageron et al. 2012; Aartsen et al. 2017). The alert system is called "TAToO" (Telescopes and ANTARES Target of Opportunity) and collects Broad-band data, from the radio range to the very high-energy γ-ray regime as Target-of-Opportunity (ToO) observations to the partners. The studies of IceCube and ANTARES correlate the space and time neutrino emission with the high-energy electromagnetic emission of a transient or flaring source. This requires a correlation between X-ray / gamma-ray flares and neutrino emission. These studies have so far failed to identify the sources of cosmic neutrinos but have succeeded in putting model constraints (Aartsen et al. 2016; Albert et al. 2017). In the coming decades KM3NeT and IceCube-Gen2 will succeed respectively at ANTARES and IceCube, significantly improving the current performances. With these upgrades and thanks to the use of multi-wavelength facilities operating at the same time we will verify a considerable improvement of the follow-up activities. Which perhaps will allow the first incontrovertible identification of the electromagnetic counterpart of astrophysical neutrinos. We would need a satellite with ToO capabilities to allow repointing of the instrument within 3-6 hours and with a large field-of-view (FoV) to increase detection probability. In the case where the neutrino flux comes from photo-hadronic processes (Murase et al. 2016), the sources of the astrophysical neutrinos could be opaque to 1÷100 GeV γ-ray, this was found connecting the pγ and γγ optical depths. Therefore, we have a population of cosmic-ray invisible accelerators in GeV-TeV γ-ray but bright in the X-ray and MeV range (Senno et al. 2016). The new satellite with its wide FoV in addition to detecting variable point-like sources (such as microquasars, AGNs, etc) will rebuild their MeV lightcurves. These will serve to identify neutrino counterparts. In addition, the doublehumped SED of blazars peaks at MeV energy and can be described by both hadronic and leptonic processes. The new satellite will also have to be sensitive in the MeV range so as to choose the best candidate for a neutrino emission, and to have a good polarimetric capability to reveal the structure of the magnetic field and test the presence of hadrons in relativistic jets.

We don’t know what processes generate observed cosmic neutrinos (pγ or pp processes). But the pp models would be in tension with isotropic extragalactic γ-ray background (IGBR) this makes the pp origin of the cosmic neutrino flux observed by IceCube unlikely. To limit the population models of the extragalactic gamma-ray background (EGB) it will be important to measure the spectral features in the 10 - 200 MeV range this will detect the multi-messenger connection between gamma-rays and neutrinos.

1.2.3 Gravitational Waves

On 14 September 2015 the two Advanced LIGO interferometers detected for the firsttime gravitational waves (GWs) from the merging binary black hole (BBH) system (GW150914; Abbott et al. 2016a). After this first detection, another three have followed, again from BBH mergers (GW151226; Abbott et al. 2016b, GW170104; Abbott et al. 2017, and GW170814) reported by both the Virgo and LIGO collaborations.

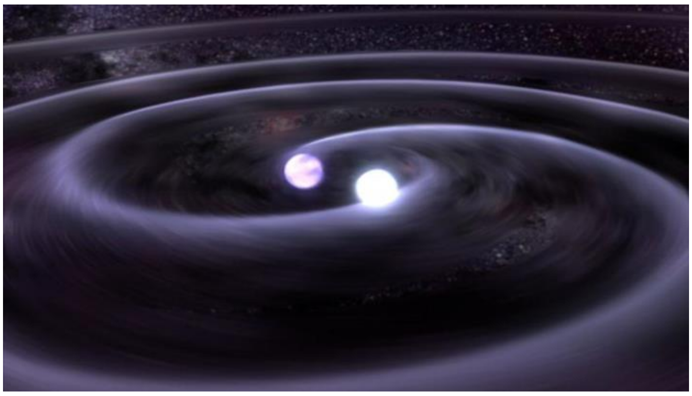

Figure 16: *This illustration shows the gravitational waves thought to be produced by two orbiting white dwarf stars in a binary system called J0651, according to an August 2012 study [NASA].*

Moreover, on 17 August 2017 LIGO and Virgo have detected the first GWs signal GW170817 from the coalescence of two neutron stars about 1.7 s before the gamma-ray signal detected by the Fermi-GBM instrument. The event GW170817 marks an important goal because thanks to the subsequent follow-up it was possible to identify for the first time the electromagnetic counterparts in the visible, X-ray and radio bands (Abbott et al. 2017) making possible a multimessenger campaign.

However, LIGO and Virgo are more suitable for the detection of coalescences of binary systems made by two neutron stars (NS-NS) or a neutron star and a stellar mass black hole (NS-BH). These systems are expected to emit short Gamma-ray Bursts (GRBs) (see sections 1.3.1, 4.2 and Berger 2014) and this is supported by the association between GW170817 and the GRB 170817A detected by Fermi-GBM (Goldstein et al. 2017). While NS-NS mergers entail significant mass ejection, which interacts with the surrounding medium producing a remnant in which the accelerated electrons can produce synchrotron radiation in X-rays (Takami 2014). GW and electromagnetic emission (EM) give complementary information as GW gives information on the physics of the source (i.e. the mass and the distance) while EM give information on the position of the burst. The identification of the EM counterpart of GW presents difficulties, since the current ground-based interferometers provide a sky localization in order of tens of hundreds of square degrees (Abbott et al. 2016c) in which there are hundreds of optical transients spatially and temporally coincident with GW (Nissanke et al. 2013). The search is simplified to gamma ray energies as the number of transient events is smaller. In NS-NS mergers the EM counterparts are short GRBs accompanied by a thermal signal associated to the “kilonova” emission (Barnes et al. 2016; Hotokezaka et al. 2016). The short GRBs emission is believed to be beamed, and unfortunately in most NS-NS merger events, this emission occurs off-axis given the small opening angle ~ 10^{o} of the jet (Fong et al. 2014). To detect these off-axis GRBs we need very sensitive gamma-ray instruments.

There is polarization in the eventuality that jet launching is driven by magnetic energy. This polarization can be accentuated if there exists an anisotropy caused by off-axis observations (Hotokezaka et al. 2016; Granot 2002). When we look at high-energy MeV-GeV emission, the polarization can allow us to distinguish different emission processes such as inverse Compton acceleration of leptons (no polarization) and synchrotron polarized emission from hadrons. When there will be the third generation of ground-based interferometer projects a satellite will be necessary that is also sensitive in the gap in the energy region from X-rays up to GeV and TeV gamma-rays. In addition there will be the space detector eLISA which will detect GWs coming from massive $10^4 \div 10^6$ M_{SUN} BHs that are thought to possess magnetized circumbinary disks powering EM emission. The new satellite must have a large FoV to maximize detection probability and establish an accurate sky localization so as to facilitate the follow-up of the GW events by other telescopes. As we have already said for neutrinos, even in the case of GWs we need time analysis of the ToO type. Thanks to the joint emission of GW / EM we will have important information about the formation and evolution of compact objects of different mass through cosmic history.

1.3 Time-resolved Gamma-Ray Astronomy

1.3.1 Gamma-ray Bursts and Polarization

Gamma Ray Bursts (GRBs) were first observed in 1967 by the Vela satellite Network (Klebesadel, Strong, & Olson 1973). The Burst and Transient Source Experiment (BATSE) on the Compton Gamma Ray Observatory (CGRO) observed the light curves of several GRBs discovering that they are very different and structured (Marani et al. 1997). Furthermore, the BATSE observations of GRBs provided the first clear indication of their extragalactic origin given their isotropic distribution (Metzger et al. 1997).

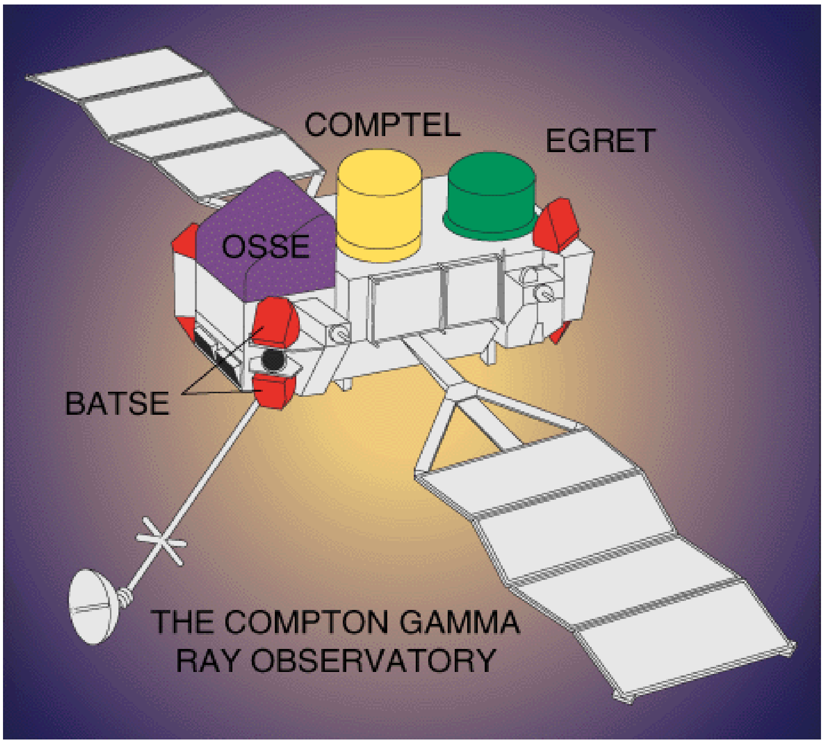

Figure 17: *The Compton Gamma Ray Observatory.*

GRBs are subdivided into two categories: the long GRBs originated by the core collapse of massive stars, and the short GRBs (<2 seconds) linked to the merging of two compact objects (NS-NS or NS-BH). In both cases the central engine is probably a compact object (BH or highly magnetized NS - magnetar) which is able to emit (through neutrino and / or magnetic processes) to (isotropic equivalent) energy of $10^{52\div54}$ erg within 0.1÷100 seconds in the form of high energy keV-MeV photons. The recent observation of GWs is linked to the short GRBs. In GRBs we can distinguish two distinct phases: the first consist of prompt emission generated by a jet forming during the gravitational collapse and characterized by an initial burst of high energy gamma rays, the second one is the afterglow which consists of a long-lasting (days/months) multi-wavelength emission due to jet interactions with the ambient medium (Gehrels 2004; Mészáros 2006). The origin of prompt emission is among the most debated issues. We believe that prompt emission can be generated by energised electrons (accelerated either by internal shocks or magnetic reconnection events) that radiate via synchrotron emission (Meszaros & Rees 1993). In this case we can expect different intensities of linear polarization (Fan et al. 2004; Zhang et al. 2011) according to the different models:

- In the ordered-field model (SO) we have a highly polarized emission produced by a helical magnetic field advected from the central engine. The emitted photons would be polarized at a variable angle over time when they emit in the line of sight (Lyutikov et al. 2003; Granot 2003; Toma et al. 2009), due to patches of different polarization over the emitting shell.
- In the random-field model (SR), sizable magnetic fields on plasma skin depth scales are produced with random directions in the collisionless shocks that are formed in the jet. These fields then generate synchrotron emission and axisymmetric polarization along the line of sight. If one observes on-axis (i.e. the angle between the line of sight and the jet axis is less than the jet opening angle), the polarization vectors cancel each other out, and we have a small measured polarization. If instead we observe that off-axis the polarization vectors do not fully cancel and we have a degree of observed polarization of 30% or 50% depending on the Lorentz bulk factor (Granot 2003; Nakar et al. 2003; Toma et al. 2009).
- In the synchrotron model with random fields on hydrodynamic scales (SH) the internal shocks may also produce strong magnetic fields with random directions, much larger than the plasma skin depth scales with respect to the previous model. The polarization in this model is small (Inoue et al. 2013; Toma 2013).

Other possible models are: the photospheric model with a maximal polarization degree of 40% (Beloborodov 2011; Toma 2013), or models (Beloborodov et al. 2014) that suppose that the high-energy photons are generated by inverse Compton scattering of the prompt shock with time delays, strength and spectral shape depending on the surrounding wind density. It is difficult to distinguish one of these models from a single GRBs observation. The physics at play can be understood from the correlation of the polarization degree and angle with other parameters while time-delays and polarization changes in the MeV range (Toma 2013; Rybicki et al. 1979) can be used to find

Lorentz invariance violation. Returning to the electrons that radiate via synchrotron emission, a possible solution to the discrepancy between the observed keV-MeV spectral shape and the expected synchrotron spectrum (Preece et al. 2000; Ghirlanda et al. 2003; Frontera et al. 2009; Vianello et al. 2009; Nava et al. 2011; Goldstein et al. 2012; Sakamoto et al. 2011) is in the synchrotron radiation in moderately fast cooling.

We have little knowledge in the 1÷100 MeV energy range of the GRB prompt emission. Until now it has not been possible to observe the prompt emission high energy spectral tail due to the poor effective area of the current satellites in the 1÷100 MeV range. According to Vianello et al. (2017) (Vianello et al. 2017) there are two interesting cases (GRB 100724B and GRB 160509A) in which we observe that the prompt keV÷MeV spectrum has an softening (located at 20÷60 MeV and 80÷150 MeV, respectively) which can be well described by an exponential cutoff. From these data we deduce that the Lorentz factors are in the range Γ=100÷300. Ackermann et al. (2012) were able to see the presence of a cutoff only in six cases out of a sample of 288 GRBs by calculating Lorentz factors in the range ~ 200 to ~ 600. EGRET (e.g. Gonzales et al. 2004) was the first to detect the presence in addition to the prompt emission, of another spectral component participating to the emission at energies above 10-50 MeV. The duration of this high-energy emission is often longer ($\geq$a factor of 10) than the duration than the prompt, moreover its onset is delayed by few seconds, and its spectrum is generally harder than the keV÷MeV component (Ghisellini et al. 2010; Panaitescu 2017).We must study the spectrum at MeV-GeV energies in order to understand the two little-known acceleration processes: the mildly relativistic shocks and the acceleration in magnetic reconnection. A break occurs in the high energy powerlaw behavior when γ-γ absorption within the source becomes relevant producing a cutoff whose position depends on the value of the bulk Lorentz factor. The presence or absence of this cutoff allows to calculate (or place constraints on) the bulk Lorentz factor. We can see that there is a peak in the light curve due to the afterglow component when the outflow is decelerated. Through this peak we can deduce the maximum velocity attained during the fireball expansion before the deceleration. Through this fundamental parameter the modeling of GRB emission is possible. Fermi / LAT measured the largest Γ_0 using the GeV light curve peak (Ghirlanda et al. 2010; Ghirlanda et al. 2012; Liang et al. 2010; Liang et al. 2013). To understand what is the shape of the high energy part of the prompt spectrum and what are the properties of the high energy synchrotron afterglow spectrum we must distinguish between the two components (prompt and afterglow) using the observations in the 10 MeV-1 GeV range. We need a satellite that covers the energy range in which the prompt and afterglow emission is superimposed and that responds to a series of questions still open: such as what is the electron acceleration mechanism? and what is the dynamic of the outflow? The answer to these questions will be studying the high energy prompt emission spectrum and checking if it is a powerlaw or has a cutoff and how it evolves in time (softening or hardening). We could also calculate the highest bulk Lorentz factors in long and short GRBs, the properties of ultra-relativistic shocks, the fireball energy content during the afterglow phase, and the effciency of the prompt mechanism.

Finally, we will measure the MeV-GeV characteristics and polarization in the prompt and afterglow phases and having information on the delay between GRBs and gravitational waves and new limits for the Lorentz invariance violation over a very wide energy range.

1.3.2 Active Galactic Nuclei in flare

The identification of the processes in the central engine responsible for the highest energy photons in Active Galactic Nuclei (AGN) is of primary importance. Their variability features are still not understood unlike their stationary SEDs that can be explained by different models. Lepto-hadronic models can explain complex variability patterns depending on the dominant process responsible for the gamma-ray emission while in the leptonic models we assume simultaneous flux increase in the low energy and high energy peak. Markarian 421 and Markarian 501, two of the most luminous blazars known, have been the subject of multifrequency campaign (Abdo et al. 2011a; Acciari et al. 2011; Abdo et al. 2011b; Fossati et al. 2008; Pian et al. 2013; Lichti et al. 2008) which led to the conclusion that their quiescent-state SED can be described either by leptonic or hadronic models.

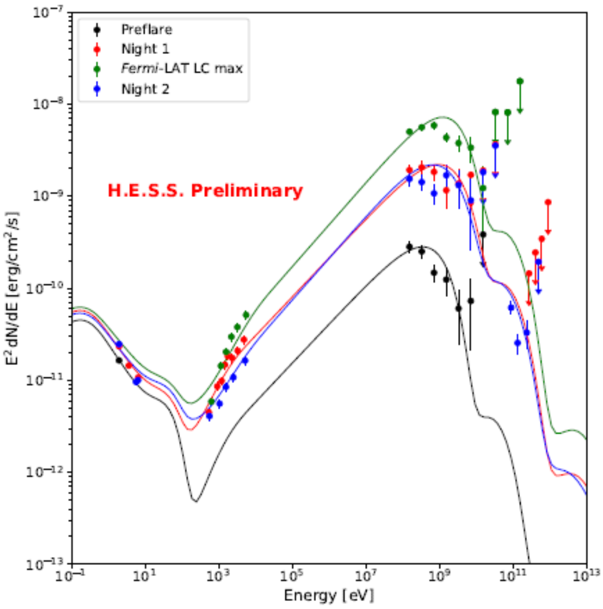

Figure 18: *Multi-wavelength spectral energy distribution (Swift-XRT, Fermi LAT and H.E.S.S.) for different flux states superimposed with fits of an hadronic model. Courtesy: arXiv:1708.00882*

Several time-resolved spectral energy distributions (Dorner et al. 2017) were collected by First G-APD Cherenkov Telescope (FACT) (Anderhub et al. 2013) who observed bright TeV blazars providing an excellent temporal coverage. In Synchrotron Self-Compton models is supposed a quadratic dependence between the synchrotron and the inverse-Compton flux. There can be a very clear time lag between the two synchrotron components (Spanier & Weidinger 2012) due to the ratio between the acceleration timescales of electrons and protons. Orphan flares are an important phenomenon in blazars that are difficult to explain with leptonic models. Orphan flares consist of outbursts in gamma rays not accompanied by a low energy counterpart. We need to perform a continuous monitoring of the SED to be able to distinguish these events from time to lags and from changes in the spectral shape. Some models of the core regions of blazars provide for periodic modulations of the gamma-ray emission. For example, in a multi-wavelength campaign (Ackermann et al. 2015) it was possible to observe a possible quasi-periodic oscillation in PG1553 + 113 on a time-scale of about two years. The periodic emission can be explained with different models such as binary black hole systems (Begelmann et al. 1980; Komossa 2003), accretion flow instabilities (Honma et al 1992; Ackermann et al. 2015) or helical jet motion (Rieger 2004; Ackermann et al. 2015). We need a satellite that in addition to having a good spectral coverage also has a good temporal coverage in order to understand the mechanisms in the central engine of AGN. The new satellite must also have the possibility of to probe different ranges of the high energy part of the SED depending on the position of the high energy peak of the source. We can constrain models and deduce information on the dominating emission process thanks to unprecedented time-resolved SEDs conducted in multi-wavelength campaigns. Measurements of different classes of AGN can be compared. The Cherenkov Telescope Array (CTA) and the new satellite could work together to study time-resolved SEDs with unprecedented sensitivity and precision. Moreover, the new satellite will have to cover a large energy range in gamma rays, in order to fill the gap in the spectral energy distributions, which is in the MeV range, and this will allow to constrain the models. The AGN catalog will be completed with new MeV sources. The orphan flares will probally observed also from sources other than blazars and it will be possible to distinguish these special flares from the low and high energy peak and from the changes in the spectral shape.

1.4. Active Galactic Nuclei

1.4.1 Blazars

Blazars describe the class of AGN which are observed at a very small angle between the rotational axis of the accretion disc and the line of sight of the observer, hence in the direction of the jet. They are a small but important fraction of the entire population of active galactic nuclei and consist of a supermassive black holes ($M \geq 10^9 M_{SUN}$) accreting material and ejecting part of it in a jet. Blazars are further divided into two sub class: flat spectrum radio quasars (FSRQs) and BL Lac objects (BL Lacs), depending on the characteristics of their optical spectrum. The blazar SED, dominated by the jet emission, presents two peaks: one at low frequency (from 10^{12} to $>10^{18}$ Hz) due to synchrotron radiation emitted by ultra-relativistic electrons, and the second at higher frequencies ($>10^{21}$ Hz) whose nature is debated in particular the contribution of hadrons in addition to the inverse-Compton emission (Böttcher et al. 2013).

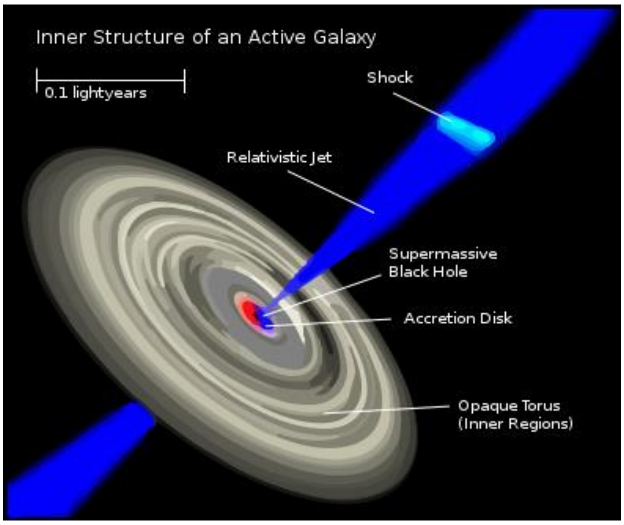

Figure 19: *The inner structure of a galaxy with an active galactic nucleus.*

The blazar sequence consists of an anti-correlation between the bolometric luminosity and the location of the synchrotron peak (Fossati et al. 1998; Ghisellini et al. 2017). The synchrotron peak is at low frequencies (IR - optical) in the FSRQs while in the BL Lacs there is a lower luminosity and the peak shifted to higher frequencies. The blazer SED, in the MeV range, can exhibit the second peak (in FSRQs), the valley between the two peaks (in low and intermediate synchrotron peaked BL Lac objects, LBL/IBL) or even part of the synchrotron peak (in high synchrotron peaked BL Lac objects, HBL).

In the "extreme blazars" (Costamante et al. 2001) the synchrotron peak can reach energies exceeding the hard X-ray band, that leads us to wonder what the limit of particles acceleration is in the blazar jets. There is also an hadronic component in the jet in certain extreme blazars, like 1ES 0229 + 200. It is necessary to measure the missing part of the SED in the MeV range in order to distinguish between leptonic and hadronic models. In fact for example the SED of Markarian 421 (Mrk 421, see Fig. 20) can be modeled or with a hadron model, eg Synchrotron-Proton Blazar (SPB) model of Mücke et al. (2001, 2003) or with a leptonic model of the type one-zone synchrotron self compton (SSC) (Finke et al. 2008). In the SPB model electrons and protons are co-accelerated at the same site in the jet and the relativistic electrons injected in the strongly magnetized emission region, or “blob”, which moves relativistically along the jet axis, lose energy through synchrotron emission. The resulting synchrotron radiation of the primary electron component dominates the low energy bump of the blazar SED, and serves as target photon field for interactions with the instantaneously injected relativistic protons, which follow a power law energy spectrum, and pair (synchrotron-supported) cascading (Mücke et al. 2003 Abdo A. A. LAT) . While in the SSC the radio through X-ray emission is produced by synchrotron radiation from electrons in a homogeneous, randomly oriented magnetic field and the high energy γ-rays are produced by inverse Compton scattering of the synchrotron photons by the same electrons which produce them (Abdo A. A. LAT).

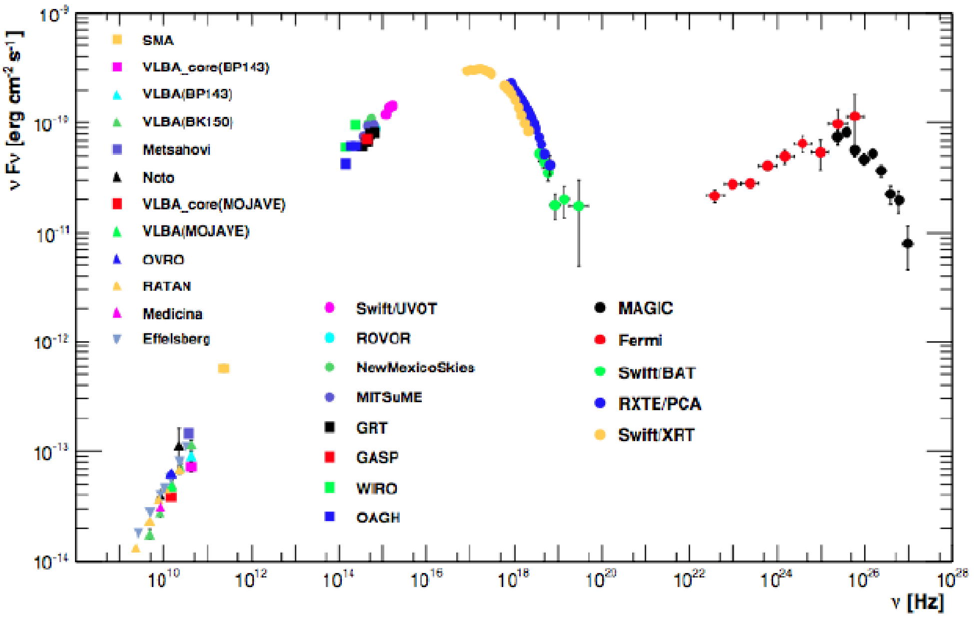

Figure 20: *The SED of Mrk 421, a HBL object, taken during the multifrequency campaign in January 2009. The corresponding instruments used are shown in the legend (Abdo A. A. LAT). For this HBL object the synchrotron emission lies in the optical/soft X-ray energy range.*

MeV-blazars are the most luminous objects of their class and are found at high redshift (z > 2) but few have been observed (Bloom and Marscher 1996; Collmar 2006; Sambruna et al. 2006; Ajello et al. 2009; Ajello et al. 2016; Sbarrato et al. 2013; Tagliaferri et al. 2015). Their distance makes them ideal probes of the distant and young Universe (Kaufmann et al. 2017; Ghisellini et al. 2017; Ackermann et al. 2017; Ghisellini et al. 2014). In the MeV blazars SED the ratio of the inverse Compton to synchrotron luminosity is of the order of 100 (Compton dominance). Since the synchrotron Self-Compton alone would produce a much less luminous Compton peak the presence of an external photon field, in addition to the photons produced by the synchrotron, is required, in order to explain the high inverse Compton flux (Ajello et al. 2016). This external photon field, responsible for the Compton dominance, may be in the broad line region (BLR) or in the torus region. From the variability time scale of the X-ray and gamma-ray emission we can deduce the size of the emitting region and then choose between the two options (day time scale for the BLR and five times longer for the torus option). In both regions the ratio between radiation and magnetic energy density are large enough to account for the Compton dominance (Ajello et al. 2016). The detailed modeling of the Compton dominated SED is required to identify the physical properties of the MeV blazars. It would be interesting to understand how the violent outbursts occur at hard X-rays (Sambruna et al. 2006) that can probably be observed in the MeV range and understand what their duty cycle is.

In the blazars the electromagnetic radiative bolometric power can be dominated by the sub-GeV and MeV gamma-ray emission, which makes these sources targets for astrophysical "tomography" in the MeV range. Einstein in the General Relativity theory predicted the gravitational lensing of electromagnetic radiation from distant sources (Einstein 1936). Since then after the first detection of multiple images of SBS 0957 + 561 (Weymann et al. 1979) hundreds of radio/optical lens systems have been discovered. If the observer, the lensing galaxy/quasar and the distant source, are along a straight line, a circle can be formed called Einstein ring (Schneider et al. 1992). Time delays between the diffraction mirage images are generated by these gravitational lenses that magnify the radiation from distant blazars. These delays depend on the position of the emitting regions in the source plane and in AGN/galaxy-scale lenses, range from hours to weeks. AGILE and Fermi have seen, in the GeV band, the MeV-peaked FSRQ, PKS 1830-211, which is located at z = 2.507 (Donnarumma et al. 2011; Abdo et al. 2015), which is a clear example of (spatially unresolved) strong-lensing. This source had already been observed by COMPTEL (Collmar 2006) in 0.75÷30 MeV band and is the brightest strong lens in the sky at cm, hard X-ray, MeV gamma-ray energies. Fermi (and MAGIC at E > 100 GeV; Ahnen et al. 2016) also observed the GeV lensed blazar, S3 0218 + 35 (lens B0218 + 357, z = 0: 6847), with the smallest separation lens known. Thanks to Fermi LAT data we obtained for this source the first gamma-ray delay measurement. In two sources S3 0218 + 35 (Cheung et al. 2014) and PKS 1830-211 (Martí-Vidal et al. 2013; Barnacka et al. 2015; Neronov et al. 2015) it was possible to derive independent γ-ray delay measurements from strong macro-lensing and obtain measurements of the projected size of the gamma- ray emission regions in the central engine and the jet.

The study of variability of gravitationally lensed blazars is emitting in the 0.2 MeV÷3 GeV band, can be very interesting:

- To deduce blazar particle acceleration and emission processes, the combination and interplay of different leptonic inverse-Compton mechanisms (SSC, BLR, torus, diffuse dust photon fields) or hadronic emission processes (photopion, em cascades, proton synchrotron, Bethe -Heitler) MeV data are required.

- To study the engine and jet structures and the origin of the HE emission, it is useful to analyze the MeV temporal / spectral variability generated by unresolved lensing of distant FSRQs.
- Temporally delayed events and micro-lensing signals are enhanced by MeV data, placed around the emission peak with more pronounced variability and flares.
- With measured delays in MeV band it is possible to find more, small separation, lenses that cannot be resolved.

Multi-messenger particles (gamma-ray photons, massive-neutrinos, gravitational waves, even massive axions and gravitons) should have differential arrival times depending from particle properties, cosmological parameters, masses and separations of elements in the lensing system. An interesting physics phenomenon to observe would consist of multimessenger detections of different time delays from a lensed MeV FSRQ.

FSRQs are the most persistent powerful hard X-ray sources in the Universe. The Burst Alert Telescope (BAT) onboard Swift observed the 15÷150 keV spectrum of FSRQs finding that it is very flat (photon spectral index Γ_X <1: 5), this, together with gamma-ray data from Fermi/LAT, there leads us to think that their high energy SED peaks around 0.5÷3 MeV, range where most of their electromagnetic power comes out. The 15-55 keV luminosity of the high-z FSRQ cited by Blandford et al. (1977) (Blandford & Znajek 1977) (10 objects at z > 2, and 5 at z > 3) is $L_X > 2\times10^{47}$ erg s^{-1} and a bolometric luminosity exceeding 10^{48} erg s^{-1}. This view was then further confirmed by the observations of Nuclear Spectroscopic Telescope Array (NuSTAR). The fact that the X-ray spectrum of PMN J0641-0320 is extremely flat ($\Gamma_X \sim 1$) makes it possible to have information about the region of the jet where most of the power comes out and on the details of the acceleration /cooling of the emitting electrons. The accretion disk component prevails on optical emission in the FSRQs because the synchrotron emission peaks at smaller frequencies. When we can detect the peak of the disk emission: once it is fitted with a standard disk model, we can have information on the black hole (BH) mass and the accretion rate with a margin of error lower than what we would have if we used the virial method (based on the FWHM of the broad emission lines). Sbarrato et al. (2016) has plotted the number density of black holes with $M>10^9$ M_{SUN} as a function of redshift.

For radio-quiet quasars the number density peaks at z ~2÷2.5 while for radio-loud quasars it peaks at z ~ 4. From this diversity of behavior we can understand that there are two different epochs for formation of massive BH, and that systems with jets form earlier.

It arises spontaneously to ask ourselves whether it is the jet that increases the mass accretion rate or vice versa. In the high-z powerful FSRQs we can determine the BH mass, the accretion rate and the jet power. For each of these sources pointing towards us in which the produced radiation is collimated within an angle ~ 1/Γ (where Γ it is the bulk Lorentz factor), other 2 Γ^2 sources point in other directions but with the same intrinsic properties.

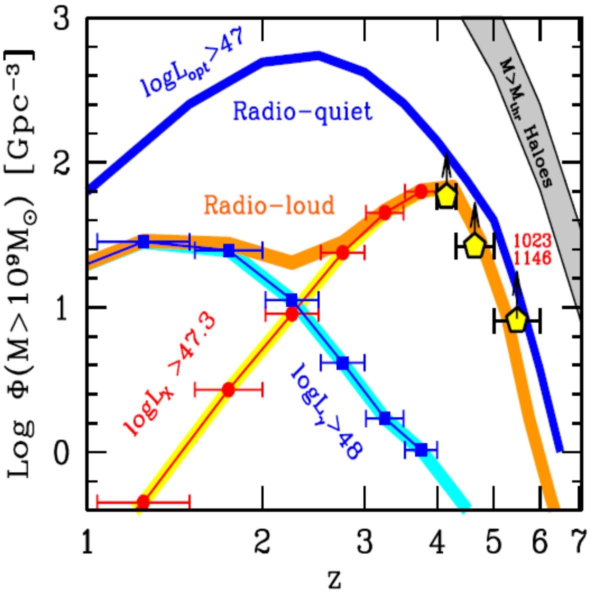

Figure 21: *The number density of black holes with M>10^9M_{SUN} as a function of redshift. Adapted from Sbarrato et al. 2015.*

In the BL Lacs there are no or very weak emission lines in their optical spectra. There are two broad nonthermal continuum peaks in their radio to gamma-rays SED (see Fig. 20). A double power-law can represent the electron energy distribution responsible for the non-thermal emission:

$$N(\gamma) = \begin{matrix} K\gamma^{-n_1} & ;\gamma_{\min} < \gamma < \gamma_{br} \\ K\gamma_{br}^{n_2-n_1} & ;\gamma_{br} < \gamma < \gamma_{\max} \end{matrix}$$

where $\gamma_{\min}, \gamma_{br}, \gamma_{\max}$, are the lowest, break, and highest Lorentz factors of the electron energy distribution, K is the normalization constant, and n_1, n_2, are, the slopes below and above the break. The kinetic energy density of relativistic electrons can be calculated as:

$$U_e = m_e c^2 \int_{\gamma_{\min}}^{\gamma_{\max}} \gamma N(\gamma)(\gamma - 1) d\gamma \cong m_e c^2 N \langle \gamma \rangle$$

where, N is the integrated electron density. If $n_1 \approx 2$ the average Lorentz factor of the particle is:

$$\langle \gamma \rangle \cong \gamma_{\min} \ln(\gamma_{br} / \gamma_{\min})$$

$\gamma_{\min}$ is important in the estimation of U_e / U_B ratio of the jet, where U_B is the magnetic energy density. This ratio U_e / U_B is far from particles-field equilibrium (except for a few sources) because electrons dominating over the field by orders of magnitude (Mankuzhiyil et al. 2012; Tavecchio & Ghisellini 2016; Kino et al. 2002).

Fermi-LAT (Ackerman et al. 2015) has cataloged 600 BL Lac objects. Unfortunately the BL Lacs that emit Very High Energy gamma-ray (VHE) are few (~ 50) due to insufficient sensitivity of the current generation Cherenkov Telescopes and the γ-γ attenuation from the the extragalactic background light (which is significant for high redshift sources; $z \geq 0.5$). However, thanks to the simultaneous multi-wavelength campaigns on BL Lacs, much more information on the jet energetics can be collected. The observational quantities, for example the peak frequencies (together with their peak luminosities) of the synchrotron and inverse Compton peaks, spectral slopes, flux variability of the source etc. allow us to derive the non-thermal emission parameters of blazars. To constrain $\gamma_{\min}$ serve the spectral information at the rising part of the synchrotron or SSC peak.

Figure 22: *An artist's impression illustrates how high-speed jets from supermassive black holes would look.*

Thanks to the Fermi-LAT and AGILE satellites it has been possible to detect many blazars at energies above 100 MeV. In particular Fermi-LAT has detected 1591 sources belonging to three categories BL Lacs, FSRQs, and unknown type of blazars. Only a few FSRQs and BL Lacs emit very high-energy gamma rays (VHE, E> 100 GeV). Only 70 sources were detected at TeV energies mainly HBLs. In fact, the instruments available today are able to detect only the most powerful and nearby objects. It is expected that the new Cherenkov telescope array (CTA) will be able to detect more than 1000 sources above 100 GeV. Below 100 MeV the number of detected blazars are few due to low sensitivity of the instruments. It is thought that some objects (FSRQs and extreme HBLs) can emit a large fraction of their power in this band. The SEDs of a considerable number of blazars have been studied in the last decade at different bands, from radio to VHE gamma rays. These studies allow to determine the physical conditions responsible for the emission at the site. The study of the low-energy bump allows to establish the electron acceleration in the jet, while the study of the high-energy bump puts limits to the presence of the eventual hadronic component in the jet or the presence of external radiation fields. Through the study of the hard spectrum it is possible to place new constraints on the extragalactic background light (EBL) itself in the IR regime (Aharonian et al. 2007) and establish an upper limit on the intergalactic magnetic field (Taylor et al. 2011; Finke et al. 2015). It is supposed to have hadronic origin, the peculiar TeV spectrum (Cerruti et al. 2015; Tavecchio and Bonnoli 2015) of the EHBL object 1ES 0229 + 200 (located at redshift 0.14). This hadronic origin could generate a significant neutrino emission as well as being the site of ultra-high energy cosmic ray acceleration. To place limits on the leptonic component of the emission, it is necessary to have a better knowledge of the MeV spectrum, as this is correlated with the synchrotron emission of the electrons.

Only by studying the MeV bright blazars in detail is it possible to describe the physical parameters of MeV blazar jets. Due to the absorption by the EBL at gamma-ray energies we have that the redshift distribution of the MeV blazars can reach much higher redshift than the GeV observed blazars. Detailed information about the source intrinsic spectra may come from the study of high-redshift blazars at MeV energies. This intrinsic spectra are useful to verify the EBL model predictions for TeV blazars.

It would be interesting to be able to perform a multi-wavelength observation campaign on a sample of extreme blazars with the aid of a new satellite with a higher sensitivity at MeV energies in order to obtain the most accurate and complete characterization of the SED and to determine the location of the synchrotron peak of these extreme, intriguing sources. The new satellite will have to be able to see many MeV gamma-ray flares, including those from lensed FSRQs and new high-redshift FSRQs undetected by the Fermi LAT. It is possible to have an improvement in spatial resolution at gamma-ray energies by a factor of 10^4 (Barnacka et al. 2015; Neronov et al. 2015) combining time-series and spectral analysis of gamma-ray variability with the lens of radio observations (SKA, ALMA, etc.) or IR / optical observations (LSST, Euclid, JWST, etc.). Multi-messenger studies will be conducted in conjunction with the new satellite and large scale neutrino array experiments (KM3NeT and other). Hypothesizing that the lens magnification of the neutrino flux is equal to that of gamma-ray photon flux we could derive the measure the intrinsic neutrino luminosity of powerful MeV-GeV FSRQs. The new satellite must have a sensitivity in the range 0.3-100 MeV at least one or two orders of magnitude better than that of previous instruments. In this way we will have a more detailed study of the underlying emission processes and we could identify the characteristic parameters for the general class of blazars. Through Gamma-ray observations in the MeV energy range we can increase the number statistics of the MeV blazars and so we will see if Compton dominance is a general characteristics of the MeV blazars and that external photon fields are necessary to explain their high luminosity at MeV energies. With sensitive observations in the MeV gamma-ray regime it is possible to understand the combination and interplay of external-jet infrared photon field Comptonization and in-jet synchrotron self-Compton. With the new satellite we will detect hundreds of MeV-blazars even at high redshift, allowing us to deepen the evolution models and revolutionizing our understanding of blazars emission processes. The upcoming X-ray surveys (i.e. by e-ROSITA) in the 2-10 keV range will allow us to select the best candidates for FSRQs. Then we must select the hardest sources, cross them with radio (> 1 mJy is enough) samples, and find the redshift if unknown. at this point we have a perfect pointed target for the new satellite, with adequate exposure.

Studying the blazars seen with Fermi (whose maximum redshift is ~ 3 and mostly located at z ~1; Ghisellini et al. 2014) it was discovered that the jet power is greater than the luminosity of the accretion disk. Discovering new sources where the jet emission peaks (i.e. at ~ 1 MeV) could allow us to detect even more dominant jets. At this point we can ask ourselves if the generation process of jets is the Blandford-Znajek mechanism or if instead, part of the gravitational energy of the accreting matter goes into amplifying the magnetic field, instead of heating the disk. This second option could be the cause of why we observe that jetted sources have black holes that grows at earlier epochs than in radio-quiet quasars.

1.4.2 Seyfert 1 galaxies

Radio-loud Narrow-Line Seyfert 1 galaxies are a peculiar class of AGN with relatively low black hole masses ($10^6 \div 10^8$ M_{SUN}; Boroson 2002), but near-Eddington accretion rates. However, treir accretion rate is much higher than those estimated for the class of blazars (Foschini 2013). Narrow-Line Seyfert 1 (NLSy1) galaxies have been classified as Seyfert 1 galaxies as they are characterized by broad permitted and narrow forbidden lines in their optical spectra. We can see that the NLSy1 has a Seyfert 1-like spectrum with unusually narrow permitted lines. In fact, the FWHM of Hβ was < 2000 km s^{-1}. The ratio of [O III] to Hβ is smaller than 3, and there ia a bump due to Fe II (Pogge 2000). Zhou et al. (2006) conducted a detailed study of a 2011 NLSy1 galaxies sample based on the observations of the Sloan Digital Sky Survey Data Release 3 (SDSS DR3). In radio-loud NLSy1 (7% of the NLSy1, $S_{4.85GHz}/S_{440nm} > 10$; Komossa et al. 2006) galaxies it was possible to confirm thanks to the observation of high-energy gamma-rays and their variability (Abdo et al. 2009a; Abdo et al. 2009b) the existence of powerful relativistic jets (Foschini 2014). For these radio-loud NLSy1 galaxies, Padovani (Padovani 2017) proposed to rename them as jetted NLS1. The NLSy1 galaxies show (as for example FSRQs) a MeV peaked spectral emission that should be studied in a more complete way. SSC emission from the high energetic jet and the External Compton (EC) characterizes the keV-GeV peak (in νF_ν presentation). In this scenario, a photon field close to the jet (generally from the broad-line region) come in contact with relativistic electrons and undergo IC scattering.

Figure 23: *Seyfert Type I galaxy NGC 1097, photographed by the Spitzer telescope.*

Using measurements of the polarization we could understand the different contributions of the SSC (polarized) and the EC (un-polarized) emission.

According to Foschini (Foschini 2017) there is a sequence NLS1s → FSRQs → BL Lac Objects going from small-mass highly-accreting to large-mass poorly-accreting black holes. These would be different stages of the cosmological evolution of the same type of source (young → adult → old).

The flux variability study will allow us to understand the simultaneous existence of the jet and a very high accretion rate. Since the gamma ray of NLSy1 galaxies is variable (Abdo et al. 2009a; Tibolla et al. 2013) the jet may be formed accompanying with weak soft X-ray, as was commonly seen in X-ray binaries.

Based on multi wavelength spectral studies of jetted NLSy1 galaxies is supposed to exist a peak of the gamma-ray emission in the MeV energy band, as in the other jetted AGN. Unfortunately, it is to underline a lack of data in the 100 keV-100 MeV energy band. The relationship between the SSC and EC components can be clarified with gamma-ray observations on jetted NLSy1 galaxies in the gap in the MeV energy band, and with polarization measurements. The presence of EC components is required to describe the detected GeV gamma-ray emission. In particular it is possible to calculate the strength of the magnetic field using the SSC contribution. Indications on the location of the external photon field responsible for the IC emission will be deduced from the measurement of the time scale of the flux variability in the X-ray (e.g. monitoring observations expected from eROSITA) and gamma-ray range. The gamma ray from the parent population of beamed NLS1 is steeper (Liao et al. 2015) for this reason the detection below 100 MeV could be an asset with respect to Fermi LAT. Foschini et al. (2015) have conducted a multiwavelength survey of 42 radio-loud NLSy 1 galaxies studying the SED in detail.

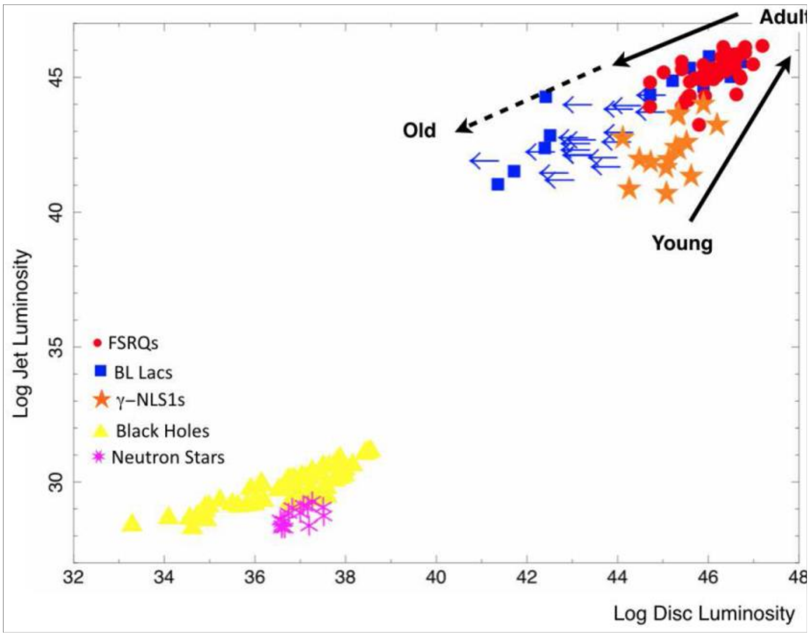

Figure 24: *Implications of the unification of relativistic jets: cosmological evolution (Tibolla et al. 2013).*

Based on these studies and on the spectral characteristics in the X-ray regime we expect to be able to detect many MeV peaked NLSy1 galaxies. According to Berton et al. (2015) the Square Kilometer Array (SKA), with its superior sensitivity will observe thousands of jetted NLS1 for which a multi-wavelength coverage will be required.

1.4.3 Galaxy Clusters

Galaxy Clusters are the largest gravitationally bound systems in the Universe. Following the hierarchical scenario of structure formation, galaxy clusters have formed from small galaxy groups that later merged and formed a cluster. The typical masses of clusters of galaxies are ~ 10^{13}÷10^{15} M_{SUN} and their sizes are of the order 4 Mpc. The closest galaxy cluster is the Virgo Cluster which contains hundreds of galaxies (mostly spirals and irregulars). Through observations with radio frequencies it has been possible to identify a number of large Mpc-scales diffuse halos of polarized synchrotron emission in a large number of merging clusters. This synchrotron emission makes us deduce the presence of a population of relativistic electrons (Ferrari et al. 2008). The presence of these cosmic ray (CR) electrons poses some questions as the primary CR electrons, escaping from the denser core region, would lose energy too fast, due to the short cooling time, to account for the radio emission. Furthermore, due to the Inverse Compton (IC) scattering of these CR electrons we should also observe hard X-ray emission in addition to the soft X-ray emission from ambient gas. X-ray or radio observations are not able to explain the distribution of cosmic rays, nor to understand the role of CR protons in galaxy clusters. Galaxy clusters may be interesting candidates for the search for the signatures of Dark Matter decay and annihilation (Conrad et al. 2015), as they possess high mass to light ratios. Moreover, although the astrophysical factor of the nearest clusters is about 1-2 orders of magnitude smaller than what is found in the nearby dwarf spheroidal galaxies, we have the advantage that the clusters are much more numerous (Lisanti et al. 2017). Cherenkov Telescope Array will study the Coma cluster hosting a giant radio halo.

Two possible scenarios have been proposed to explain the emergence of large scale radio emission: the first scenario is pure hadronic, while in the second primary CRs, both electrons and protons, are subject to in-situ re-acceleration providing the necessary ingredients to account for the measured radio emission (Brunetti & Jones 2014). For both scenarios the release of kinetic energy associated with major mergers is probably sufficient to accelerate these particle populations. Inelastic pp-collisions occur, in the pure hadronic scenario, between high energy CR protons and the ambient gas.

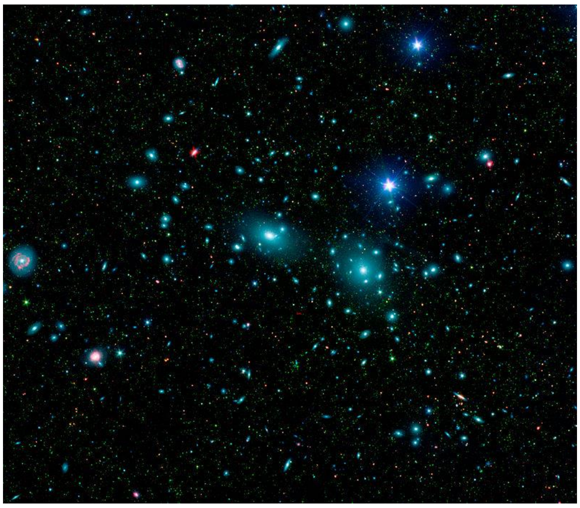

Figure 25: *This false-color mosaic of the central region of the Coma cluster combines infrared and visible-light images to reveal thousands of faint objects (green). Follow-up observations showed that many of these objects, which appear here as faint green smudges, are dwarf galaxies belonging to the cluster. Two large elliptical galaxies, NGC 4889 and NGC 4874, dominate the cluster's center. The mosaic combines visible-light data from the Sloan Digital Sky Survey (color coded blue) with long- and short-wavelength infrared views (red and green, respectively) from NASA's Spitzer Space Telescope.*

These interactions produce pions, both neutral and charged ones, and the latter decaying produce highly energetic (secondary) CR electrons and radio emission. We are still looking for the flux of γ-rays from the intracluster medium (ICM) produced by the decay of neutral pions in two photons. In the second scenario CRs are accelerated for instance through turbulence, (probably due to merger processes) but there is olso the re-acceleration of CR protons that interact with the ambient gas as in the pure hadronic scenario. To thoroughly study CR protons may be useful gamma-ray observations of clusters, especially, at low energies. It is probable that CR acceleration is lower than previously thought or that volume-averaged CR is a thermal pressure ratio of protons in the ICM is less than 1% (Ackermann et al. 2014), given the lack of gamma-rays from clusters. In the re-acceleration scenario, the gamma-ray flux is lower, thus existing constraints are weaker.

In hadronic scenarios we have that the predicted gamma-ray spectrum depends on both the assumption of the magnetic field in the cluster and the parent CR proton distribution. While in the re-acceleration scenario the situation becomes more difficult as there are additional degrees of freedom (such as the re-acceleration time τ_{acc}, and period $\Delta\tau_{acc}$) and the enlarging the parameter space. It is difficult to distinguish between Galactic diffuse emission component and the eventual low brightness emission from the ICM, because the production processes of the gamma-ray emission are the same.

1.5 Cosmology, Exotic Physics and Dark Matter

1.5.1 Primordial Black Holes

The Primordial Black Holes (PBHs) would have formed in the early universe, during the Big Bang, due to the high densities and inhomogeneous conditions that led to the collapse of local overdensities, but there are also other theories that provide domain walls, cosmic strings, etc. (see Carr 2005). Since PBHs are expected to have formed in a narrow time period, they should have a very narrow mass distribution. Their masses ranging from few grams to millions of solar masses depending on the model and the formation epoch. The Hawking mechanism causes the PBHs to radiate particles (Hawking 1974) and photons, in this way they lose mass and increase in temperature according to the law:

$$T_{BH} = (8\pi G M_{BH})^{-1}.$$

This formula, however, is valid only for BHs that do not accrete material, and in this case the temperature of BH increases to the point of causing its evaporation. The lapse time to evaporation is given by:

$$\tau \sim G^2 M_{BH}^3 \hbar^{-1} c^{-4}.$$

It is estimated that the PBHs born with masses smaller than 10^{-19} M_{SUN} would have already evaporated today. PBHs with small masses can interfere with some cosmological observables such as the CBM spectrum and the Big Bang nucleosynthesis (BBN), or being involved in baryogenesis, etc. While PBHs with large masses could be detectable. The still existing PBHs could form part of the dark matter (DM). The spectra of the instantaneous gamma-ray rate for different BH temperatures consist of two components: the primary component from the Hawking mechanism and the second component, that peaks around E = 68 MeV (MacGibbon and Webber 1990), from the decay of hadrons produced by the fragmentation of the primary quarks and gluons, and by the decay of gauge bosons. Particles from the Hawing radiation have a small impact on the energy budget of the Universe or the CMB number of photons but they alter the optical depth of the CMB photons. The discovery of a PBH would constitute a confirmation of the predictions of quantum field theory. PBHs with masses $10^{15÷17}$ g in which the peak intensity occurs at 130 MeV may have injected a large amount of MeV radiation into the Universe that could constitute the unresolved part in the MeV component of the extragalactic gamma-ray background (EGB). All non-accreting BH are destined to explode and vanish and the energy and time scales of this phase is governed only by the mass (or temperature) scale. According to the Standard Model (SM) we will be able to see the final phase of a PBH, but there are less conventional theories (Fichel et al. 1994) that increase this possibility. For example, it is hypothesized that the formation a fireball at the quantum chromodynamic (QCD) temperature could explain short-period gamma-ray bursts (Cline and Hong 1992).

The abundance of PBHs with masses $10^{15÷16}$ g is strictly constraint by Planck data, while the EGB prevails for smaller masses. It is required that the integrated MeV contribution not to be larger than that of the measured EGB.

1.5.2 Matter-Antimatter Annihilation

It is clear that we live in a local universe dominated by matter and the little antimatter we find is of secondary origin, produced in space by collisions of high energy particles. There are two important issues to consider: the first is that matter and antimatter have quite similar properties and the second that this observed asymmetry must have been produced by some mechanism necessarily immediately after inflation (Dolgov, hep-ph/0511213). Also, the matter-antimatter asymmetry is a strong signal for new physics as it can not be explained by the standard model of particle. There are three possible scenarios of matter-antimatter asymmetry (Dolgov, hep-ph/0211260):

1. Universe is matter dominated.
2. There are domains of matter and antimatter.

3. Matter dominates but there are lumps of antimatter

Models of bariogenesis can lead indifferently to any of these three scenarios. To be able to test these scenarios we would have to reach such high energies in which they operate that it is difficult to think of being able to obtain on Earth. While scenario 2 seems to be excluded on an observational basis (Cohen et al. 1998), scenario 3 is intriguing because it presupposes the possibility that there exist objects formed only of antimatter in our vicinity with the possibility of observing matter-antimatter annihilation (Bambi and Dolgov 2007; Blinnikov et al. 2015). A direct search for the presence of primordial antimatter consists of the observation of sufficiently heavy anti-nuclei such as helium-4. It is preferable to study the flow of anti-helium-4 as the anti-deuterium can be produced in energetic cosmic rays reactions while the production of anti-nucleus heavier is much lower (for example, the flow of the secondary produced anti-helium-4 is 17 orders of magnitude below the observed flux of normal helium). So far, we can only calculate upper bounds on the flux of cosmic anti-helium-4 (for example according to BESS $\overline{He^4}\big/He^4 < 3\times10^{-7}$). The indirect research of primordial antimatter is based on the observation of the electromagnetic radiation generated in the matter-antimatter annihilation. In this case we should detect an excess of 100 MeV photons from proton-antiproton annihilation and from 0.511 MeV line from electron-positron annihilation at low energies. If we also suppose the existence of anti-stars, the anti-stars star ratio must be 10^{-6} (Steigman 2008). The antimatter compact objects would be distributed in galactic halos which makes them much more difficult to observe. The scenarios involving lumps of antimatter could explain both the matter-antimatter asymmetry in the Universe and the origin of dark matter (Dolgov et al. 2009; Duperray et al. 2005) especially if we consider antimatter objects in the form of primordial black holes (Blinnikov et al. 2016). In indirect research, as we have already said, the gamma rays between 0.5 and 100 MeV are involved, corresponding to the energy range between the electron and the pion masses. The Alpha Magnetic Spectrometer (AMS) experiment aboard the International Space Station (ISS) has detected 4-5 candidates anti-helium-3 particles (Sokol 2017) which may suggest the possibility of finding us in scenario 3.

1.5.3 Extragalactic MeV Background

The origin of the MeV background, in the 0.2-100 MeV gap region, remains unknown. The first detection of a “MeV bump” was made by the APOLLO 15/16 missions (Strong & Moskalenko 1998). Unfortunately, this "MeV bump" has not been seen by subsequent HEAO-4, SMM and COMPTEL missions (Kinzer et al. 1997; Watanabe et al. 1999b; Weidenspointner et al. 2000). Various theories have been proposed to explain at least in part the MeV background as: dark matter annihilation (Ahn & Komatsu 2005), non-thermal emission from Seyfert galaxies (Inoue et al.

2008), nuclear decays from Type Ia supernovae (Clayton & Ward 1975; Ruiz-Lapuente et al. 2016), and emission from blazars (Ajello et al. 2009) and radio-galaxies (Inoue 2011).

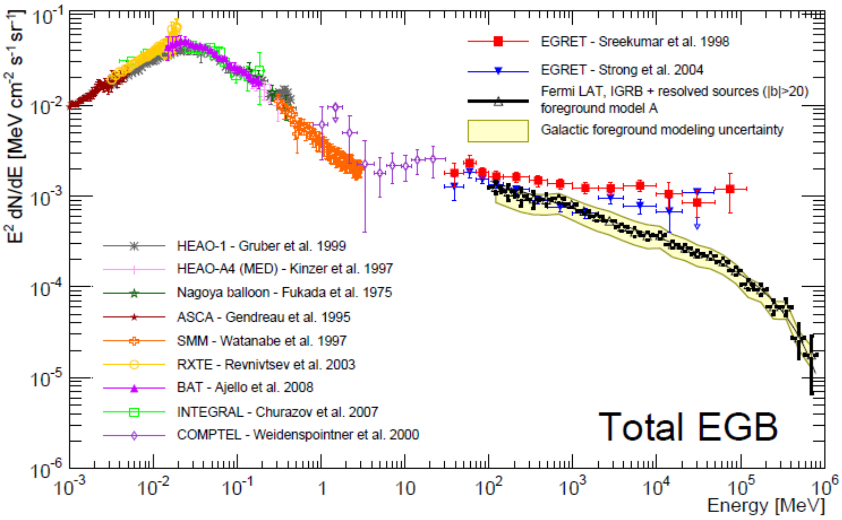

Figure 26: *Spectrum of the high-energy background from X-ray to GeV -rays. Adapted from Ackermann et al. 2015.*

Some of these contributions are certain such as blazars, radio-galaxies, and type Ia supernovae while others are more uncertain as dark matter interaction or the non-thermal emission of Seyfert galaxies. However, regarding the latter if we impotizate that non-thermal electrons exist in radio-quiet AGN coronae we can explain not only the X-ray and MeV backgrounds but also the power-law shape of the low-energy part of the MeV background. The emission of extremely powerful blazars with very hard power-law spectra (Ajello et al. 2009) can explain the MeV background below 3 MeV. Observing the spectrum in the Figure 26 we can see that the MeV background must harden at around 40-60 MeV this can be explained with an additional source that exhibits a spectral bump that could be given by the Star-forming galaxies (Lacki et al. 2014). The prediction of the contributions of populations like blazars, star-forming and radio galaxies to the background may come from measurements of luminosity functions. The measurement of the MeV background will require careful modeling of the Galactic diffuse emission and of the instrumental background.

1.5.4 Dark Matter

The presence of an unknow and yet unidentified type of matter (i.e. non barionic) was confirmed by many indirect gravitational observations in particulary through galactic rotational curves and through the anisotropies of Cosmic Microwave Background (CMB) (Bertone 2010). This Dark Matter (DM) component accounts for about 85% of the total mass content in the universe and for about 27% of the total energy and must consist of eletrically neutral stable (within cosmologial time scales) particle, thermally produced in the early universe, relic from Big Bang. Furthermore, these particles must be “cold” (i.e. non relativistic) at the onset of structure formation.

The characteristic properties of gamma rays make them perfect for indirect detection of dark matter annihilations and and decays. In fact, they do not scatter appreciably in their travel through the Galaxy pointing back directly to the annihilation site moreover the cross-section for scattering on electrons and nuclei for MeV to TeV photons is small. It is therefore possible to easily separate a signal from astrophysical foreground or backgrounds using the properties of the energy distribution resulting. The expected signals have to be extremely weak. The DM decay signal is proportional to the DM density, while the DM annihilation signal is proportional to the density squared; in both cases the emission is peaked at low redshift, say $z < 0.3$. Redshift is useful for distinguishing DM signals from astrophysical phenomena related to star formation history that peak at higher redshifts The indirect DM searches has many possible astrophysical target such as the Galactic Center and the dwarf spheroidal satellite galaxies. As the N-body high-resulation cosmological simulation tell us the distribution of DM in Milky-Way like galaxies exhibite a wealth of substructures, or subhalos, at all spatially-resolved mass scale (Springel et al. 2008; Diemand and Moore 2011; Garrison-Kimmel et al. 2014). There should be a large population of subhalos virtually invisibile not massive enough to have star with very dense dark matter cores and some of these might be located sufficiently close to Earth so to produce detectable signals of decay or annihilation of dark matter. Telescopes sensitive to the energy range of the dark matter mass (in the MeV (Gonzalez-Morales, Profumo, and J. Reynoso-Córdova); or GeV range (Bertone et al. 2005)) may observe the constant dark-matter-induced gamma-ray emission from these subhalos that might appear as point-like or extended sources. There would be two interesting sources observed by Fermi LAT in the GeV gamma-ray band without observable counterparts at other wavelengths that show the typical characteristics of what we expect from subhalos that annihilate dark matter (Bertoni et al. 2016; Xia et al. 2017). Also, the Cherenkov telescopes MAGIC (MAGIC Collaboration, Nieto et al. 2011) and VERITAS (VERITAS Collaboration, Nieto 2015) have performed observations of dark matter subhalo candidates.

A promising source for dark matter searches is the Galactic halo even if the source is diffuse and signal and background separation creates problems. Another promising targets for indirect DM searches is the Galactic Center (GC) in fact the annihilation luminosity scales with the DM density squared, which is expected to be highest at the center of galaxies (Bringmann and Weniger 2012). Towards the GC have been performed by FERMI-LAT (>200 MeV) and HESS (>200 GeV) (Ackermann et al. 2015; Abdalla et al. 2016) searches for monocromatic lines from DM.

Possible signals could also came from dwarf spheroidal (dSph) satellite galaxies of the Milky

Way, in fact neither astrophysical gamma-ray sources (supernova remnants, pulsar wind nebulae…) nor gas as target material for cosmic rays have been observed in these systems. The dSphs are perhaps the smallest (size ~ 1 kpc) and faintest ($10^2 – 10^8$ L_{Sun}) object whose dynamic is dominated by DM (mass-to-light ratios M/L ~ 1000 M_{Sun}/L_{Sun} for the ultra-faint ones). To study the dynamics of the satellites dSphs we use optical telescopes while to test their DM content we use instruments working in the high-energy (from MeV up to TeV) band. MAGIC have performed searches (>100GeV) for monochromatic lines and other spectral features from DM towards the Segue 1 dSph (Aleksić et al. 2014). Although DM gamma-ray induced flux is less intense than what is expected from GC, the the dSphs satellite of the Milky Way are close (from few tens of kpc up to few hundreds of kpc) and very numerous and represent clean targets for DM in the gamma-ray energy domain, there being astrophysical sources present generally negligible (Bergstrom 2012). In addition, most dSphs are located at intermediate or high galactic latitudes where Galactic foregrounds are suppressed. DSphs discovery has made considerable progress with the use of instruments that can perform deeper photometric and astrometric scan of the sky (Walker [arXiv:1205.0311]). New discoveries of satellite dSphs will be possible with the new sky surveys (Pan-STARRS (Chambers et al. [arXiv:1612.05560]), DES (Drlica-Wagner et al. 2015), GAIA (Antoja et al. 2015), LSST (Jurić et al. [arXiv:1512.07914]), etc.).

We need surveys with large coverage and sub-degree angular resolution for both the γ-ray and gravitational measurements to carry out measurements of the angular cross-correlation between the γ-ray and the large-scale structure distribution in the Universe with significant statistics.

There being poor sensitivity of current γ-ray experiments in the MeV range we have no constraints on DM with masses ≤ 1 GeV. The solar modulation makes the detection of MeV-DM through the measurement of the local cosmic-ray flux impossible and the underground direct detection experiments are rendered insensitive due to the small recoil energies.

1.5.4.1 WIMP and other DM Candidates

Among the most promising DM candidates are Weakly Interacting Massive Particles (WIMPs) that emerge from the supersimmetric extension of the Standard Model (SM). WIMPs have masses $\geq$ 1 GeV. The WIMPs can self-annihilate and / or decay producing a flux of gamma rays up to the DM mass with sharp spectral features, which could be observable by space-and ground-based γ-ray instruments. The self-annihilation cross-section has a value of approximately 3×10^{-26} cm^3 s^{-1} (Steigman et al. 2012). The typical search strategies for WIMPs are based on collider searches, underground direct detection experiments, and indirect detection. However so far all these researches have not led to any positive outcome. Therefore, we started thinking about considering that the dark matter particle could have a sub-GeV mass. In this context several MeV DM models have been proposed as self-interacting DM (Boehm and Fayet 2004; Pospelov et al. 2008), “cannibal” DM (Pappadopulo et al. 2016), strongly-interacting DM (Hochberg et al. 2014) and axion-like-particles. For the DM with MeV masses (emitting γ-rays in the MeV range) there is only a limited number of kinematically-allowed final states. CMB experiments (Slatyer 2016) can strongly limit DM candidates annihilating into leptonic final states or charged pions through s-waves. However, even the same WIMP could be a MeV-ish particle and decay into light SM particles, and in particular into photons if we hypothesize mechanisms for the genesis of non-thermal dark matter.

The WIMP tipically can self annihilate into several different channels depending of his mass:

- $\chi\,\chi \to \gamma\,\gamma$ a photon pair
- $\chi\,\chi \to \pi^0\,\gamma$ a neutral pion and photon
- $\chi\,\chi \to \pi^0\,\pi^0$ a neutral pion pair
- $\chi\,\chi \to l\,\bar{l}$ lepton-antilepton pair (electron, muon, tauon)

and more complicated cascade annihilations. The γ-ray flux from a DM dominated regions depends on the so-called astrophysical (or J) factors

$$\Phi_s(\Delta\Omega) = \frac{1}{4\pi}\frac{\langle\sigma v\rangle}{2m_\chi^2}\int_{E_{MIN}}^{E_{MAX}} dE_\gamma \frac{dN_\gamma}{dE_\gamma} \times J(\Delta\Omega)$$

where $\langle\sigma v\rangle$ is the self-annihilation cross-section averaged on the local relatively velocity, m_χ denotes the dark particle mass, E_{MIN} and E_{MAX} are the energy limits for the measurement, and dN_γ/dE_γ stand for the energy spectrum of the gammas produced in the annihilation. The J-factor is defined as the integral along the line of sight (l.o.s.) of the squared DM mass density profile:

$$J = \int_{l.o.f} ds\rho^2(s,\vartheta)$$

where s is the distance along the line of sight ϑ is the l.o.s angle and is defined as

$$r^2 = s^2 + R_0^2 - 2sR_0\cos\vartheta$$

where $R_0 \approx 8$ kpc that is the solar distance from the galactic center.

ρ is the density profile and is usually parametrized in the analytic form as:

$$\rho(r) = \frac{\rho_0}{(r/R)^\gamma[1+(r/R)^\alpha]^{(\beta-\gamma)/\alpha}}$$

where α, β, γ are model parameters, R is the characteristic length scale and ρ_0 is the local DM density , approximatively 0.4 GeV cm^{-3}. These are some of the possible models: the Navarro-Frenk-White (NFW) model $(\alpha = 1.0,\ \beta = 3.0,\ \gamma = 1.0,\ R = 20\text{ kpc})$, the Moore model $(\alpha = 1.5,\ \beta = 3.0,\ \gamma = 1.5,\ R = 28\text{ kpc})$, and the isothermal halo model $(\alpha = 2.0,\ \beta = 2.0,\ \gamma = 0,\ R = 3.5\text{ kpc})$.

For $\chi\,\chi \to \gamma\,\gamma$ annihilation the expected photon flux spectrum has a spike

$$\frac{dN_\gamma}{dE_\gamma} = 2\delta(E - m_\chi)$$

while for $\chi\,\chi \to \pi^0\,\pi^0$ the chiral anomaly causes the subsequent decays $\pi^0 \to \gamma\gamma$ the flux spectrum can be descibed as a box-like distribution (Boddy and Kumar 2015)

$$\frac{dN_\gamma}{dE_\gamma} = \frac{4}{E_+ - E_-}\Theta(E_+ - E)\Theta(E_- - E) \qquad\qquad E_\pm = \frac{m_\chi}{2}\left(1 \pm \sqrt{1 - \frac{m_\pi^2}{m_\chi^2}}\right) \quad .$$

The $\chi\,\chi \to \pi^0\,\gamma$ leads to a box feature and a monochromatic line (Boddy and Kumar 2015)

$$\frac{dN_\gamma}{dE_\gamma} = \delta(E - E_0) + \frac{2}{\Delta E}\Theta(E'_+ - E)\Theta(E - E'_-)$$

where

$$E_0 = m_\chi - \frac{m_{\pi_0}^2}{4m_\chi}, \quad \Delta E = m_\chi - \frac{m_{\pi_0}^2}{4m_\chi} \quad \text{and} \quad E'_\pm = \frac{m_\chi}{2}\left[\left(1 + \frac{m_{\pi_0}^2}{4m_\chi^2}\right) \pm \left(1 - \frac{m_{\pi_0}^2}{4m_\chi^2}\right)\right].$$

In the case of $\chi\,\chi \to e^+\,e^-$ we can have a large contribution from Bremsstrahlung emission. Now we discuss another possible DM model.

Recently a complete hidden sector of new particles has been taken into consideration. Through the so-called mediator the dark sector interacts with a reduced number of processes with the visible sector. As also in this case the DM particle will be a weakly interacting particle, its annihilation and/or decay will involve the leptons in the final state.

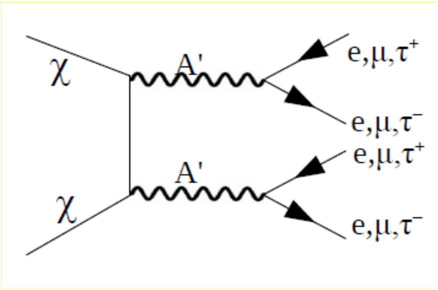

Figure 27: *Feynman diagram for Dark matter annihilation into lepton final states.*

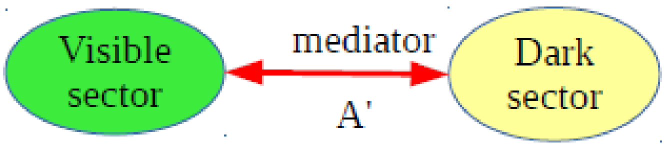

Figure 28: *Through the so-called mediator the dark sector interacts with a reduced number of processes with the visible sector.*

As can be seen in Fig. 27 there may be final states in which they are present τ^+e τ^-but the cross-section for formation of two-tauon bound state is negligible, so it is difficult to observe signature of true taonium. While the muonium annihilation lines have advantages because the muon mass is larger than the electron mass. The process can be described by:

$$L \sim g'q'\bar{\psi}(\gamma_\mu + \alpha'\gamma_\mu\gamma^5)\psi A'^\mu$$

where A' is the mediator between the dark and the visible sectors, ψ is the leptonic field and g' is the new interation constant. The charges, q_i, are in general free parameters. There is a threshold of 1022 keV for $e^\pm$ creation and 210 MeV for $\mu^\pm$ creation. Other channels are enabled at higher energies. Because of the lepton non-universality, the scenarios in which the mediator decays in pairs muon anti-muon in the annihilation process $\chi\,\chi \to \mu^+\mu^-$ could be favored. In fact, thanks to the studies on the proton radius (Benett et al. 2006; Bayer et al. 2017; 2014 CODATA recommended values) and the muon magnetic moment (Benett et al. 2006) it is understood that electrons and muons present a different behavior with respect to the weak interaction. A new weakly interacting particle, beyond the SM, could be related to the $g_\mu - 2$ anomaly. This particle could be the DM particle we are looking for. Since the positrons are generated by different processes (nuclear reactions and decays, black hole evaporation, decay and / or annihilation of Dark Matter particles) it is difficult to understand their origin and to distinguish the processes leading to DM creation. Instead the muons and the tauons unlike electrons and positrons with their masses of 105.6 MeV and 1777 MeV (Olive et al. 2014) respectively can not be produced in radioactive decays of atomic nuclei. So from $\mu^+\mu^-$ e/o $\tau^+\tau^-$ annihilation peaks we can have cleaner signal which allows us to derive new information about the sites of enhanced DM concentration in a way that complements the data obtained from the all-sky mapping of the 511 keV line. Naturally in high energy astrophysical environments, leptons can also be produced in reactions: $\gamma\,\gamma \to l^+\,l^-$ and $e^+\,e^- \to l^+\,l^-$. But the muons generated by these reactions have energies much higher than the ionization energy ($E_{ion} \approx 1.4$ keV) of the true muonium (Ellis and Bland-Hawthorn 2015) therefore only the pairs with energies smaller than E_{ion} will stay in a bound system. The two states of the muonium, depending on the spin orientation, are the para- and orto-muonium. The first decays via two-photon annihilation and the energy released is E = 105.66 MeV (Ellis and Bland-Hawthorn 2015) while the second via electron-positron annihilation. The detection of gamma rays produced in the muonium annihilation will allow to know their production mechanism. The finite lifetimes of muons (2.2 μs). means that they decay in the radius of about 1000 km which provides the possibility to map the DM regions with great precision as the annihilation could only happen close to their production site.

Chapter 2

Design of a new nano-satellite mission

2.1 Introduction

The electromagnetic spectrum in the high-energy band is object of observation by both space and ground-based telescopes. For example, we can mention at energies above 500 GeV operates the ground-based Cherenkov telescope like Hess, MAGIC and Veritas (Hinton 2009) and that soon the Cherenkov Telescope Array (CTA) will cover the energy higher than 100 GeV (Acharya et al. 2013). In the space we can remember AGILE (Tavani et al. 2009) and Fermi-LAT (Atwood et al. 2009) which rapresent the best instruments available today in the energy band between 20 MeV and 2 TeV. In Fig. 29 we can see the Fermi LAT structure.

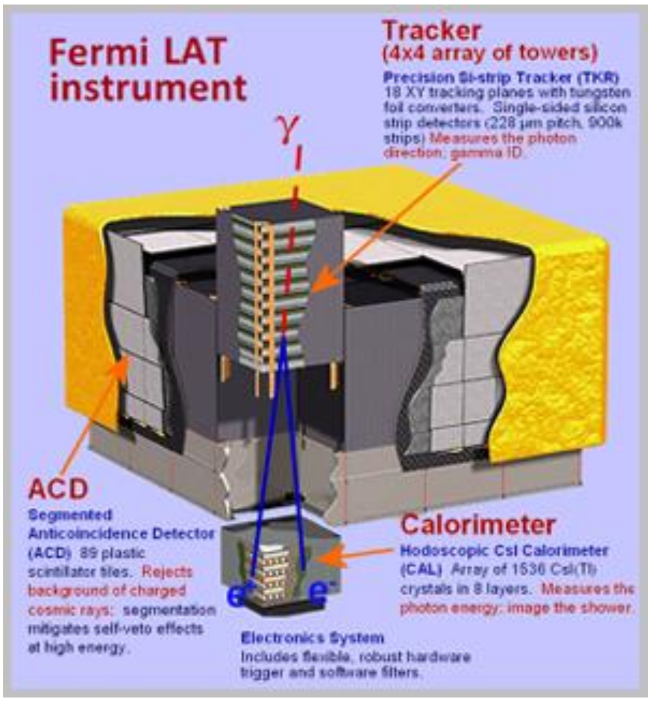

Figure 29: *The Fermi LAT structure.*

In the lower energy band we can mention the Nuclear Spectroscopic Telescope Array (NuSTAR) (Harrison et al. 2013) between 3 and 79 keV, the Swift Gamma Ray Burst Explorer (Gehrels et al. 2004) between 0.2 and 10 keV and between 15 and 150 keV, and the INTErnational Gamma-Ray Astrophysics Laboratory (INTEGRAL) between 15 keV e 10 MeV (Winkler et al. 2011).

At energies around about 1 MeV we unfortunately have only the contribution that has left the satellite COMPTEL, which operated in the 90’ aboard the Compton Gamma-Ray Observatory (CGRO) (Schoenfelder et al 1993), but currently it is expected that with a time-scale of about 10 years and a cost of about half a billion euros (De Angelis et al. 2017; Andritschke et al. 2005; Mizumoto et al., 2015) will launch a new satellite to observe this region of the electromagnetic spectrum with an improved sensitivity of at least one order of magnitude compared to COMPTEL. The structure of a Compton satellite optimized for the MeV regime must consist of three main detectors:

- A **Silicon microstrip tracker**, to reconstruct the electron recoil from the Compton interaction.
- A **Calorimeter**, composed of scintillating crystals readout by photodetectors able to absorb all the particles due to the Compton interaction and measure the interaction position as well as the deposited energy.
- An **Anticoincidence Detector (ACD)**, composed of plastic scintillators covering the whole instrument capable of detecting single charges relativistic with an efficiency exceeding 99.99%, and to reject charged-particles background events.

This structure has already been tested in previous missions such as Fermi-LAT (see Figure 29) and AGILE in energy ranges where pair production prevails, but it is thought that it can be easily adapted, thanks to complex event reconstruction process, to operate in the energy range between 0.1 and 10 MeV where Compton interaction prevails (see Figure 30).

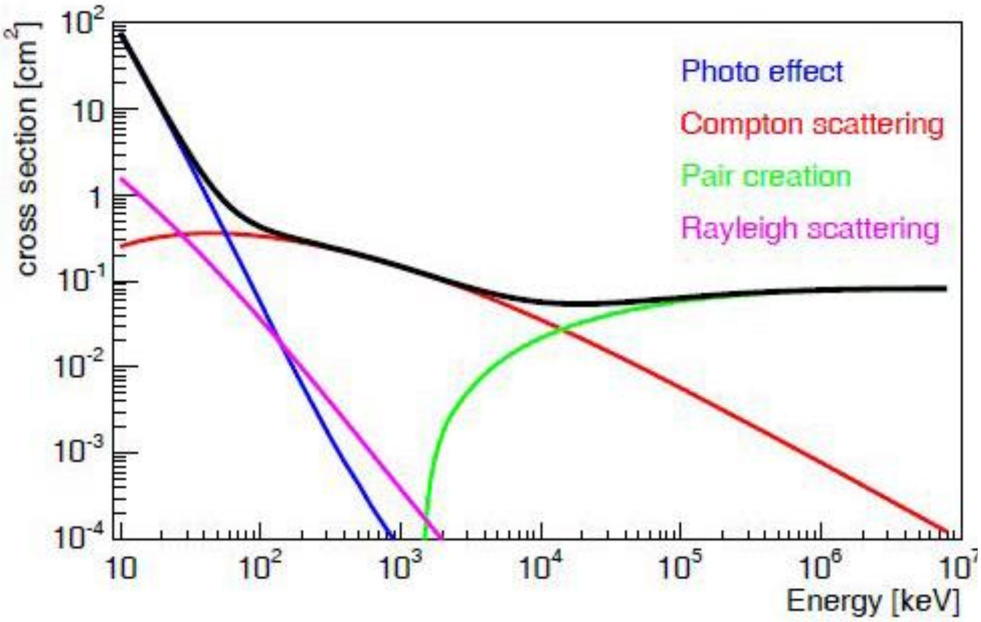

Figure 30: *Cross-section for the four dominating photon-interaction mechanisms in Silicon (Zoglauer A. C. 2005).*

As we have just said, the time-scale for the realization of a Compton telescope is about 10 years. But on a much shorter time-scale (about 18 months) and with costs much lower, equal to about half a million Euro, it is possible to send a nano-satellite MeV telescope into orbit. Despite the satellite performing less than a larger telescope, it will still be a source of valuable information, in particular about the charged background and the activation, and a valid test bench for algorithms and technologies for future larger missions. The chapter is structured in this way: in paragraph 2.2 we will describe in detail the structure of this nano-satellite MeV telescope on the basis of the CubeSat standard, in paragraph 2.3 we discuss the expected performance of the nano-satellite, in 2.4 we descibe the simulation methodology, and in 2.5 we discuss the performance estimate.

2.2 Nano-Satellite MeV Telescope Design

Our nano-satellite MeV telescope will have a size of $10 \times 20 \times 20$ cm^3 and weighs less than 2.66 kg equal to exactly 2U CubeSat[1], but with the addition of the flight system and on-board electronics will reach 4U to 6U. We developed a first version of our nano-satellite which was subsequently modified making the bottom calorimeter thinner and replicating the design on the four sides. This choice was made because we realized that the detector was performing poorly in the pair-production, so we decided to dedicate ourselves to a purely Compton detector. The technology that will be used has already flown into space, being the same technology that has been used to build AGILE (Tavani et al. 2009) and that won the bid to build up the tracker of Fermi LAT (Atwood et al. 2009).

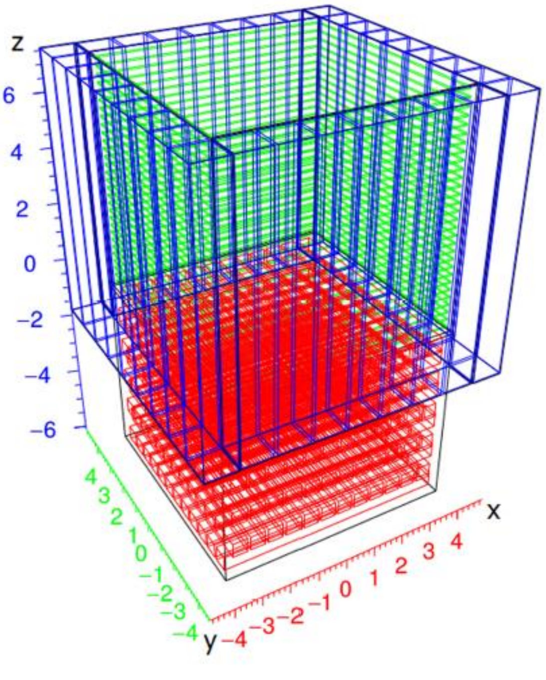

Figure 31: *The nano-satellite structure without ACD for the first version (see Lucchetta et al. 2017).*

---

[1] The CubeSat standard provides a miniaturized cube-shaped satellite with a volume of 1 dm^3 and a weight of 1.33 kg.

In Figure 31 we can see the first structure of our nano-satellite as described in Lucchetta et al. (2017), without the anti-coincidence system (in green the tracker, in red the bottom calorimeter, and in blue the lateral calorimeter). In Figure 32 we can observe instead the update version of our nano-satellite: in green the Si tracker, in red the Cesium Iodine calorimeter, in magenta the anti-coincidence detector.

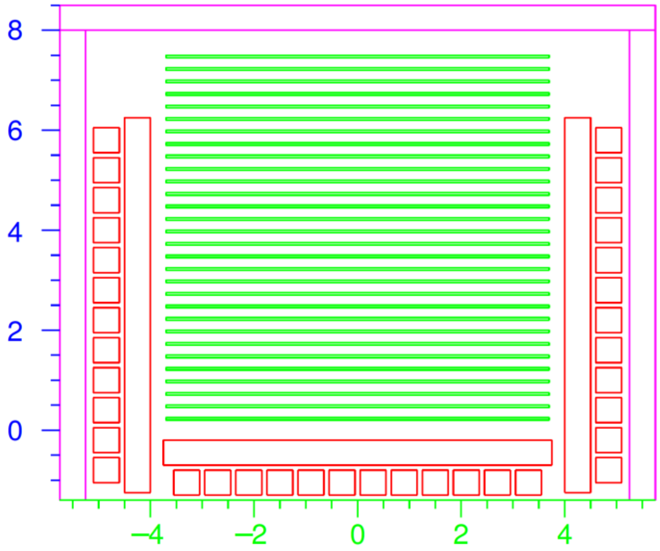

Figure 32: *The nano-satellite structure with ACD for the updated version. For clarity, it should be noted that the front and back calorimeter modules do not appear in the figure (see Rando et al. 2019).*

2.2.1 The Silicon Tracker

The Tracker will work with both Compton scattering and pair production for this reason a large cross-section will be needed compared to these two interactions and low Doppler-broadening. For these two reasons we prefer to opt for low *Z* materials. We therefore choose semiconductor detectors for their ability to provide good position and energy resulution with respect to the secondary electrons and positrons. Furthermore, it is preferred to choose Silicon detectors with respect to Germanium detectors either because the Silicon allows to reach a better angular resolution and because the Germanium detectors are very expensive and operate at reduced temperatures.

Single-Sided Strip Detectors (SSSD) have been used in the AGILE and Fermi-LAT missions to detect the pair production of high energy gamma-ray photons, but Double-Sided Strip Detectors (DSSDs) are required for a Compton scattered MeV mission. to obtain precise information on electron directions. Furthermore, there must be no tungsten layers (unlike Fermi-LAT) and there must be an ultra-light mechanichal structure to minimize the amount of passive material within the detector volume. In this way we can perform the tracking of low-energy Compton electrons and reduce the effects of multiple Coulomb scattering and the background caused by the activation. At this point it was necessary to evaluate both the number of layers (20 at the beginning, 30 in later designs, see the Silicon Tracker specification in Table 1 and in Table 2) and the layers thichness, the strip pitch etc.

In fact, for example, if we consider a decrease of the strip pitch we would get a better spatial resolution but we should consider the read-out of a greater number of channels and therefore greater power comsumptions. Layer thickness is also very important as a charged particle that crosses the silicon layer volume undergoes many Coulomb scattering with latex atoms. We can use the average scattering angle to describe the phenomenon

$$\theta = \frac{13.6\ \text{MeV}}{\beta cp} Z \sqrt{\frac{x}{X_0}}$$

where X_0 is the radiation length. According to this formula, we will have a greater particles deviation (with consequent greater errors in the trajectory reconstruction) and greater leakage current, if we consider higher thicknesses. We therefore opted for a tracker composed of 30 layers, with layers thickness of 500 µm and strip pitch of 150 µm (see Table 1), capable of tracking the electron and to reconstruct its position on the *xy* plane (assuming that the layers are positioned along the *z* axis).

Despite all these precautions we will be able to reconstruct the scattered electrons only for 14% of the total event at 500 keV, 30% at 1 MeV, and at 28% at 3 MeV.

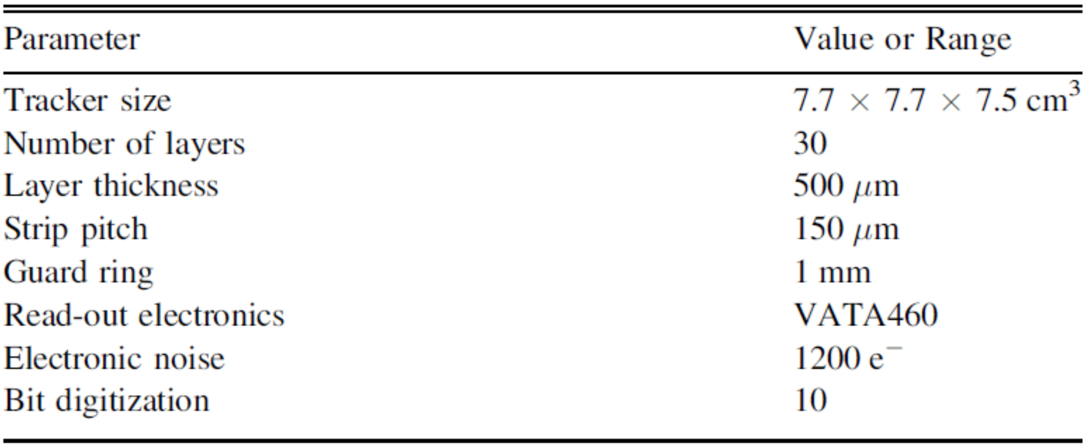

Parameter	Value or Range
Tracker size	$7.7 \times 7.7 \times 7.5\ \text{cm}^3$
Number of layers	30
Layer thickness	500 μm
Strip pitch	150 μm
Guard ring	1 mm
Read-out electronics	VATA460
Electronic noise	1200 e^-
Bit digitization	10

Table 1: *Silicon Tracker specification for the first version(Lucchetta et al.2017).*

Regarding the read-out of the signal we have to choose an analog read-out as for the AGILE tracker that allows to reach a spatial resolution below 40 µm (much inferior to the values 1.5 ÷ 2.3 cm achieved by COMPTEL (Schönfelder et al 1993). It is also necessary an ultra-noise front-end electtronics because in this way it is possible to obtain an accurate measurement with good spectral resolution of the low energy deposits due to Compton scattering.

As Application Specific Integrated Circuit (ASIC), the VATA460 has been chosen which has an input charge range of 95fC, a shaping time of ~ 2 μs, a power consumption of 0.3 mW/ch, and trigger capabilities (Odaka et al., 2012). Moreover, it has been calculated that thanks to a 10 bit digitization we can reach a reading accuracy of 2.1 keV. The equivalent noise charge is around 1200 e^- which corresponds to an electronic noise of about 4.3 keV. Thanks to these parameters we have calculated to reach an energy resolution around 5 keV (1σ).

Parameter	Value or range
Si tracker: layer area	$7.4 \times 7.4\,\mathrm{cm}^2$
Si tracker: layer thickness	$500\,\mu\mathrm{m}$
Si tracker: number of layers	30
Si tracker: strip pitch	$500\,\mu\mathrm{m}$
Calorimeter: crystal dimensions	$0.5 \times 0.5 \times 7.5\,\mathrm{cm}^3$
Calorimeter: depth resolution ($1\,\sigma$)	0.5 cm
ACD: thickness	0.5 cm

Table 2: *Design specifications for the updated version of the nano-satellite (see Rando et al. 2019).*

2.2.2 Calorimeter

The calorimeter is composed of CsI (Tl) crystals. The characteristics of this material, already tested by previous missions such as Fermi-LAT, are the following:

- It provides a good energy absorption of the photons even at high energies, thanks to its high density, its Molieré[2] radius, and its radiation length (see Table 2, Berlato 2016).
- CsI (Tl) crystals are very cheap and for this reason they have a low impact on the total cost of our nano-satellite.
- The decay time of CsI (Tl) consists of more than one component. The fastest component has a value of about 0.6μs, the slowest 3.5μs. From this we can deduce that the scintillation decay is quite fast with an average decay time of about 1μs for γ-rays, which allows an overall fast response of the calorimeter to photons.
- The CsI (Tl) is well-suited for photodiode readout due to its characteristic of having most of its emission in the long wavelength part of the spectrum (the crystals have an emission peak at 550 nm).

---

[2] The Molieré radius (from the physicist Paul Friederich Gaspard Gert Molière 1909-64) is defined as the radius of a cylinder containing on average 90% of the energy of an electromagnetic shower initiated by a photon, and it is a characteristic constant of the material. It is related to the radiation length X_0 by the following approximate relations:
$R_M = 0.0265\ X_0(Z+1.2)$ where Z is the atomic number.

Density (g/cm^3)	4.51
Moliefe radius (cm)	3.57
Radiation length (cm)	1.86
Wavelength of max emission (nm)	550
Lower wavelength cutoff (nm)	320
Primary decay time (ns)	1000
Light yield (ph/keV)	54

Table 3: *CsI (Tl) crystal specifications (Belato 2016).*

We have therefore coupled the CsI (Tl) crystals to a common photodiode read-out, choosing the Hamamatsu S3590. For each keV of absorbed energy, ~ 360e would be emitted in the photodiode, and a reading accuracy of ~ 2.3 keV would be achieved. In Table 4 we can see some rough estimates for the read-out performance.

Energy (keV)	Scintillation photons	e^- photodiode
100	$5.4 \cdot 10^3$	$3.6 \cdot 10^4$
500	$2.7 \cdot 10^4$	$1.8 \cdot 10^5$
1000	$5.4 \cdot 10^4$	$3.6 \cdot 10^5$
2000	$1.1 \cdot 10^5$	$7.2 \cdot 10^5$
3000	$1.6 \cdot 10^5$	$1.1 \cdot 10^6$
5000	$2.7 \cdot 10^5$	$1.8 \cdot 10^6$

Table 4: *CsI (Tl) scintillation photons produced at varius energies (Berlato 2016).*

We have chosen for simplicity the use of the same ASIC for the calorimeter as in the tracker (see Table 4). Our calorimeter is divided into 2 modules: a bottom one and a lateral one. The lateral module is useful for detecting very low energy Compton scattering, while the bottom one is able to detect high energy Compton scattering and pair production.

Parameter	Value or Range
Bottom crystals size	$0.5 \times 0.5 \times 7.5$ cm^3
Lateral crystals size	$1.0 \times 1.0 \times 8.5$ cm^3
Depth resolution (1σ)	1 cm
Photodiode read-out	Hamamatsu S3590
Read-out electronics	VATA460
Crystals per bottom plane	12
Bottom planes	10

Table 4: *CsI(Tl) Calorimeters specifications for the first version of the nano-satellite (Lucchetta et al.2017).*

In the bottom calorimeter, for both configurations, the crystals dimensions are 0.5 × 0.5 × 7.5 cm^3. In the first design the layers were arranged in a hodoscopic configuration with the crystals arranged along the x and the y axes so that the read-out electronics is located at the edges of the calorimeter. This particular arrangement allowed to reduce the amount of passive materials. The lateral calorimeter istead surrounds the tracker and, in the first version, its crystals had the dimensions of 1.0 × 1.0 × 8.5 cm^3 and were arranged so as to be an approximately 1 cm overlap with the bottom calorimeter. In the new design the crystals of the lateral calorimeter have the same dimensions (0.5 × 0.5 × 7.5 cm^3) as the bottom calorimeter with a depth resolution (1σ) of 0.5 cm.

2.2.3 Anti-Coincidence Detector (ACD)

The primary purpose of the ACD is to provide an optimal charge-particle background rejection. In our case we expect to be able to get a rejection efficiency > 99.99%. The ACD completely surrounds the detectors of our nano-satellite and consists of several slabs of plastic scintillator (0.5 cm thick) connected to Silicon photomultipliers. In this configuration, they have been in Fermi-LAT (Atwood et al 2009) and AGILE (Tavani et al. 2009) thanks to their low cost and high performance.

2.3 Expected Performance of the Nano-Satellite

The most important parameters that describe and quantify the performance of each telescope are: the effective area, the energy resolution, and the angular resolution (all assumed to be independent from one another). Among these parameters, the one with the most complexity in a Compton telescope is the angular resolution. While in pair events it is represented by the point-spread funcion (PSF) (see Ackermann et al. 2013), in the case of Compton scattering the angular resolution can be divided into two additional parameters (as already described in Bloser et al., 2004): the Angular Resolution Measure (ARM), and the Scatter Plane Deviation (SPD). The ARM parameter quantifies the smallest angular distance between the known original direction of the photon, $\vec{e}_i$, and the photon scatter cone represented by the measured direction of the scattered γ-ray. This small angular direction corresponds, according to Zoglauer (2005), to the difference between the Compton scatter angle, φ, represented by the measured energies, and and the angle between the known direction of the initial and measured direction of the scattered gamma ray.

$$\Delta\varphi_{ARM} = \arccos(\vec{e}_i \circ \vec{e}_g) - \varphi$$

From this we obtain that we can have a positive $\Delta\varphi_{ARM}$ in the case in which we have an incompletely absorbed recoil electron, while in the case in which an incompletely absorbed scattered gamma ray occurs, the $\Delta\varphi_{ARM}$ is negative.

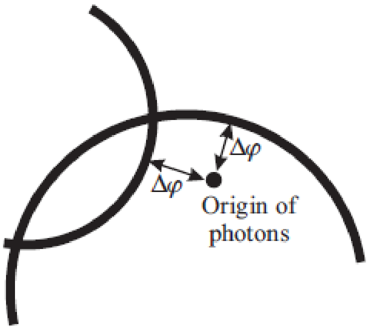

Figure 33: *The angular resolution measure (ARM) quantifies the smallest angular distance between the known original direction of the photon, and the photon scatter cone represented by the measured direction of the scattered γ-ray (Zoglauer 2005).*

The second quantity, SPD, instead represents the angle between the true scatter plane (defined by $\vec{e}_i$ and $\vec{e}_g$) and the measured one spanned by $\vec{e}_g$ and $\vec{e}_e$. Where $\vec{e}_e$ is the direction of the recoil electron, while $\vec{e}_g$ is the direction of the scattered photon.

$$\Delta\nu_{SPD} = \arccos((\vec{e}_g \times \vec{e}_i)\circ(\vec{e}_g \times \vec{e}_e))$$

The SPD is always equal to the maximum value of 180° in untracked events (Zoglauer 2005). Moreover, the SPD allows to provide a measure for the length of the Compton scatter arc, and depends directly on the accuracy with which the direction of the recoil electron can be measured.

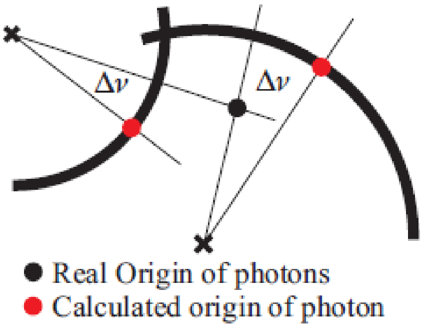

Figura 34: The scatter plane deviation (SPD) describes the angular distance on the Compton cone between the known origin of the photons and the calculated one (Zoglauer 2005).

Through these two parameters (ARM and SPD) we can can get to build a final resolution element on the sky map, which generates this solid angle $\Delta\Omega$:

$$\Delta\Omega = \left[\cos(\bar{\varphi}-\sigma_{ARM}) - \cos(\bar{\varphi}+\sigma_{ARM})\right]\cdot 2\sigma_{SPD}$$

where σ_{ARM} and σ_{SPD} represent the ARM Full Width at Half Maximum (FWHM) and the SPD Half Width at Half Maximum (HWHM) respectively and $\bar{\varphi}$ is the average photon scatter angle.

To the parameters described before we must add the sensitivity that describes the ability of a telescope to detect the weakest source in presence of background. The sensitivity is calcolated through Poisson statistics with a certain statistical significance z (in units of σ). The sensitivity for a

Compton and pair telescope is divided into three quantities: the continuum sensitivity, the (narrow) line sensitivity, and the polarization sensitivity. For point-like sources the sensitivity has the following formula (Zoglauer 2005):

$$F_z = \frac{z\sqrt{N_s + N_B}}{T_{eff} A_{eff}}$$

here T_{eff} is the effective observation time, A_{eff} the effective area of a telescope, N_B the number of background photons in the resolution element (this value can be obtained in a semi-analytical way using the data obtained from the simulations), and N_s the number of source photons. If we consider that the number of sources photons for a source at the sensitivity limit is given by:

$$N_s = F_z T_{eff} A_{eff}$$

we have that F_z can be rewritten as follows:

$$F_z = \frac{z^2 + z\sqrt{z^2 + 4N_B}}{2T_{eff} A_{eff}}$$

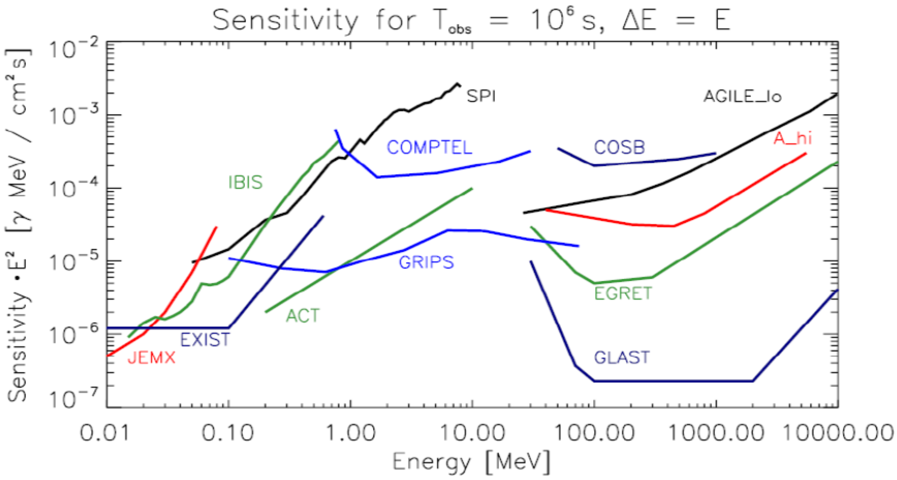

Figure 35: *Point source continuum sensitivity of different X-and γ-ray instruments.*

2.4 Simulation Methodology

To perform the simulation, the open-source object-oriented MegaLib software library was used, which includes all the necessary simulation and data analysis tools, including: geometry construction, Monte-Carlo simulation, response creation, event reconstruction, image reconstruction, and other high-level data-analysis tools (see Zoglauer et al. 2008). In the simulation, an isotropic source with a power law (energy index –1) was used. The simulated energy range is between 0,1 and 10 MeV. We chose to divide the data obtained from the simulation into different event classes. In order to evaluate the performance of our telescope we have divided the data into tracked and untracked events. The study of only tracked events allows to obtain a great improvement of the angular resolution element (largely due to the PSD) but at the expense of the effective area. On the other hand, if untracked events are taken into account, a larger effective area can be obtained, but this also leads to a noticeable deterioration of the angular resolution element.

The nano-satellite will orbit, like other Compton telescopes, in a quasi-equatorial Low Earth Orbit (LEO; ~ 500÷600 km, equatorial), pointing at the zenith. The choice of this orbit has two main reasons. First it is only marginally affected by the South Atlantic Anomaly and therefore represents a low-particle orbit background. Secondly there are no precipitating particles originating from solar flares.

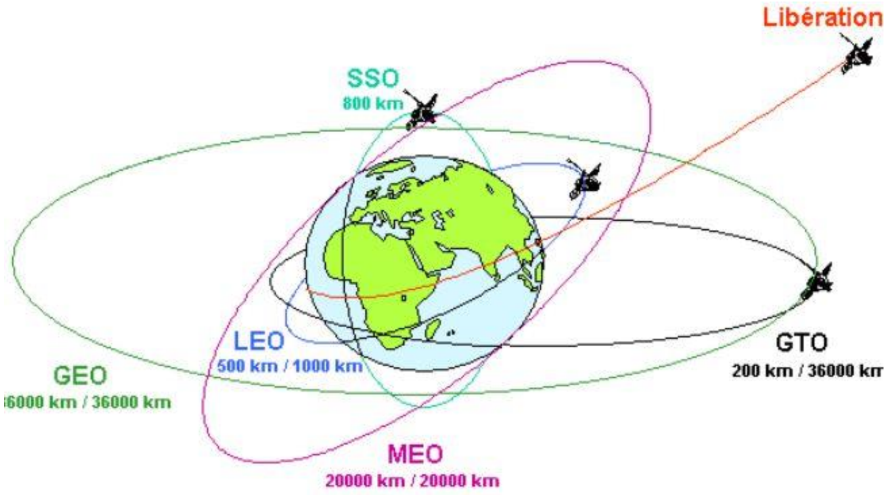

Figure 36: *Different possible orbits of satellites, including the LEO in blue.*

To obtain an accurate estimate of the sensitivity is necessary to know and estimate well all the sources of background events. The largest background contributions in the LEO are mainly due to (see De Angelis et al. 2017):

- Extra-galactic background: this diffuse, isotropic and homogeneous photon background is caused by the presence of unresolved sources.
- “Albedo” photons: a great gamma-rays flux generated by primary cosmic rays hitting the Earth's atmosphere (Earth’s gamma emission). This background is the major source of disturbance.
- Charged background: this background is due by charged cosmic rays but can be significantly reduced (> 99.99%) using the anticoincidence detector.
- Pair production events: it is possible that the positron (see Figure 37) can generate a pair of additional gamma-rays that could escape the thin calorimeters. This effect can lead to reconstructing these events as Compton interactions (we will see in the next chapter how to solve it).

- Activation: fast protons and alpha particles present in the cosmic rays hitting the satellite can activate the materials present in the satellite. To limit this type of background it is necessary to study carefully with which materials to build our satellite and its geometry. the Activation scales with the amount of passive material present in the satellite.

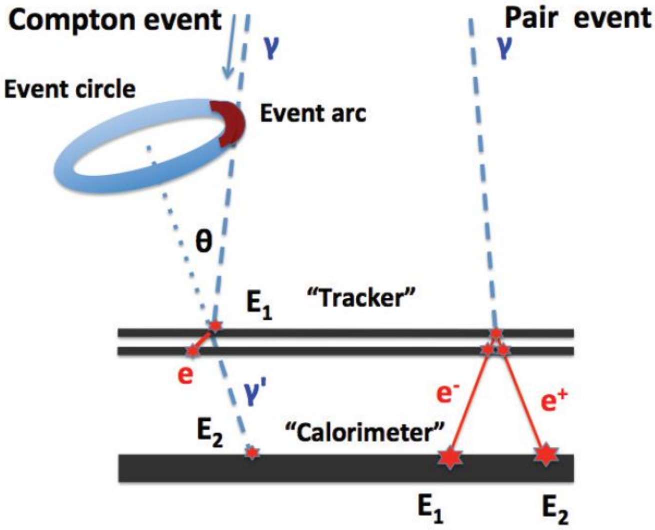

Figure 37: *The Compton (on the left) and pair interaction (on the right) in the satellite. In blue we can see the photon tracks while in red the electron and positron tracks (Moiseev et al. 2007).*

To estimate these backgrounds, we can use the data that come from previous missions. For example, we can derive the flux of "albedo" photons from De Angelis et al. (2017) while the contribution due to the extra-galactic background from Georg (1999), extended at lower energies. We have also calculated that the largest contribution to the charged background for a satellite operating in the MeV energy range and flying in a low Earth orbit is represented by secondary electrons (see De Angelis et al. 2017). Running secondary electrons simulations for several hours in our energy range we have concluded that their event rate is negligible (less than 10^{-4} Hz with respect to ~ 1 Hz for the EGB) and too small to estimate their spectrum. The problem in our simulation is in considering that the ACD is completely hermetic, in reality there will be several sources of inefficiencies of the ACD assembly (such as the seams) that will be decisive in determining the true charged background. Since at this stage these inefficiencies are not yet clear, we impose for simplicity that the number of events coming from charged particles is $N_{chg} = 0$.

As we said in the previous paragraph the continuum sensitivity can be calculated by estimating the background with a semi-analytical method. The total number of background events can be obtained from:

$$N_B \cong N_{egb}(1+R)$$

here R is the ratio between "albedo" emission and the extra-galactic gamma-ray background (EGB) and N_{egb} is the number of EGB events inside the angular resolution element:

$$N_{egb} = F_{egb} \cdot A_{eff} \cdot T_{eff} \cdot d\Omega .$$

The value of the sensitivity is better if our satellite is pointing outwards from Earth (i.e. at the zenith) and our source is located at the zenith angle $\Theta = 0$. Unfortunately, despite the fact that the flux of “albedo” photon from Earth at angles $\Theta < 90^0$ is null it is possible that a small fraction of events has a large SPD. In this case it may happen that the Compton arc may be partially in the sky map element we are observing. For this reason and considering that the flux of "albedo" photons in the LEO is remarkable, the Earth's gamma emission represents the major contribution to the background of our nano-satellite

Comptel solved this problem simply because of its photomultiplier tubes and the time-of-light measurements with which he could make the distinction between upward and downward events. For our nano-satellite we can only try to use some kind of trigger that is able to reject the majority of “albedo” events.

2.5 Performance Estimate

Figure 38 shows the effective area calculated at the zenith angle as a function of the incident photon energy for tracked at untracked Compton events. This figure does not report the uncertainties that are more significant than statistical errors, while the systematic errors can not be calculated until the final design of the satellite is established. We can see that the effective area in tracked events takes on interesting values above several hundreds of keV. While the effective area in untracked events has a remarkable peak around 200÷300 keV which means that our telescope is able to detect sources at lower energies. In Figure 39 where the effective area for tracked events is reported we can see that there is not a large dependence of the effective area on the polar angle Θ. Based on the results of the simulation we have found that the difference in energies of about 1 MeV between the effective area calculated for normal incidence and that for an angle of 90º is less than 15%. From this we can conclude that the field-of-view is very large compared to that of Comptel (see Kappadath 1998). The second parameter we estimate is the energy resolution. This, in addition to being weakly dependent on the selected event class, significantly improves with increasing energy. For example at 100 keV the energy resolution is ~ 20%, at 1 MeV it is 4.6% and at ~3 it is 3%. However, we must pay attention to the fact that at energies exceeding few MeV there is a severe issue due to incomplete energy absorption due to the limited size of the detector. In Figure 40 we can see the estimated angular resolution. To obtain it we estimated the values of the ARM and the SPD both in tracked and in untracked events.

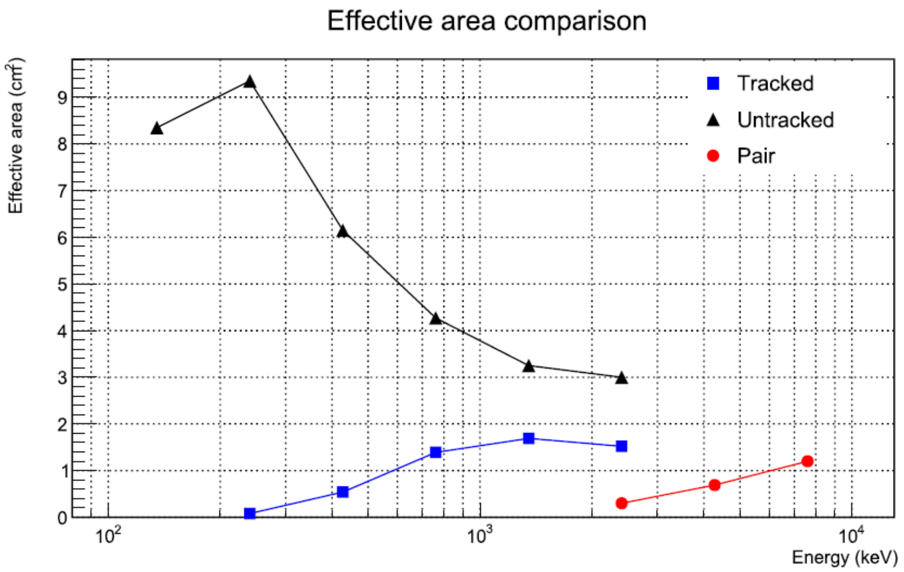

Figure 38: *Effective area comparison for Compton (both tracked and untracked) and pair events (at the zenith angle) (Lucchetta et al. 2017).*

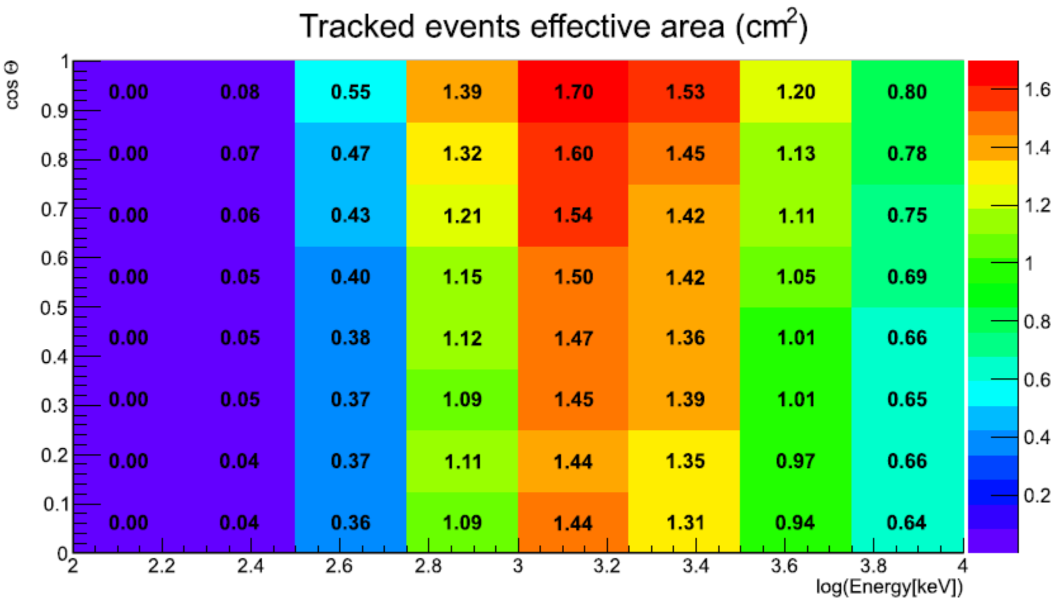

0.00	0.08	0.55	1.39	1.70	1.53	1.20	0.80
0.00	0.07	0.47	1.32	1.60	1.45	1.13	0.78
0.00	0.06	0.43	1.21	1.54	1.42	1.11	0.75
0.00	0.05	0.40	1.15	1.50	1.42	1.05	0.69
0.00	0.05	0.38	1.12	1.47	1.36	1.01	0.66
0.00	0.05	0.37	1.09	1.45	1.39	1.01	0.65
0.00	0.04	0.37	1.11	1.44	1.35	0.97	0.66
0.00	0.04	0.36	1.09	1.44	1.31	0.94	0.64

Figure 39: *Tracked events effective area in the function of Monte Carlo energy and direction of the initial photon (cosΘ = 1 for normal incidence) (Lucchetta et al. 2017).*

Regarding the ARM we have calculated the FWHM even if we must be careful that this value takes into consideration only the peak of the spectrum neglecting the contribution from the tails of the distribution. However, it is also true that in the range of energy to which we operate the ARM distribution is quite regular so as not to introduce an issue due to the presence of significant tails. Instead for the SPD we estimated the HWHM of the distribution. In the graph of Figure 40 we can see that in the case of tracked events the ARM assumes larger values than untracked events.

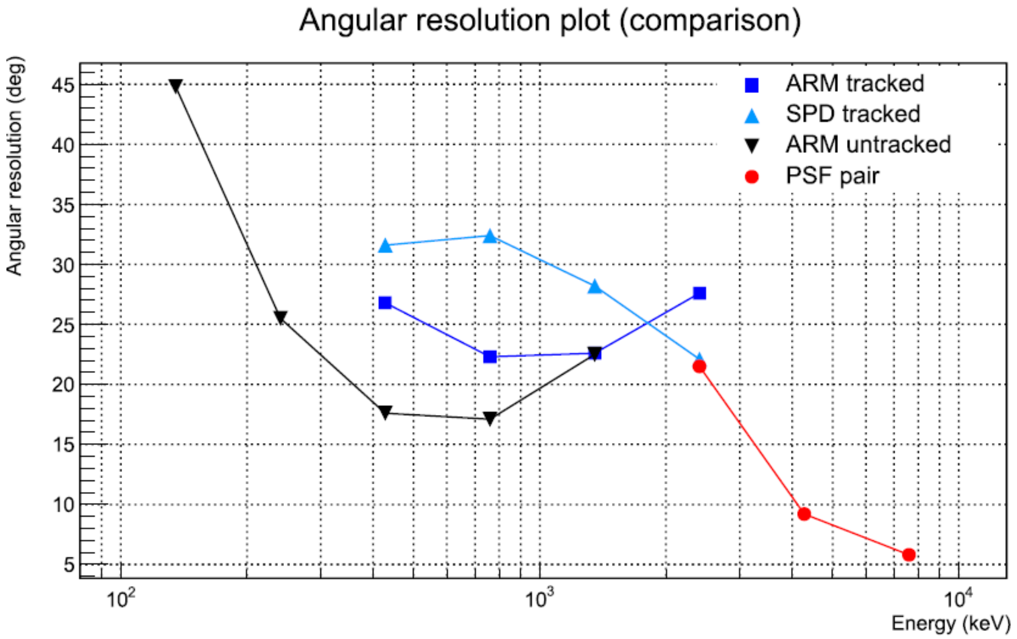

Figure 40: *Estimated ARM and SPD for Compton events (both tracked and untracked), and PSF for pair events (Lucchetta et al. 2017).*

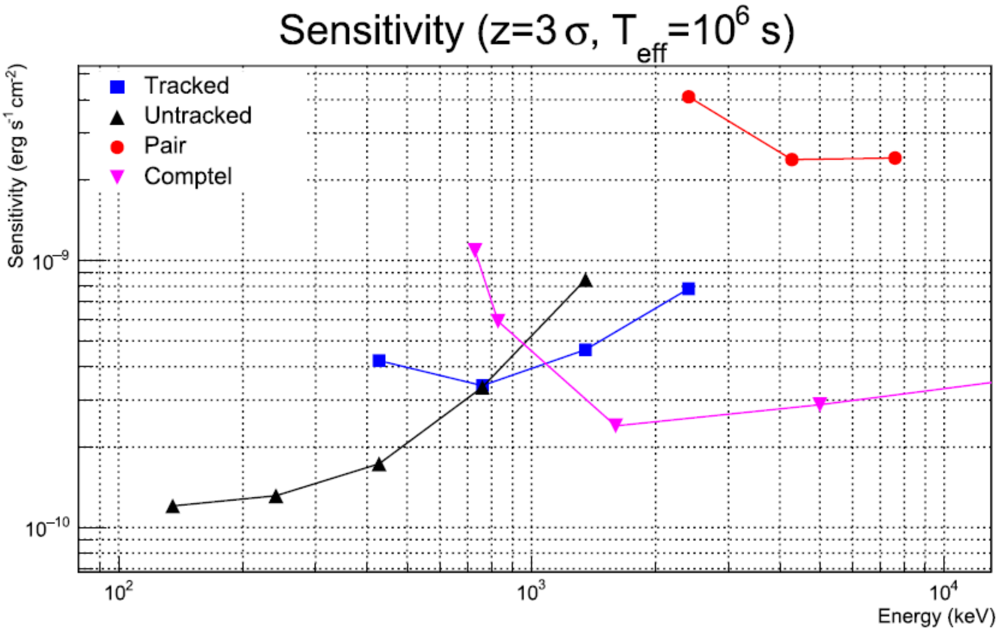

Figure 41: *Estimated continuum sensitivity for Compton (both tracked and untracked) and pair events, in comparison to that of COMPTEL (Lucchetta et al. 2017). COMPTEL sensitivity values are taken from Schönfelder (2004).*

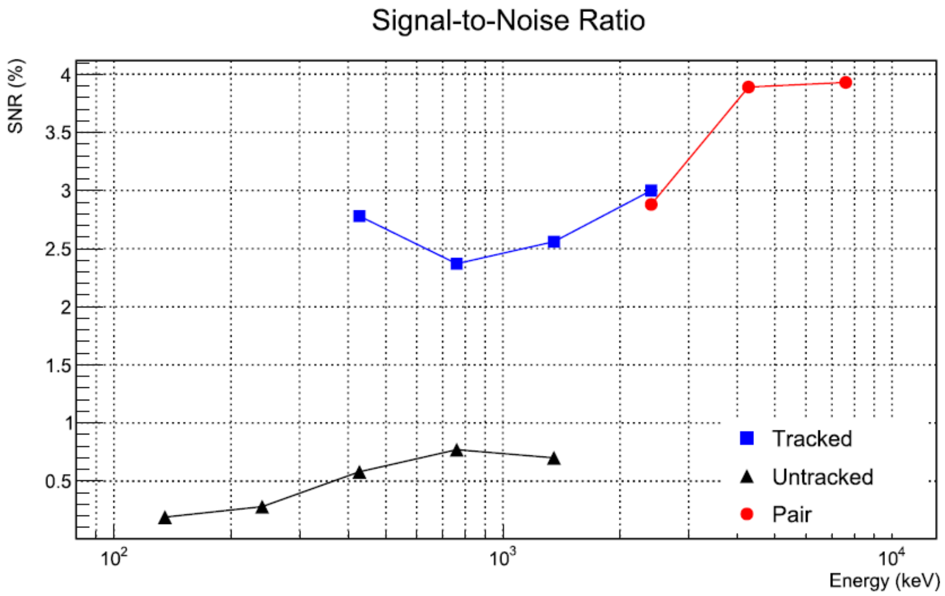

Figure 42: *Estimated signal-to-noise ratio for Compton (both tracked and untracked) and pair events (Lucchetta et al. 2017).*

In Figure 41 we can see the continuum sensitivity obtained with the semi-analytical method assuming that effective observation time of $T_{eff} = 10^6$ and the significance level of $z = 3$ and that the source is near the zenith. Since the effective area is very small in untracked events, it translates into the fact that the sensitivity is better in untracked events than in tracked events. Based on this we can deduce that our satellite can operate with untracked events at energies < 500 keV while with tracked events at energies > 500 keV.

In Figure 42 is reported the signal-to-noise ratio (S/N) both for untracked events and for tracked events. We can see that the S / N is much lower in untracked events which makes us conclude that the systematics will be a big problem as a percent level control will be needed.

We would get an improvement of the sensitivity but not the S / N if we increase the effective area (and unfortunately also the background). We caculated instead that the sensitivity varies little (15 ÷ 20% worsening) reducing the material and the read-out eletronics. We could see about 30 steady sources (as in Comptel; Schönfelder et al. 2000) based on the design of our satellite and considering the large angular resolution and our sensitivity.

We have calculated that with a depth resolution for the calorimeter crystals of 0.5 cm we have a noticeable improvement of the ARM with an ARM FWHM reduced by 40% at energies ~ 1 MeV and normal incidence with a consequent improvement of ~ 35% in the sensitivity and S / N.

Even if the cross section for pair production between 2 MeV and 10 MeV is very small in Figures 38, 40, 41 and 42 we have also reported the performance for pair production. As expected, our satelite's performance is not adequate for pair production.

As the last thing we considered Crab Nebula spectrum and we calculated the number of expected photon observed from this source (N_S) for tracked events. We have $N_S \sim 1.7 \cdot 10^4$ photon for an effective oservation time of 10^6 s with S / N of ~ 25%. While in untracked events N_S is about $2.0 \cdot 10^5$ photons with S / N of ~ 6%.

Chapter 3

Reconstruction and analysis software for the nano-satellite

3.1 Introduction

As we saw in the previous chapter our nano-satellite consists of a tracker, of a calorimeter and an ACD, and will orbit in the LEO. We remember then that the main sources of background in this orbit are mainly caused both by the "albedo" photons generated by the primary production of gamma rays and the pair production in which the positron produced in turn produces a pair of gamma rays that can escape the thin calorimeter with the consequence of misreconstructing the pair production event as a Compton interaction. In the latter case, the direction of the primary gamma ray is completely incorrectly reconstructed with an energy estimate in defect by (a multiple of) 511 keV. In this chapter we see how to develop a technique to reject these two types of unpleasant background that have a cost both in terms of effective area and in worsening the performance of our satellite. Two algorithm solutions have been developed, implemented as two binary classifiers able to identify and reject both misclassifiel pair events and "albedo" events. In this way a noticeable increase in satellite sensitivity can be noticed. These two binary classifiers were designed using machine learning models such as the Neural Network (NN) algorithms able to achieve outstanding performance on some classified tasks (Srivastava et al. 2014; Glorot and Bengio 2010; Ioffe and Szegedy 2015; Nair and Hinton 2010; Sutskever et al. 2013).

The chapter is structured in this way: in paragraph 3.2 we will discuss the machine learning, in paragraph 3.3 we will introduce a new metric for the detector sensitivity with two methods to improve the continuum sensitivity, while in paragraph 3.4 we will report the experimental results.

3.2 Machine Learning

The term machine learning was coined by Arthur Samuel in 1959 in order to define a set of statistical methods designed to progressively improve the performance of an algorithm in the study of a data pattern. Using machine learning algorithms it is possible to construct a mathematical model of sample data, known as "training data" in order to make predictions or decisions without being explicitly programmed to perform the task (Arthur Samuel 1959).

The Random Forest (RF) (Ho 1995; Breinman 2001), a powerful machine learning algorithm, is a combination of Decision Tree (DT) (the basic building block of a random forest) such that each tree depends on the values of a random vector sampled independently and with the same distribution for all trees in the forest. DTs are excellent classifiers because they have high execution speed and can learn a series of questions to infer the class labels of the samples.

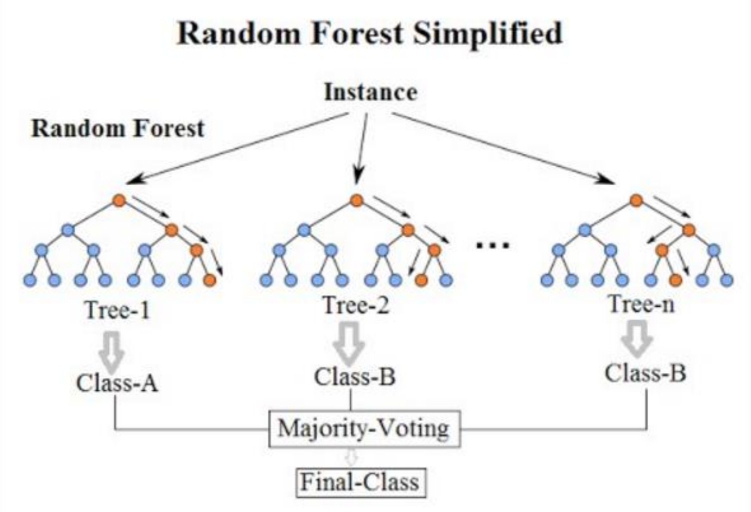

The multilayer perceptron (MLP) is a class of feedforward artificial neural network. MLP is characterized by at least three layers of nodes: an input layer, a hidden layer and an output layer. if we exclude the input nodes, all nodes are represented by a bias neuron that uses a nonlinear activation function. Since MLPs are fully connected, each node in one layer connects with a certain weight to every node in the following layer. For training the MLP a supervised learning technique called backpropagation algorithm (Rumelhart et al. 1988) is used.

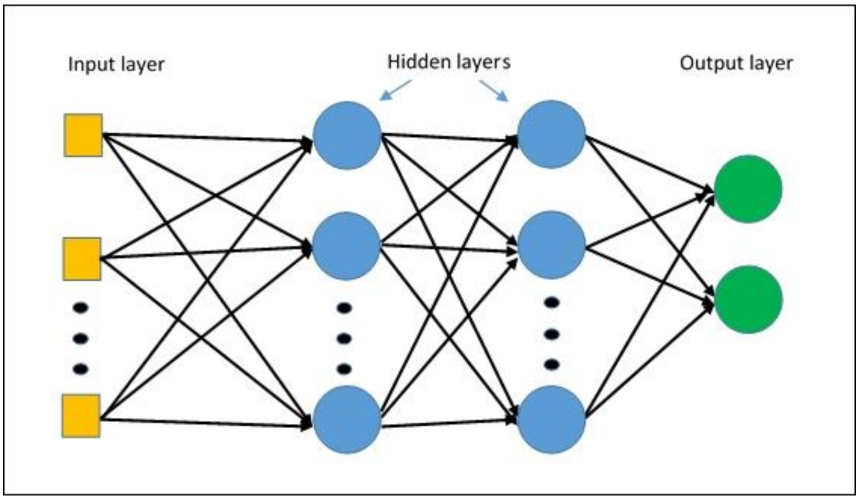

The Generative Adversarial Nets (GAN) were proposed by (Goodfellow et al. 2014). GAN is characterized by a system of two neural networks contesting with each other in a zero-sum game framework. A generator creates samples and the a discriminator evaluates them. The discriminator determines whether a sample comes from real data or has been created by the generator. The generator instead tries to build samples that seem to come from real data in order to deceive the discriminator. Through the GAN model it is possible, for example, to produce samples of photorealistic images.

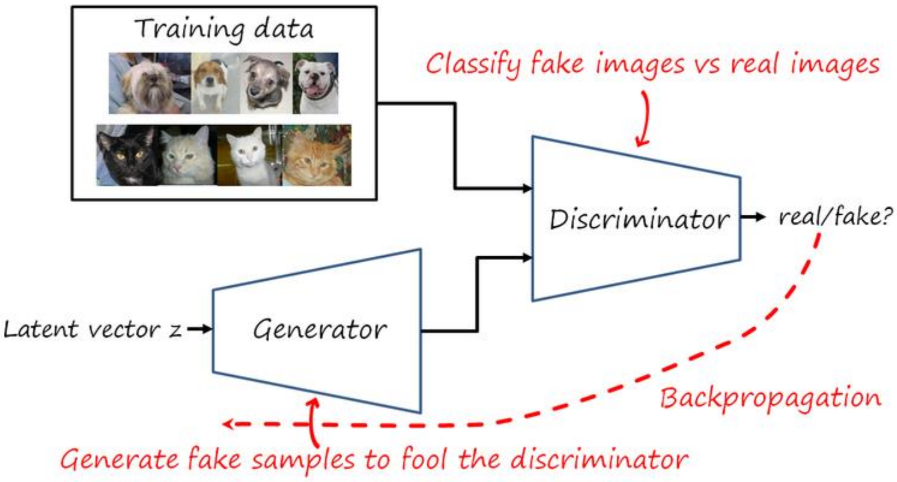

The ensemble methods (Freund and Schapire 1995) combines well-trained predictors together to create a better classifier. The predictors will have to work independently from one another. An efficient ensemble predictor can be obtained by aggregating the trained RF, MLP, and GAN model together, in this way it is possible that each classifier can perform diffent types of errors. The ensemble methods are divided into two categories: hard and soft. In the hard procedure, the prediction of all the classifiers are grouped by predicting the class that reaches the highest number of votes. Instead, in the soft method, the class that obtains the highest probability is predicted, and averages on each classifier that can estimate class probabilities. Comparing the two strategies, the soft one probably manages to achieve better performance as it provides more weight to the highly confident (Géron 2017) and allows to provide each classifier with a weight proportionate to his performance (the higher the weight).

To make the performance faster the machine learning programs are developed on multi-CPU (Pedregosa et al., 2011), while the NN on the General Porpose Graphic Processing Unit (GPGPU) (Abadi et al., 2016).

3.3 New metric for The Continuum Sensitivity

If we consider the problem of the wrong classification of pair events as Compton interaction one can think of taking as performance metric the accuracy, and in this case the greater the precision the better. If instead we want to distinguish the gamma-ray coming from the sky from the "albedo" photons coming from the Earth our metric must be the continuum sensitivity (which we have already discussed in the previous chapter). Unlike accuracy, the lower continuum sensitivity the better, i.e. a low continuum sensitivity allows us to identify the real gamma-ray correctly. Recalling the formula of Zoglauer 2005 (see paragraph 2.3) and fixing the statistical significance z = 3 we can rewrite the formula in a different way if we plan to put the number of "albedo" events N_{albedo} approximately equal to the number of background events N_B, consider that the effective area A_{eff} may be proportional to the number of real gamma events N_{gamma}. Then the formula for continuum sensitivity becomes:

$$F_z \propto \frac{\sqrt{N_{albedo}}}{N_{gamma}}$$

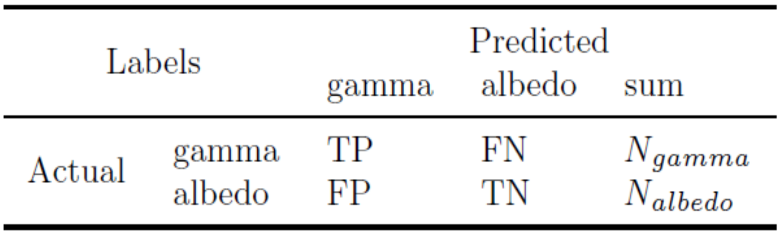

Labels		Predicted		
		gamma	albedo	sum
Actual	gamma	TP	FN	N_{gamma}
	albedo	FP	TN	N_{albedo}

Table 5: *Confusion matrix of the classified task (Cao et al. 2018).*

If we consider the confusion matrix of the classified task in Table 5 we can define a new metric to establish the classifiers:

$$\eta = \frac{\sqrt{FP}}{TP}$$

we can derive that $F_Z \propto \eta$ and considering that the machine learning introduces the concept of metric precision, we have that:

$$precision = \frac{TP}{FP + TP}$$

from which we derive that we can write the new metric as:

$$\eta = \sqrt{\frac{\frac{1}{precision} - 1}{TP}}$$

the lower the F_z the better the performance of our detector, and remembering that $F_Z \propto \eta$ we can infer that the higher the $precision$ the better the detector[1].

---

[1] This is only a hypothesis because the denominator TP is not considered, but we believe that based on our numerical range it can be true.

At this point we also introduce an increase rate - *improvement* which quantifies how much the sensitivity of our satellite has improved:

$$improvement = \frac{\eta_0 - \eta}{\eta_0}$$

where

$$\eta_0 = \frac{\sqrt{FP_{total}}}{TP_{total}}$$

identifies the original fixed level of the detector's sensitivity. $FP_{total} = N_{albedo}$ is the total “albedo” background events and $TP_{total} = N_{gamma}$ is the total of real gamma-ray events.

This our new metric will be correlated to the precision score and in order to improve the precision we allow that some positive samples to be classified as negative while we can not accept the opposite i.e., that negative samples are accepted as positive. Now we introduce two possible methods to improve the precision score of MLP and GAN models[2] identifying how much the continuum sensitivity improves. These two methods are:

- Modifying the loss function to be positive weighted (cost-modifying method)
- Introducing a threshold parameter on the output layer

3.3.1 Cost-Modifying Method

This method has been described by Japkowicz and Stephen 2002 regarding the class imbalance problem. We have already said that we accept that positive samples are negative misclassifyng while we do not accept the vice versa. It all leads to an imbalance problem where misclassfying negative samples to be positive must have more penalty than the miscallssifying positive samples to be negative. According to Janocha and Czarnecki (2016) it is useful to introduce different loss functions in the creation of neural networks. In Table 5 are reported different non-classical loss functions with their positive weighted formula. Each of these positive weighted formula has a different penalties on misclassification.

3.3.2 Set Threshold Level

If we focus on the output layer of neural networks, the prediction is given by the output unit that achieves the highest predicted score. To improve accuracy we want to make sure that a particular sample is predicted positive by the model only if its positive output unit (whose index is 1) has a high predicted score. To do this we decide to impose a threshold value P $(P \geq 0.5)$ on the positive output unit. In this way it becomes more difficult for the binary classifier to determine if a sample is positive (in the balanced case $P = 0.5$). So we have that:

---

[2] Unfortunately these two methods do not work with the random forest model.

$$\begin{cases} p(y_1) \geq P & \text{predizione =1} \\ p(y_1) < P & \text{predizione =0} \end{cases}$$

where $p(y_1)$ is the predicted score of the positive output unit.

Loss function	**Weighted expression**
L2 loss	$(\lvert y_0 - l_0 \rvert^2 + \lvert y_1 - l_1 \rvert^2) \cdot (y_0 + \mathrm{w} \cdot y_1)$
expectation loss	$(\lvert y_0 - \sigma(l_0) \rvert + \lvert y_1 - \sigma(l_1) \rvert) \cdot (y_0 + \mathrm{w} \cdot y_1)$
regularised expectation loss	$(\lvert y_0 - \sigma(l_0) \rvert^2 + \lvert y_1 - \sigma(l_1) \rvert^2) \cdot (y_0 + \mathrm{w} \cdot y_1)$
Chebyshev loss	$\max(\lvert y_0 - \sigma(l_0) \rvert, \lvert y_1 - \sigma(l_1) \rvert) \cdot (y_0 + \mathrm{w} \cdot y_1)$
hinge loss	$(\max(0,\ 0.5 - \hat{y}_0 \cdot l_0) + \max(0,\ 0.5 - \hat{y}_1 \cdot l_1)) \cdot \mathrm{w}_h$
squared hinge loss	$(\max(0,\ 0.5 - \hat{y}_0 \cdot l_0)^2 + \max(0,\ 0.5 - \hat{y}_1 \cdot l_1)^2) \cdot \mathrm{w}_h$
cubed hinge loss	$(\max(0,\ 0.5 - \hat{y}_0 \cdot l_0)^3 + \max(0,\ 0.5 - \hat{y}_1 \cdot l_1)^3) \cdot \mathrm{w}_h$
log (cross entropy) loss	$-y_0 \cdot \log\sigma(l_0) - y_1 \cdot \log\sigma(l_1) \cdot \mathrm{w}$
squared log loss	$(y_0 \cdot \log\sigma(l_0))^2 + (y_1 \cdot \log\sigma(l_1))^2 \cdot \mathrm{w}$
Tanimoto loss	$-\frac{(\sigma(l_0) \cdot y_0 + \sigma(l_1) \cdot y_1) \cdot (y_0 + \mathrm{w} \cdot y_1)}{\sigma(l_0)^2 + \sigma(l_1)^2 + (y_0)^2 + (y_1)^2 - \sigma(l_0) \cdot y_0 - \sigma(l_1) \cdot y_1}$
Cauchy-Schwarz Divergence	$-(y_0 + \mathrm{w} \cdot y_1) \cdot \log \frac{\sigma(l_0) \cdot y_0 + \sigma(l_1) \cdot y_1}{\sqrt{\sigma(l_0)^2 + \sigma(l_1)^2} \cdot \sqrt{(y_0)^2 + (y_1)^2}}$

Table 6: *Different non-classical weighted loss functions where* $0 < w < 1$ *and* $w_h = \hat{y}_0(1.5 - 0.5 \cdot w) + \hat{y}_1 + 0.5 \cdot w + 0.5 y_0$, y_0 *and* y_1 *are true label as one-hot encoding,* $\hat{y}_1$ *and* $\hat{y}_0$ *are true label as +1/-1 encoding ,* l_0 *and* l_1 *the negative output and the positive output of the last layer (the output layer has only two neural units), respectively, and* $\sigma(\cdot)$ *denotes the outputs of the last layer after softmax function (Cao et al. 2018).*

3.4 Experimental results

We decided to build two binary classifiers using three different machine learning models (RF, MLP and GAN) in order to fulfill our two classified tasks. The dataset (from "tracked events") have been divided into:

- "spd" dataset: containing both real Compton events and pair events misclassified as Compton.
- “alb” dataset: containing both real Compton events from the sky (zenith to equator) and "albedo" events from Earth.

We simulated a diffuse source which was isotropic with an incidence angle from zenith to equator and a power low spectrum with index -1 from 100 keV to 10 MeV, in order to produce the real Compton events. Although a spectral index of -1 is perfect in order to have a good statistical coverage on all energy bands, it is not suitable value for a realistic source and therefore improving the average sensitivity we do not obtain an improvement of the sensitivity for realistic point source. Therefore, we have also simulated a point source positioned at the local zenith with a low-power spectrum with index –2, to see if the estimates of the optimized model are correct. We used the Medium Energy Gamma-ray Astronomy library (MEGAlib) to create the samples (Zoglauer et al. 2008).

3.4.1 "spd" dataset

For the "spd" dataset we first built the RF, MLP and GAN models independently and then aggregated them in two ways: soft and hard. In the first method the weights for the individual classifiers were identified by using of grid search (in Table 7 we can see the results). Based on the results, it can be seen that the MLP models at GAN achieve a greater weight than the RF, moreover the weighted voting classifier obtains the best performances. We calculated that most of the misclassified pair events are rejected with high accuracy score 77.22%.

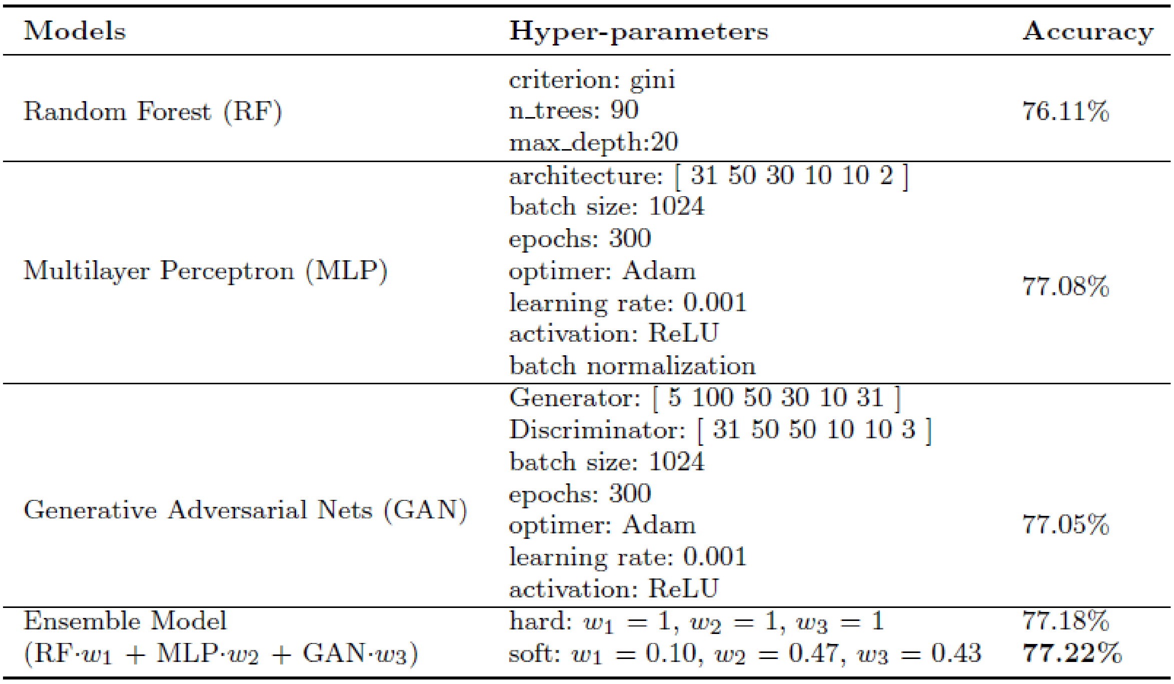

Models	Hyper-parameters	Accuracy
Random Forest (RF)	criterion: gini n_trees: 90 max_depth:20	76.11%
Multilayer Perceptron (MLP)	architecture: [31 50 30 10 10 2] batch size: 1024 epochs: 300 optimer: Adam learning rate: 0.001 activation: ReLU batch normalization	77.08%
Generative Adversarial Nets (GAN)	Generator: [5 100 50 30 10 31] Discriminator: [31 50 50 10 10 3] batch size: 1024 epochs: 300 optimer: Adam learning rate: 0.001 activation: ReLU	77.05%
Ensemble Model (RF$\cdot w_1$ + MLP$\cdot w_2$ + GAN$\cdot w_3$)	hard: $w_1 = 1$, $w_2 = 1$, $w_3 = 1$ soft: $w_1 = 0.10$, $w_2 = 0.47$, $w_3 = 0.43$	77.18% **77.22%**

Table 7: *The accuracy results of different models tested on "spd" dataset (Cao et al 2018).*

3.4.2 “alb” dataset

Also for "alb" dataset we have used the grid search method to report the performance of different models that used modified weighted loss functions with different threshold values on the positive output units. Then using the equations given in section 3.3 we can calculate how much the sensitivity of our satellite has improved and consequently also the increase rate of the new metric η.

Figure 43 shows the results of the weighted cross entropy loss function with the different output threshold levels (in 43 (a) we can see the accuracy score, in 43 (b) the precision score and in 43 (c) the increase rate). Observing Figure 43 (a) and (b) we can deduce that the relationship between the positive weights with the accuracy score is almost monotonic, while that between threshold values with the accuracy score is almost monotonic decreasing. While between the positive weights and the precision score and between the threshold values and the precision score there is a dependence respectively monotone decreasing and monotone increasing.

Table 8 shows the results of the tests performed using the non-classical loss functions listed in Table 6 from which we can deduce that there is a different behavior for the different loss functions and that a considerable improvement in the detector can be obtained thanks to the methods of improving precision score of a classifier model. Also, always in Table 8, we can see the results obtained using the realistic point source (spectrum index -2) from which we can see that the sensitivity improvement of our detector has achieved 35.14%.

Model	Modified loss function	Threshold	Weight	Improvement of η	
				index=-1	index=-2
MLP	L2 loss	0.6	1.0	16.07%	11.91%
	expectation loss	0.7	0.4	15.48%	19.88%
	regularised expectation loss	0.5	0.4	15.94%	21.14%
	Chebyshev loss	0.7	0.4	15.61%	20.53%
	hinge loss	0.5	0.4	15.35%	20.25%
	squared hinge loss	0.5	0.4	16.20%	20.74%
	cubed hinge loss	0.5	0.4	**16.41%**	21.95%
	log (cross entropy) loss	0.7	1.0	16.20%	**35.14%**
	squared log loss	0.6	1.0	15.68%	13.07%
	Tanimoto loss	0.8	0.4	15.48%	20.98%
	Cauchy-Schwarz Divergence	0.6	0.9	15.87%	12.95%
GAN	L2 loss	0.6	0.7	15.87%	15.82%
	expectation loss	0.7	0.3	16.15%	17.61%
	regularised expectation loss	0.7	0.8	16.00%	13.37%
	Chebyshev loss	0.7	0.4	15.94%	14.93%
	hinge loss	0.9	0.6	15.29%	11.00%
	squared hinge loss	0.5	0.05	13.92%	**22.63%**
	cubed hinge loss	0.6	0.8	13.99%	14.52%
	log (cross entropy) loss	0.6	0.4	16.07%	14.27%
	squared log loss	0.5	0.00001	16.07%	21.39%
	Tanimoto loss	0.6	0.0001	**16.20%**	17.87%
	Cauchy-Schwarz Divergence	0.6	0.3	16.00%	16.18%

Table 8: *The increase rate results come from different modified loss functions (Cao et al 2018).*

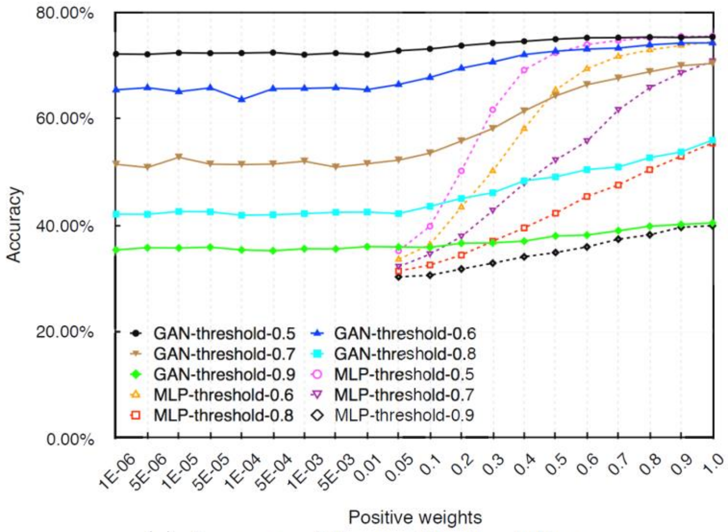

(a) Accuracy of the combined solution

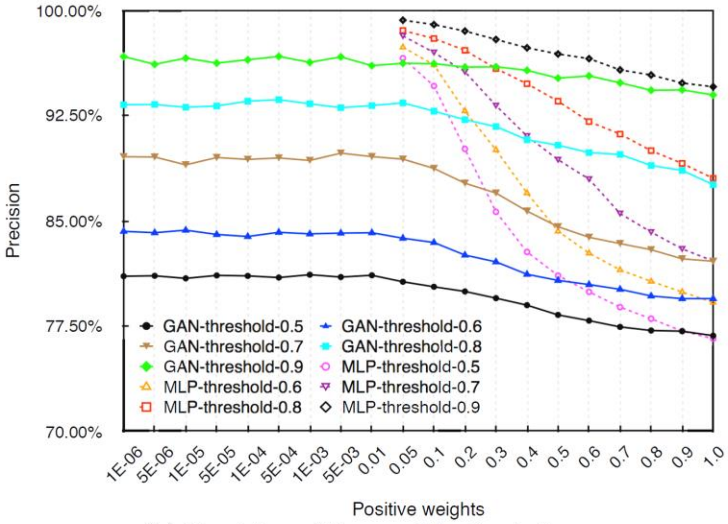

(b) Precision of the combined solution

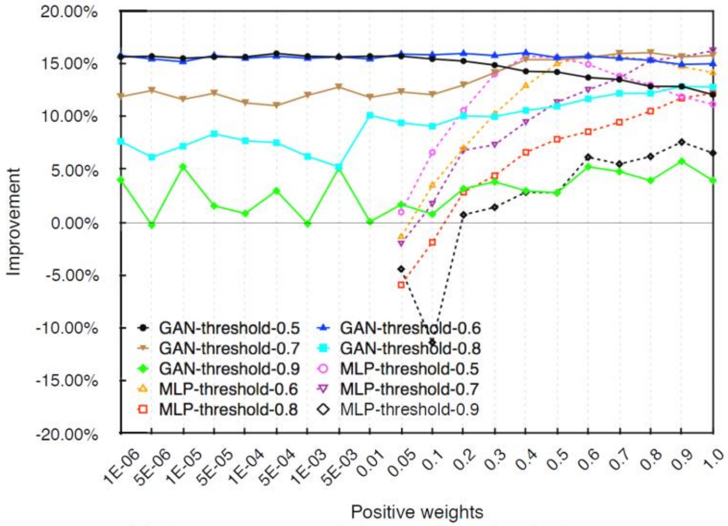

(c) Increase rate of the combined solution

Figure 43: *The results of the solution which combines positive weighted cross entropy loss function and threshold value setting (Cao et al 2018).*

Chapter 4

Characterization of energy and angular resolution

4.1 Introduction

This chapter is dedicated to calculating the energy and angular resolution of our nano-satellite. For this purpose, I performed simulations using MEGAlib, a set of software tools that are designed to simulate and analyze data of gamma-ray detectors, with a specialization on Compton telescopes that I will describe in detail in section 4.3. Since we will surely have many problems with the background noise in our nano-satellite I have chosen as the sources for my simulations, the Gamma-ray bursts, as they are able to emit many photons in a short time and this allows to minimize the background.

In the next section we will describe in detail the main features of the GRBs, in paragraph 4.4 we will see how the GRBs were selected, while in paragraph 4.6 the results of the simulation are reported.

4.2 Gamma ray bursts

Gamma-ray bursts (GRBs) are the the farthest and most luminous explosions in the universe. They are unannounced and non-repetitive flashes of X and gamma-rays detected from random places in the Universe at random times, and in few seconds, GRBs emit as much energy as our Sun will release in its entire 10 billions years lifetime. In fact if we assume that the GRBs emit radiation isotropically, we can determine that the isotropic equivalent luminosity is given by the formula $L_{ISO}=F\cdot 4\pi d^2$ (where F are the observed fluxes and d the known distances) and is equal to $L_{ISO}\sim 10^{40}\div 10^{47}$ W which corresponds to a total isotropic energy output for these events of $E_{ISO}\sim 10^{42}\div 10^{48}$ J comparable to the rest energy of the Sun. Since the Earth's atmosphere is not transparent to gamma rays, the discovery of the GRBs occurred only after the advent of the era of satellites.

They were first discovered in the late 1960s by Vela military satellites (Klebesadel et al. 1973) monitoring the Earth for secret nuclear weapons tests. It was soon understood that these flashes of gamma rays originated from outside our Solar System but the publication of their discovery occurred only several years later (see Klebesadel et al. 1973; and Mazets et al. 1974). In the early 1990s thanks to the Burst and Transient Source Experiment (BATSE) onboard the Compton Gamma Ray Observatory it was possible to obtain the positions of several thousand GRBs. In Figure 44 we can see that the distribution of GRBs in the sky, detected during the BATSE mission, is clearly isotropic with no concentration towards the plane of the Milky Way or towards the Galactic centre, which suggests they must be objects of the distant Universe (cosmological entities) and not Galactic in nature as was initially hypothesized.

GRBs are characterized by a collimated initial flash of gamma rays and hard X-rays powered by a compact central engine which launches a highly relativistic, and jetted electron/positron/baryon plasma. After this prompt emission there is a fading afterglow emission at longer wavelength (X-ray, ultraviolet, optical, infrared, microwave and radio), powered in part by the expanding outflow, (the interaction of the jet with the ambient material) and in part by continuous energy injection by the central engine which can last from few hours to weeks, sometimes months. The outflow is composed of three components: matter, magnetic fields, and photons. Based on the spectroscopic observations of the afterglows of GRBs and host galaxies we were able to measure their cosmological redshifts *z* and deduce their distances. The historical model used to explain the GRB phenomenon is called the "fireball" model (Wijers et al. 1997; Mészáros 1998, 2006) but according to Willingale et al. (2007) this model presents problems in explaining the temporal and spectral indices of about 50% of light curves (i.e. flux in gamma rays vs time). In the fireball model the matter is the dominant component of the outflow and magnetic field does not play a kinematically dominant role.

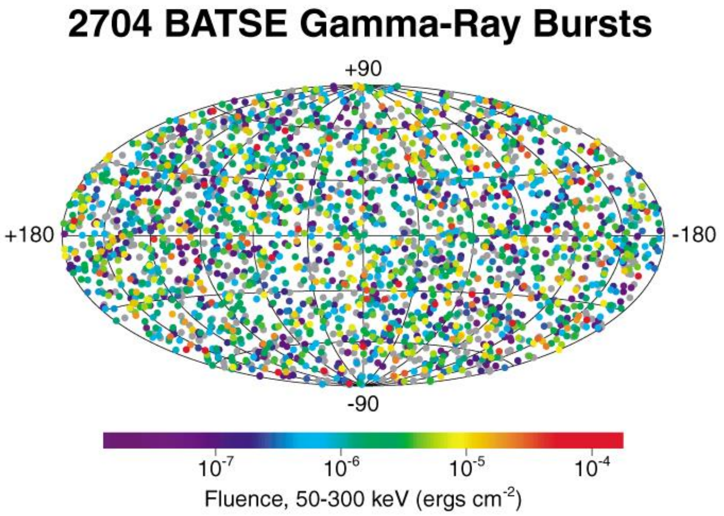

Figure 44: *Positions on the sky of all gamma-ray bursts detected by the BATSE instrument during after more than eight years of observation.. The distribution of bursts on the sky is isotropic rather than a concentration mainly in the plane of the plane of the Milky Way, which runs horizontally through the center of the image (NASA).*

The expanding fireball transforms most of its thermal energy into the kinetic energy of its baryons, which become highly relativistic. In this scenario we have that if the outflow is not completely homogeneous, the expanding plasma consists of several shells with slightly different Lorentz factors. At this point the faster shells catching up the slower ones creating internal shocks.

in these collision-less plasma shocks, in which amplified magnetic fields are present, the electrons emit via a synchrotron process, and probably in some cases also via inverse Compton processes. This is the prompt GRB emission. The fireball expands and can impact with surrounding material, in this way it dissipates kinetic energy in so-called external shocks, which are generated between the outflow and external material. The afterglow is generated by electrons that are accelerated in the external shocks and produces synchrotron emission in locally generated magnetic fields.

The light curves of GRBs are quite variable from one GRB to another with rapid variations seen on millisecond timescales which suggests that the energy of the GRB must be emitted from a very small region. In fact if we consider that a variability on a timescale Δt can not be produced in an area which is larger than the distance light travels during this time, we can deduce that the source size to be $D \le c \cdot \Delta t \approx 300$ km.

Based on this information we can understand that we are dealing with very compact objects such as neutron stars and black holes and with relativistic events connected with the end stages of stars.

The shape of the light curves of GRBs are different as the timescales which can vary from ms to few 100 s. The time profiles may present multiple peaks well separated in time, or they can be simple without fine structure and others are very erratic, chaotic and spiky (see Fig. 46). About 25-30% of all GRB light curves are simple and contain only one pulse, while the more complex curves are generally made up of several overlapping pulses. It is also possible to note that at high energy GRB light curve appears sharper with short duration. So far no physical model for GRB light curves exists that can explain all the properties of all GRBs.

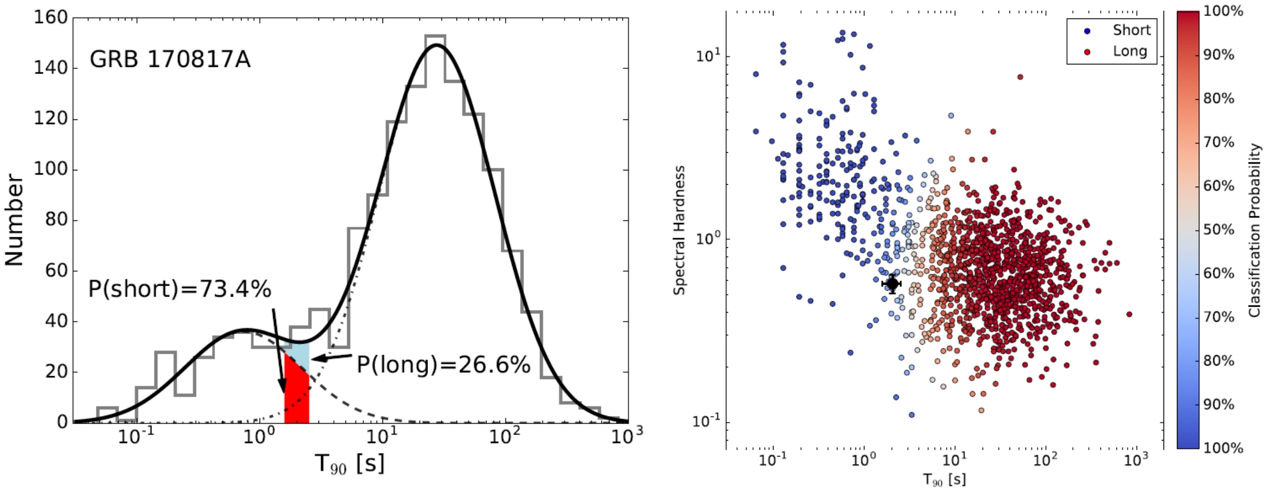

Figure 45: *(On the left) The GBM T_{90} distribution fit with two log normal distributions. The red region represents the probability that the event belongs to the short class, while the light blue represents the probability that it belongs to the long class. (On the right) The duration (T_{90}) vs the hardness ratio, an analog for the spectral hardness of the burst. Red dots characterize those most likely to belong to the long class while blue dots those most likely belong to the short class (Goldstein et al. 2017).*

The distribution of GRB durations observed by the BATSE instrument (Fishman et al., 1989) is characterized by two peaks: the first at T_{90} ~0.2 s and the second at T_{90} ~20 s with a boundary at T_{90} ~2 (Kouveliotou et al., 1993; where T_{90} is defined as the time in which the 90% (between 5% and 95%) of radiation is emitted in the prompt emission). This proves the existence of two different classes of bursts: long-duration gamma-ray bursts (LGRBs) and short-duration gamma-ray bursts (SGRBs). These two classes are related to different processes, but the end result in both cases is a brand new black hole. However, according to Norris and Bonnell (2006) there was a possible intermediate class or SGRBs with Extended Emission (SGRBsEE), that showed mixed properties between short-duration bursts bursts and long-duration with 2.5 sec $<T_{90}<7$ sec. Long-duration bursts account for about 70% of the gamma-ray bursts. They last anywhere from 2 seconds to a few hundreds of seconds (several minutes) and are usually associated to the core collapse of massive stars (Woosley and Bloom, 2006) leading to supernovae (CCSNe) of type Ib, Ic or II (Woosley & Bloom 2006; Hjorth & Bloom 2012; Hjorth et al. 2003) and occurs in star forming regions of blue dwarf galaxies.

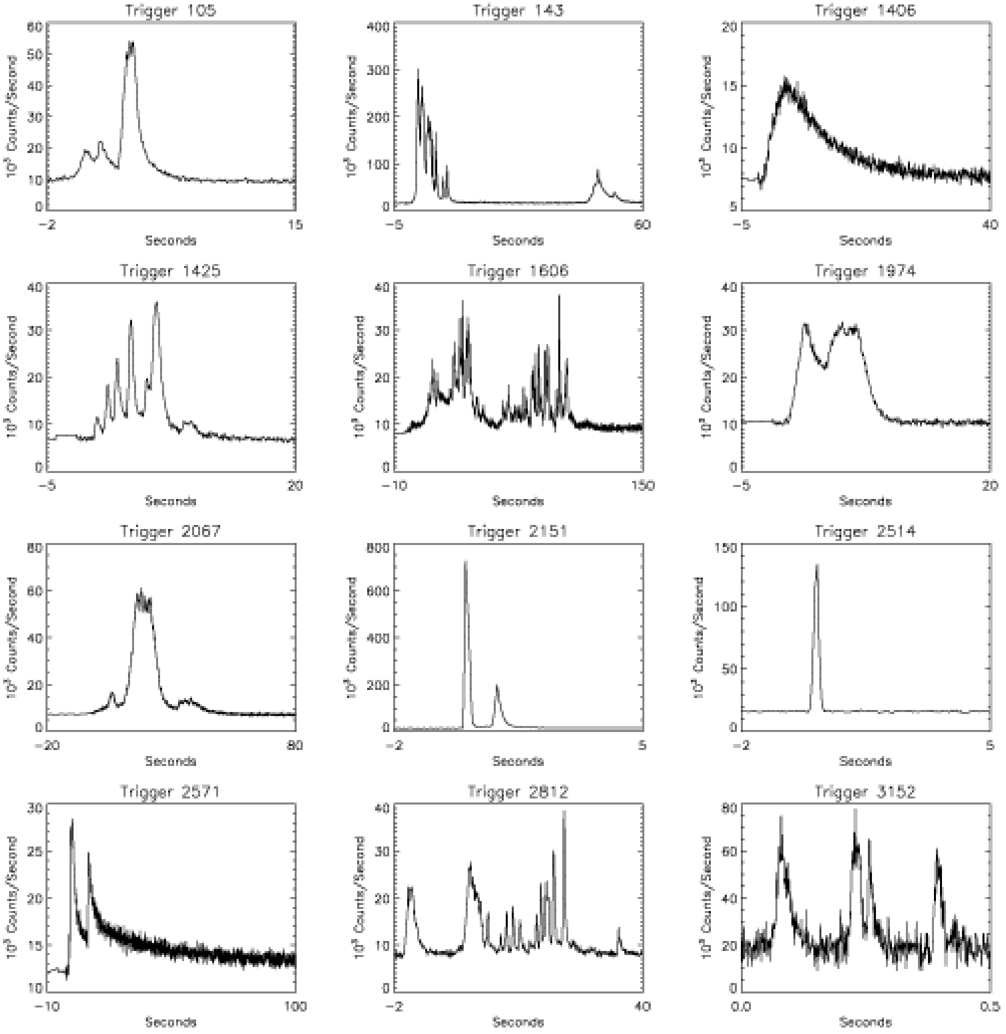

Figure 46: *Plots showing the number of gamma rays detected versus time (NASA).*

In the so-called Collapsar model (Woosley 1993), when the nuclear fusion reactions stop in the massive iron core of a rapidly rotating Wolf-Rayet[3] massive star, the core (which have a mass of about 10 M_{SUN} and a size of the Sun) becames unstable and it collapses to a black hole (either directly or during the accretion phase that follows the core collapse) with a few M_{SUN}. At this point a massive accretion disk is formed around this black hole with a mass of around 0.1 M_{SUN}, and because in the equatorial plane (perpendicular to the star's rotation axis) the material has too large angular momentum to fall directly into the black hole, a 'low density funnel' forms in the envelope along the rotation axis, where the stellar material has relatively little rotational support and can undergo almost free-fall. Accretion of this disk onto the black hole takes place in several dozen seconds and powers the GRB.

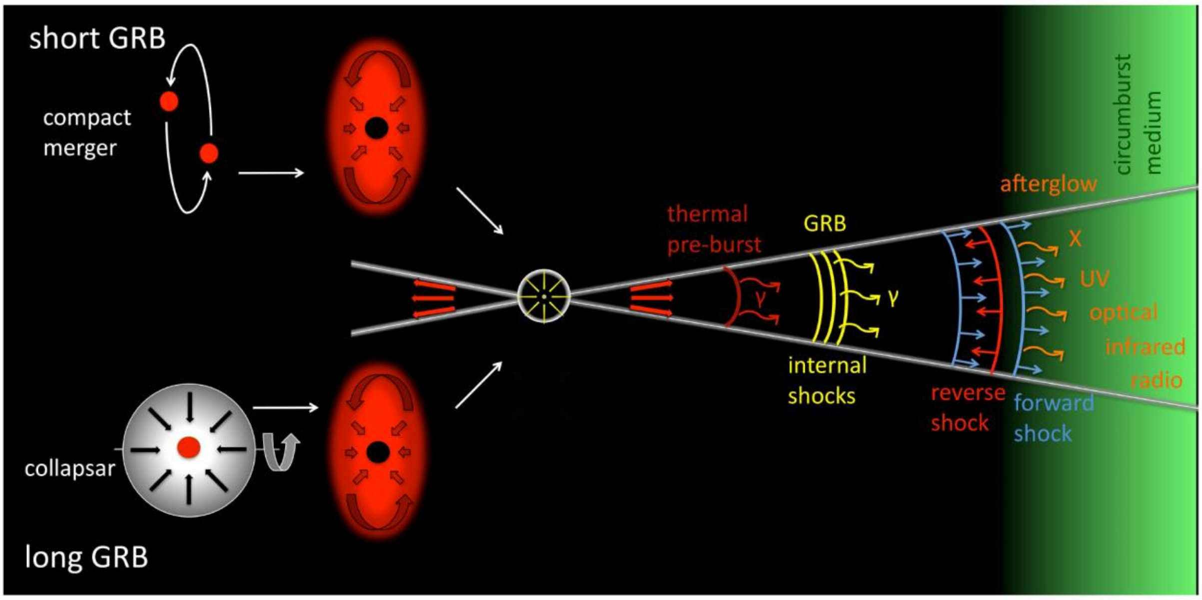

Figure 47: *(On the left) Progenitor models for short and long GRBs. (On the right) Production sites of gamma-rays and afterglow emission in the fireball model (Gomboc 2012).*

In fact if enough energy is injected into this region, it can push material along the rotation axis for as long it takes to cross the star (a few ~ 10 s), so that outflow eventually breaks through the star's surface. Subsequently the energy deposited in the surrounding matter will leak out along the rotation axis and if the outflow is collimated by the pressure from the stellar mantle, and gains high Lorentz factors as it breaks through the surface, will produce collimated relativistic outflows or jets with opening angles of < 10°. If the jets are powerful enough they would penetrate in the stellar envelope and produce the GRB. Therefore we have three necessary conditions for the progenitor star to evolve up to the emission of a gamma-ray burst: a mass greater than 40 M_{SUN}, a rapidly

---

[3] Wolf-Rayet stars are a normal stage in the evolution of very massive stars with a high rate of mass loss, typically 10^{-5} M_{SUN} /year. They are very hot, evolved, massive stars (masses typically greater than 25 times that of the Sun) with very strong stellar wind and short lifetime of ~ 10^7 yr.

rotating Wolf-Rayet star, and a low metallicity, so as to lose a sufficient part of the external hydrogen envelope so that the jets can reach the surface. This explains why only a small fraction of core collapse supernovae collapse with the emission of LGRBs (with a rate around 10^{-7}/ galaxy/ yr).

Short-duration bursts last from a few milliseconds to 2 seconds with an average duration of about 0.3 seconds (or 300 milliseconds), and appear to originate from the merger of two neutron stars into a new black hole or a neutron star with a black hole to form a larger black hole (Nakar, 2007). The short-duration bursts is found in both old[4] and star-forming galaxies. The merger of two neutron stars[5] (with masses between 1.4 M_{SUN} and 2 M_{SUN}) begins with the slow inspiral phase. During this inspiral phase, which only lasts $10^6 \div 10^9$ yr, the system emits gravitational waves, and the orbital period and separation of stars decrease. The closer the two neutron stars get the more the process undergoes a rapid acceleration and the final 100 km taking less than a second. When the distance between the two stars is only a few of their radii, the tidal interaction distorts their shapes. This happens immediately before they merge within about ~ ms. In this stage there are two long spiral arms that carry the excess angular momentum and wrapped around the central object which collapses to a black hole.

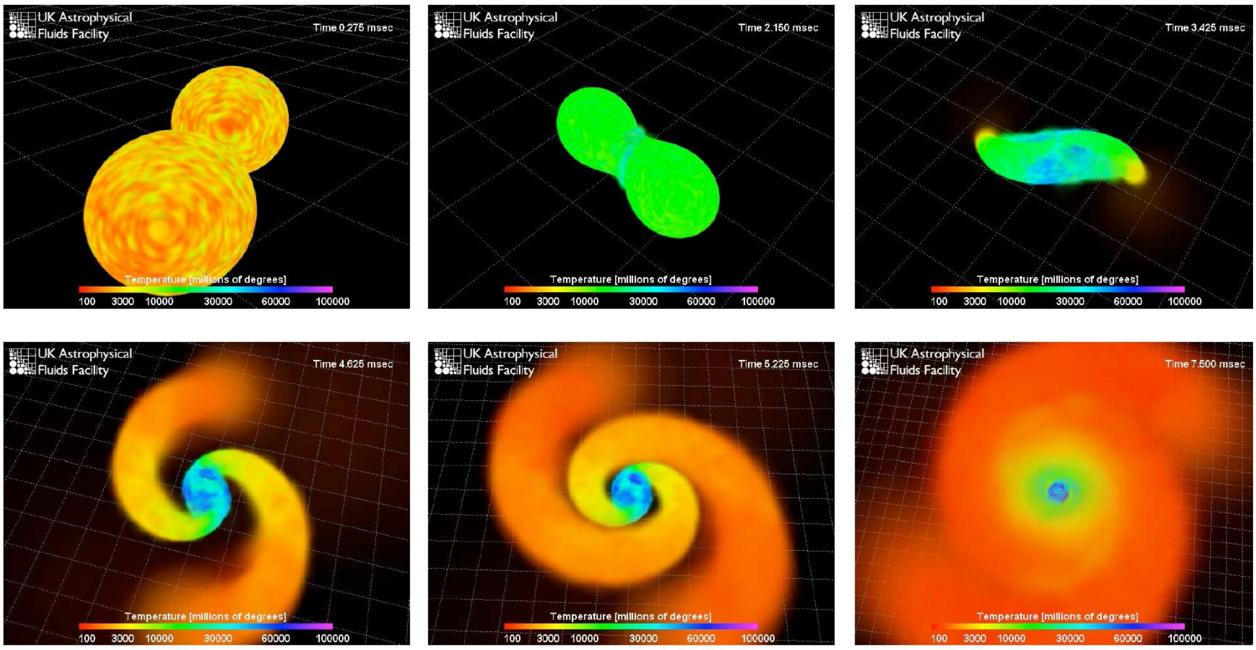

Figure 48: *The simulation of two neutron stars merger (simulation by Stephan Rosswog, visualization by RichardWest, http://www.uka.ac.uk/movies/nsmerger).*

The merger process between a neutron star and a black hole follows a similar pattern but is more complicated due to the transfer of mass from a neutron star to a black hole. In the final stage we

---

[4] It often happens that neutron stars can undergo substantial kicks when they are formed during a supernova explosion, this can lead them outside of star forming regions and even outside their galaxies.

[5] Neutron stars are very compact objects with size of only 10 km and densities of the order of a few 10^{17} kg/m^3.

have a situation that looks very much like the one we reach in the central region of a collapsar: a low-mass black hole surrounded by a massive accretion disc (see Fig.47). In the compact binary mergers there are two possible sources of energy: gravitational and rotational but also the magnetic fields of (one or two) neutron stars, amplified during the merger, could contribute in the launch of the outflow.

Since long-duration bursts tend to show the brightest afterglows and that represent the majority of the population, they have been studied in much greater detail than their short counterparts. Despite this, the mechanism responsible for the afterglow emission and its connection to the prompt γ-ray emissionof GRBs is still much debated.

The short gamma-ray burst GRB180817529 detected by the Fermi Gamma-ray Burst Monitor (GBM) on August 17, 2017 at 12:41:06 UTC turned out to be extremely important, because about 1.7 s prior to the GBM trigger, the Laser Interferometer Gravitational-Wave Observatory (LIGO) detected gravitational-wave (GW) from a binary compact merger candidate associated with the GRB. So the GRB180817529 represents the first unambiguous coincident observation of gravitational waves and electromagnetic radiation from a single astrophysical source and marks the birth of the new multi-messenger astronomy.

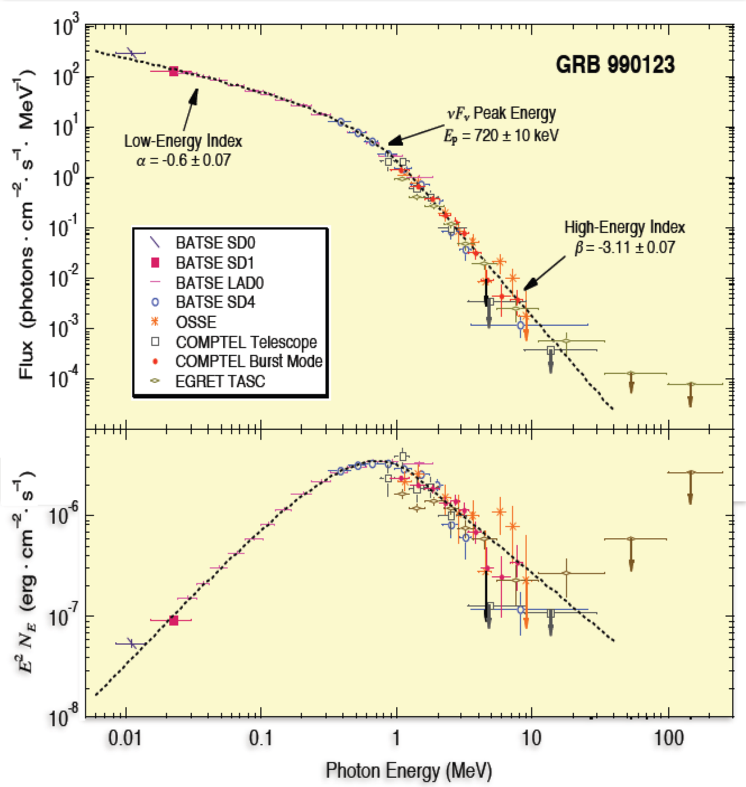

Figure 49: *The high energy spectrum of GRB990123 from the BATSE detectors, shown both as photon counts N_E and in E^2N_E units, where E is the energy of detected photons. The quantity E^2N_E tells us the amount of energy emitted in certain energy band (Briggs et al.1999).*

The observed time-resolved non thermal spectra of GRBs varies strongly from one burst to another but they are all successfully fit with the Band's GRB function (Band et al. 1993), an empirical formula used for GRBs that describes two power laws, continuous and smoothly joined at a break energy:

$$f(E)=\begin{cases} A\left(\dfrac{E}{100}\right)^{\alpha} e^{-E(2+\alpha)/E_{peak}} & \text{if } E<\dfrac{(\alpha-\beta)E_{peak}}{(2+\alpha)}\equiv \mathrm{E}_{break} \\ A\left[\dfrac{(\alpha-\beta)E_{peak}}{100\cdot(2+\alpha)}\right]^{(\alpha-\beta)} \exp(\beta-\alpha)\left(\dfrac{E_i}{100}\right)^{\beta} & \text{if } E\geq\dfrac{(\alpha-\beta)E_{peak}}{(2+\alpha)}\equiv \mathrm{E}_{break} \end{cases}$$

where α is the low-energy spectral index, β is the high-energy spectral index and E_{break} is the break energy. The energy flux peaks at a few hundred keV and in many bursts there is a long high energy tail extending in cases up to GeV. The typical energies of gamma ray photons emitted during a GRB are between 30 ÷ 1000 keV with the most energy emitted around 200 keV.

4.3 MEGAlib

The design of X-ray and gamma-ray detectors requires a tool that is able to determine the performance of the instruments with respect to the desired science objectives. Simulations are an essential step that allows the optimization of the design through trade-offs of different types of detector setup (such as various instrument orbits, shielding thicknesses, optimization of the passive material with respect to detector activation). Moreover through simulations it is possible to understand calibrations and measurements of the instrument. To determine the energy and angular resolution of our nano-satellite we used MEGAlib.

MEGAlib, the Medium-Energy Gamma-ray Astronomy library, is a simulation and data analysis tool for hard X-ray and low-to-medium-energy gamma-ray telescopes. It is an open-source object-oriented software. MEGAlib was developed by Andreas Zoglauer and originally designed for the combined Compton and pair telescope MEGA (hence the name; Zoglauer 2005). Its first purpose was to compare the performance of MEGA with other detector techniques but successfully applied to a wide variety of hard X-ray/gamma-ray telescopes in space and on ground, such as COMPTEL (Schönfelder et al. 1993), NCT (Boggs et al. 2005), ACT (Boggs 2006), NuSTAR (Harrison 2005), GRIPS (Greiner et al. 2009), and HEMI (Zoglauer, Galloway et al. 2009). Although it was initially developed for astrophysics it was subsequently expanded and used for ground based applications such as medical imaging and environmental monitoring. The tools in MEGAlib comprise the the whole data analysis path from simulations to highlevel data analysis such as image reconstruction. MEGAlib is written in C++ and utilizes ROOT software library (for its graphical user interface and its data display) and Geant4. Its principal libraries are:

1. Geomega (Geometry for MEGAlib)
2. Cosima (Cosmic Simulator for MEGAlib)
3. Revan (Real Event Analyzer)
4. Minrec (MEGAlib image reconstruction)
5. Fretalon (MEGAlib's calibration framework) and Melinator (MEGAlib's line calibrator)
6. Responsecreator
7. Realta (MEGAlib's real-time analyzer)
8. Spectralyzer (MEGAlib's spectral analyzer)
9. Eview (the event viewer of MEGAlib)

The first four libraries are described in detail in the following paragraphs.

4.3.1 Geomega

Geomega is the universal geometry and detector description library of MEGAlib which allows us to describe in detail different detector types: 2D or 3D strip detectors, voxel detectors, drift chambers, MEGA-like calorimeters, Anger-cameras, etc. Geomega includes in addition to a library also a graphical user interface that allows a geometry display using ROOT's standard or openGL display. All information about the geometry is stored in a simple object oriented ASCII file (with features such as constants, math functions, for-loops, if conditions, matrices, etc.), which describes the volume tree, the materials, volumes and detectors properties of the telescopes, the trigger criteria, noise properties, etc. In each geometry file we can identify the following five key sections:

1. A global section which contains: the name, the version, the included files, constants, etc.
2. A section in which is reported a list of all used materials and their parameters
3. A section in which is described the volumes and their placement
4. A section for the detector types and their characteristics defining the detector effects engine (including energy, position, time resolutions, noise and trigger thresholds, ADC overflows, etc.)
5. A section for the complex trigger criteria: by detector type or by individual detector, trigger or veto, by channel or by detector

Furthermore it is possible to divide the geometry into several files which can then all be included in a master geometry file. Geomega is essential for all other programs of MEGAlib in particular for Cosima.

4.3.2 Cosima (Cosmic Simulator for MEGAlib)

Cosima is the Geant4-based (see Zoglauer et al. 2006) cosmic simulator tool of MEGAlib. Cosima is able to simulate many of the measurement scenarios that can occur at energies that can range from a few keV to hundreds of MeV both in space telescopes and groundbased. The simulation needs a parameter file (also known as source file) which consists of a description of the sources (geometry, energy, intensity, etc.) as well as general information about the simulation, how to store the data, which physics lists to use, geometry, etc. (a detailed description of the source file can be found in section 4.5). The output of Cosima is a sim-file which consists of a header section and an event section. The sim-file is compatible with all other MEGAlib programs (such as Revan).

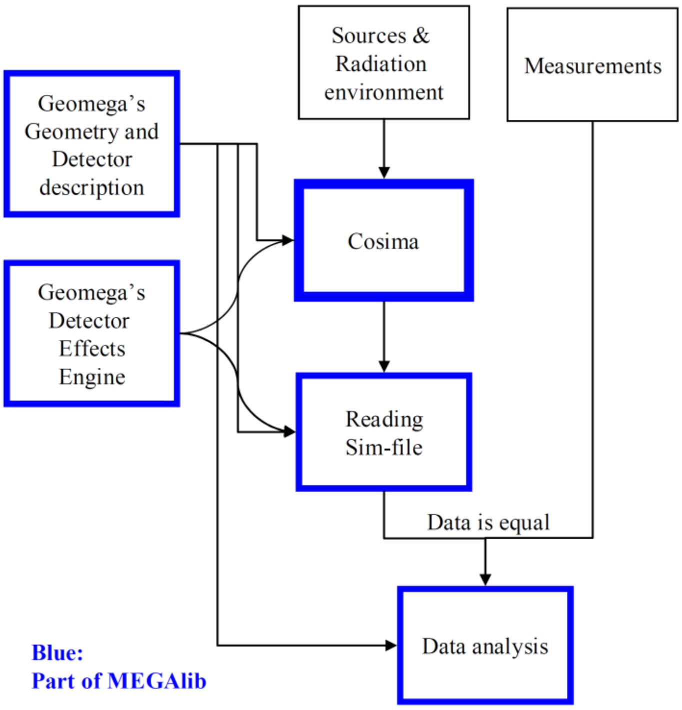

Figure 50: *An overview of the simulation and data analysis path within MEGAlib (Zoglauer et al. 2009).*

In Fig. 50 it is possible to see an overview of the simulation and data analysis path within MEGAlib. The first input to the simulator consists of the geometry description (volumes of certain shapes and materials at certain positions) together with the detector description (e.g. a pixel detector with certain energy resolution, etc.). The second input instead consists of the source description (e.g. some point sources and background distributions for astrophysics).

4.3.3 Revan (Real Event Analyzer)

Revan is able to reconstruct events in MEGAlib through the data provided by the detector characteristics and the energy and position informations of individual hits. The primary purpose of Revan is to establish the original interaction process (such as photo effects, Compton scattering, pair creation, radioactive decay etc.). But in particular Revan is specialized in Compton event reconstruction, and has a series of specific algorithms to determine the event type and Compton interaction sequence (classic and Bayesian algorithms). The process of reconstructing the events begins with the identification of the most simple structures like pair events and muons first, and continues with the search for the much more complex structures of Compton events in the remaining events. The reconstruction algorithm consists of four subsections:

1. clustering (blobbing adjacent hits into one larger hit)
2. tracking (finding showers, muons, pair events and Compton electron tracks)
3. Compton sequence reconstruction (identifying the sequence of Compton interactions)
4. decay detection (identifying events, which might originate from decays; e.g. special beta-decays)

4.3.4 Mimrec (MEGAlib image reconstruction)

Mimrec is the versatile, highly-optimized image reconstruction tool of MEGAlib. Mimrec uses list-mode-likelihood imaging methods such as the classic maximum-likelihood expectation maximization approach (Lange & Carson 1984). In this way it is able to performs list-mode-likelihood image deconvolution in spherical, Galactic, as well as Cartesian coordinates (2D, 3D) including different response calculation approaches (from quick and dirty to slow and sophisticated) which are mostly optimized for Compton image reconstruction. Mimrec also includes the analysis of energy spectra, ARM distributions, Compton and pair image reconstruction etc., and enables event selections on various parameters of Compton and pair events.

4.4 The selection of GRBs

From the Fermi GBM Burst Catalog[6] I have chosen the following parameters for each GRB:

- **Flnc_Band_Ampl**: The amplitude of a Band function fit to a single spectrum over the duration of the burst, in photon/cm^2/s/keV.
- **Flnc_Band_Epeak**: The peak energy of a Band function fit to a single spectrum over the duration of the burst, in keV.
- **Flnc_Band_Alpha**: The power law index, α, of a Band function fit to a single spectrum over the duration of the burst.
- **Flnc_Band_Beta**: The power law index, β, of a Band function fit to a single spectrum over the duration of the burst.
- **T90**: The duration, in seconds, during which 90% of the burst fluence was accumulated. The start of the T90 interval is defined by the time at which 5% of the total fluence has been detected, and the end of the T90 interval is defined by the time at which 95% of the fluence been detected. The fluence for the T90 calculation is measured between duration_energy_low and duration_energy_high.
- **Fluence**: The fluence (the energy flux integrated over the burst duration, 100% level) in the flu_low - flu_high energy band, nominally 10-1000 keV, in erg/cm^2.

---

[6] //heasarc.gsfc.nasa.gov/W3Browse/fermi/fermigbrst.html

- **Flnc_Band_Phtflux**: The average photon flux, between 10-1000 keV, in photon/cm^2/s, for a Band function law fit to a single spectrum over the duration of the burst.
- **Flnc_Band_Phtflnc**: The photon fluence, between 10-1000 keV, in photon/cm^2, for a Band function fit to a single spectrum over the duration of the burst.

I selected for the simulation with Cosima the GRBs mainly among those that have a greater Fluence (44 GRBs) but also some of those with a high Flnc_Band_Phtflux (5 GRBs). I also included GRB170817529 in my analysis for its great multi-messenger importance.

I am interested in calculating the flux between 100 and 10000 keV but the Fermi GBM Burst Catalog gives me only the value between 10 and 1000 keV for this reason I considered the difference between the base-10 logarithm of E_{max}=10000 keV and E_{min}=100 keV and I divided it into 50 steps

$$\frac{\log_{10} 10000 - \log_{10} 100}{50} = 0.04$$

in this way I get the multiplier, b= $10^{0,04}$ and starting from E_{min} = 100 keV, I have the following values of energy from $E_i = E_{i+1} \cdot b$.

Using the Band function, I calculated the flux for each P_i points, and with the formula

$$\frac{\log f(E_{i+1}) - \log f(E_i)}{\log E_{i+1} - \log E_i} = I_i$$

I obtain the spectral index of a power law that connects the points P_{i+1} and P_i with the energies E_{i+1} and E_i. At this point I calculate the integral of the power law in the interval i, i +1:

$$\frac{f(E_i)}{(I_i + 1) / E_i^{I_i}} \left(E_{i+1}^{I_i+1} - E_i^{I_i+1} \right)$$

and making the sum of all these contributions I get the INTEGRAL FLX between 100-10000 keV.

At this point, to calculate the flow between 100 and 10000 keV we just have to calculate:

$$\text{Flux } 90\% = 0{,}9 \cdot (\text{Flnc\_Band\_Phtflnc})/T_{90}$$

from which we get the:

$$\text{Scale Factor} = \text{Flux } 90\% / \text{Flnc\_Band\_Phtflux}$$

which allows me to calculate the:

$$\text{Flux} = \text{Scale Factor} \cdot \text{INTEGRAL FLX 100-10000 keV.}$$

In Table 9 we can see the list of GRBs selected as sources for the simulation, with their Band parameters, the flux between 100 and 10000 keV, and the total number of Compton events observed in the simulation. In red are highlighted the GRBs that I discarded from my analysis as they have a number of events less than 1600.

Source	T$_{90}$ (s)	α	β	E$_{peak}$(keV)	Flux (ph/cm^2/s)	Tot. Compton Evts
GRB081009140	41.345	- 1.582	- 4.701	29.294	0.502	6
GRB090618353	112.386	- 1.114	- 2.239	149.040	3.738	3171
GRB090820027	12.416	- 0.684	- 2.576	212.294	22.191	2012
GRB090902462	19.328	- 1.008	- 9.722	1055.44	22.604	2847
GRB090926181	13.760	- 0.848	- 2.378	333.817	19.541	1712
GRB100724029	114.690	- 0.833	- 1.965	358.182	3.793	2722
GRB100728095	165.378	- 0.510	- 2.542	253.910	1.379	1518
GRB100826957	84.993	- 0.811	- 1.918	263.254	3.979	2007
GRB100918863	88.834	- 0.777	- 3.312	503.275	2.924	1615
GRB101014175	449.415	- 1.121	- 2.056	201.803	0.644	2083
GRB101123952	103.938	- 0.895	- 2.106	484.601	2.020	1228
GRB110920546	160.771	- 0.536	- 3.133	247.750	1.804	2025
GRB120204054	49.089	- 1.178	- 2.756	166.935	2.960	1055
GRB120323507	0.384	- 0.998	- 2.046	71.057	37.840	76
GRB120624933	271.364	- 0.916	- 2.217	637.649	1.246	1866
GRB120707800	40.960	- 1.031	- 2.190	157.314	3.650	1034
GRB120711115	44.033	- 0.984	- 2.796	1317.518	7.595	1812
GRB120728434	100.481	- 1.170	- 2.922	88.104	1.665	1228
GRB130306991	120.578	- 1.000	- 3.138	349.431	2.310	1832
GRB130427324	138.242	- 1.018	- 2.829	824.987	16.705	14096
GRB130504978	73.217	- 1.164	- 2.116	538.631	3.055	1323
GRB130606497	52.225	- 1.115	- 2.073	432.374	7.005	2425
GRB130720582	199.172	-1.074	- 2.538	62.869	0.557	554
GRB130925173	215.555	- 0.111	- 2.006	23.163	0.584	258
GRB131014215	3.200	- 0.434	- 2.532	325.735	10.757	202
GRB131028076	17.152	- 0.751	- 3.268	898.667	15.305	1433
GRB131231198	31.232	- 1.218	- 2.304	178.085	7.592	1786
GRB140206275	146.690	- 1.402	- 2.040	475.834	1.395	1206
GRB140416060	31.744	- 1.166	- 2.479	96.931	3.316	721
GRB150118409	40.193	- 0.966	- 4.059	770.113	6.002	1430
GRB150330828	153.859	- 0.904	- 2.021	230.680	1.738	1723
GRB150627183	64.577	- 1.009	- 2.179	225.523	4.814	2082
GRB150819440	0.960	- 1.137	- 9.537	527.880	12.839	82
GRB151231443	71.425	- 0.910	- 2.519	196.538	2.207	1086
GRB160225720	70.144	- 0.800	- 2.171	81.257	0.148	59
GRB160509374	369.67	- 1.015	- 2.232	355.194	0.945	2137
GRB160625945	453.385	- 0.934	- 2.182	471.463	2.590	7512
GRB160720767	69.889	- 1.089	- 10.854	195.443	3.384	1836
GRB160821857	43.009	-1.055	- 2.305	940.628	21.351	5428
GRB161218356	25.857	- 0.479	- 2.933	209.674	6.292	1188
GRB170127067	0.128	- 0.243	- 3.901	830.000	85.525	63
GRB170214649	122.882	- 0.979	- 2.512	481.389	2.776	2049
GRB170409112	64.001	- 0.860	- 2.712	953.989	8.270	3116
GRB170808936	17.664	- 1.090	- 2.290	262.112	11.263	1234
GRB170817529	2.048	- 0.149	-8.941	214.703	0.127	0
GRB171010792	107.266	- 1.089	- 2.191	137.661	9.513	7502
GRB171227000	37.633	- 0.875	- 2.572	898.715	13.501	2887
GRB180113418	24.576	- 0.608	- 2.013	261.302	11.975	1772
GRB180201780	0.640	- 1.722	- 2.229	407.968	2.627	10
GRB180720598	48.897	- 1.171	- 2.490	636.040	10.556	3366

Table 9: *The list of GRBs selected as sources for the simulation, with their Band parameters, the flux between 100 and 10000 keV, and the total number of Compton events observed in the simulation.*

Among the discarded ones, we can see that all five SGRBs that I had chosen as sources for the simulation are present, including unfortunately also the GRB170817529. This implies as a consequence that our nano-satellite is not able to observe the SGRBs and therefore cannot contribute to multimessenger campaigns. Therefore the GRBs that I will use to calculate the energy resolution become 27.

4.5 The source file

The source file is a simple ASCII input file. In a typical source file there are five main sections: geometry, physics, output format, runs and sources. I prepared 27 source files (one for each GRBs). In my simulation the first input consists of the file containing the final updated version of the geometry (described in paragraph 2.2). In the physics section where there are the requested physics lists, I chose to include the low-energy Livermore EM-processes (includes Doppler-broadening). In the output format DiscretizeHits is turned on so that the energy deposits are centered in the individual voxels (volumetric picture element) of the detector (voxelization of the energy deposits). A run defines a file to which the data is stored, a stop criterion, a trigger criterion, and one or more sources. In the run section there are three possible keywords (Events, Triggers and Time) that define the stop criteria. I chose the T_{90} time as stop criterion, then I defined the source and type of particle (photons).

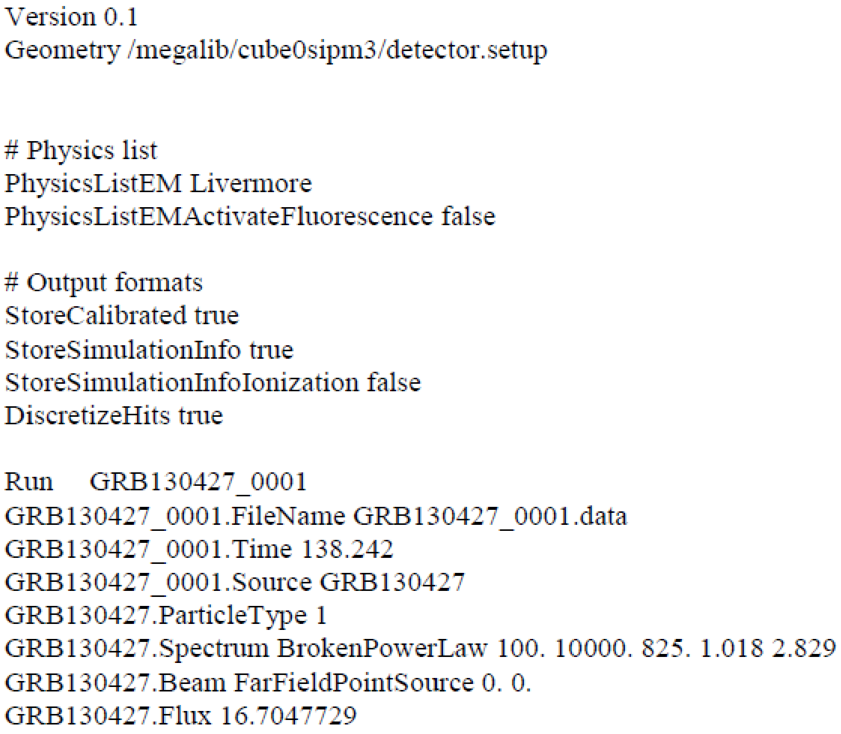

```
Version 0.1
Geometry /megalib/cube0sipm3/detector.setup


# Physics list
PhysicsListEM Livermore
PhysicsListEMActivateFluorescence false

# Output formats
StoreCalibrated true
StoreSimulationInfo true
StoreSimulationInfoIonization false
DiscretizeHits true

Run     GRB130427_0001
GRB130427_0001.FileName GRB130427_0001.data
GRB130427_0001.Time 138.242
GRB130427_0001.Source GRB130427
GRB130427.ParticleType 1
GRB130427.Spectrum BrokenPowerLaw 100. 10000. 825. 1.018 2.829
GRB130427.Beam FarFieldPointSource 0. 0.
GRB130427.Flux 16.7047729
```

Figure 51: *The source file used to simulate with cosima the observation of GRB130427324 with our nano-satellite.*

For the spectrum I chose the option BrokenPowerLaw (which requires the parameters: minimum energy in keV, maximum energy in keV, break energy in keV, photon index min, photon index max) while as beam categories I considered FarFieldPointSource. With the latter option the particles are emitted from the disk defined by the surrounding sphere defined in the geometry file with a direction of emission given by the angles Theta and Phi. For the flux between 100 and 10000 keV I included the value obtained from the calculation described in paragraph 4.4. In Figure 51 we can see one of the 50 source files prepared to simulate the observation of GRB130427324 with our nano-satellite.

4.6 The simulation results

In this section I present the results of the simulation. First of all I report the energy and angular resolution tables for all the 27 GRBs I have considered (Tables 10 to 25 for the energy resolution and Tables 26 to 39 for the angular resolution). It can be noticed immediately that the first bin is artificially high, in all the tables on energy resolution, because we have to understand how to clean up from the badly reconstructed events that affect a total less than 5%, but all end up on the first bin. Regarding GRB120624933 (see Table 23, 24 and 25) it can be noted that there are large discrepancies between true value and reconstructed around 500 keV, which from further analysis does not seem to be attributable to mistagged pair production. After the tables relating to the individual GRBs I report the total energy resolution (Table 40) which shows a trend in line with what is expected (see Fig. 54) at least away from the threshold, but there is an anomalous trend around 200 keV that we wanted to investigate.

GRB150627183			
N. Total Events 2082			
Energy (keV)	Events	<E> (keV)	FWHM (%)
E<133	413	105.7	24.75
133<E<175	417	154.0	11.87
175<E<225	411	199.7	9.41
225<E<320	412	265.1	9.81
320<E	429	493.0	10.27

GRB100826957			
N. Total Events 2007			
Energy (keV)	Events	<E> (keV)	FWHM (%)
E<141	404	108.2	79.20
141<E<191	403	166.2	10.88
191<E<256	408	220.0	9.58
256<E<390	403	312.0	13.26
390<E	389	570.9	17.22

Table 10: *Energy resolution for 2 GRB.*

GRB101014175			
N. Total Events 2083			
Energy (keV)	Events	<E> (keV)	FWHM (%)
E<129	409	98.66	12.89
129<E<165	411	147.3	15.39
165<E<208	406	185.2	9.82
208<E<305	414	249.1	9.61
305<E	443	478.4	9.35

GRB090820027			
N. Total Events 2012			
Energy (keV)	Events	<E> (keV)	FWHM (%)
E<130	397	103.1	54.36
130<E<165	402	147.1	11.58
165<E<207	400	185.9	12.54
207<E<275	409	236.4	7.21
275<E	404	420.6	9.99

Table 11: *Energy resolution for 2 GRB.*

GRB170214649			
N. Total Events 2049			
Energy (keV)	Events	<E> (keV)	FWHM (%)
E<143	407	107.7	46.57
143<E<194	408	166.7	14.74
194<E<263	410	227.1	38.88
263<E<415	409	325.9	5.30
415<E	415	593.1	8.66

GRB110920546			
N. Total Events 2025			
Energy (keV)	Events	<E> (keV)	FWHM (%)
E<133	399	106.0	18.33
133<E<173	401	153.5	14.88
173<E<215	403	193.9	9.67
215<E<272	406	240.3	9,02
272<E	416	383.0	5.23

Table 12: *Energy resolution for 2 GRB.*

For this purpose we have collected the GRBs forming 3 groups of 9 selected based on the value of the alpha and beta parameters, peak energy, their flux, the number of events and their T_{90}.

The data for the 3 groups are shown in Tables 41 to 46 for energy resolution and 48 to 53 for angular resolution. Also in all the graphs in Figures 73 to 78 there is a minimum around 200 keV. This behavior is due to an edge effect as we are close to the threshold.

GRB160509374			
N. Total Events 2137			
Energy (keV)	Events	<E> (keV)	FWHM (%)
E<138	419	101.9	59.69
138<E<185	420	160.5	9.56
185<E<253	421	215.2	27.04
253<E<367	423	300.7	7.02
367<E	454	536.5	16.71

GRB130306991			
N. Total Events 1832			
Energy (keV)	Events	<E> (keV)	FWHM (%)
E<138	370	107.8	20.88
138<E<176	365	157.5	14.45
176<E<225	364	200.0	26.87
225<E<307	365	263.8	10.33
307<E	368	433.3	12.97

Table 13: *Energy resolution for 2 GRB.*

GRB150330828			
N. Total Events 1723			
Energy (keV)	Events	<E> (keV)	FWHM (%)
E<135	346	104.0	47.89
135<E<176	346	155.2	8.60
176<E<234	348	203.4	16.73
234<E<345	348	281.9	22.37
345<E	335	531	11.14

GRB160625945			
N. Total Events 7512			
Energy (keV)	Events	<E> (keV)	FWHM (%)
E<142	1496	105.2	38.69
142<E<196	1510	168.0	16.37
196<E<269	1503	230.5	17.41
269<E<424	1502	333.9	5.11
424<E	1501	601.0	8.56

Table 14: *Energy resolution for 2 GRB.*

We then shown the ARM of some selected GRBs taking as a sample the number of events (Fig. from 79 to 84). After that we split the total angular resolution for all 27 GRBs into intervals depending on the energy (see Fig. from 85 to 89). It can be seen that in the two graphs with higher energy intervals a second component appears (Fig 88 and 89) this is due to a high energy leak through the calorimeter.

The results of the total ARM divided in the various energy intervals are summarized in Table 49 and in the graph in the Figure 90.

GRB131231198			
N. Total Events 1786			
Energy (keV)	Events	<E> (keV)	FWHM (%)
E<124	356	91.72	56.07
124<E<154	360	139.6	9.73
154<E<196	360	173.7	13.11
196<E<263	365	224.6	8.92
263<E	345	411.7	8.73

GRB171010792			
N. Total Events 7502			
Energy (keV)	Events	<E> (keV)	FWHM (%)
E<123	1513	95.22	27.40
123<E<151	1489	136.6	14.47
151<E<191	1518	170.0	13.96
191<E<270	1506	224.3	13.69
270<E	1476	430.0	16.16

Table 15: *Energy resolution for 2 GRB.*

GRB160720767			
N. Total Events 1836			
Energy (keV)	Events	<E> (keV)	FWHM (%)
E<119	357	96.42	15.86
119<E<140	357	129.3	13.93
140<E<161	357	150.5	10.57
161<E<186	367	173.1	8.06
186<E	398	208.5	8.27

GRB120711115			
N. Total Events 1812			
Energy (keV)	Events	<E> (keV)	FWHM (%)
E<161	361	122.0	13.44
161<E<237	364	196.1	27.02
237<E<351	360	283.6	21.16
351<E<699	359	483.3	13.24
699<E	368	824.8	6.68

Table 16: *Energy resolution for 2 GRB.*

If we are interested only in the value of the ARM we can make a cut at high energy based on the SequenceLength (number of hits in the Compton sequence) by setting SequenceLength = 2.

GRB090926181			
N. Total Events 1712			
Energy (keV)	Events	<E> (keV)	FWHM (%)
E<141	343	109.0	13.60
141<E<186	341	161.9	11.31
186<E<245	342	213.5	9.22
245<E<340	342	287.9	7.67
340<E	344	501.2	8.81

GRB180113418			
N. Total Events 1772			
Energy (keV)	Events	<E> (keV)	FWHM (%)
E<148	353	111.0	47.80
148<E<198	353	172.7	9.72
198<E<258	355	226.7	36.90
258<E<378	354	304.4	11.96
378<E	357	563.5	14.03

Table 17: *Energy resolution for 2 GRB.*

GRB100724029			
N. Total Events 2722			
Energy (keV)	Events	<E> (keV)	FWHM (%)
141>E	544	106.4	84.60
141<E<191	549	165.6	11.04
191<E<267	545	225.7	8.89
267<E<416	543	329.3	5.05
416<E	541	612.6	5.84

GRB100918863			
N. Total Events 1615			
Energy (keV)	Events	<E> (keV)	FWHM (%)
E<145	322	111.5	13.28
145<E<194	324	169.5	13.75
194<E<269	325	230.8	10.00
269<E<370	322	315.7	7.73
370<E	322	534.1	14.25

Table 18: *Energy resolution for 2 GRB.*

GRB090902462			
N. Total Events 2847			
Energy (keV)	Events	<E> (keV)	FWHM (%)
E<140	565	106.1	15.53
140<E<191	568	163.6	12.29
191<E<265	567	225.8	9.55
265<E<429	566	332.6	5.85
429<E	581	640.1	4.97

GRB170409112			
N. Total Events 3116			
Energy (keV)	Events	<E> (keV)	FWHM (%)
E<150	624	110.6	24.52
150<E<221	622	184.1	10.09
221<E<321	621	265.9	9.92
321<E<599	620	435.4	15.22
599<E	629	774.8	2.78

Table 19: *Energy resolution for 2 GRB.*

GRB090618353			
N. Total Events 3171			
Energy (keV)	Events	<E> (keV)	FWHM (%)
E<123	639	97.69	36.14
123<E<150	629	135.8	10.77
150<E<188	628	167.3	11.46
188<E<261	633	218.5	11.71
261<E	642	412.2	4.69

GRB171227000			
N. Total Events 2887			
Energy (keV)	Events	<E> (keV)	FWHM (%)
E<152	577	109.4	78.19
152<E<215	580	181.0	13.10
215<E<311	582	257.5	13.43
311<E<560	576	415.5	7.32
560<E	572	752.8	8.09

Table 20: *Energy resolution for 2 GRB.*

GRB180720598			
N. Total Events 3366			
Energy (keV)	Events	<E> (keV)	FWHM (%)
E<137	675	102.8	22.25
137<E<184	675	160.8	11.11
184<E<257	678	216.6	11.25
257<E<415	673	319.9	25.36
415<E	665	612.4	11.13

GRB160821857			
N. Total Events 5428			
Energy (keV)	Events	<E> (keV)	FWHM (%)
E<140	1073	106.2	44.10
140<E<198	1090	167.9	7.57
198<E<289	1084	238.0	16.44
289<E<541	1085	385.5	12.69
541<E	1096	725.9	8.07

Table 21: *Energy resolution for 2 GRB.*

GRB130427324			
N. Total Events 14096			
Energy (keV)	Events	<E> (keV)	FWHM (%)
E<134	2377	100.0	35.26
134<E<177	2359	154.7	9.60
177<E<234	2339	203.2	11.08
234<E<323	2356	272.7	17.14
323<E<536	2342	412.1	14.91
536<E	2332	725.0	10.74

GRB130606497			
N. Total Events 2425			
Energy (keV)	Events	<E> (keV)	FWHM (%)
E<132	401	94.98	66.57
132<E<168	406	149.5	14.49
168<E<217	404	190.9	13.59
217<E<286	407	248.2	8.05
286<E<435	404	342.6	6.15
435<E	403	619.1	14.06

Table 22: *Energy resolution for 2 GRB.*

GRB120624933			
N. Total Events 1866			
Energy (keV)	Events	<E> (keV)	FWHM (%)
138>E	311	100.5	56.08
138<E<184	314	160.2	13.30
184<E<245	311	213.6	20.79
245<E<350	306	290.2	20.89
350<E<635	312	460,6	38.33
635<E	312	788.5	6.35

Table 23: *Energy resolution for GRB120624933.*

GRB120624933			
N. Total Events 1866			
Energy (keV)	Events	<E> (keV)	FWHM (%)
128>E	232	89.41	63.03
128<E<160	232	143.8	20.70
160<E<197	235	176.9	11.52
197<E<244	230	220.1	20.61
244<E<312	231	274.7	22.03
312<E<448	234	370.7	13.28
448<E<760	235	576.9	30.43
760<E	237	884.1	8.75

GRB120624933			
N. Total Events 1866			
Energy (keV)	Events	<E> (keV)	FWHM (%)
148>E	378	108.0	52.84
148<E<207	373	175.1	13.95
207<E<297	373	248.4	18.12
297<E<540	370	396.1	44.41
540<E	372	731.5	8.76

Table 24: *Energy resolution with different energy intervals for GRB120624933.*

GRB120624933			
N. Total Events 1866			
Energy (keV)	Events	<E> (keV)	FWHM (%)
160>E	464	116.6	49.21
160<E<244	465	198.3	22.76
244<E<450	468	323.8	18.69
450<E	469	656.2	27.00

Table 25 *Energy resolution with four energy intervals for GRB120624933.*

GRB150627183			
N. Total Events 2082			
Tot. ARM 22.01 FWHM (°)			
Energy (keV)	Events	<E> (keV)	FWHM (°)
E<133	413	105.7	46.61
133<E<175	417	154.0	29.54
175<E<225	411	199.7	18.43
225<E<320	412	265.1	16.13
320<E	429	493.0	11.38

GRB100826957			
N. Total Events 2007			
Tot. ARM 15.24 FWHM (°)			
Energy (keV)	Events	<E> (keV)	FWHM (°)
E<141	404	108.2	40.04
141<E<191	403	166.2	18.21
191<E<256	408	220.0	17.41
256<E<390	403	312.0	19.83
390<E	389	570.9	6.62

Table 26: *Angular resolution for 2 GRB.*

GRB101014175			
N. Total Events 2083			
Tot. ARM 19.64 FWHM (º)			
Energy (keV)	Events	<E> (keV)	FWHM (º)
E<129	409	98.66	35.08
129<E<165	411	147.3	30.73
165<E<208	406	185.2	14.88
208<E<305	414	249.1	11.03
305<E	443	478.4	10.68

GRB090820027			
N. Total Events 2012			
Tot. ARM 18.13 FWHM (º)			
Energy (keV)	Events	<E> (keV)	FWHM (º)
E<130	397	103.1	50.50
130<E<165	402	147.1	40.03
165<E<207	400	185.9	19.29
207<E<275	409	236.4	14.98
275<E	404	420.6	9.06

Table 27: *Angular resolution for 2 GRB.*

GRB170214649			
N. Total Events 2049			
Tot. ARM 17.24 FWHM (º)			
Energy (keV)	Events	<E> (keV)	FWHM (º)
E<143	407	107.7	31.92
143<E<194	408	166.7	26.88
194<E<263	410	227.1	10.39
263<E<415	409	325.9	10.88
415<E	415	593.1	16.32

GRB110920546			
N. Total Events 2025			
Tot. ARM 17.29 FWHM (º)			
Energy (keV)	Events	<E> (keV)	FWHM (º)
E<133	399	106.0	35.72
133<E<173	401	153.5	33.77
173<E<215	403	193.9	20.41
215<E<272	406	240.3	17.25
272<E	416	383.0	8.82

Table 28: *Angular resolution for 2 GRB.*

GRB160509374			
N. Total Events 2137			
Tot. ARM 15.20 FWHM (°)			
Energy (keV)	Events	<E> (keV)	FWHM (°)
E<138	419	101.9	41.35
138<E<185	420	160.5	18.00
185<E<253	421	215.2	17.46
253<E<367	423	300.7	11.40
367<E	454	536.5	14.85

GRB130306991			
N. Total Events 1832			
Tot. ARM 18.35 FWHM (°)			
Energy (keV)	Events	<E> (keV)	FWHM (°)
E<138	370	107.8	29.60
138<E<176	365	157.5	33.46
176<E<225	364	200.0	19.61
225<E<307	365	263.8	16.42
307<E	368	433.3	10.91

Table 29: *Angular resolution for 2 GRB.*

GRB150330828			
N. Total Events 1723			
Tot. ARM 23.09 FWHM (°)			
Energy (keV)	Events	<E> (keV)	FWHM (°)
E<135	346	104.0	43.06
135<E<176	346	155.2	23.74
176<E<234	348	203.4	18.00
234<E<345	348	281.9	17.60
345<E	335	531	17.72

GRB160625945			
N. Total Events 7512			
Tot. ARM 20.15 FWHM (°)			
Energy (keV)	Events	<E> (keV)	FWHM (°)
E<142	1496	105.2	40.29
142<E<196	1510	168.0	22.55
196<E<269	1503	230.5	17.51
269<E<424	1502	333.9	12.47
424<E	1501	601.0	10.09

Table 30: *Angular resolution for 2 GRB.*

GRB131231198			
N. Total Events 1786			
Tot. ARM 23.68 FWHM (°)			
Energy (keV)	Events	<E> (keV)	FWHM (°)
E<124	356	91.72	39.68
124<E<154	360	139.6	30.36
154<E<196	360	173.7	26.40
196<E<263	365	224.6	18.65
263<E	345	411.7	14.14

GRB171010792			
N. Total Events 7502			
Tot. ARM 19.14 FWHM (°)			
Energy (keV)	Events	<E> (keV)	FWHM (°)
E<123	1513	95.22	38.28
123<E<151	1489	136.6	29.62
151<E<191	1518	170.0	23.74
191<E<270	1506	224.3	20.34
270<E	1476	430.0	13.65

Table 31: *Angular resolution for 2 GRB.*

GRB160720767			
N. Total Events 1836			
Tot. ARM 22.50 FWHM (°)			
Energy (keV)	Events	<E> (keV)	FWHM (°)
E<119	357	96.42	41.95
119<E<140	357	129.3	33.05
140<E<161	357	150.5	30.83
161<E<186	367	173.1	22.08
186<E	398	208.5	17.25

GRB120711115			
N. Total Events 1812			
Tot. ARM 16.24 FWHM (°)			
Energy (keV)	Events	<E> (keV)	FWHM (°)
E<161	361	122.0	38.15
161<E<237	364	196.1	22.52
237<E<351	360	283.6	12.63
351<E<699	359	483.3	12.16
699<E	368	824.8	11.35

Table 32: *Angular resolution for 2 GRB.*

GRB090926181			
N. Total Events 1712			
Tot. ARM 22.5 FWHM (º)			
Energy (keV)	Events	<E> (keV)	FWHM (º)
E<141	343	109.0	29.58
141<E<186	341	161.9	29.95
186<E<245	342	213.5	17.60
245<E<340	342	287.9	12.67
340<E	344	501.2	15.50

GRB180113418			
N. Total Events 1772			
Tot. ARM 18.49 FWHM (º)			
Energy (keV)	Events	<E> (keV)	FWHM (º)
E<148	353	111.0	39.87
148<E<198	353	172.7	19.51
198<E<258	355	226.7	11.40
258<E<378	354	304.4	10.64
378<E	357	563.5	7.61

Table 33: *Angular resolution for 2 GRB.*

GRB100724029			
N. Total Events 2722			
Tot. ARM 14.84 FWHM (º)			
Energy (keV)	Events	<E> (keV)	FWHM (º)
141>E	544	106.4	25.95
141<E<191	549	165.6	29.07
191<E<267	545	225.7	14.86
267<E<416	543	329.3	12.34
416<E	541	612.6	11.67

GRB100918863			
N. Total Events 1615			
Tot. ARM 15.00 FWHM (º)			
Energy (keV)	Events	<E> (keV)	FWHM (º)
E<145	322	111.5	31.81
145<E<194	324	169.5	29.74
194<E<269	325	230.8	23.75
269<E<370	322	315.7	15.81
370<E	322	534.1	8.21

Table 34: *Angular resolution for 2 GRB.*

GRB090902462			
N. Total Events 2847			
Tot. ARM 15.04 FWHM (°)			
Energy (keV)	Events	<E> (keV)	FWHM (°)
E<140	565	106.1	41.69
140<E<191	568	163.6	21.50
191<E<265	567	225.8	18.94
265<E<429	566	332.6	12.61
429<E	581	640.1	8.71

GRB170409112			
N. Total Events 3116			
Tot. ARM 18.12 FWHM (°)			
Energy (keV)	Events	<E> (keV)	FWHM (°)
E<150	624	110.6	31.92
150<E<221	622	184.1	16.02
221<E<321	621	265.9	14.60
321<E<599	620	435.4	9.19
599<E	629	774.8	10.36

Table 35: *Angular resolution for 2 GRB.*

GRB090618353			
N. Total Events 3171			
Tot. ARM 21.12 FWHM (°)			
Energy (keV)	Events	<E> (keV)	FWHM (°)
E<123	639	97.69	31.25
123<E<150	629	135.8	26.97
150<E<188	628	167.3	23.16
188<E<261	633	218.5	21.13
261<E	642	412.2	11.22

GRB171227000			
N. Total Events 2887			
Tot. ARM 14.83 FWHM (°)			
Energy (keV)	Events	<E> (keV)	FWHM (°)
E<152	577	109.4	37.77
152<E<215	580	181.0	15.13
215<E<311	582	257.5	13.45
311<E<560	576	415.5	7.99
560<E	572	752.8	11.99

Table 36: *Angular resolution for 2 GRB.*

GRB180720598			
N. Total Events 3366			
Tot. ARM 22.55 FWHM (°)			
Energy (keV)	Events	<E> (keV)	FWHM (°)
E<137	675	102.8	41.69
137<E<184	675	160.8	20.34
184<E<257	678	216.6	19.29
257<E<415	673	319.9	14.81
415<E	665	612.4	7.91

GRB160821857			
N. Total Events 5428			
Tot. ARM 15.62 FWHM (°)			
Energy (keV)	Events	<E> (keV)	FWHM (°)
E<140	1073	106.2	39.79
140<E<198	1090	167.9	22.09
198<E<289	1084	238.0	16.91
289<E<541	1085	385.5	13.45
541<E	1096	725.9	10.54

Table 37: *Angular resolution for 2 GRB.*

GRB130427324			
N. Total Events 14096			
Tot. ARM 15.62 FWHM (°)			
Energy (keV)	Events	<E> (keV)	FWHM (°)
E<134	2377	100.0	44.58
134<E<177	2359	154.7	30.72
177<E<234	2339	203.2	22.10
234<E<323	2356	272.7	16.87
323<E<536	2342	412.1	13.06
536<E	2332	725.0	15.03

GRB130606497			
N. Total Events 2425			
Tot. ARM 15.40 FWHM (°)			
Energy (keV)	Events	<E> (keV)	FWHM (°)
E<132	401	94.98	35.11
132<E<168	406	149.5	26.40
168<E<217	404	190.9	20.80
217<E<286	407	248.2	16.00
286<E<435	404	342.6	10.04
435<E	403	619.1	8.36

Table 38: *Angular resolution for 2 GRB.*

<table>
<tr><th colspan="4">GRB120624933</th></tr>
<tr><td colspan="4">N. Total Events 1866</td></tr>
<tr><td colspan="4">Tot. ARM 18.07 FWHM (º)</td></tr>
<tr><td>Energy (keV)</td><td>Events</td><td><E> (keV)</td><td>FWHM (º)</td></tr>
<tr><td>138>E</td><td>311</td><td>100.5</td><td>25.46</td></tr>
<tr><td>138<E<184</td><td>314</td><td>160.2</td><td>24.18</td></tr>
<tr><td>184<E<245</td><td>311</td><td>213.6</td><td>17.44</td></tr>
<tr><td>245<E<350</td><td>306</td><td>290.2</td><td>9.07</td></tr>
<tr><td>350<E<635</td><td>312</td><td>460,6</td><td>17.29</td></tr>
<tr><td>635<E</td><td>312</td><td>788.5</td><td>14.62</td></tr>
</table>

Table 39: *Angular resolution for GRB120624933.*

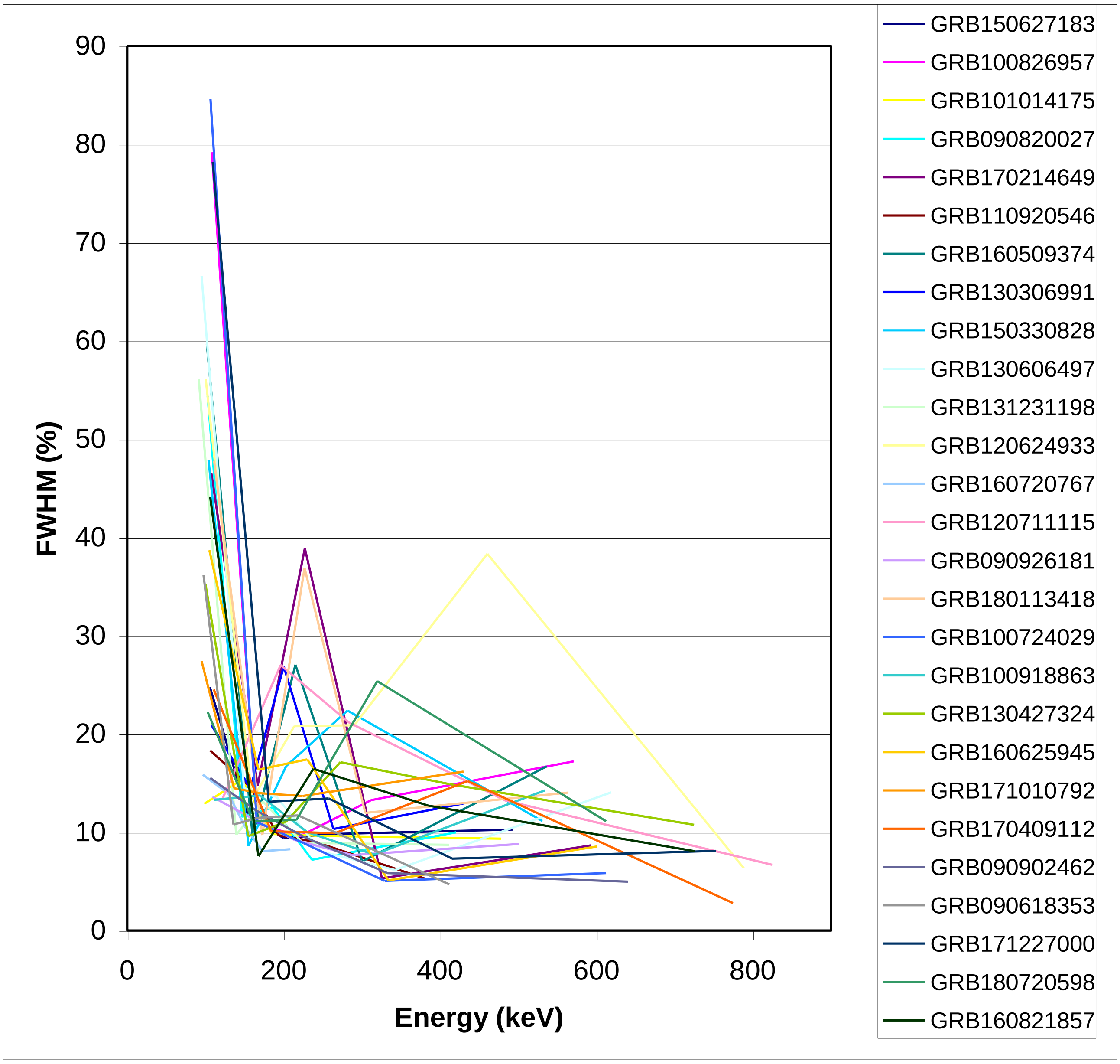

Figure 52:*Energy resulution plot for 27 GRB.*

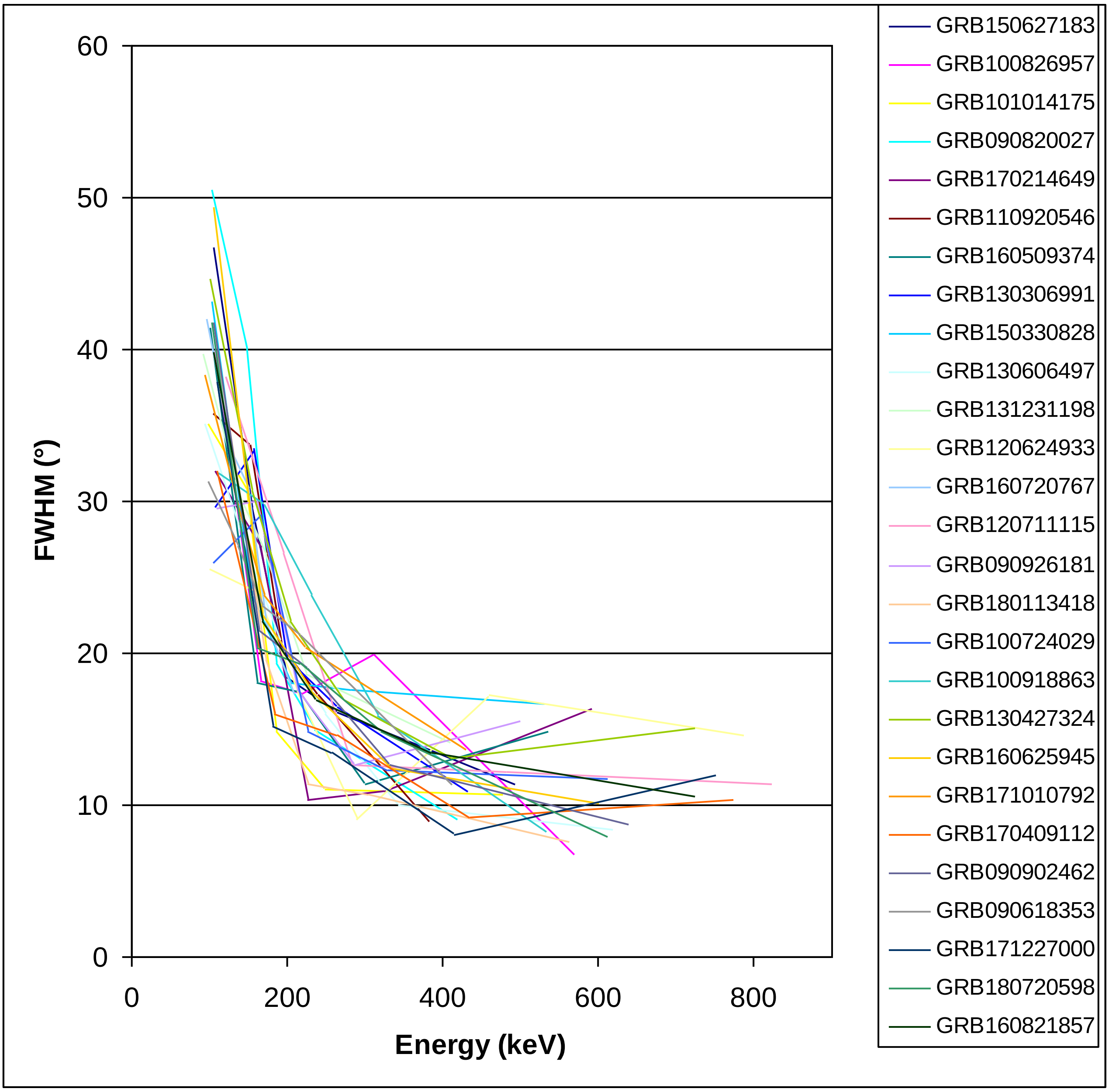

Figure 53*: Angular resulution plot for 27 GRB.*

<table>
<tr><th colspan="4">All GRB</th></tr>
<tr><td colspan="4">N. Total Events 85421</td></tr>
<tr><td>Energy (keV)</td><td>Events</td><td><E></td><td>FWHM (keV)</td></tr>
<tr><td>158>E</td><td>25913</td><td>128.0</td><td>18.40</td></tr>
<tr><td>158<E<251</td><td>26316</td><td>199.2</td><td>30.15</td></tr>
<tr><td>251<E<398</td><td>16538</td><td>310.1</td><td>26.76</td></tr>
<tr><td>398<E<631</td><td>8120</td><td>493.2</td><td>19.87</td></tr>
<tr><td>631<E</td><td>8534</td><td>1328</td><td>7.00</td></tr>
</table>

Table 40: *Total energy resolution.*

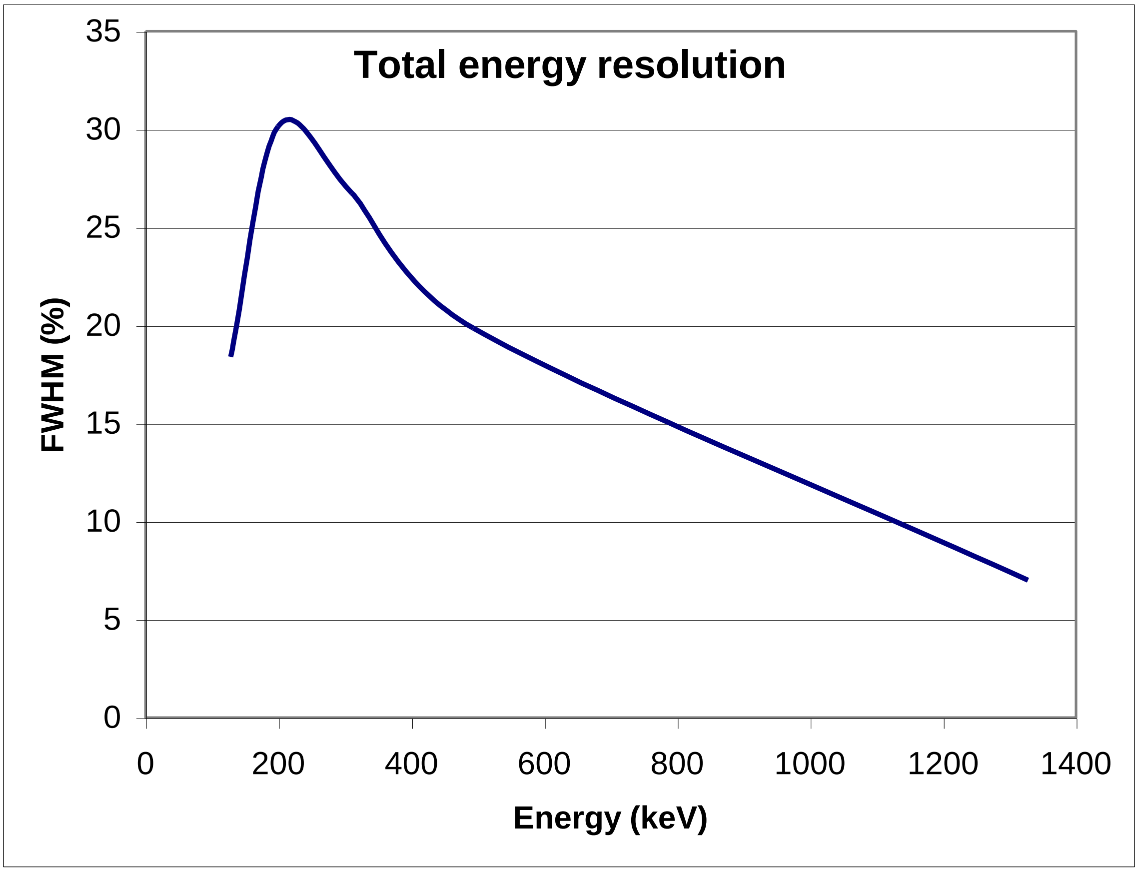

Figure 54: *Total Energy Resolution for27 GRBs.*

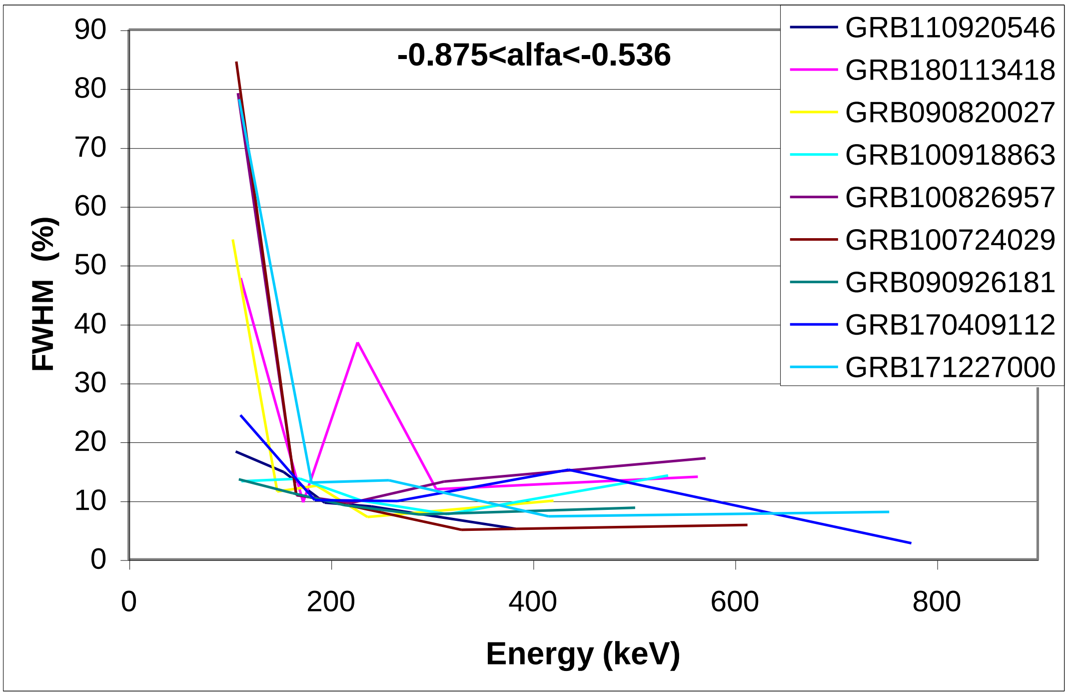

Figure 55: *Energy resolution for nine GRB with alfa between –0.875 and –0.536.*

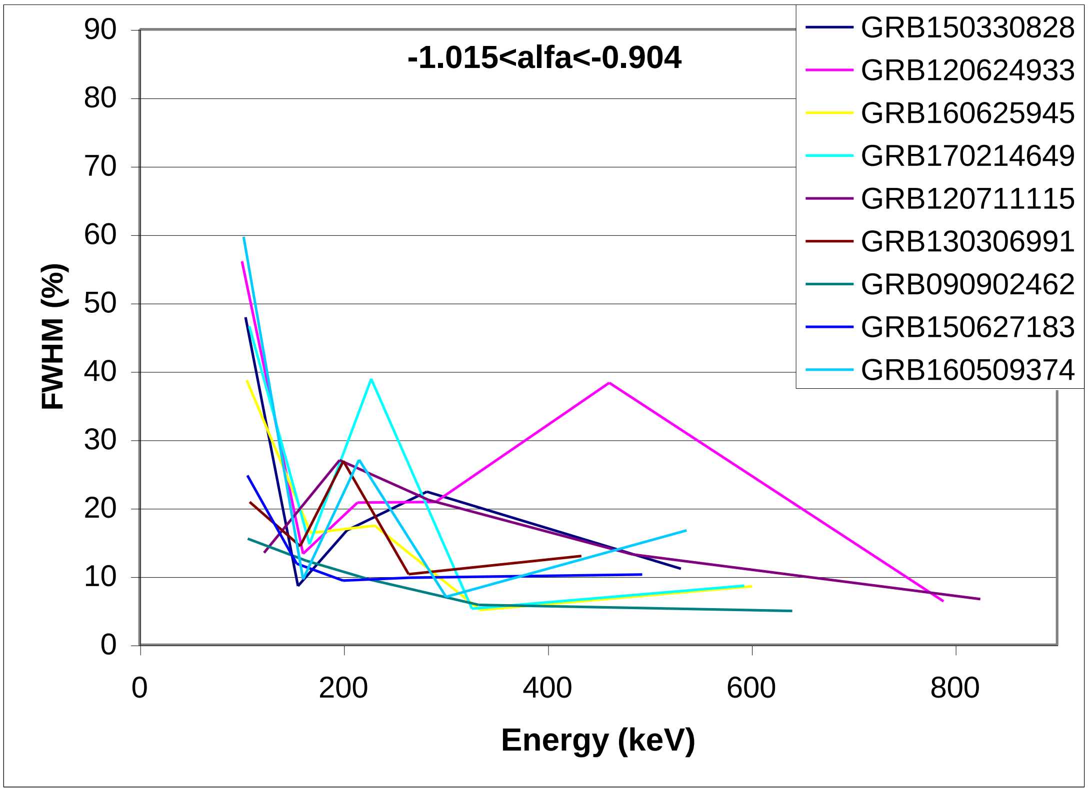

Figure 56: *Energy resolution for nine GRB with alfa between –1.015 and –0.904.*

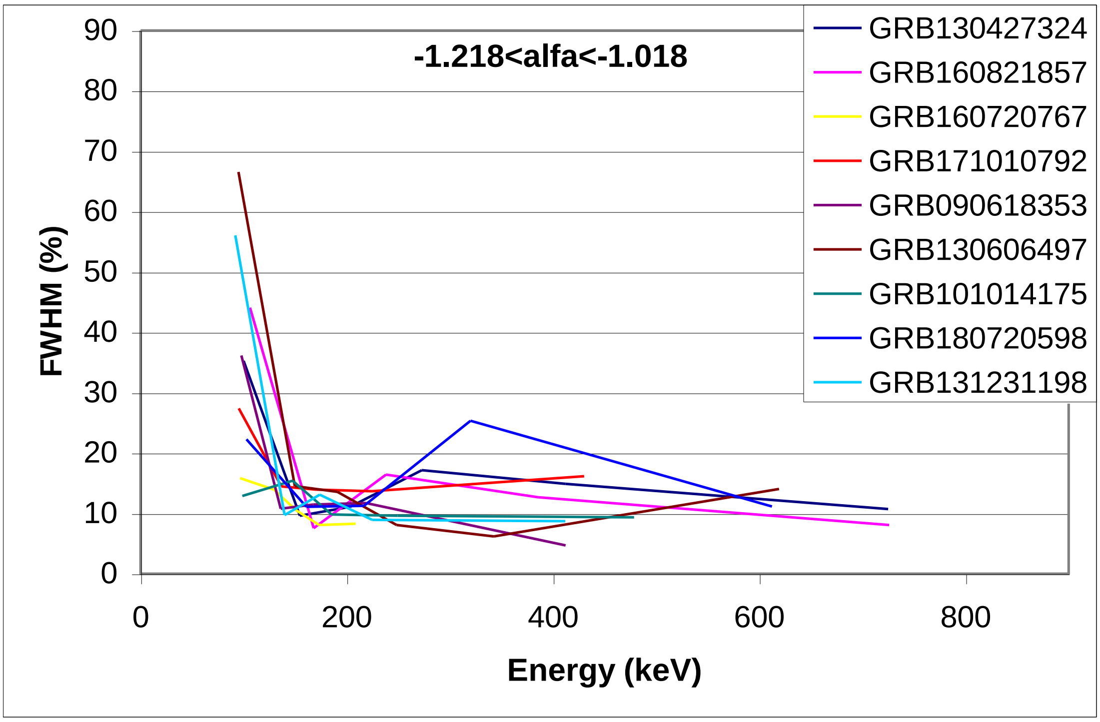

Figure 57: *Energy resolution for nine GRB with alfa between –1.218 and –1.018.*

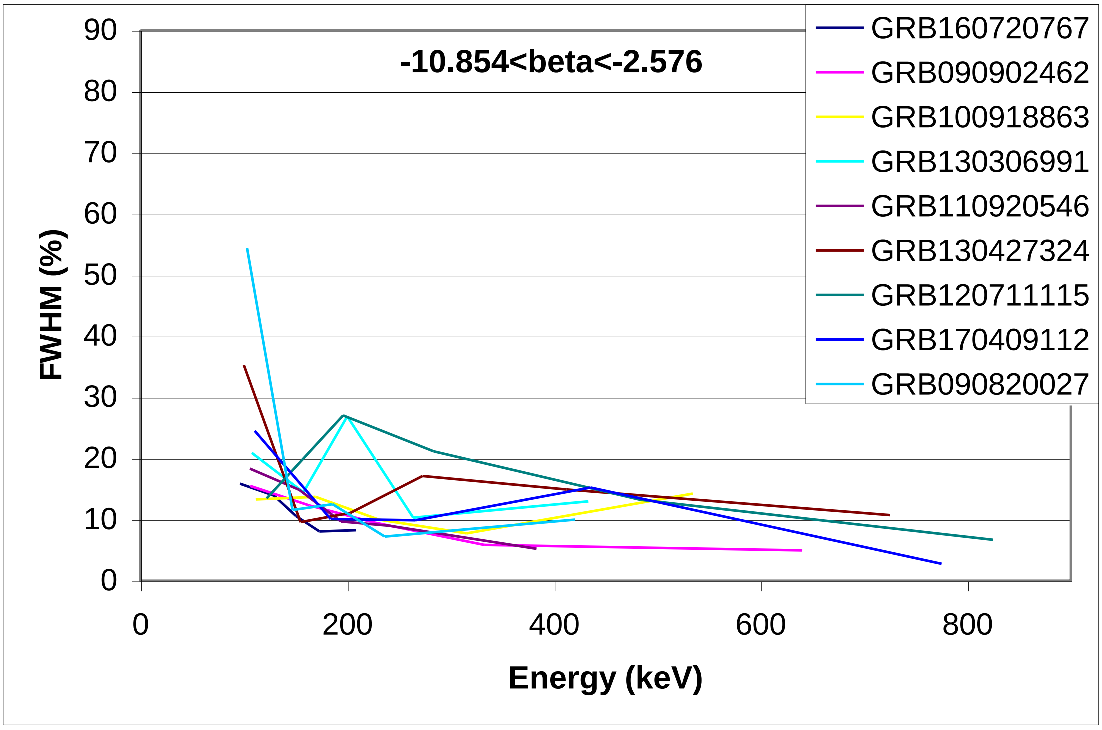

Figure 58: *Energy resolution for nine GRB with beta between –10.854 and –2.576.*

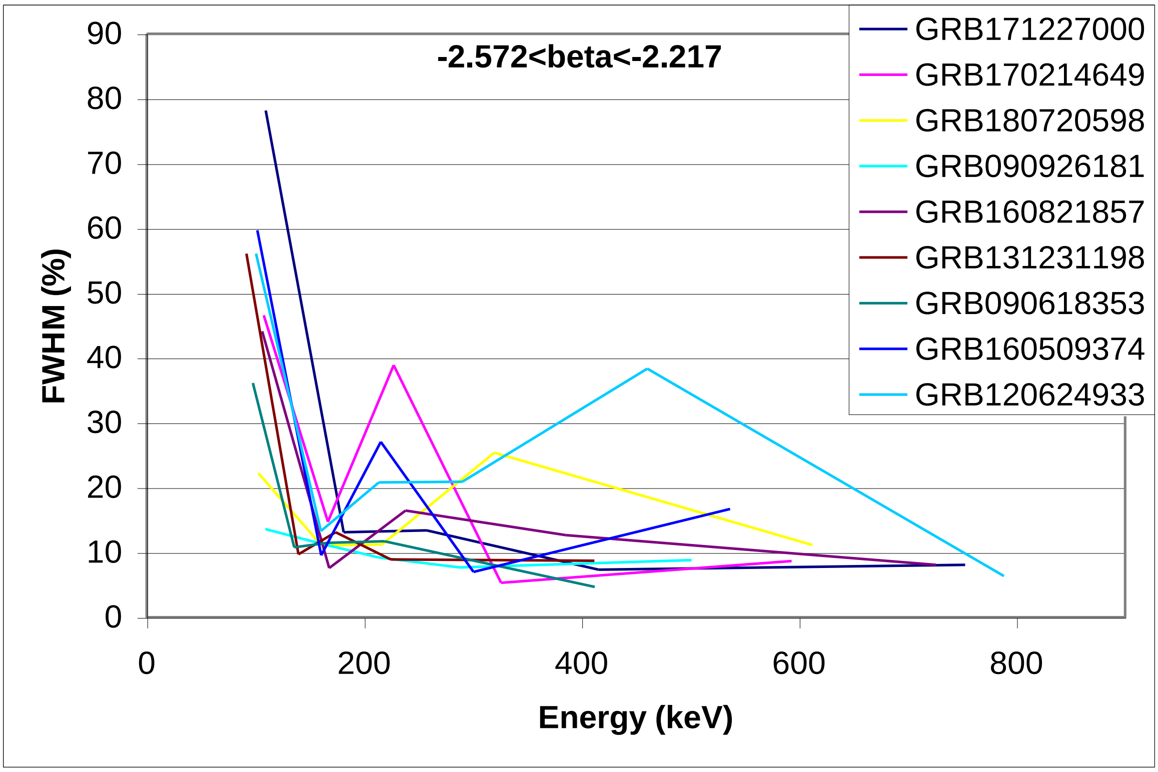

Figure 59: *Energy resolution for nine GRB with beta between –2.572 and –2.217.*

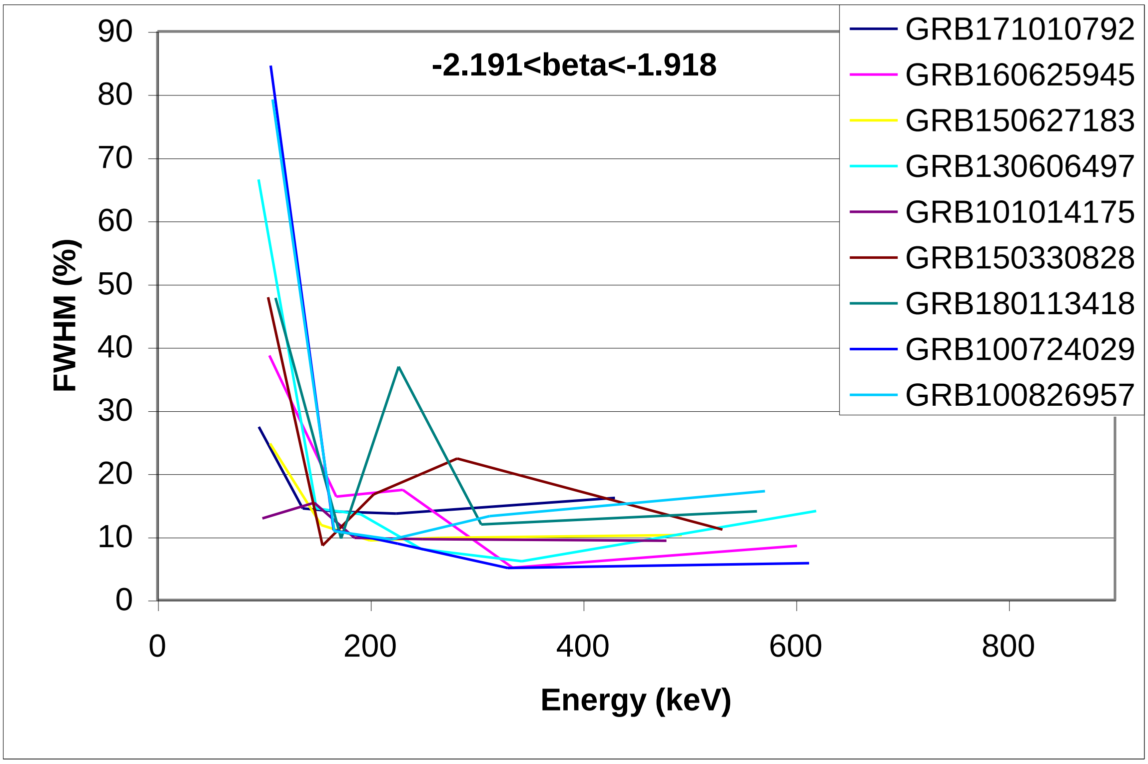

Figure 60: *Energy resolution for nine GRB with beta between –2.191 and –1.918.*

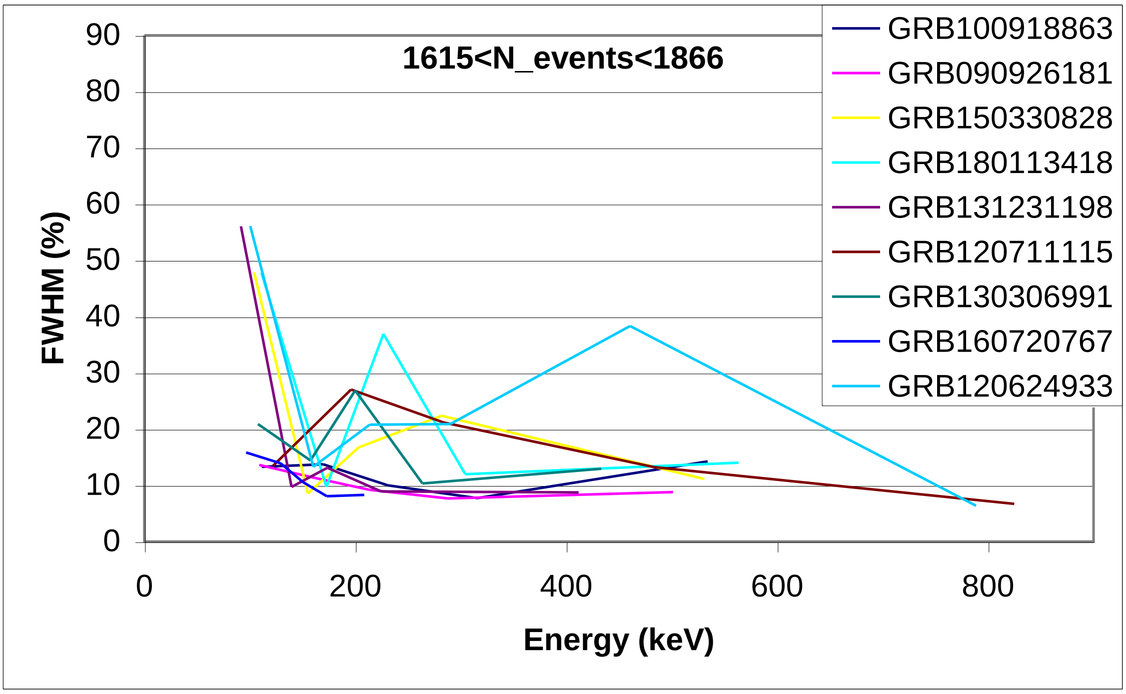

Figure 61: *Energy resolution for nine GRB with a number of events between 1615 and 1866.*

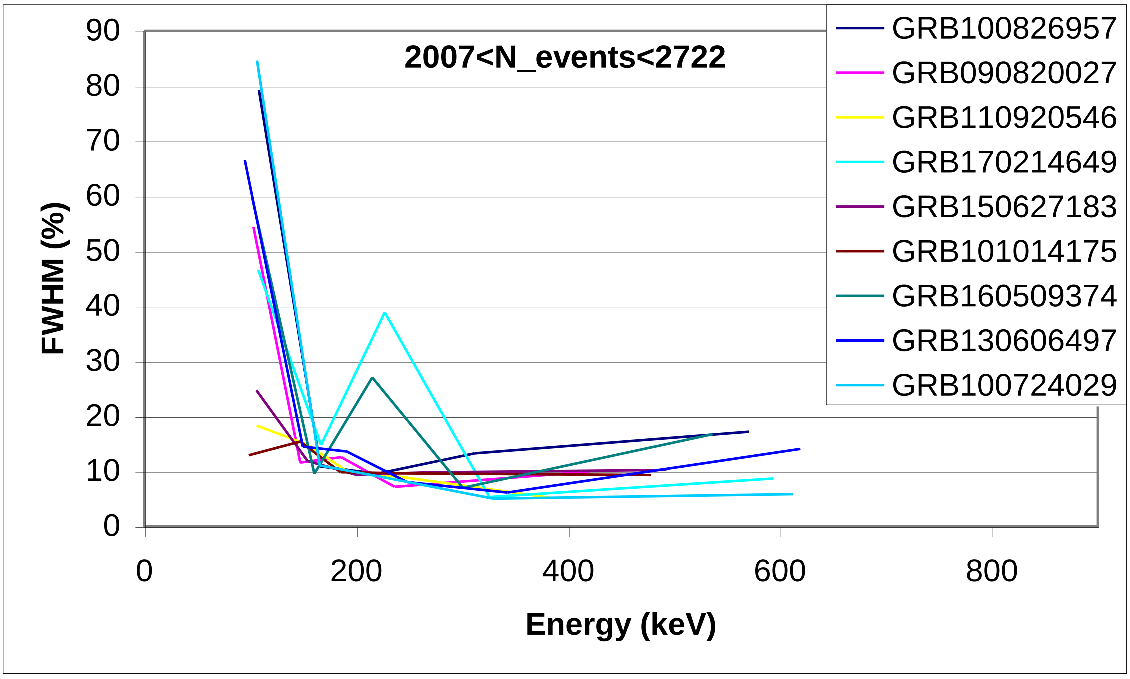

Figure 62: *Energy resolution for nine GRB with a number of events between 2007 and 2722.*

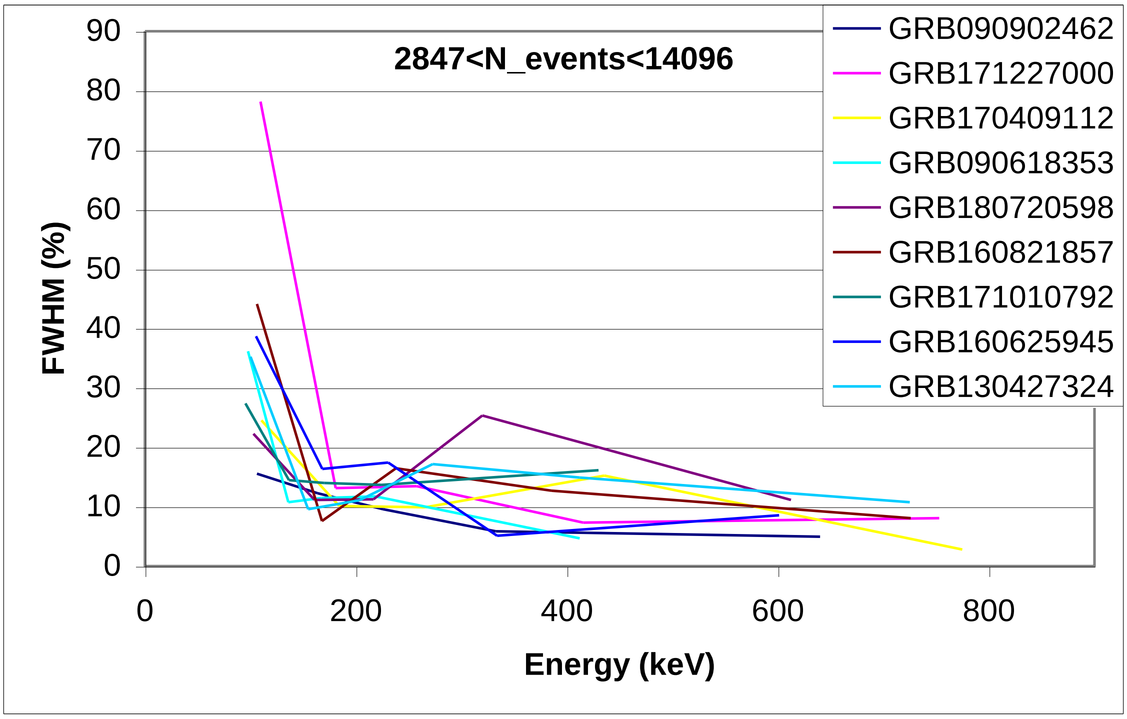

Figure 63: *Energy resolution for nine GRB with a number of events between 2847 and 14096.*

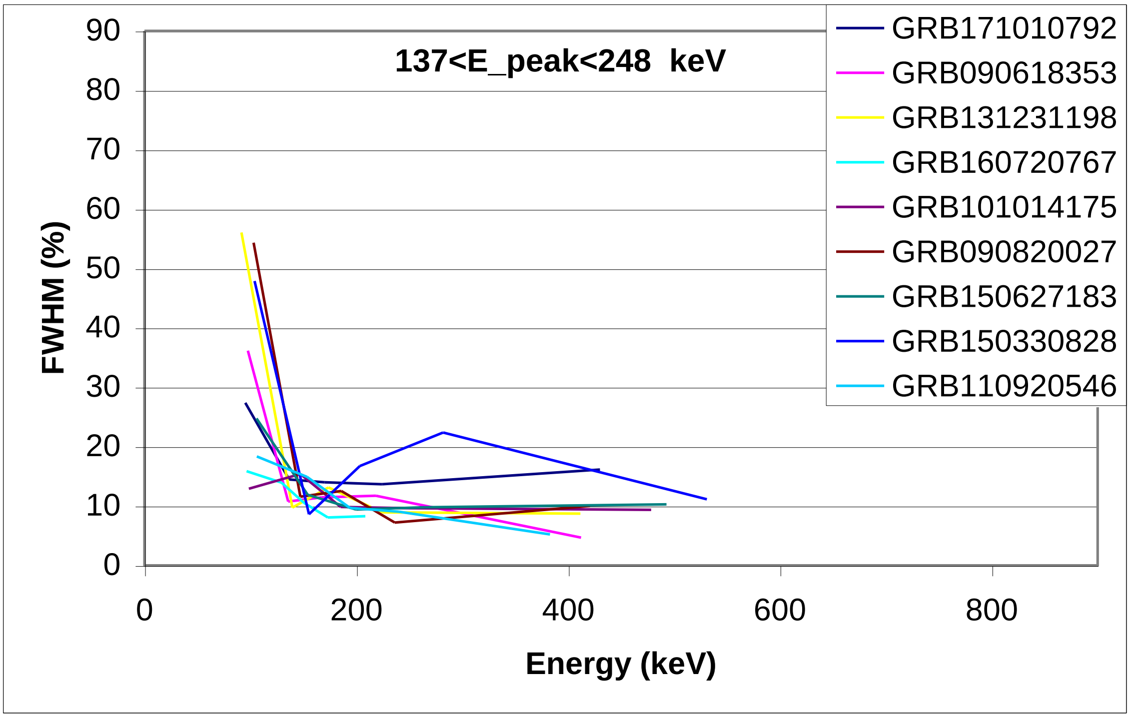

Figure 64: *Energy resolution for nine GRB with E_{peak} between 137 and 248 keV.*

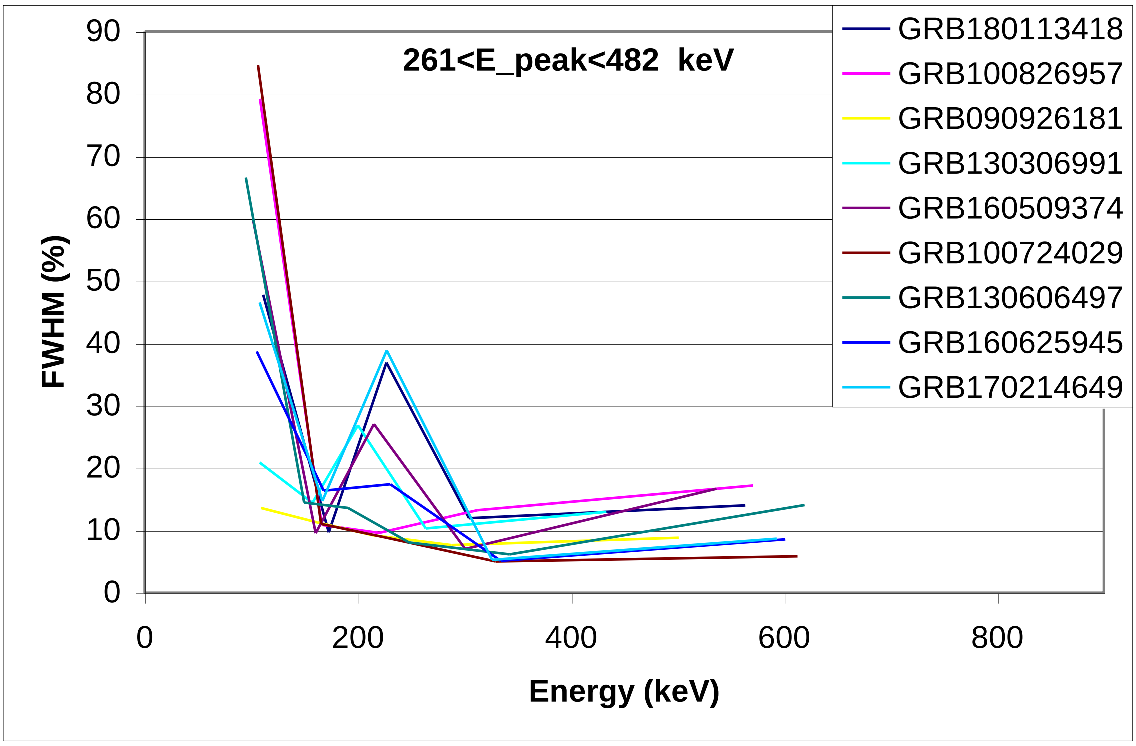

Figure 65: *Energy resolution for nine GRB with E_{peak} between 261 and 482 keV.*

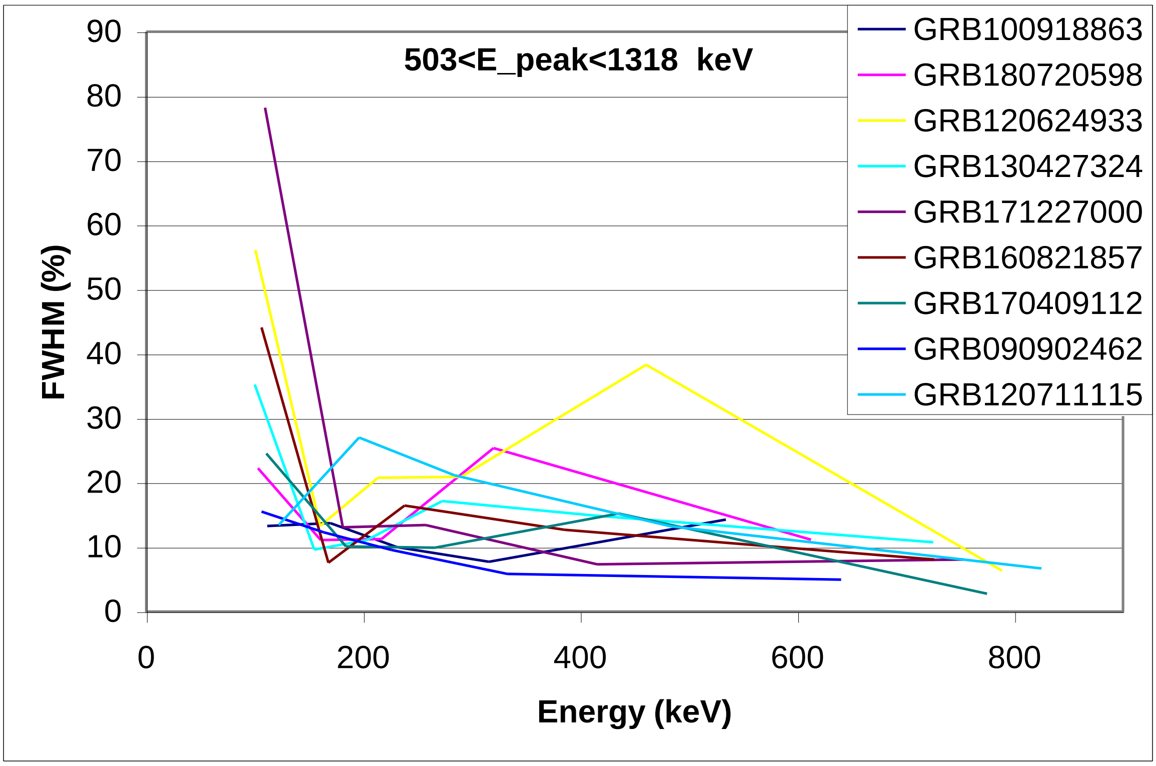

Figure 66: *Energy resolution for nine GRB with E_{peak} between 503 and 1318 keV.*

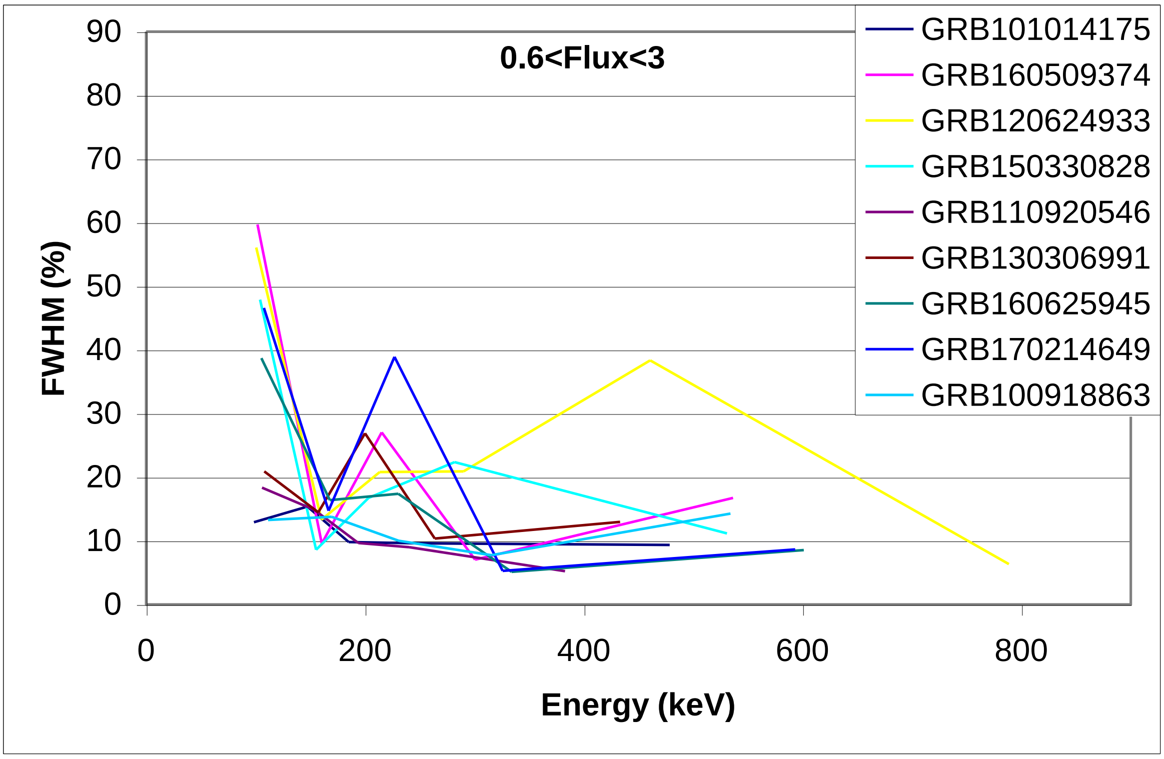

Figure 67: *Energy resolution for nine GRB with a flux between 0.6 and 3 photon/cm^2/s.*

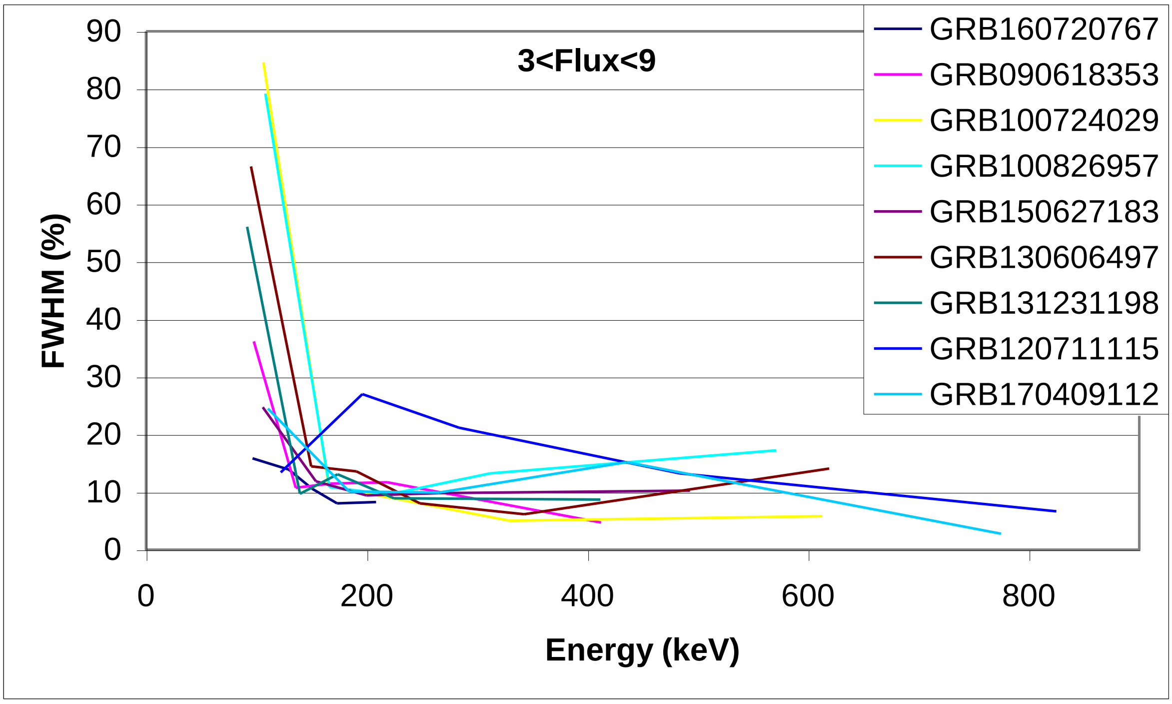

Figure 68: *Energy resolution for nine GRB with a flux between 3 and 9 photon/cm^2/s.*

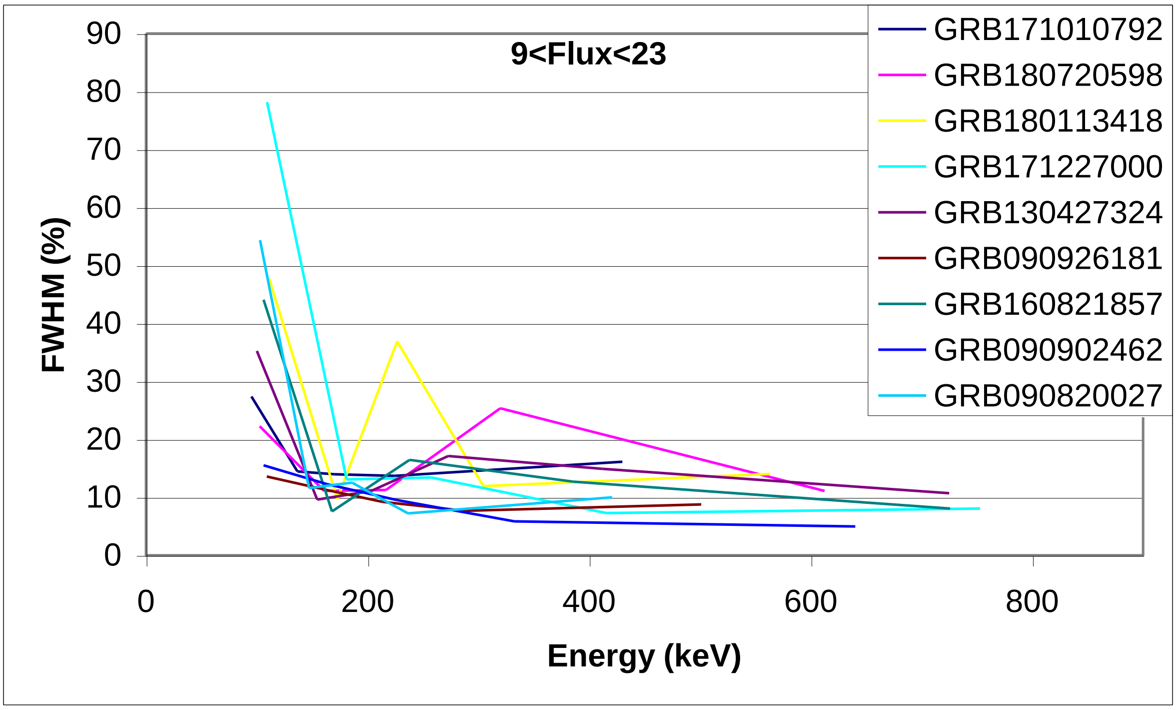

Figure 69: *Energy resolution for nine GRB with a flux between 9 and 23 photon/cm^2/s.*

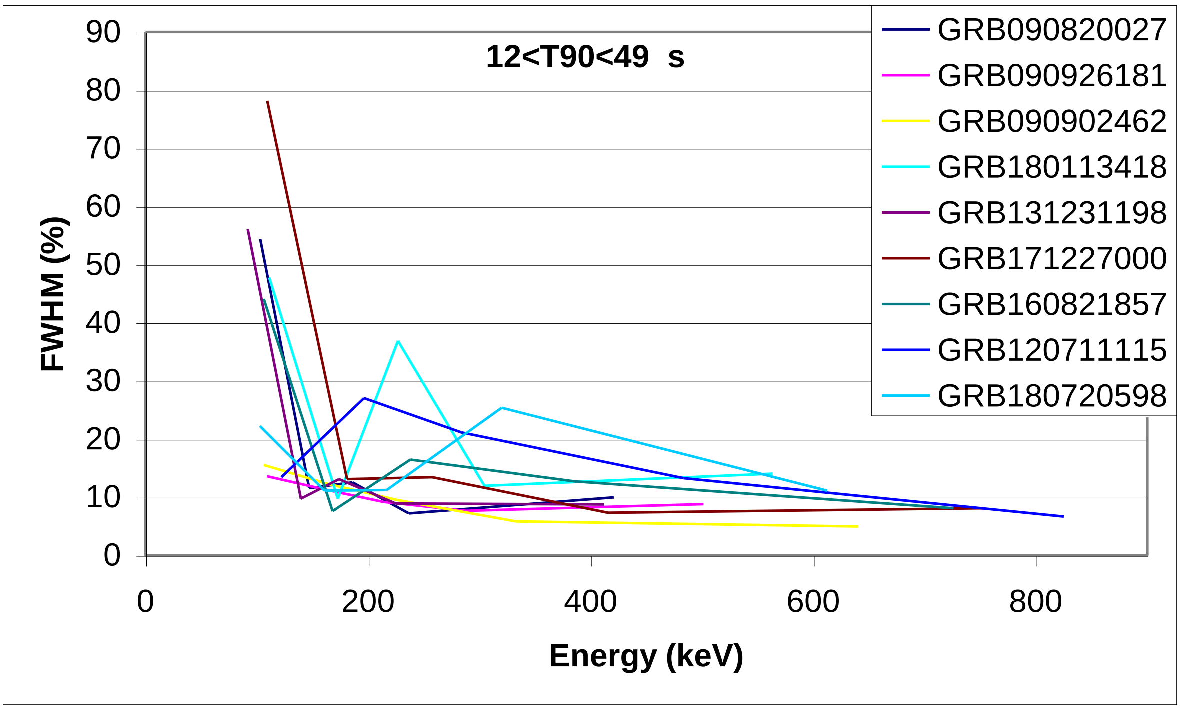

Figure 70: *Energy resolution for nine GRB with T_{90} between 12 and 49 s.*

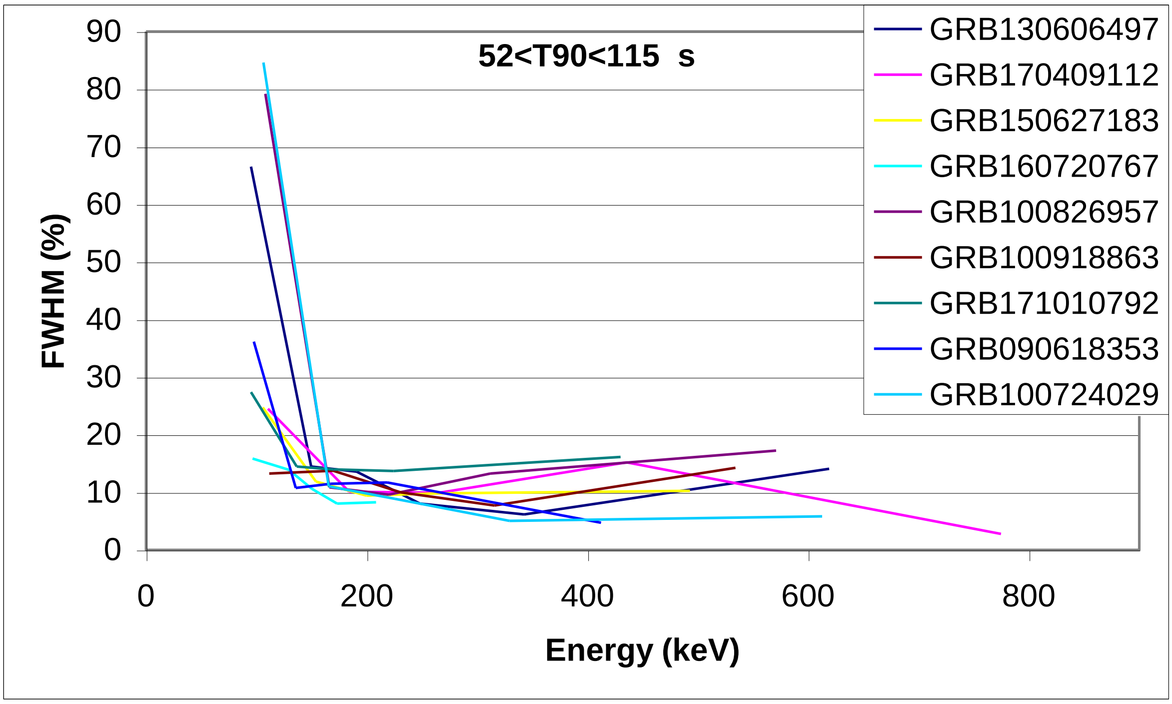

Figure 71: *Energy resolution for nine GRB with T_{90} between 52 and 115 s.*

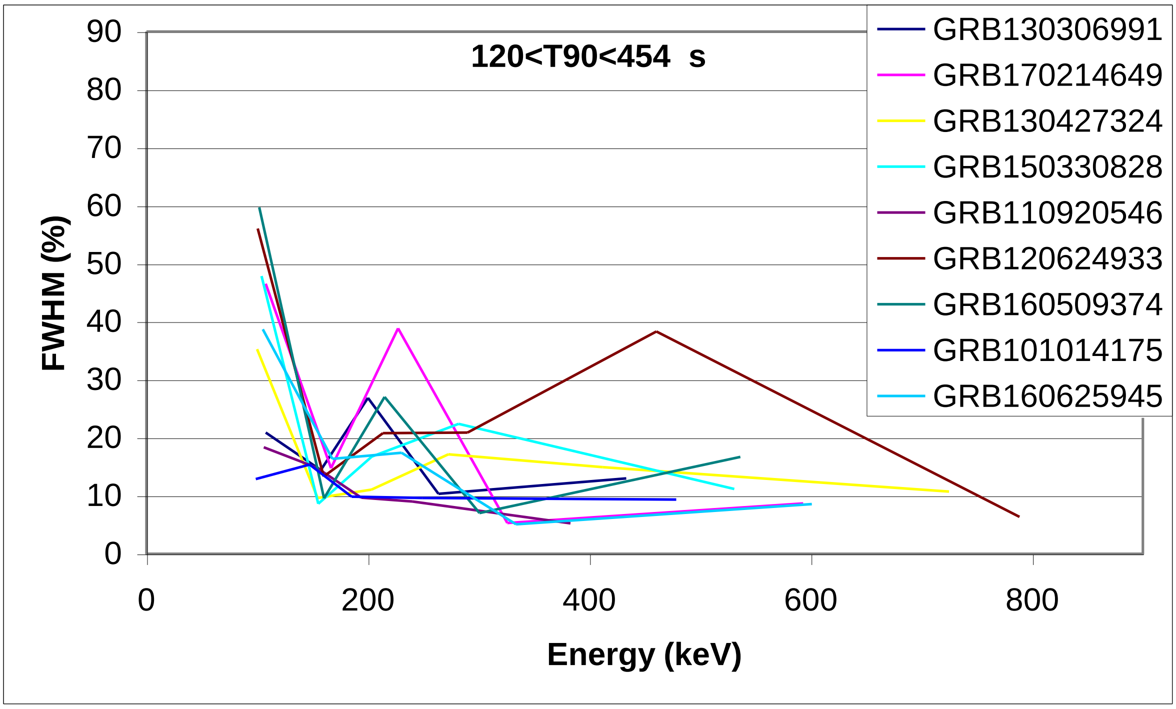

Figure 72: *Energy resolution for nine GRB with T_{90} between 120 and 454 s.*

-1.218<alfa<-1.018			
N. Total Events 41693			
Energy (keV)	Events	<E> (keV)	FWHM (%)
126>E	7059	95.35	53.36
126<E<157	6868	141.1	20.20
157<E<197	6981	176.1	8.49
197<E<262	6918	226.2	20.16
262<E<427	6921	327.0	25.19
427<E	6946	952.2	9.87

-1.015<alfa<-0.904			
N. Total Events 23860			
Energy (keV)	Events	<E> (keV)	FWHM (%)
133>E	3943	100.1	61.86
133<E<173	3959	152.6	12.10
173<E<222	3943	196.2	29.87
222<E<293	3970	254.6	23.62
293<E<456	3969	360.1	34.97
456<E	4076	1046	17.10

-0.875<alfa<-0.536			
N. Total Events 19868			
Energy (keV)	Events	<E> (keV)	FWHM (%)
134>E	3333	102.2	88.41
134<E<175	3352	154.4	15.18
175<E<223	3345	198.0	7.64
223<E<292	3330	254.4	32.55
292<E<465	3311	358.6	18.75
465<E	3197	1073	9.07

Table 41: *The energy resolutions for the simulations with different intervals of alfa.*

-10.854<beta<-2.576			
N. Total Events 31191			
Energy (keV)	Events	<E> (keV)	FWHM (%)
131>E	5149	100.1	35.00
131<E<169	5234	149.6	15.43
169<E<215	5171	190.6	28.33
215<E<287	5171	247.8	24.43
287<E<467	5216	359.5	18.79
467<E	5250	942.9	9.88

-2.572<beta<-2.217			
N. Total Events 24402			
Energy (keV)	Events	<E> (keV)	FWHM (%)
130>E	4099	97.32	88.37
130<E<166	4064	147.3	16.10
166<E<213	4057	188.1	30.55
213<E<287	4085	246.6	18.31
287<E<478	4089	362.5	22.16
478<E	4008	1096	16.24

-2.191<beta<-1.918			
N. Total Events 29828			
Energy (keV)	Events	<E> (keV)	FWHM (%)
127>E	5011	96.2	93.95
127<E<161	5001	143.5	30.45
161<E<202	4965	180.3	16.77
202<E<264	4998	230.4	36.02
264<E<400	4968	319.1	39.49
400<E	4885	1005	9.78

Table 42: *The energy resolutions for the simulations with different intervals of beta.*

1615<Events<1866			
N. Total Events 15954			
Energy (keV)	Events	<E> (keV)	FWHM (%)
129>E	2634	98.97	58.37
129<E<162	2675	145.5	18.76
162<E<200	2668	180.3	29.75
200<E<261	2642	227.7	37.53
261<E<394	2680	314.5	19.85
394<E	2655	951.1	9.38

2007<Events<2722			
N. Total Events 19542			
Energy (keV)	Events	<E> (keV)	FWHM (%)
130>E	3307	99.23	91.08
130<E<165	3216	147.4	15.46
165<E<206	3244	184.6	47.59
206<E<264	3259	232.5	24.95
264<E<385	3279	314.2	13.28
385<E	3237	934.6	10.49

2847<Events<14096			
N. Total Events 49925			
Energy (keV)	Events	<E> (keV)	FWHM (%)
129>E	8349	97.14	87.73
129<E<166	8286	146.8	16.06
166<E<215	8310	188.7	15.85
215<E<291	8314	249.1	18.51
291<E<486	8325	369.5	22.19
486<E	8341	1045	8.82

Table 43: *The energy resolutions for the simulations with different intervals of number of events.*

137<E_peak<248			
N. Total Events 24220			
Energy (keV)	Events	<E> (keV)	FWHM (%)
121>E	4071	93.74	54.11
121<E<147	4127	133.7	13.79
147<E<177	4103	161.4	14.62
177<E<218	4058	196.2	17.73
217<E<303	4038	253.4	19.03
303<E	3823	684.0	25.62

261<E_peak<482			
N. Total Events 24168			
Energy (keV)	Events	<E> (keV)	FWHM (%)
134>E	4089	100.4	91.37
134<E<174	4046	153.7	18.20
174<E<222	4026	196.8	29.24
222<E<292	4074	254.0	32.65
292<E<446	4072	353.7	11.91
446<E	3861	1079	9.11

503<E_peak<1318			
N. Total Events 37033			
Energy (keV)	Events	<E> (keV)	FWHM (%)
135>E	6150	100.8	87.77
135<E<178	6189	156.3	15.52
178<E<238	6194	206.6	25.84
238<E<329	6119	278.0	29.60
329<E<560	6176	423.9	41.22
560<E	6205	1143	8.08

Table 44: *The energy resolutions for the simulations with different intervals of* E_{peak}.

0.6<Flux<3			
N. Total Events 22842			
Energy (keV)	Events	<E> (keV)	FWHM (%)
132>E	3855	99.63	61.56
132<E<170	3816	151.0	15.37
170<E<217	3861	192.2	30.12
217<E<282	3813	246.8	18.10
282<E<428	3834	341.4	36.87
428<E	3663	997.6	17.94

3<Flux<9			
N. Total Events 20957			
Energy (keV)	Events	<E> (keV)	FWHM (%)
127>E	3483	97.18	93.47
127<E<159	3498	142.4	30.84
159<E<198	3481	177.7	11.01
198<E<261	3475	226.1	26.35
261<E<410	3420	320.3	13.09
410<E	3600	1031	9.49

9<Flux<23			
N. Total Events 41622			
Energy (keV)	Events	<E> (keV)	FWHM (%)
129>E	6885	97.23	88.28
129<E<165	6906	146.4	15.85
165<E<212	6956	187.2	16.17
212<E<285	6958	245.1	33.80
285<E<469	6930	358.4	22.84
469<E	6987	994.7	9.33

Table 45: *The energy resolutions for the simulations with different intervals of number of flux.*

12<T90<49			
N. Total Events 23622			
Energy (keV)	Events	<E> (keV)	FWHM (%)
133>E	3964	100.0	86.21
133<E<172	3968	151.9	15.46
172<E<222	3953	195.7	27.06
222<E<298	3937	256.1	32.42
298<E<508	3953	380.0	21.56
508<E	3847	1110	8.13

52<T90<115			
N. Total Events 26476			
Energy (keV)	Events	<E> (keV)	FWHM (%)
124>E	4464	95.67	95.14
124<E<153	4392	138.3	31.79
153<E<190	4487	170.8	13.76
190<E<246	4404	215.0	14.42
246<E<377	4444	299.7	14.05
377<E	4285	916.3	10.61

120<T90<454			
N. Total Events 35323			
Energy (keV)	Events	<E> (keV)	FWHM (%)
132>E	5858	98.91	61.67
132<E<171	5839	151.2	15.21
171<E<220	5882	194.0	29.90
220<E<291	5893	252.4	18.03
291<E<458	5873	359.7	34.97
458<E	5978	1006	9.24

Table 46: *The energy resolutions for the simulations with different intervals of number of* T_{90}.

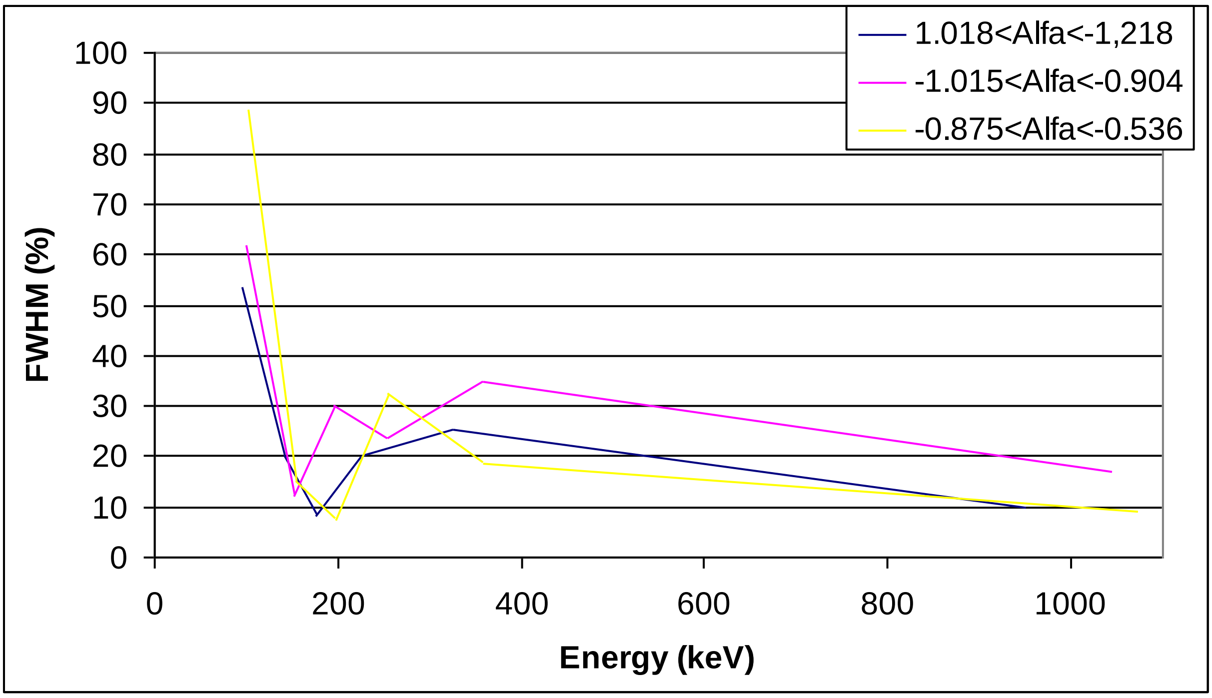

Figure 73: *Comparison of the energy resolutions for the simulations with different intervals of alfa.*

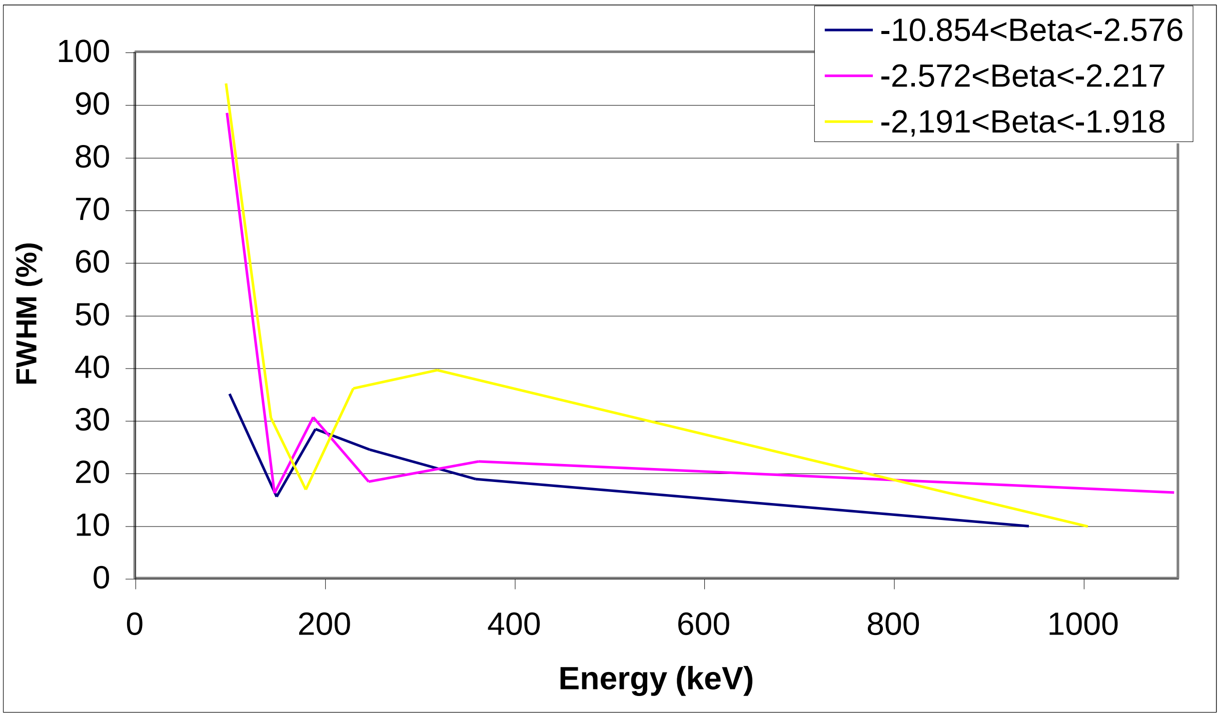

Figure 74: *Comparison of the energy resolutions for the simulations with different intervals of beta.*

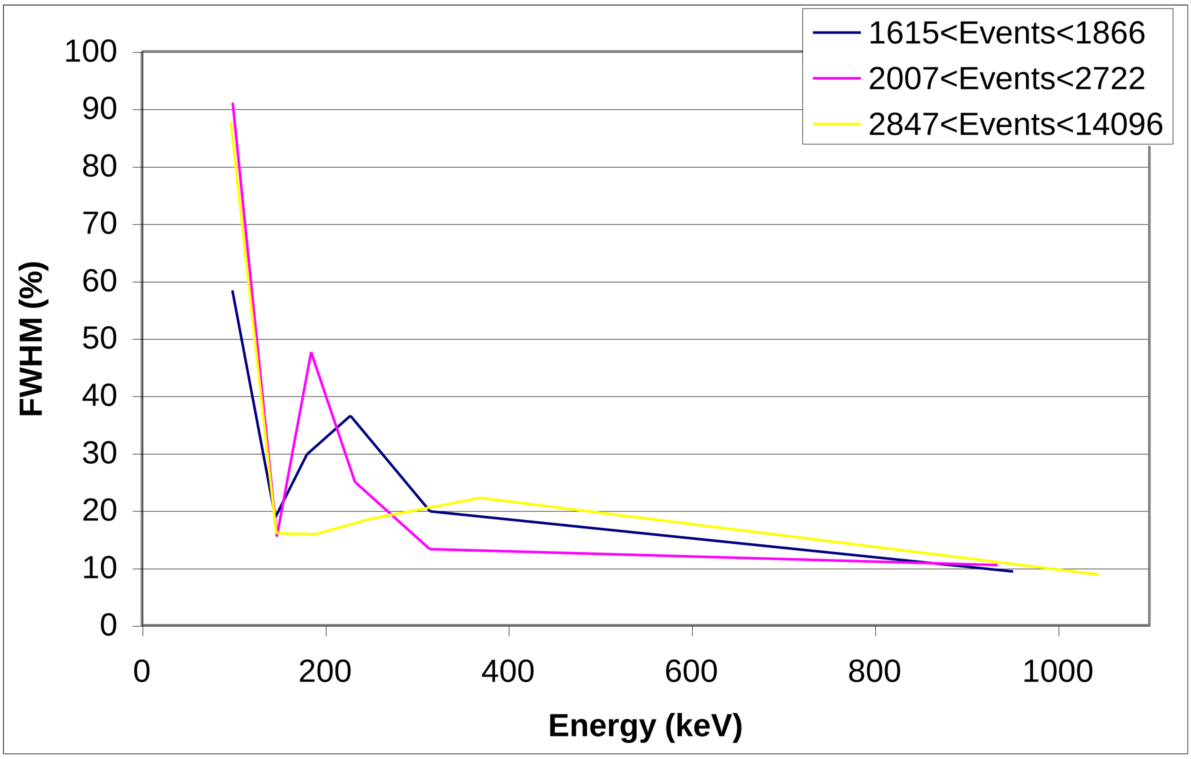

Figure 75: *Comparison of the energy resolutions for the simulations with different intervals of number of events.*

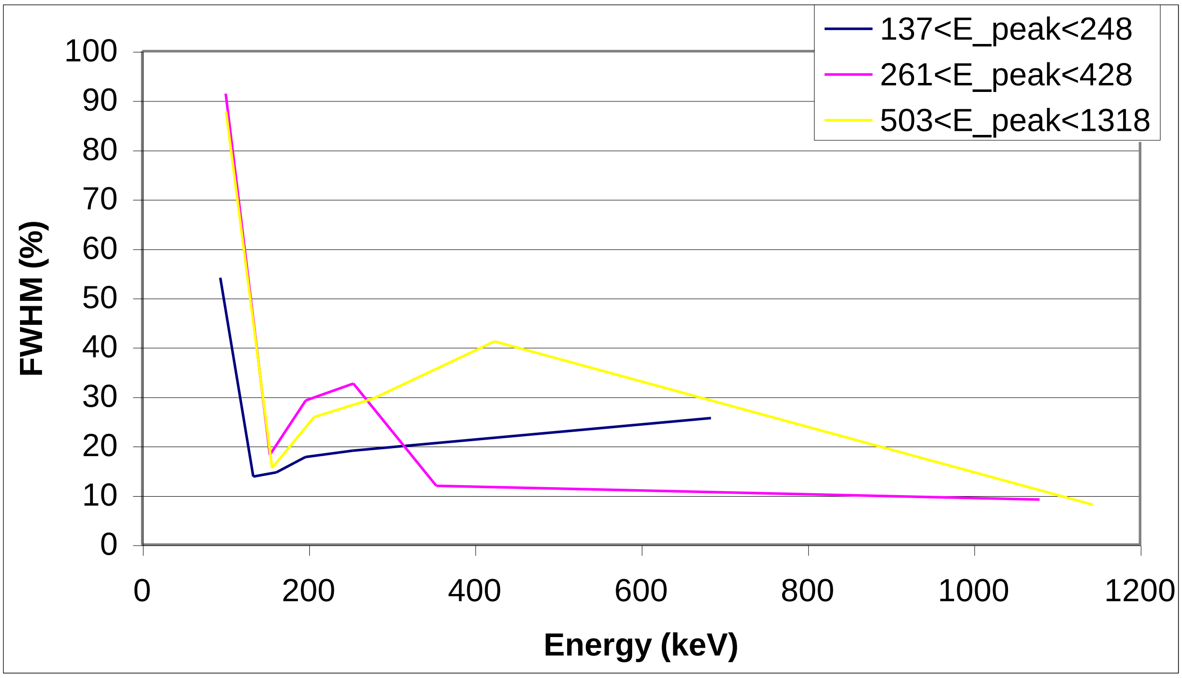

Figure 76: *Comparison of the energy resolutions for the simulations with different intervals of E_{peak}..*

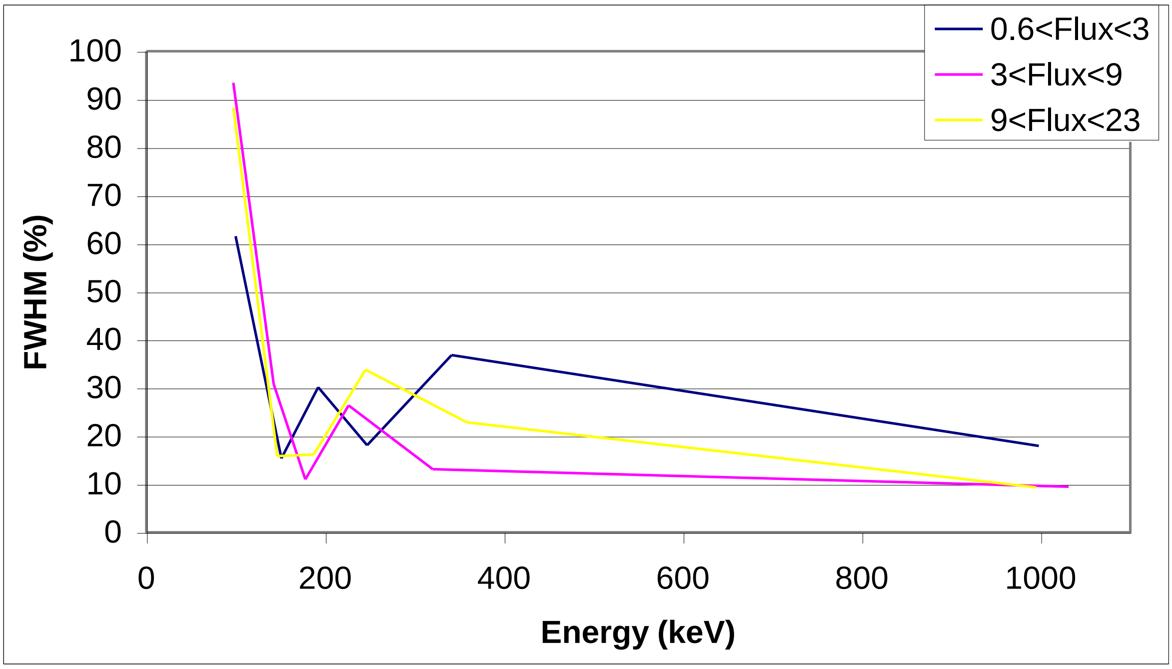

Figure 77: *Comparison of the energy resolutions for the simulations with different intervals of flux.*

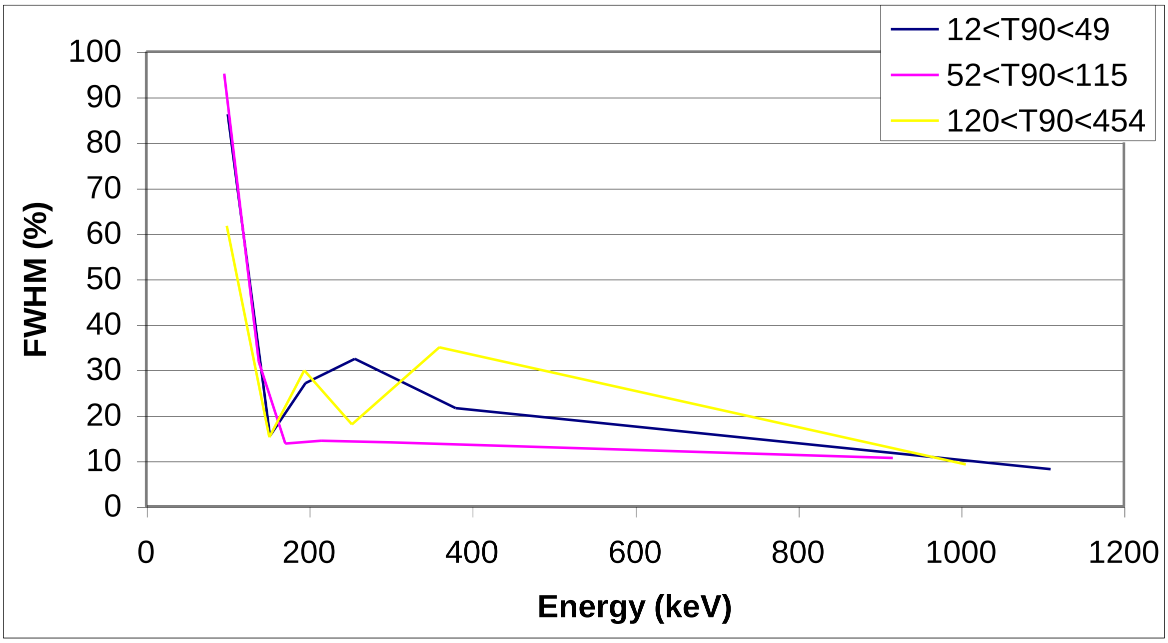

Figure 78: *Comparison of the energy resolutions for the simulations with different intervals of T_{90}.*

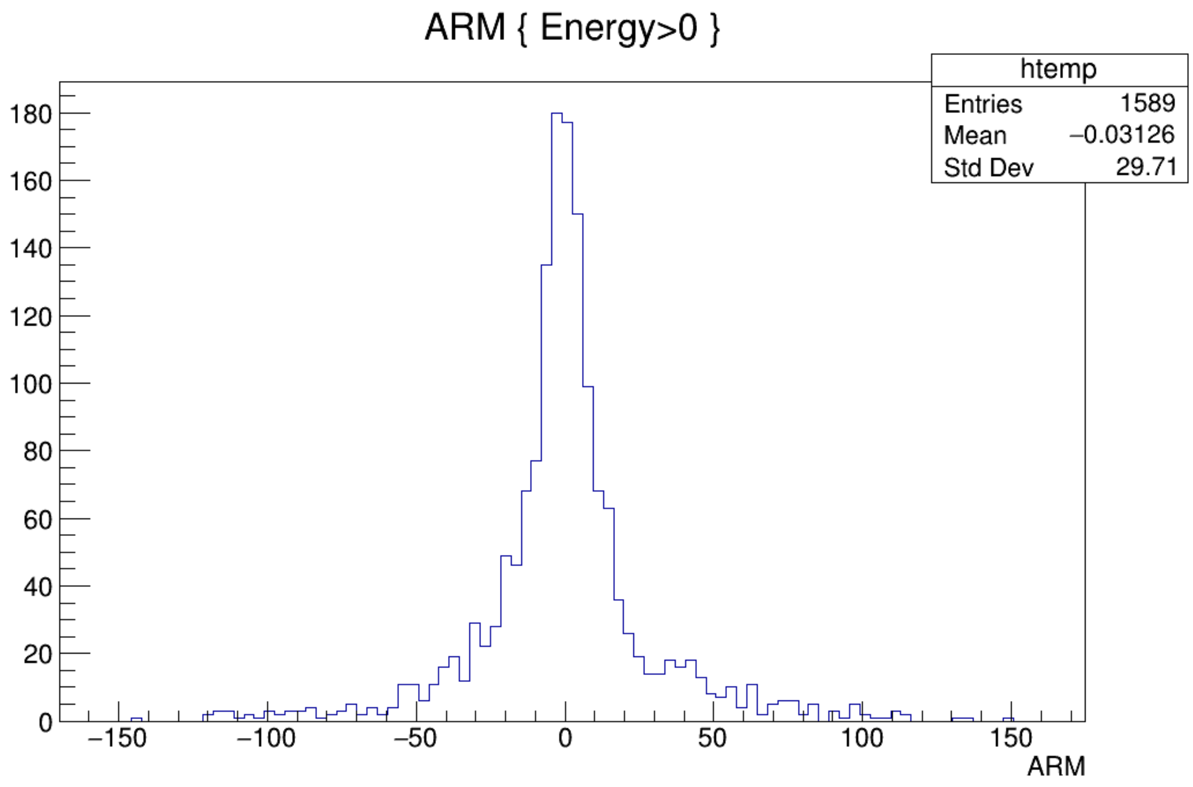

Figure 79: *ARM for GRB100918863. The difference between the number of events reported in the legend and that reported in Table 9 is due to the fact that we do not reconstruct some events.*

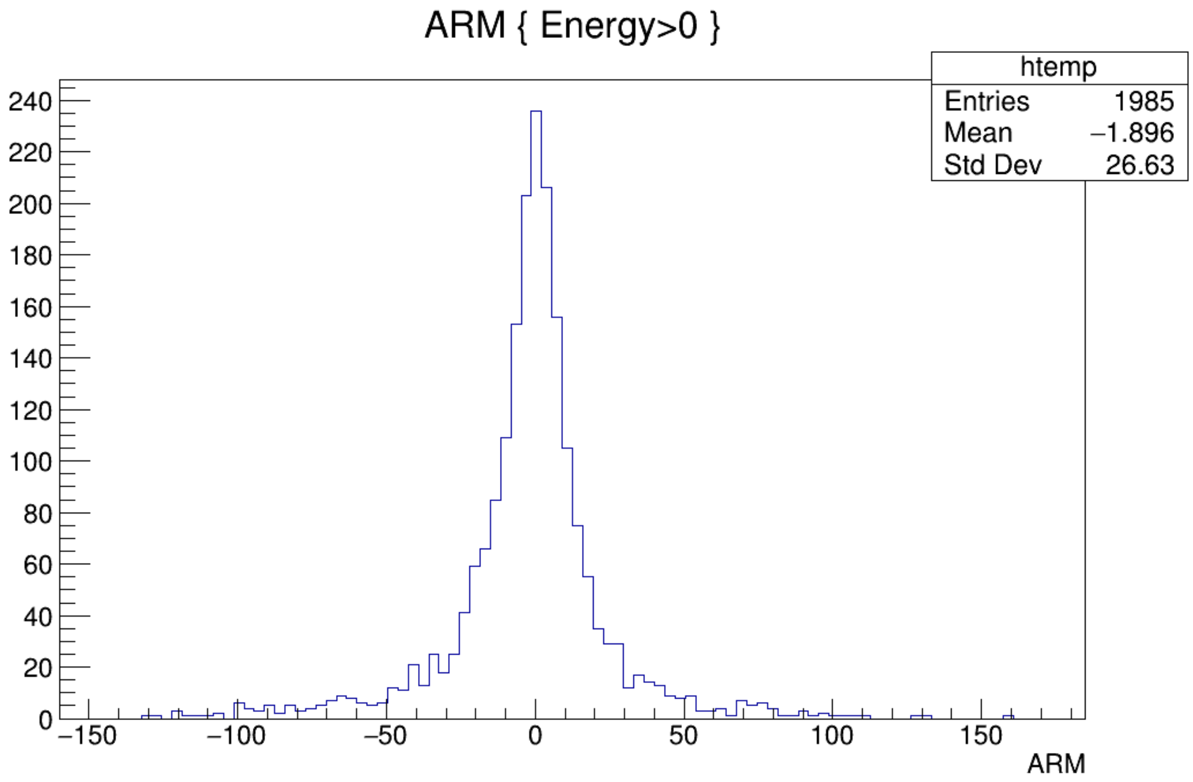

Figure 80: *ARM for GRB110920546. The difference between the number of events reported in the legend and that reported in Table 9 is due to the fact that we do not reconstruct some events.*

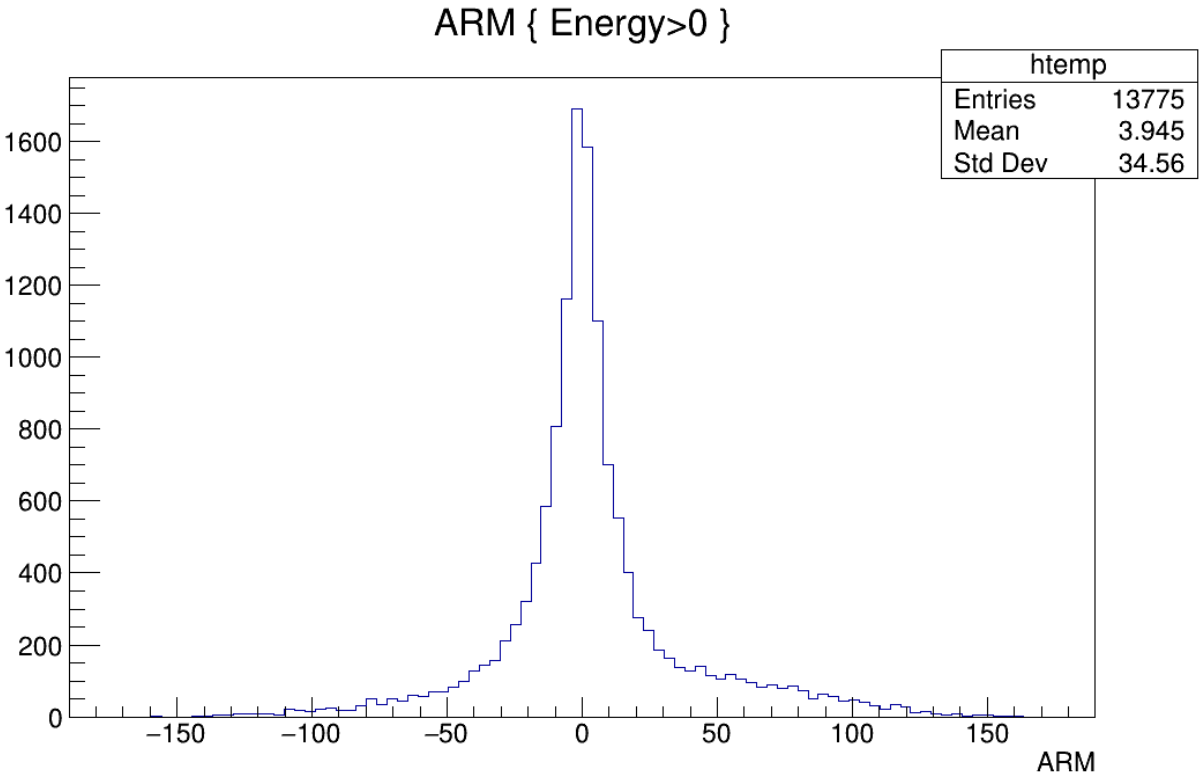

Figure 81: *ARM for GRB130427324. The difference between the number of events reported in the legend and that reported in Table 9 is due to the fact that we do not reconstruct some events.*

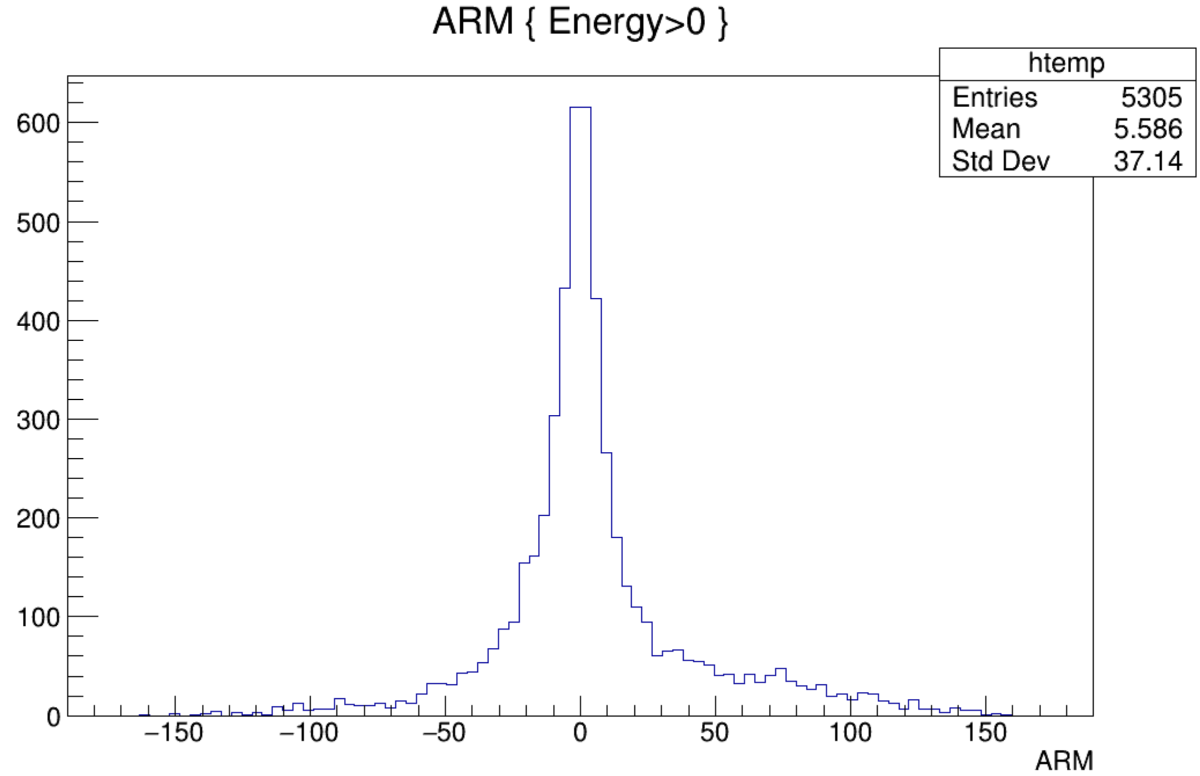

Figure 82: *ARM for GRB160821857. The difference between the number of events reported in the legend and that reported in Table 9 is due to the fact that we do not reconstruct some events.*

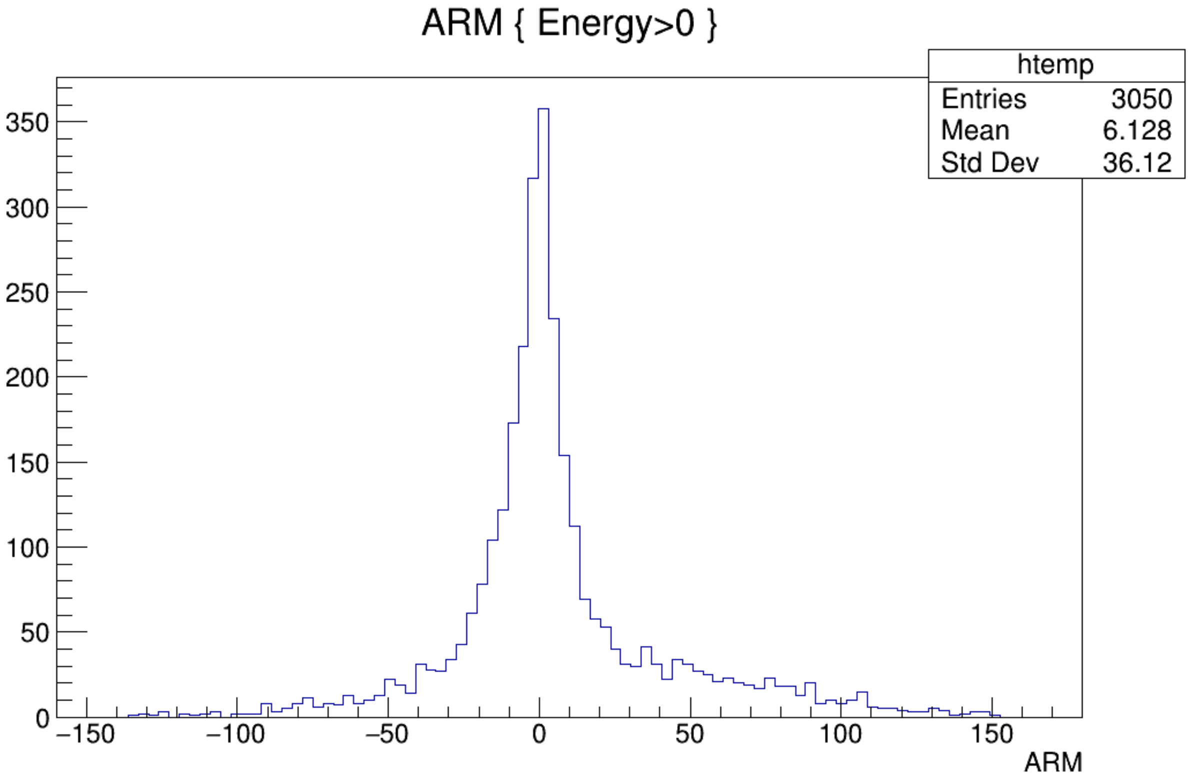

Figure 83: *ARM for GRB170409112. The difference between the number of events reported in the legend and that reported in Table 9 is due to the fact that we do not reconstruct some events.*

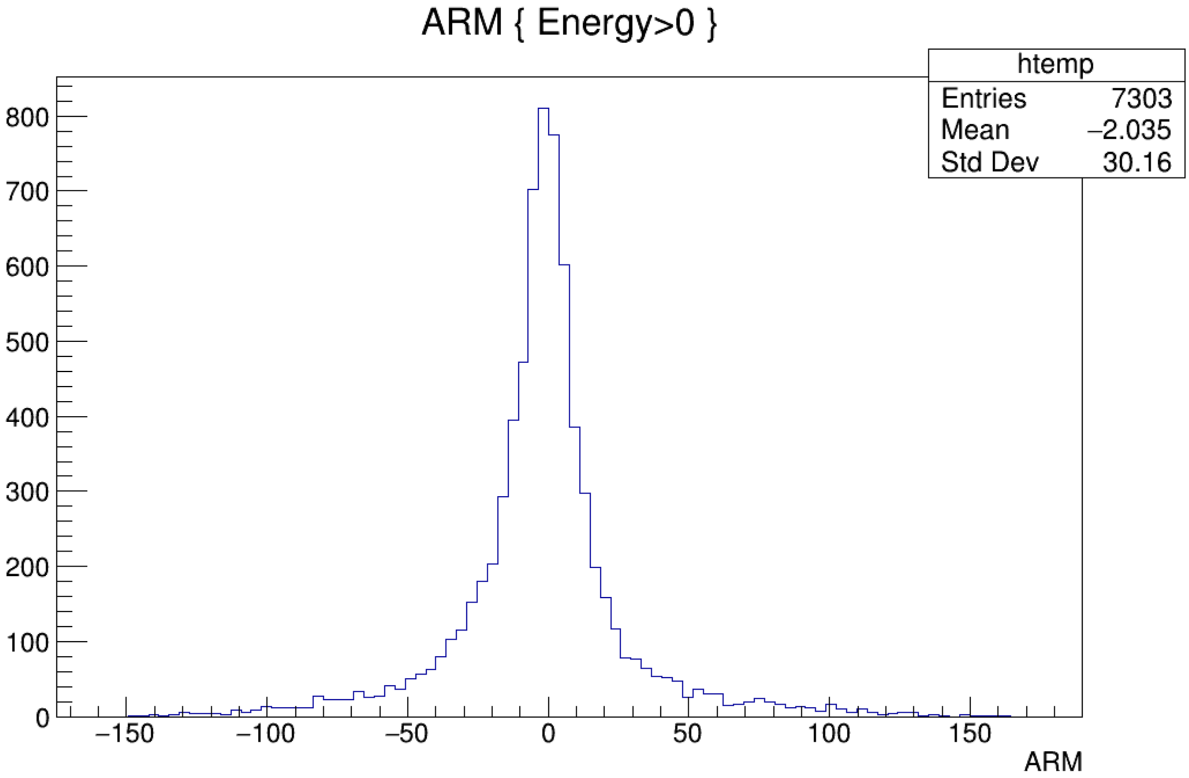

Figure 84: *ARM for GRB171010792. The difference between the number of events reported in the legend and that reported in Table 9 is due to the fact that we do not reconstruct some events.*

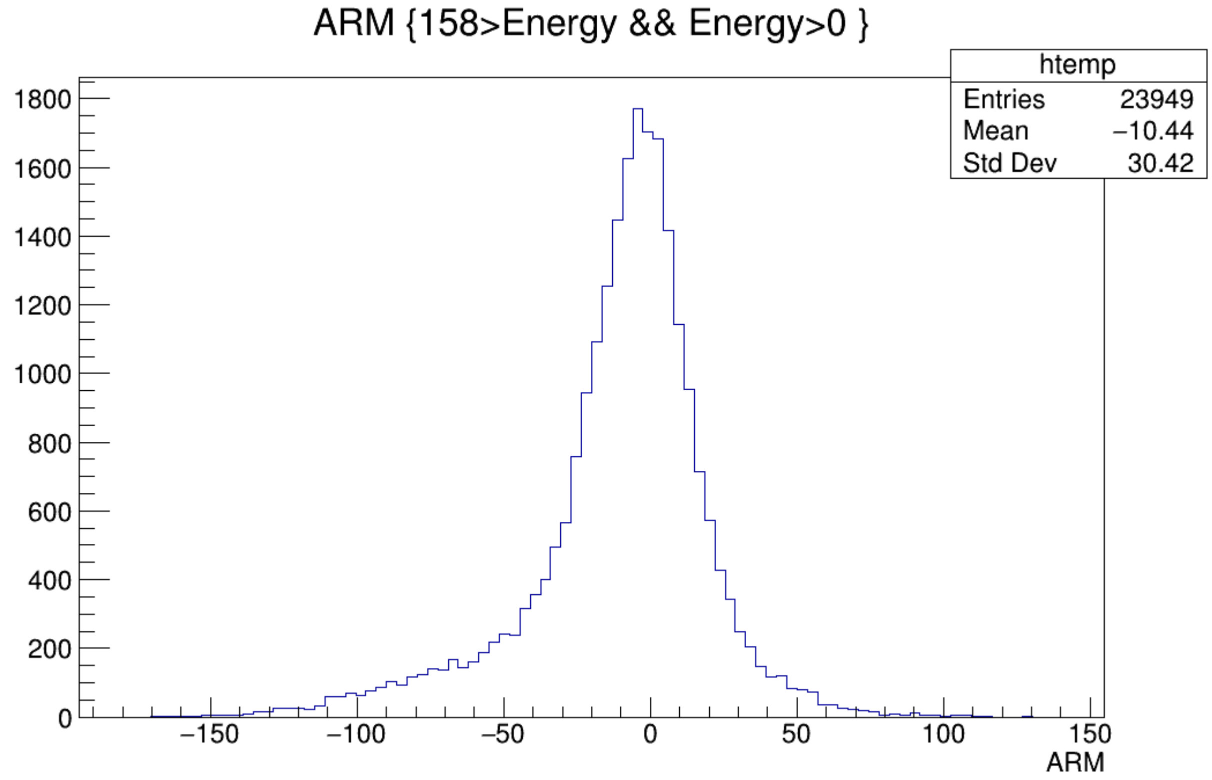

Figure 85: *The total ARM for all 27 GRBs for E <158 keV. The difference between the number of events in the legend and the number reported in Table 47 is due to the fact that we do not reconstruct some events.*

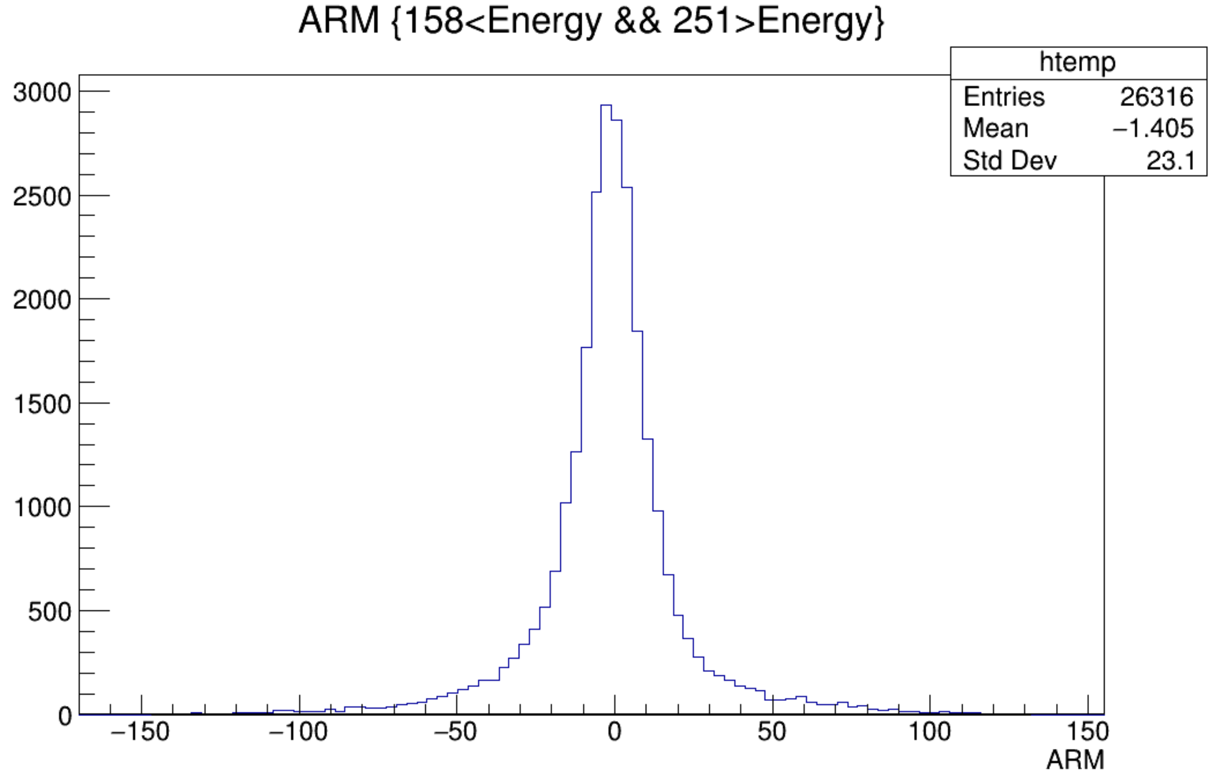

Figure 86: *The total ARM for all 27 GRBs for 158<E <251 keV.*

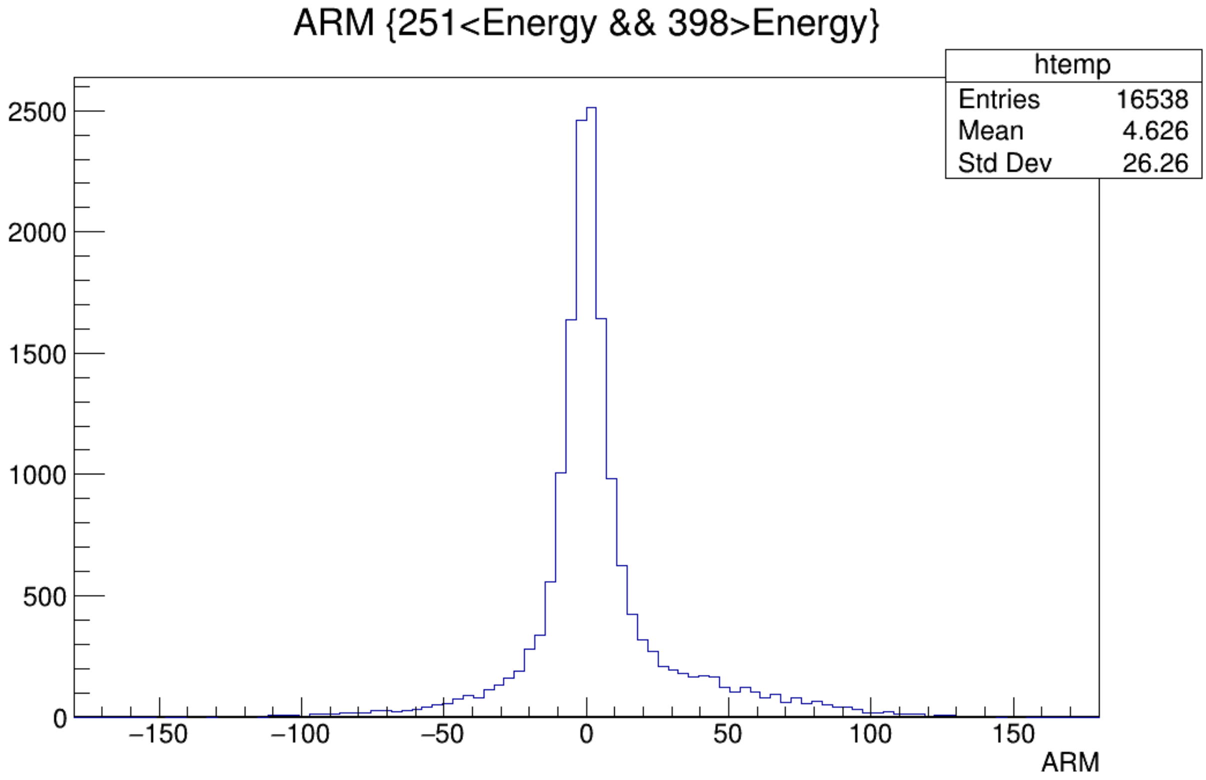

Figure 87: *The total ARM for all 27 GRBs for 251<E <398 keV.*

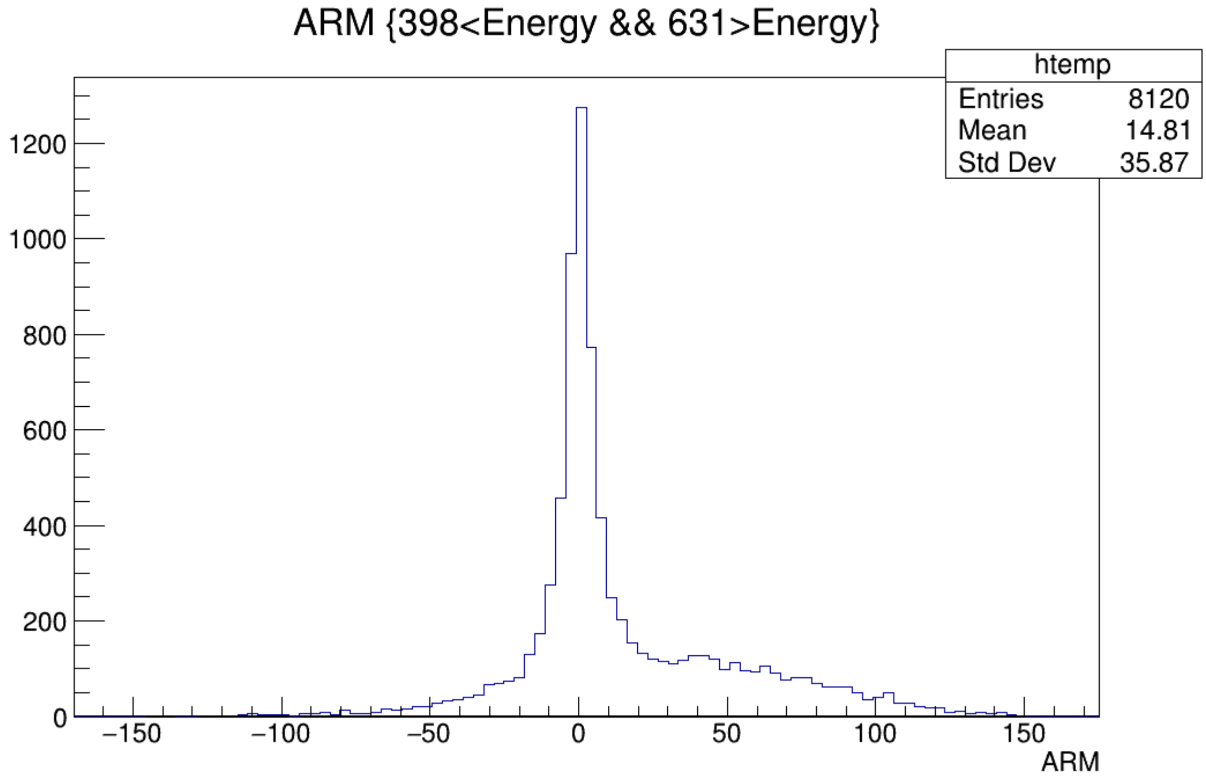

Figure 88: *The total ARM for all 27 GRBs for 398<E <631 keV.*

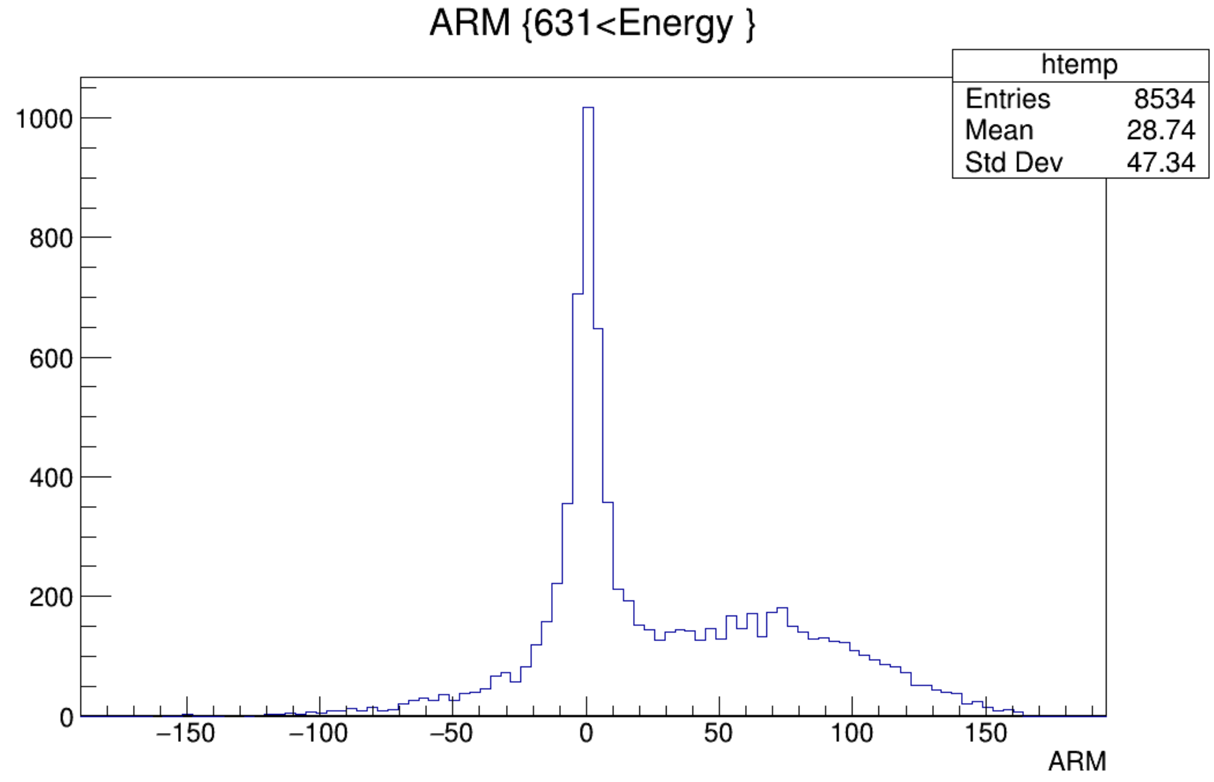

Figure 89: *The total ARM for all 27 GRBs for E >631 keV.*

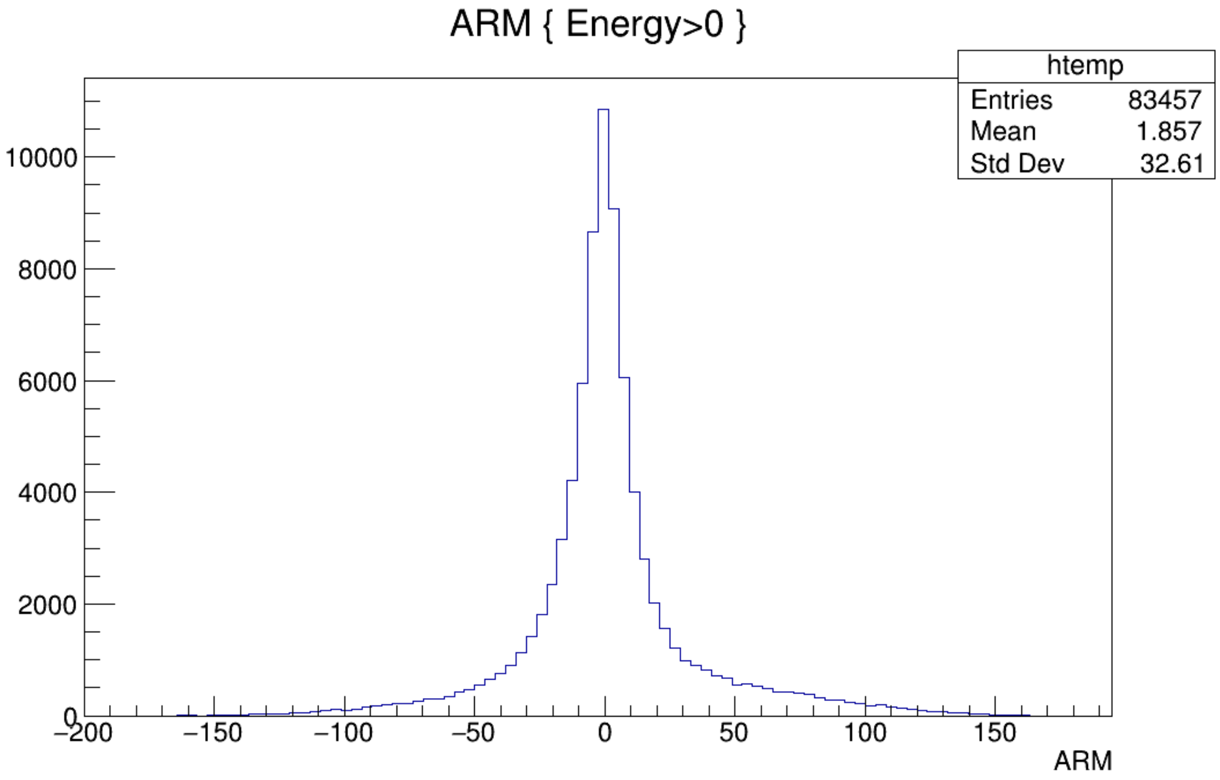

Figure 90: *The total ARM for all 27 GRBs for E >0.*

All GRB			
N. Total Events 85421			
Tot. ARM 20,31 FWHM (º)			
Energy (keV)	Events	<E>	FWHM (º)
158>E	25913	128.0	39.03
158<E<251	26316	199.2	19.39
251<E<398	16538	310.1	14.19
398<E<631	8120	493.2	10.10
631<E	8534	1328	11.27

Table 47: *Total angular resolution measure.*

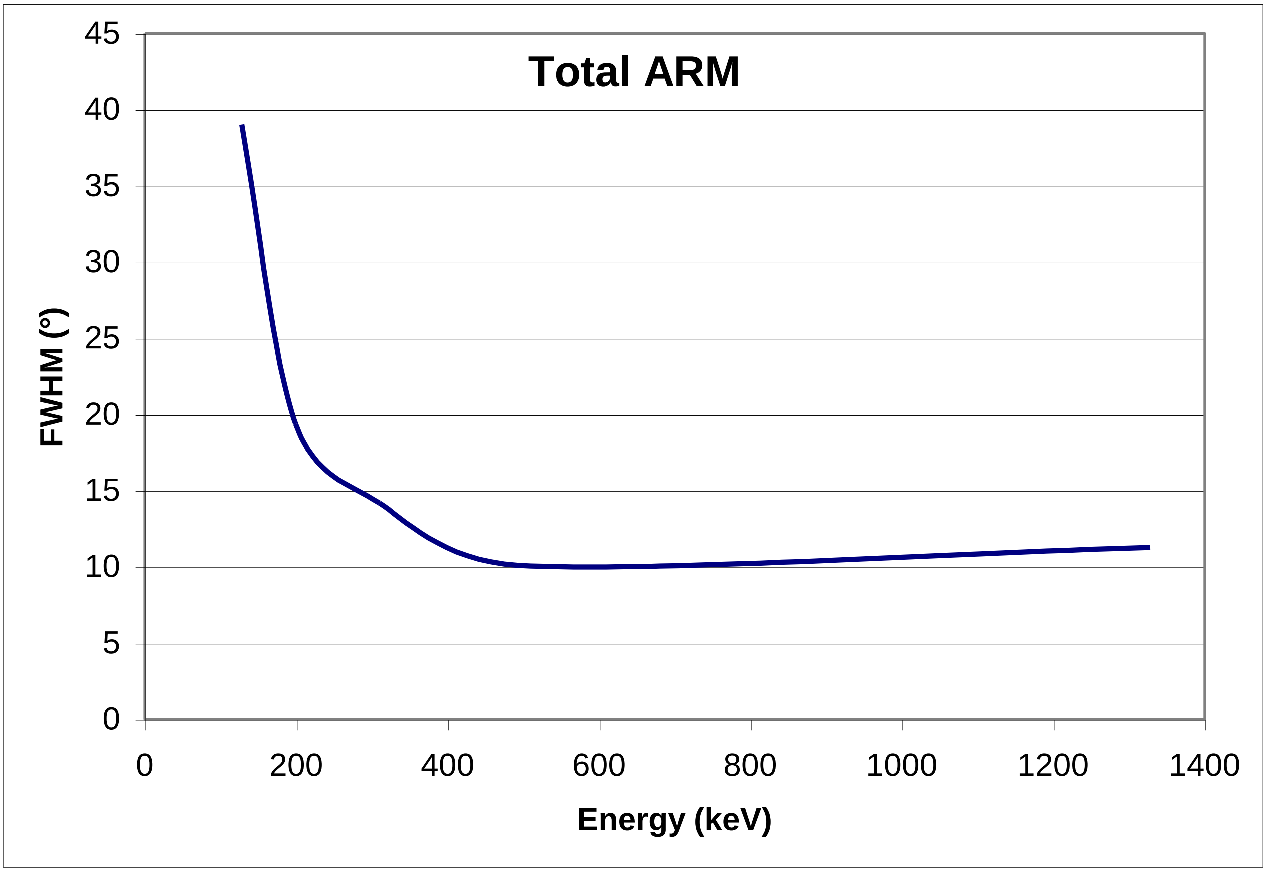

Figure 91: *Total angular resolution measure for 27 GRB.*

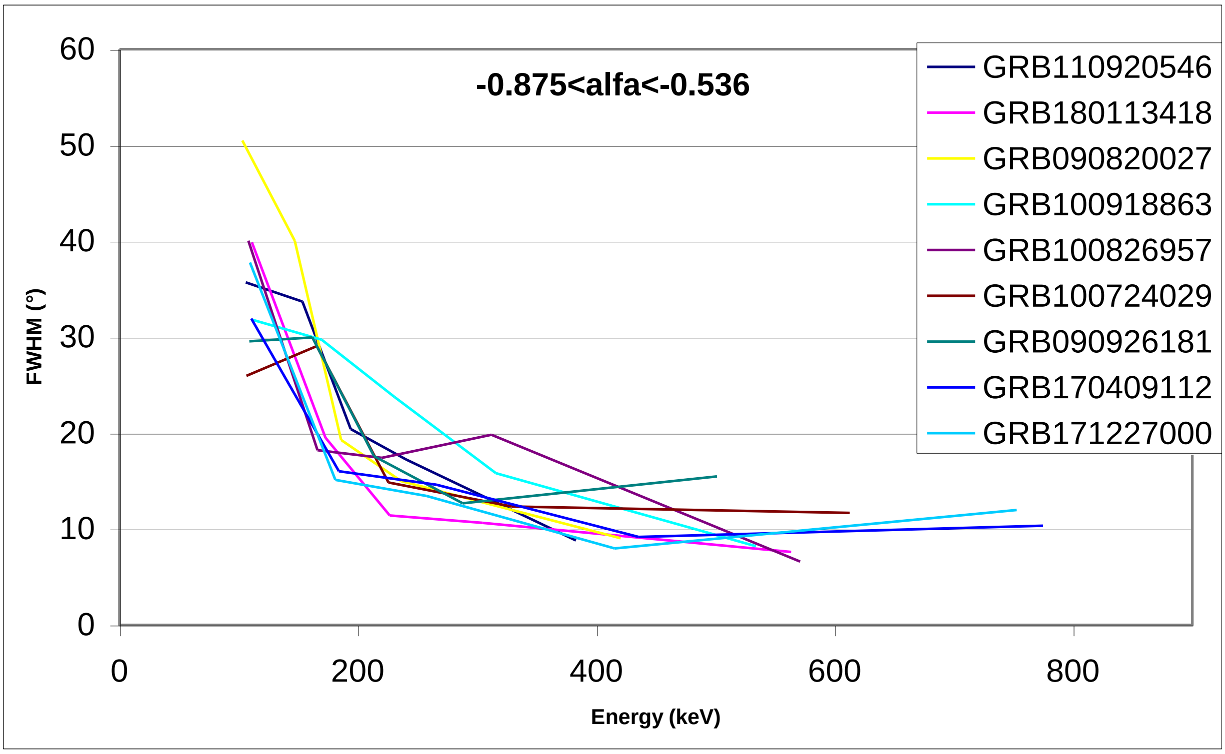

Figure 92: *Angular resolution for nine GRB with alfa between –0.875 and –0.536.*

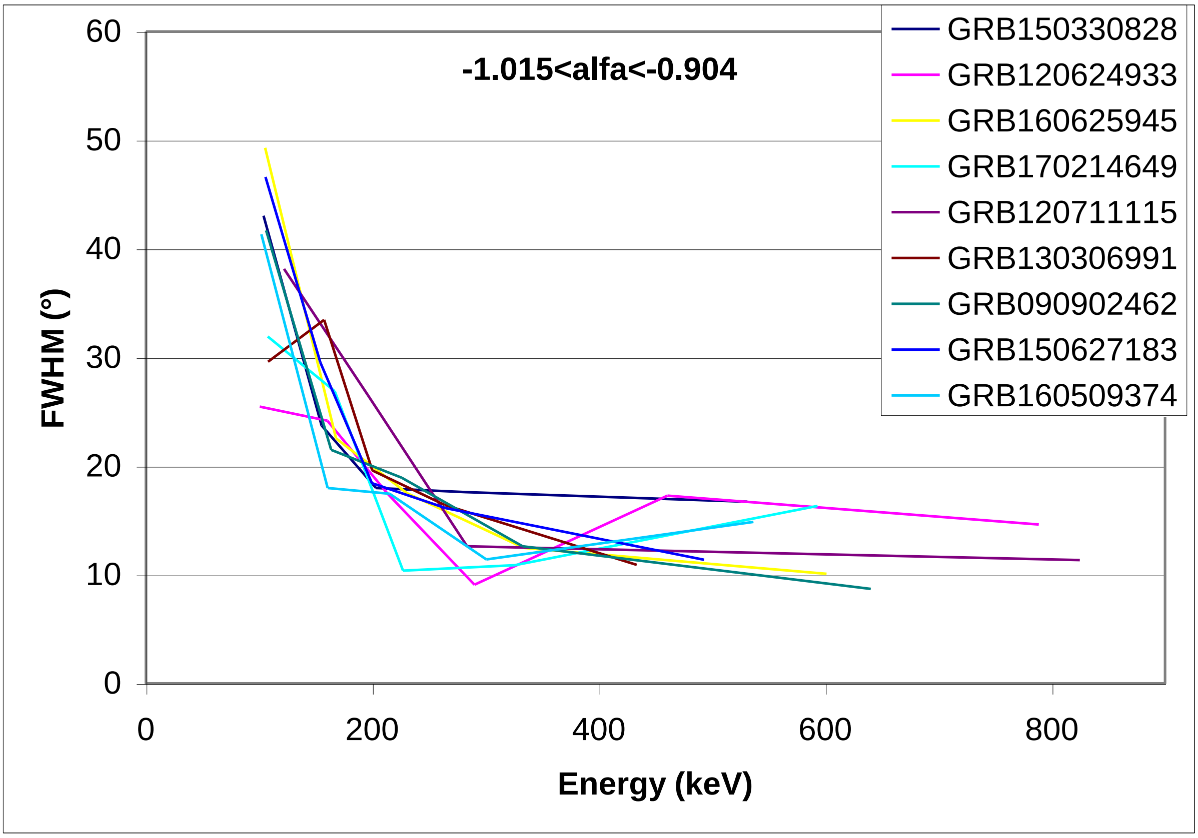

Figure 93: *Angular resolution for nine GRB with alfa between –1.015 and –0.904.*

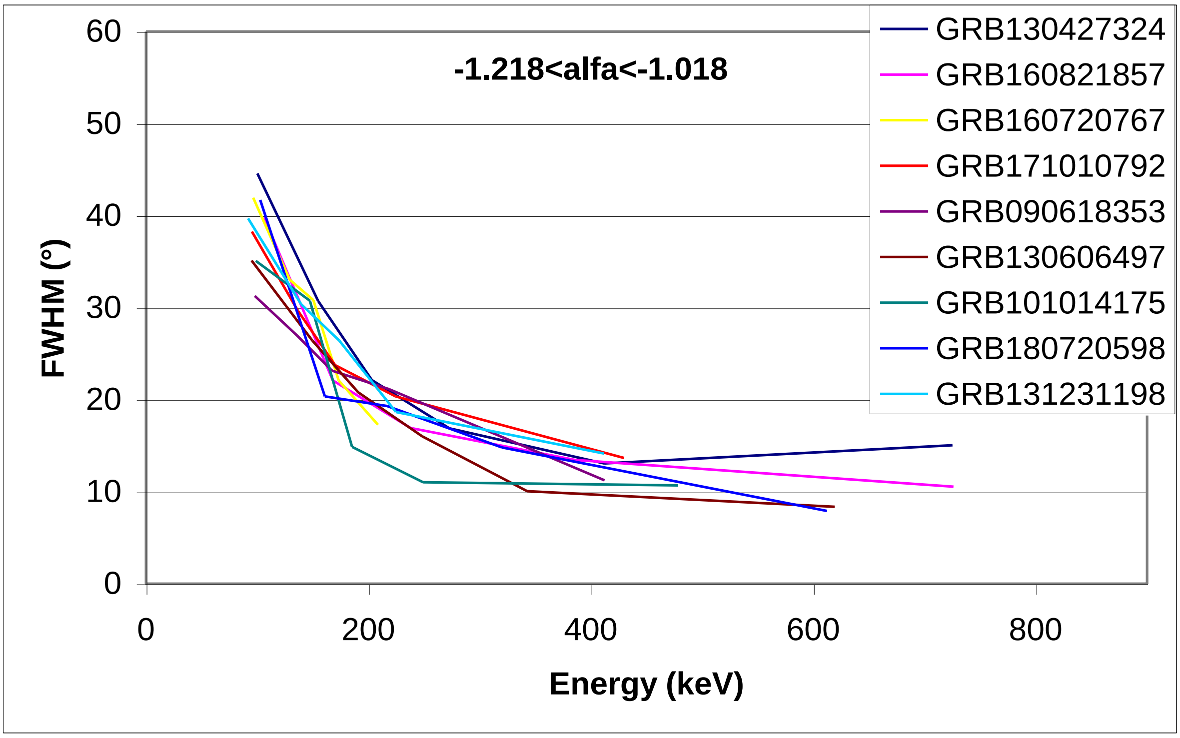

Figure 94: *Angular resolution for nine GRB with alfa between –1.218 and –1.018.*

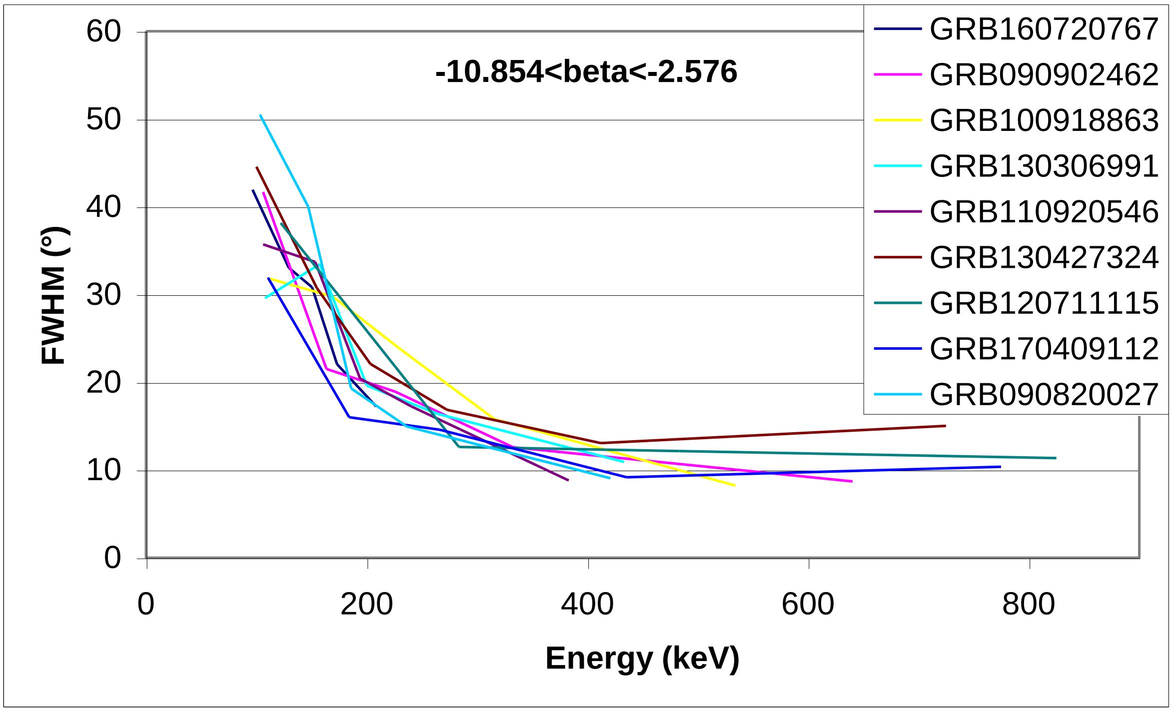

Figure 95: *Angular resolution for nine GRB with beta between –10.854 and –2.576.*

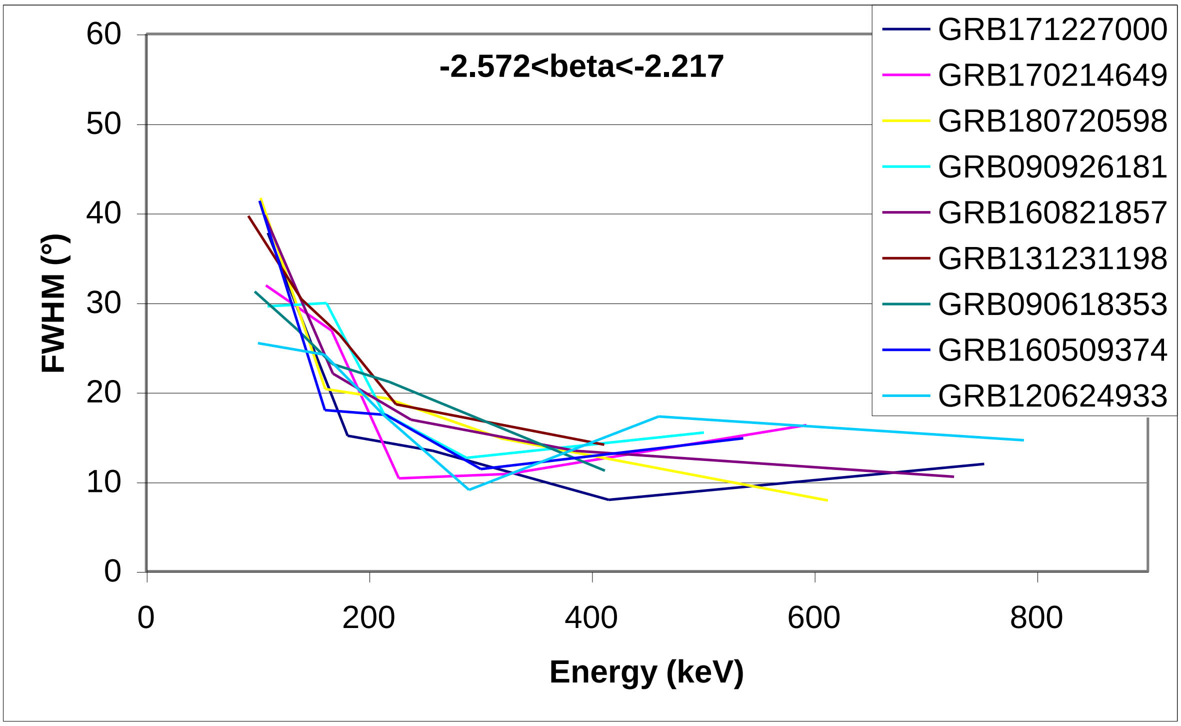

Figure 96: *Angular resolution for nine GRB with beta between –2.572 and –2.217.*

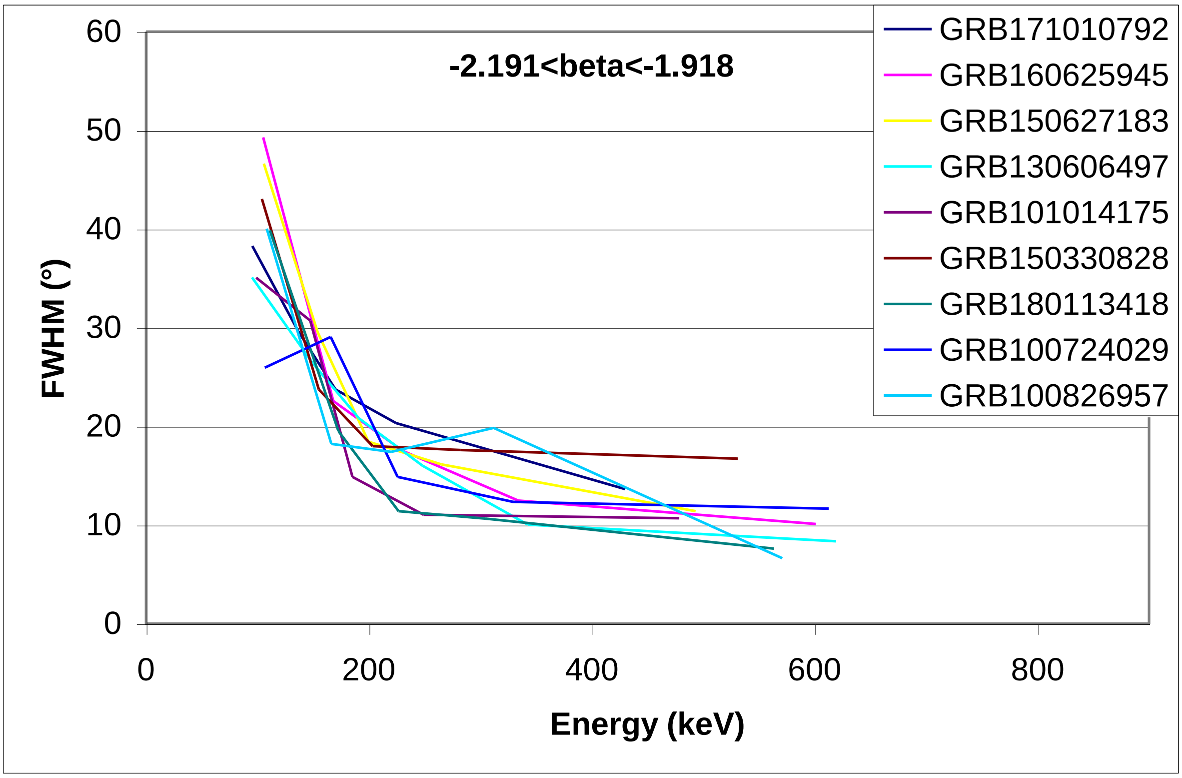

Figure 97: *Angular resolution for nine GRB with beta between –2.191 and –1.918.*

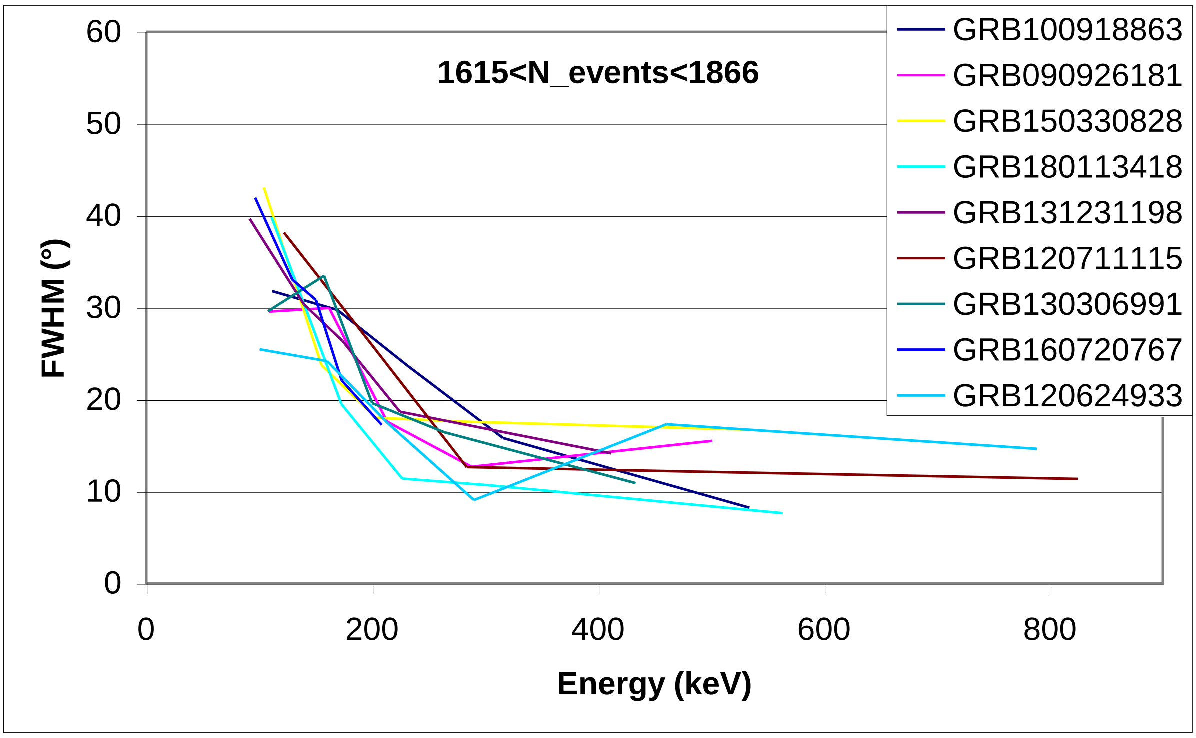

Figure 98: *Angular resolution for nine GRB with a number of events between 1615 and 1866.*

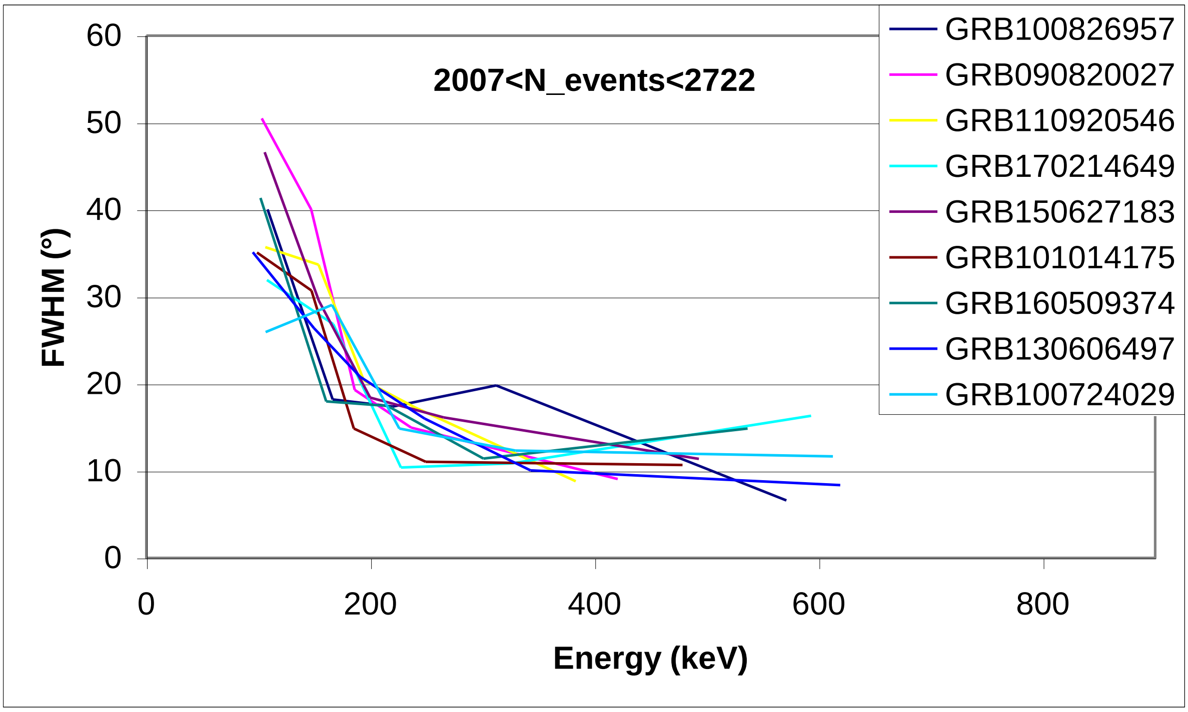

Figure 99: *Angular resolution for nine GRB with a number of events between 2007 and 2722.*

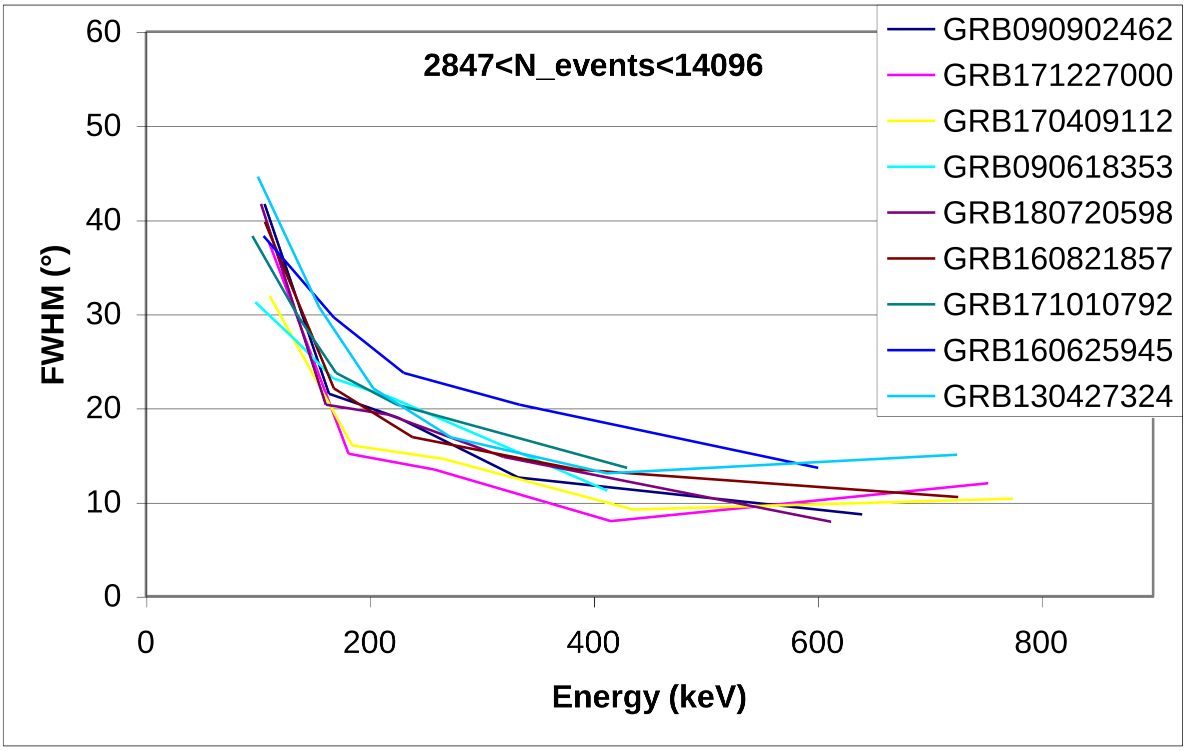

Figure 100: *Angular resolution for nine GRB with a number of events between 2847 and 14096.*

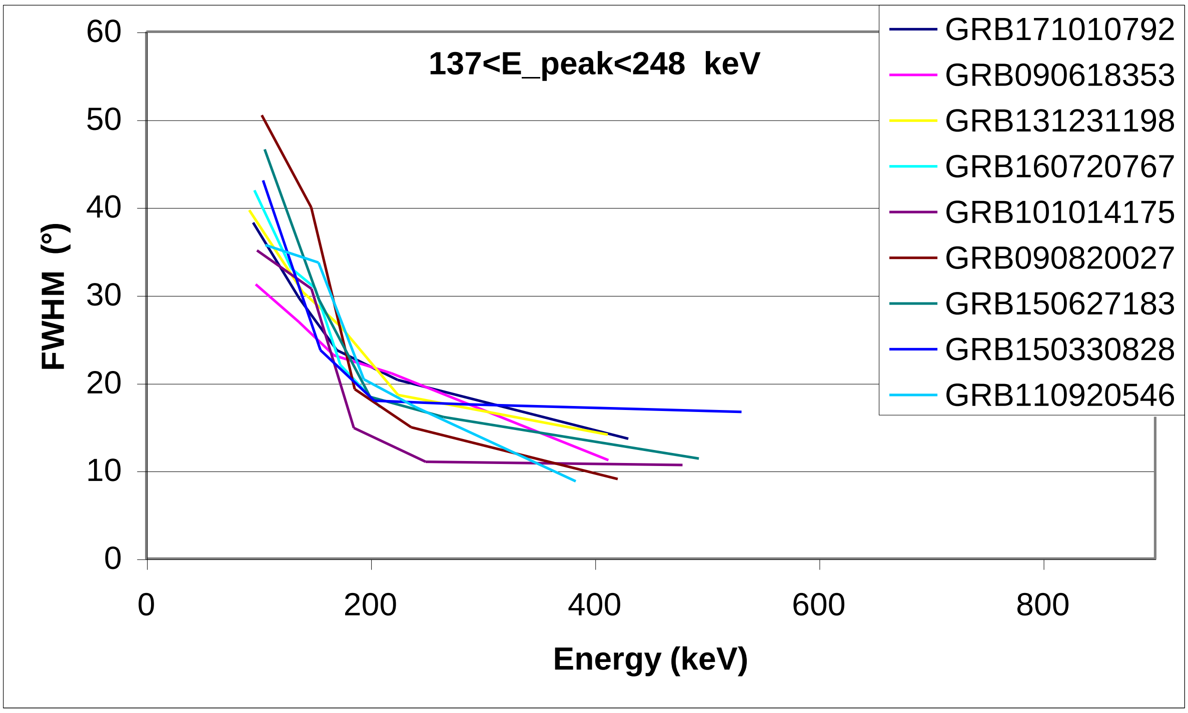

Figure 101: *Angular resolution for nine GRB with Epeak between 137 and 248 keV.*

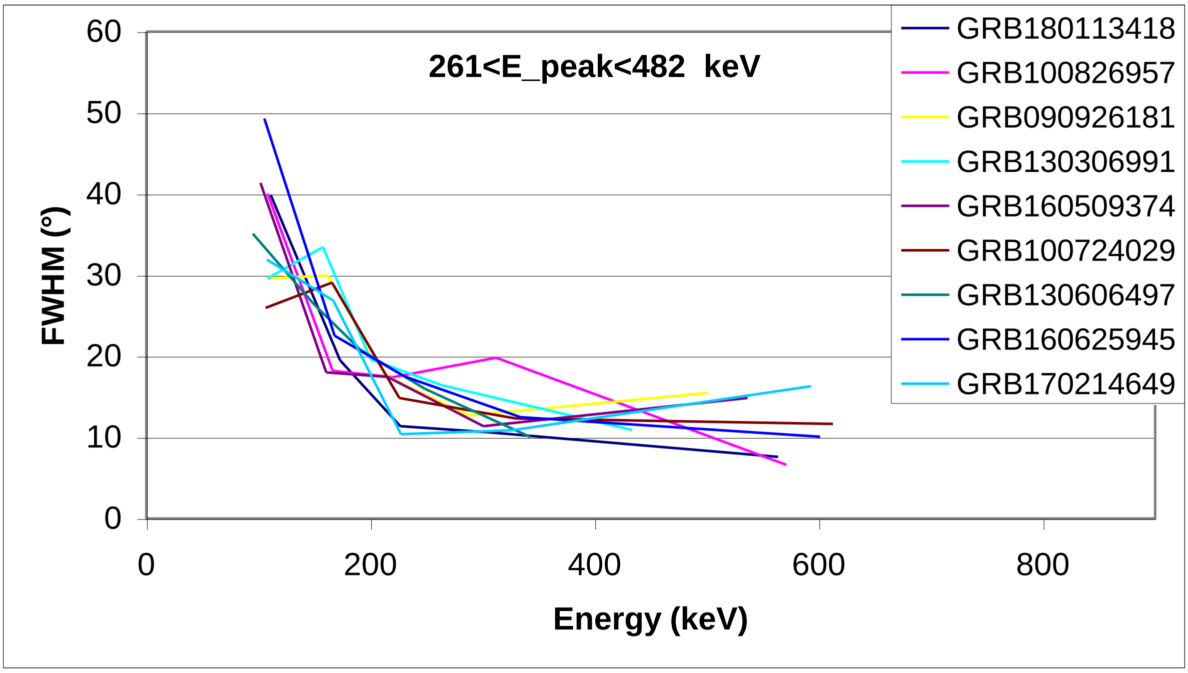

Figure 102: *Angular resolution for nine GRB with Epeak between 261 and 482 keV.*

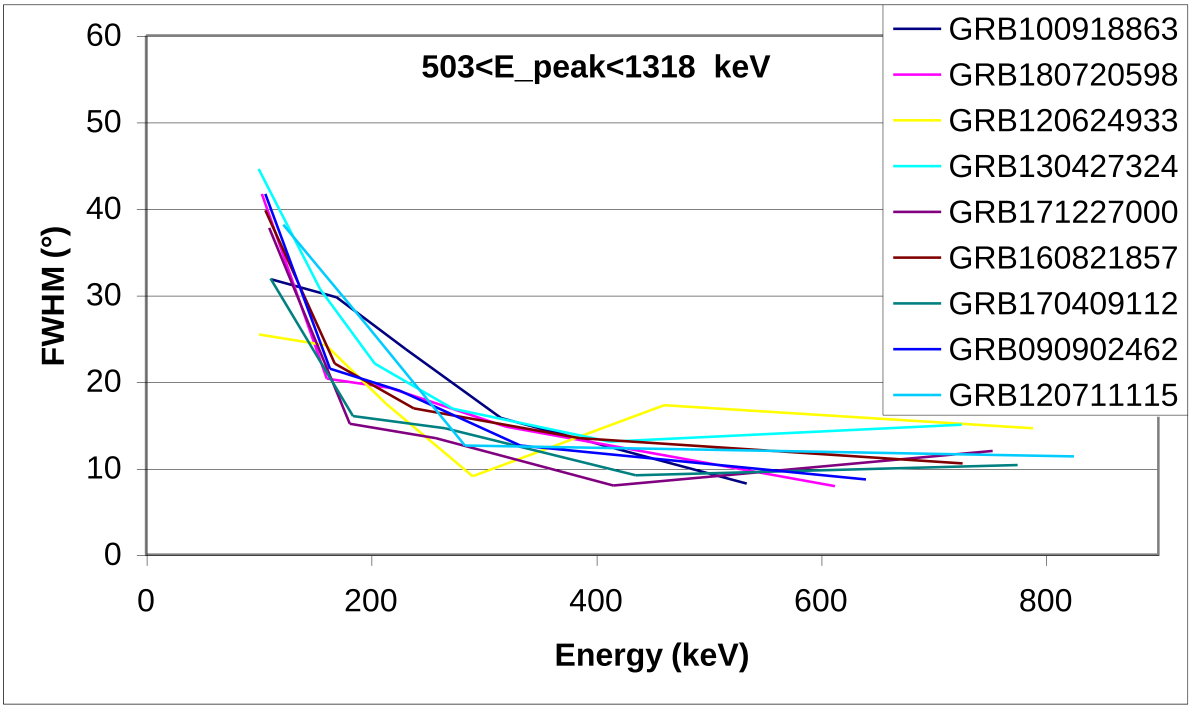

Figure 103: *Angular resolution for nine GRB with Epeak between 503 and 1318 keV.*

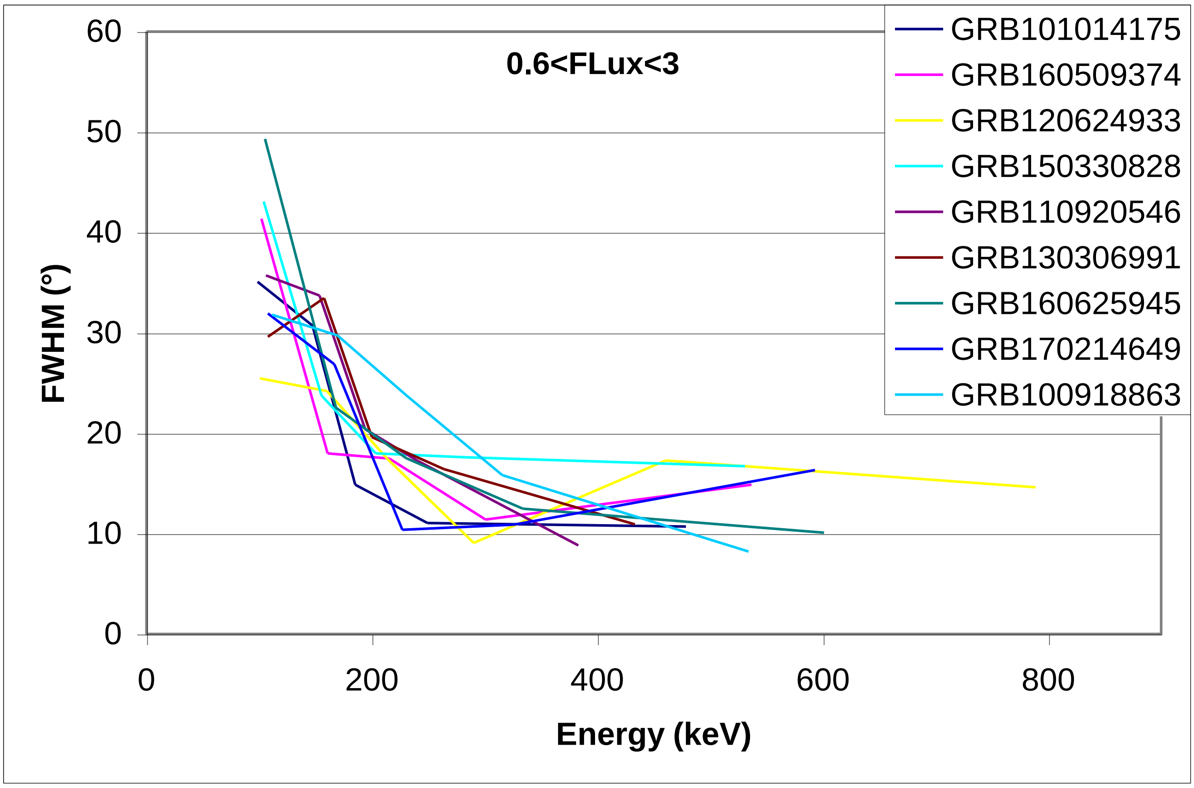

Figure 104: *Angular resolution for nine GRB with a flux between 0.6 and 3 photon/cm2/s.*

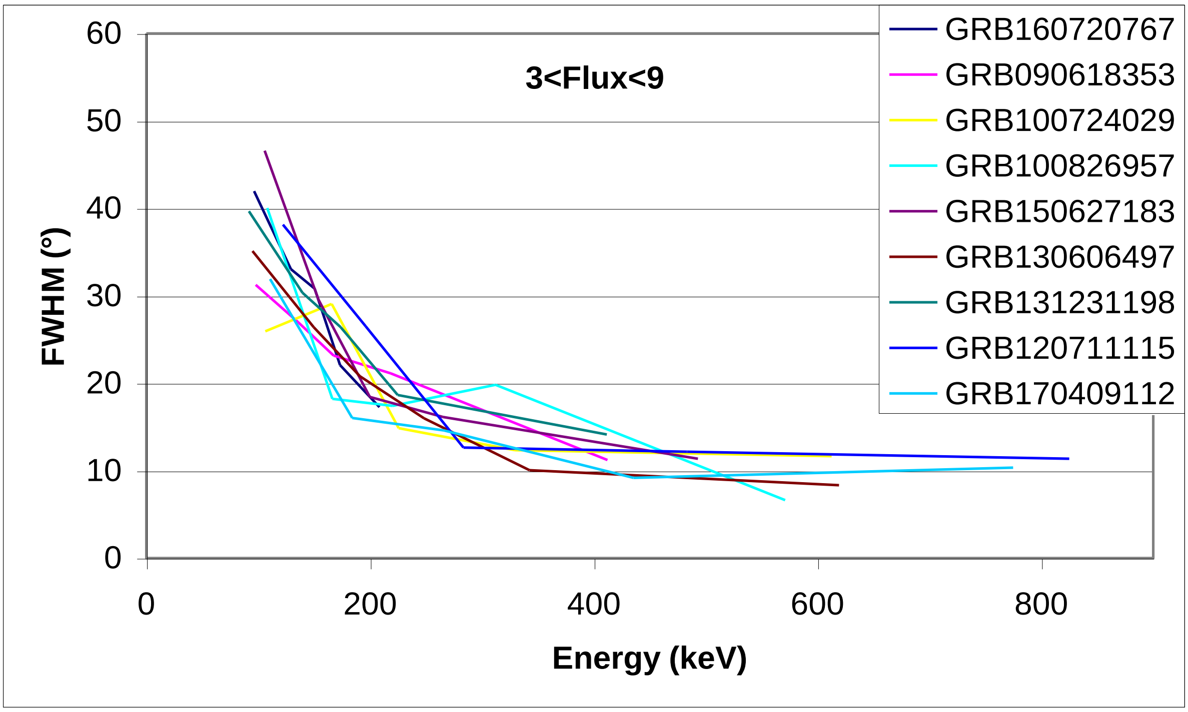

Figure 105: *Angular resolution for nine GRB with a flux between 3 and 9 photon/cm2/s.*

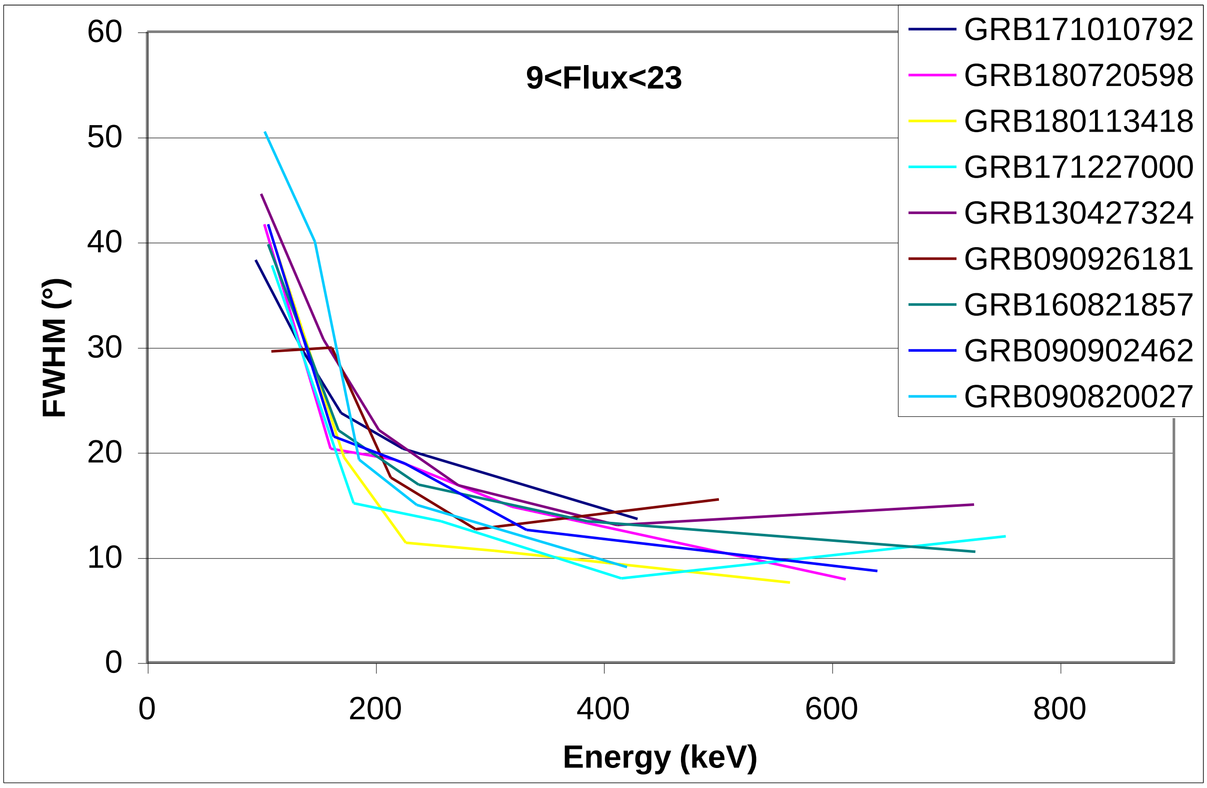

Figure 106: *Angular resolution for nine GRB with a flux between 9 and 23 photon/cm2/s.*

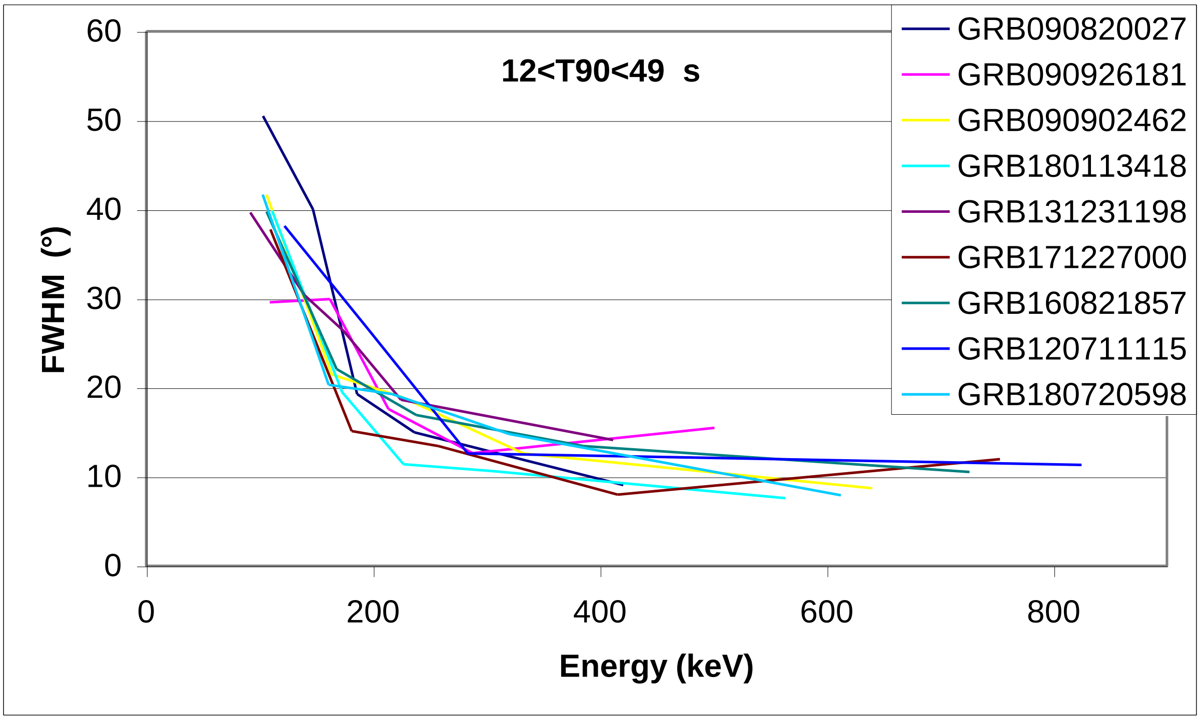

Figure 107: *Angular resolution for nine GRB with T_{90} between 12 and 49 s.*

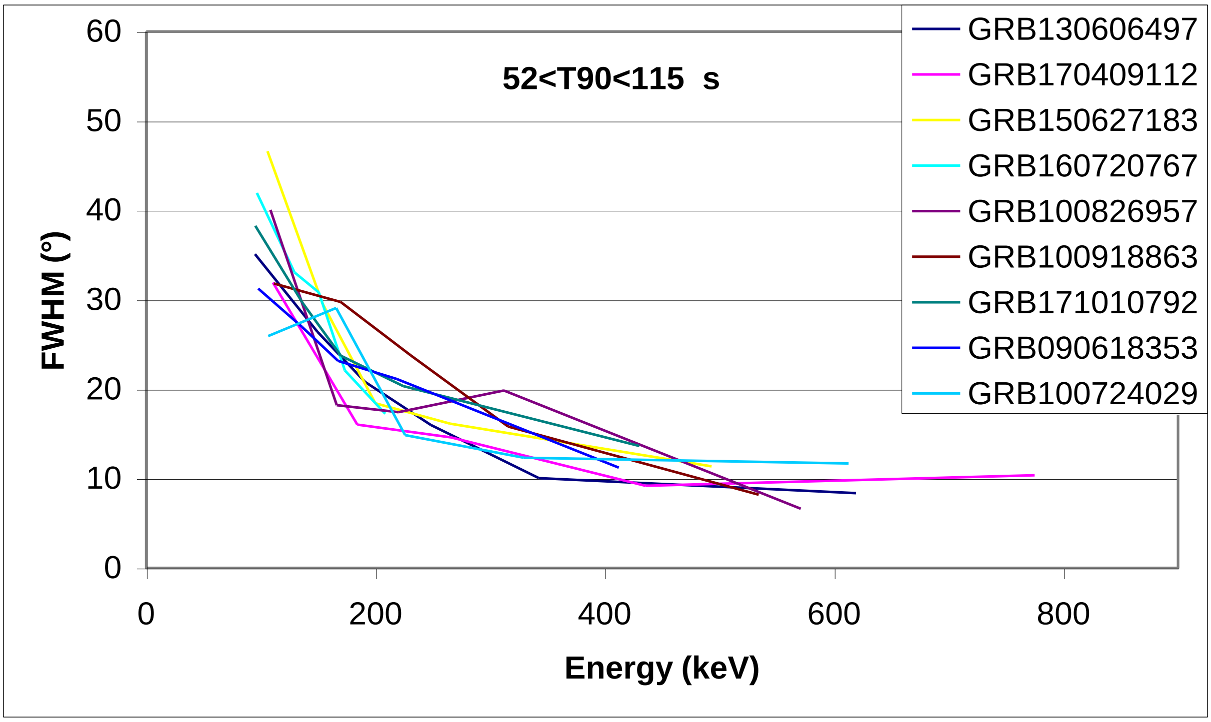

Figure 108: *Angular resolution for nine GRB with* T_{90} *between 52 and 115 s.*

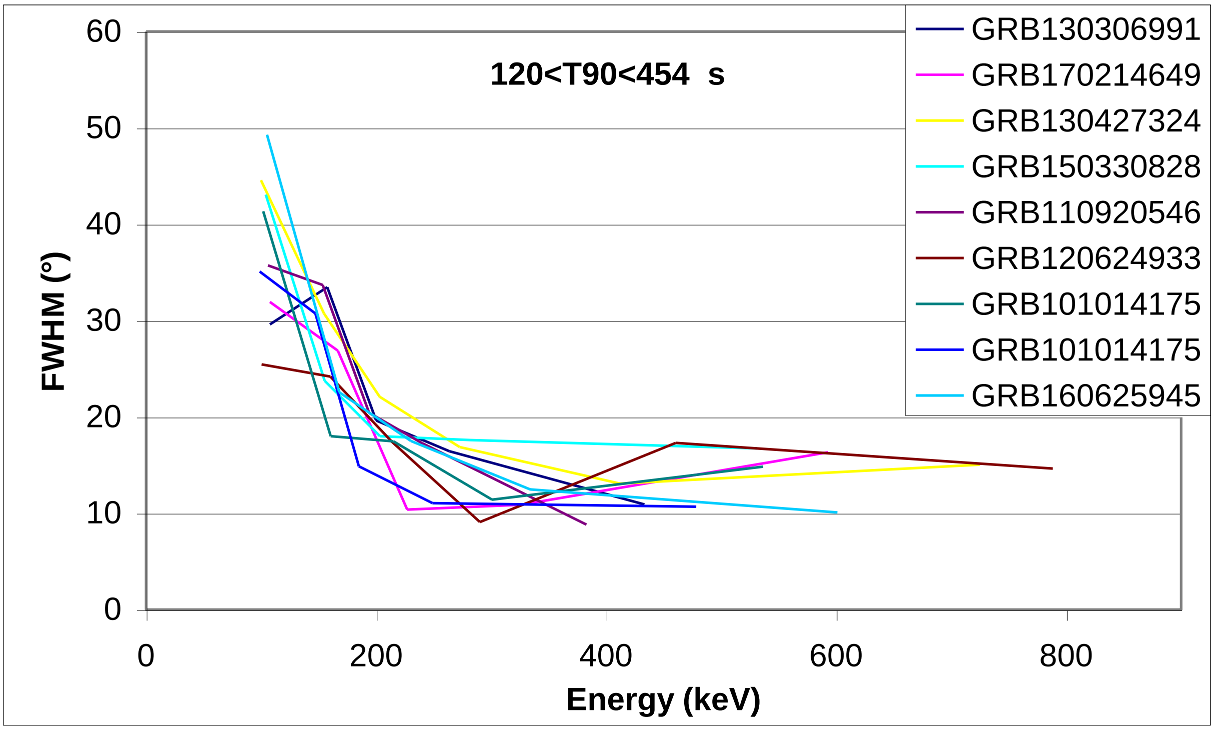

Figure 109: *Angular resolution for nine GRB with* T_{90} *between 120 and 454 s.*

-1.218<alfa<-1.018			
N. Total Events 41693			
Tot. ARM 20.65 FWHM (º)			
Energy (keV)	Events	<E> (keV)	FWHM (º)
126>E	7059	95.35	45.23
126<E<157	6868	141.1	34.82
157<E<197	6981	176.1	22.53
197<E<262	6918	226.2	16.02
262<E<427	6921	327.0	12.96
427<E	6946	952.2	11.60

-1.015<alfa<-0.904			
N. Total Events 23860			
Tot. ARM 16.02 FWHM (º)			
Energy (keV)	Events	<E> (keV)	FWHM (º)
133>E	3943	100.1	40.41
133<E<173	3959	152.6	25.75
173<E<222	3943	196.2	19.23
222<E<293	3970	254.6	17.30
293<E<456	3969	360.1	9.24
456<E	4076	1046	13.77

-0.875<alfa<-0.536			
N. Total Events 19868			
Tot. ARM 19.38 FWHM (º)			
Energy (keV)	Events	<E> (keV)	FWHM (º)
134>E	3333	102.2	38.36
134<E<175	3352	154.4	27.65
175<E<223	3345	198.0	18.92
223<E<292	3330	254.4	16.15
292<E<465	3311	358.6	13.96
465<E	3197	1073	14.99

Table 48: *The angular resolutions for the simulations with different intervals of alfa.*

-10.854<beta<-2.576			
N. Total Events 31191			
Tot. ARM 15.63 FWHM (°)			
Energy (keV)	Events	<E> (keV)	FWHM (°)
131>E	5149	100.1	43.88
131<E<169	5234	149.6	28.24
169<E<215	5171	190.6	19.40
215<E<287	5171	247.8	13.67
287<E<467	5216	359.5	9.22
467<E	5250	942.9	11.13

-2.572<beta<-2.217			
N. Total Events 24402			
Tot. ARM 20.65 FWHM (°)			
Energy (keV)	Events	<E> (keV)	FWHM (°)
130>E	4099	97.32	36.93
130<E<166	4064	147.3	30.92
166<E<213	4057	188.1	19.76
213<E<287	4085	246.6	16.47
287<E<478	4089	362.5	13.40
478<E	4008	1096	11.10

-2.191<beta<-1.918			
N. Total Events 29828			
Tot. ARM 16.02 FWHM (°)			
Energy (keV)	Events	<E> (keV)	FWHM (°)
127>E	5011	96.2	40.59
127<E<161	5001	143.5	30.90
161<E<202	4965	180.3	21.99
202<E<264	4998	230.4	17.90
264<E<400	4968	319.1	14.86
400<E	4885	1005	14.38

Table 49: *The angular resolutions for the simulations with different intervals of beta.*

1615<Events<1866			
N. Total Events 15954			
Tot. ARM 20.65 FWHM (°)			
Energy (keV)	Events	<E> (keV)	FWHM (°)
129>E	2634	98.97	45.24
129<E<162	2675	145.5	30.81
162<E<200	2668	180.3	20.95
200<E<261	2642	227.7	17.60
261<E<394	2680	314.5	15.50
394<E	2655	951.1	10.18

2007<Events<2722			
N. Total Events 19542			
Tot. ARM 19.89 FWHM (°)			
Energy (keV)	Events	<E> (keV)	FWHM (°)
130>E	3307	99.23	36.03
130<E<165	3216	147.4	29.57
165<E<206	3244	184.6	22.69
206<E<264	3259	232.5	15.28
264<E<385	3279	314.2	13.94
385<E	3237	934.6	11.09

2847<Events<14096			
N. Total Events 49925			
Tot. ARM 16.75 FWHM (°)			
Energy (keV)	Events	<E> (keV)	FWHM (°)
129>E	8349	97.14	40.59
129<E<166	8286	146.8	30.92
166<E<215	8310	188.7	22.70
215<E<291	8314	249.1	17.09
291<E<486	8325	369.5	11.04
486<E	8341	1045	11.27

Table 50: *The angular resolutions for the simulations with different intervals of number of events.*

137<E_peak<248			
N. Total Events 24220			
Tot. ARM 20.65 FWHM (°)			
Energy (keV)	Events	<E> (keV)	FWHM (°)
121>E	4071	93.74	45.20
121<E<147	4127	133.7	34.94
147<E<177	4103	161.4	25.03
177<E<218	4058	196.2	19.01
217<E<303	4038	253.4	18.53
303<E	3823	684.0	13.97

261<E_peak<482			
N. Total Events 24168			
Tot. ARM 16.02 FWHM (°)			
Energy (keV)	Events	<E> (keV)	FWHM (°)
134>E	4089	100.4	40.10
134<E<174	4046	153.7	27.46
174<E<222	4026	196.8	19.38
222<E<292	4074	254.0	15.60
292<E<446	4072	353.7	10.48
446<E	3861	1079	15.21

503<E_peak<1318			
N. Total Events 37033			
Tot. ARM 15.82 FWHM (°)			
Energy (keV)	Events	<E> (keV)	FWHM (°)
135>E	6150	100.8	43.88
135<E<178	6189	156.3	28.78
178<E<238	6194	206.6	22.09
238<E<329	6119	278.0	15.54
329<E<560	6176	423.9	10.55
560<E	6205	1143	11.77

Table 51: *The angularresolutions for the simulations with different intervals of* E_{peak}.

0.6<Flux<3			
N. Total Events 22842			
Tot. ARM 16.02 FWHM (°)			
Energy (keV)	Events	<E> (keV)	FWHM (°)
132>E	3855	99.63	40.79
132<E<170	3816	151.0	29.71
170<E<217	3861	192.2	19.28
217<E<282	3813	246.8	15.36
282<E<428	3834	341.4	9.06
428<E	3663	997.6	13.65

3<Flux<9			
N. Total Events 20957			
Tot. ARM 20.65 FWHM (°)			
Energy (keV)	Events	<E> (keV)	FWHM (°)
127>E	3483	97.18	41.29
127<E<159	3498	142.4	31.22
159<E<198	3481	177.7	21.04
198<E<261	3475	226.1	15.36
261<E<410	3420	320.3	15.26
410<E	3600	1031	10.50

9<Flux<23			
N. Total Events 41622			
Tot. ARM 15.63 FWHM (°)			
Energy (keV)	Events	<E> (keV)	FWHM (°)
129>E	6885	97.23	44.04
129<E<165	6906	146.4	27.43
165<E<212	6956	187.2	22.79
212<E<285	6958	245.1	16.61
285<E<469	6930	358.4	10.07
469<E	6987	994.7	11.62

Table 52: *The angular resolutions for the simulations with different intervals of flux.*

12<T90<49			
N. Total Events 23622			
Tot. ARM 16.4 FWHM (°)			
Energy (keV)	Events	<E> (keV)	FWHM (°)
133>E	3964	100.0	40.55
133<E<172	3968	151.9	27.00
172<E<222	3953	195.7	22.33
222<E<298	3937	256.1	17.47
298<E<508	3953	380.0	14.18
508<E	3847	1110	11.08

52<T90<115			
N. Total Events 26476			
Tot. ARM 16.40 FWHM (°)			
Energy (keV)	Events	<E> (keV)	FWHM (°)
124>E	4464	95.67	43.55
124<E<153	4392	138.3	33.08
153<E<190	4487	170.8	21.98
190<E<246	4404	215.0	15.10
246<E<377	4444	299.7	12.96
377<E	4285	916.3	11.08

120<T90<454			
N. Total Events 35323			
Tot. ARM 16.42 FWHM (°)			
Energy (keV)	Events	<E> (keV)	FWHM (°)
132>E	5858	98.91	40.59
132<E<171	5839	151.2	32.22
171<E<220	5882	194.0	22.69
220<E<291	5893	252.4	15.85
291<E<458	5873	359.7	9.58
458<E	5978	1006	11.27

Table 53: *The angular resolutions for the simulations with different intervals of* T_{90}.

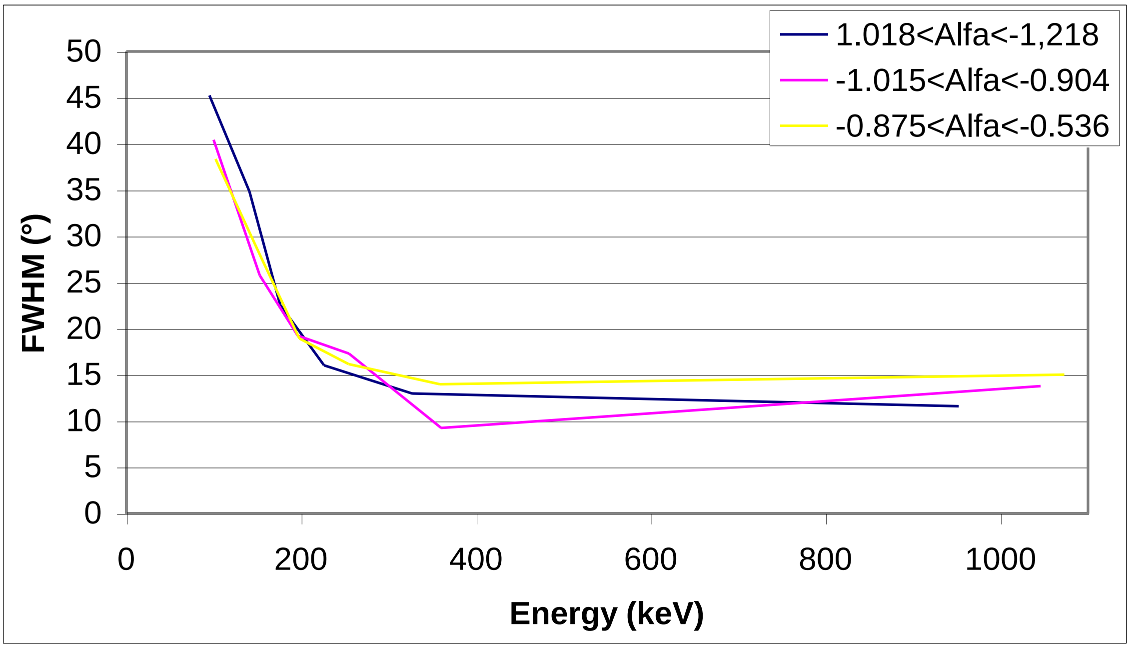

Figure 110: *Comparison of the angular resolutions for the simulations with different intervals of alfa.*

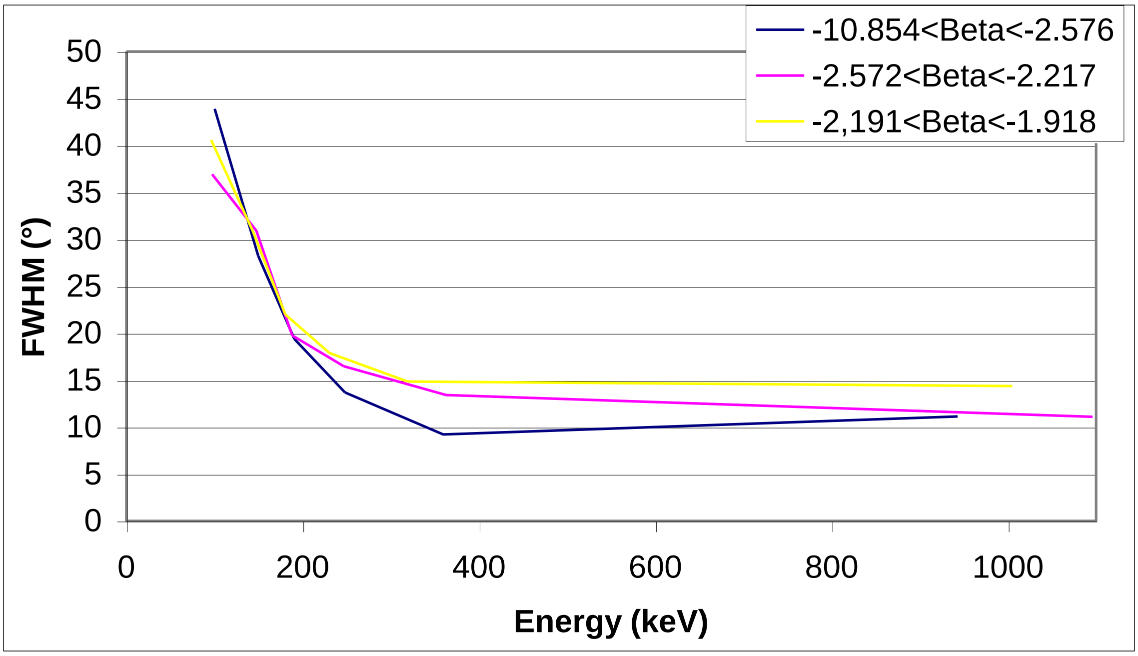

Figure 111: *Comparison of the angular resolutions for the simulations with different intervals of beta.*

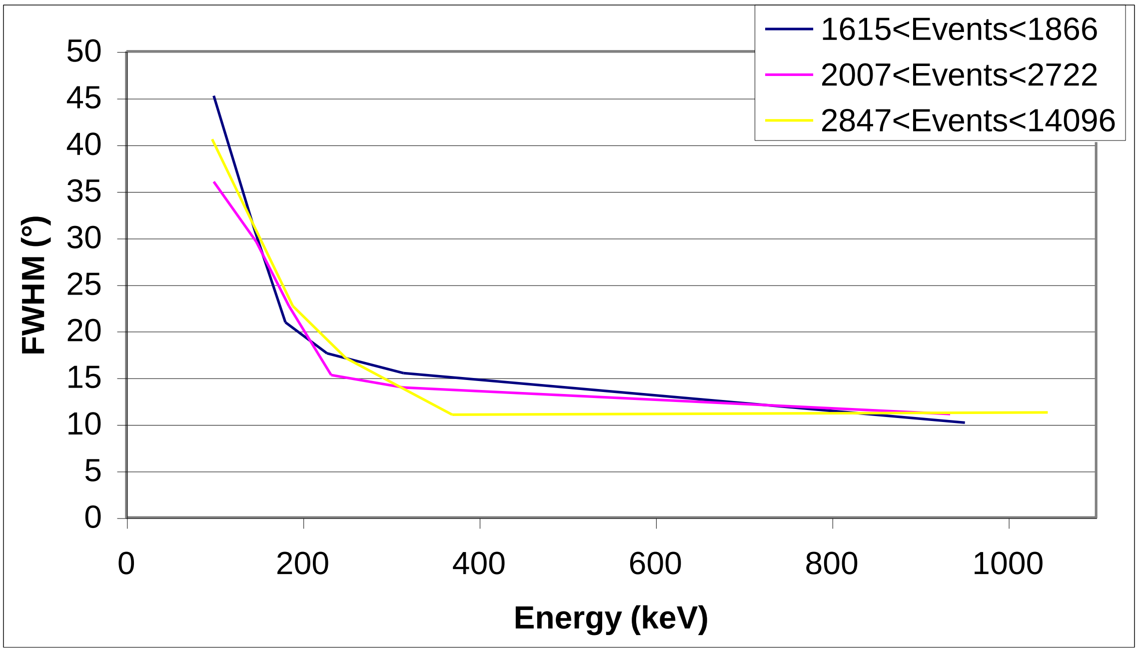

Figure 112: *Comparison of the angular resolutions for the simulations with different intervals of number of events.*

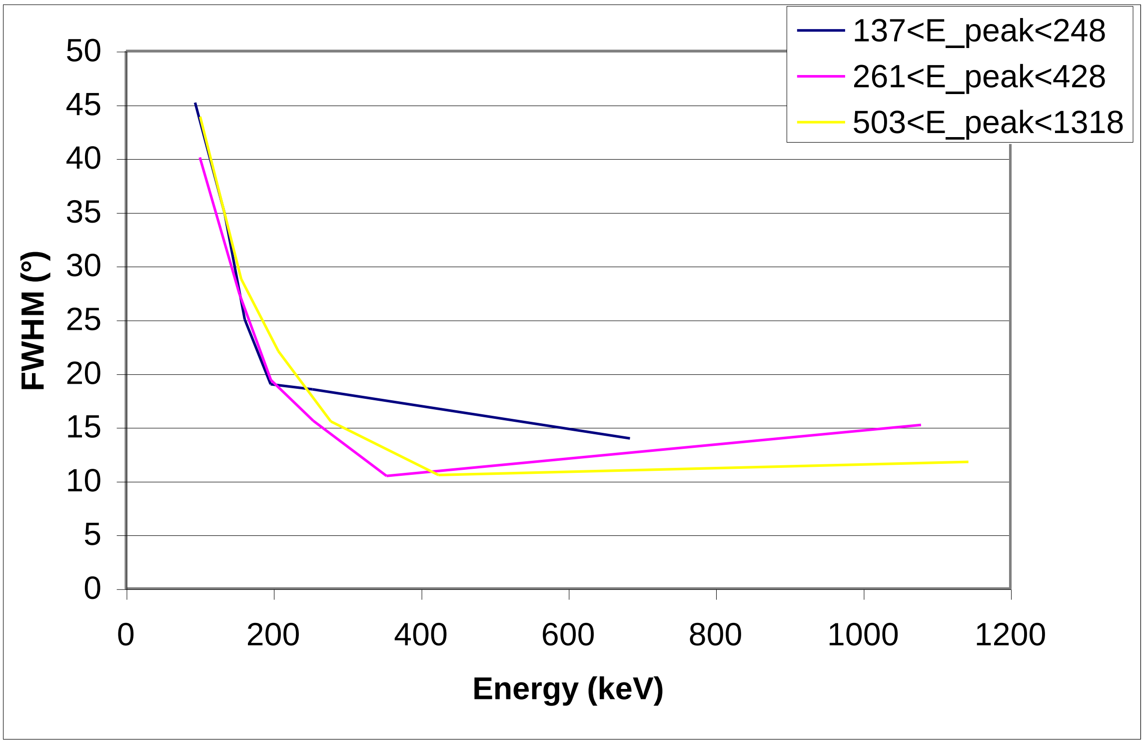

Figure 113: *Comparison of the angular resolutions for the simulations with different intervals of* E_{peak}.

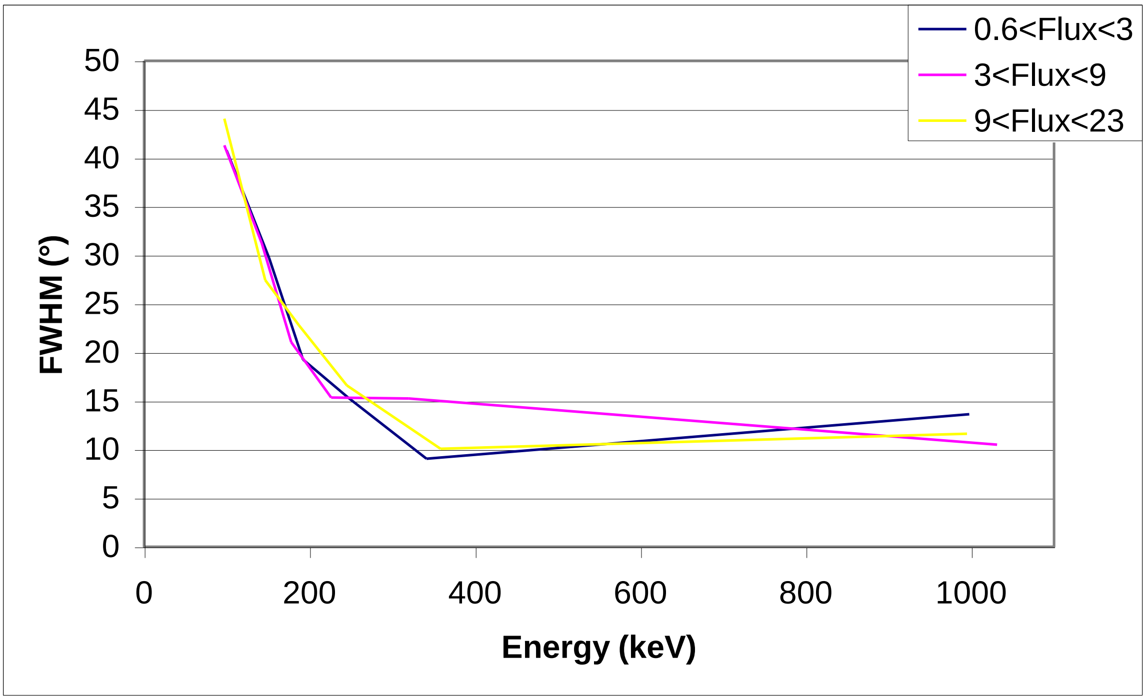

Figure 114: *Comparison of the angular resolutions for the simulations with different intervals of flux.*

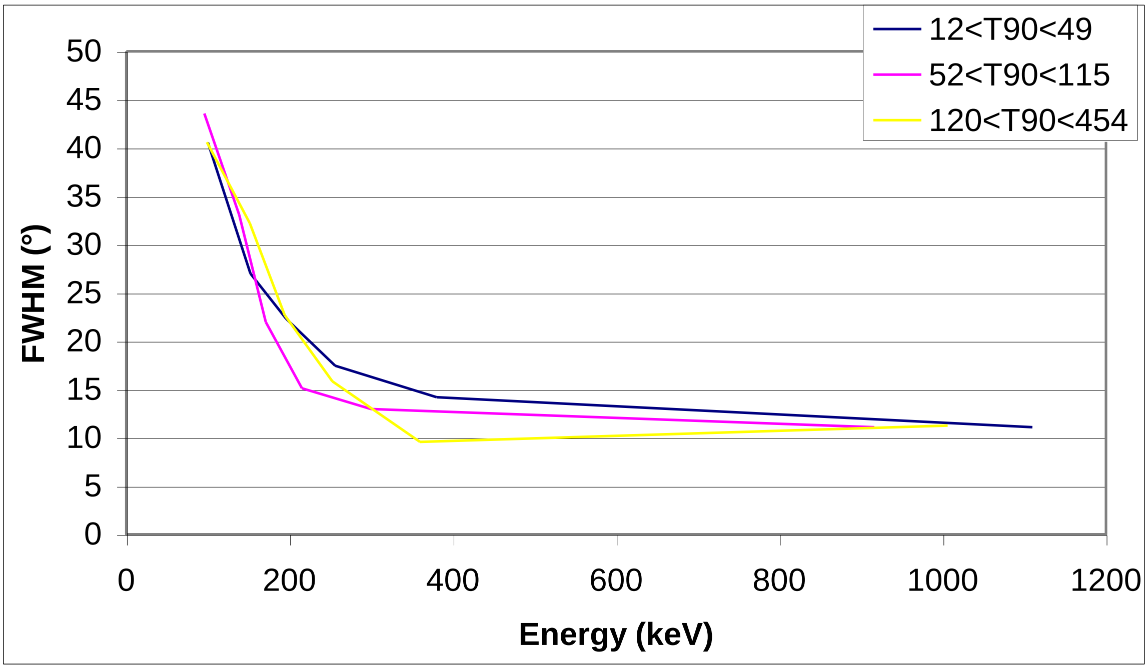

Figure 115: *Comparison of the angular resolutions for the simulations with different intervals of* T_{90}.

Conclusions

The observational gap roughly covering the range of COMPTEL has been lacking measurements since the deorbiting of CGRO in the year 2000. As it will take around one decade before having another mission (~ 1 m^3 / 1 ton payload) ready, we propose a much smaller detector to be loaded onto a small cubesat (6U). This new mission, that can be ready in around 18 months and with a total expenditure of around 500,000 €. Measuring in a low equatorial orbit fluxes of particles at energies around the MeV and, in particular, electrons and gamma-rays, could be exploited for three main reasons:

1) as a pathfinder for next-generation proposed MeV-GeV gamma-ray observatories (ESA e-Astrogam or NASA AMEGO).

2) To observe and detect GRBs and flaring AGN at energies currently not observable by other satellites or ground-based detectors (despite with low sensitivity).

3) To provide the first map of the ionizing radiation around the Earth, of the utmost importance for the first human travelers and settlers going to Mars, by providing a detailed analysis of the dosimetry (the amount of absorbed dose accumulated in tissues resulting from exposure to ionizing radiation) that can be used to evaluate the risk of developing cancer during the flight to and the permanence on Mars.

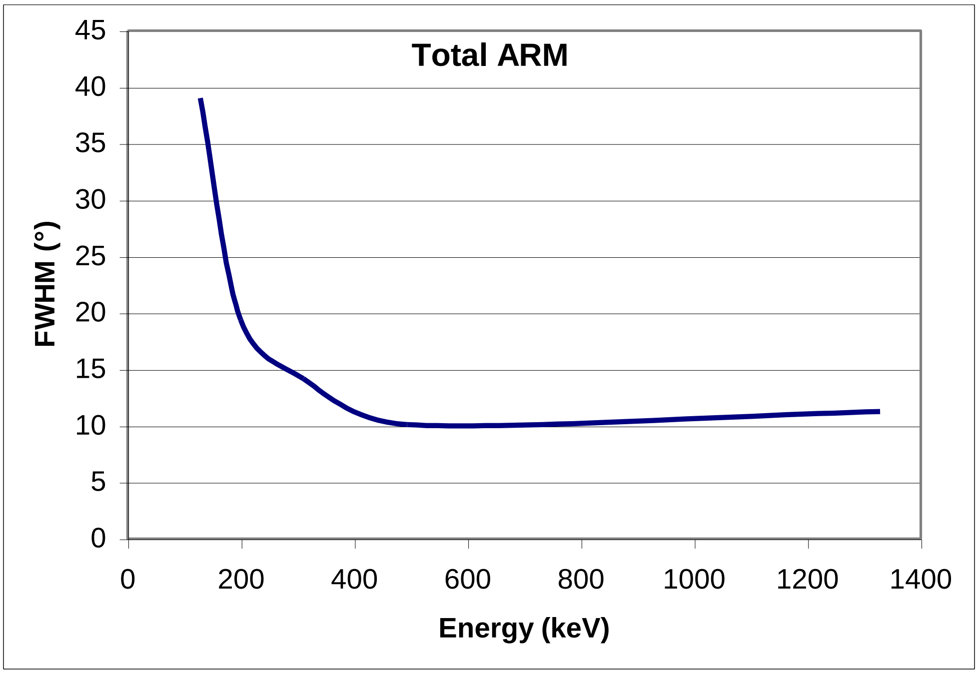

Figure 116: *Total angular resolution measure for 27 GRB.*

Whereas the technology to build it is quite safe and well tested, working at lower energies needs some new “software” technologies and algorithms for the data analysis. In particular, we found that reconstructing pair-production events is unsatisfactory, so we focused more on Compton regime. We plan to use GRB events (with highest purity, as the filtering will be done mainly by external time constraints) as calibrators, and in this concern we subdivided the energy and angular resolution estimations by grouping GRBs and classify them according to their duration and to the Band function parameters, following the same recipe used for Fermi LAT when migrating from Pass7 to Pass8.

Whereas the detailed analysis of the energy and angular resolution estimated by using GRB could be found in the last chapter, we conclude here with the overall behaviour of the energy and angular resolutions, as can be seen in figures 116 and 117.

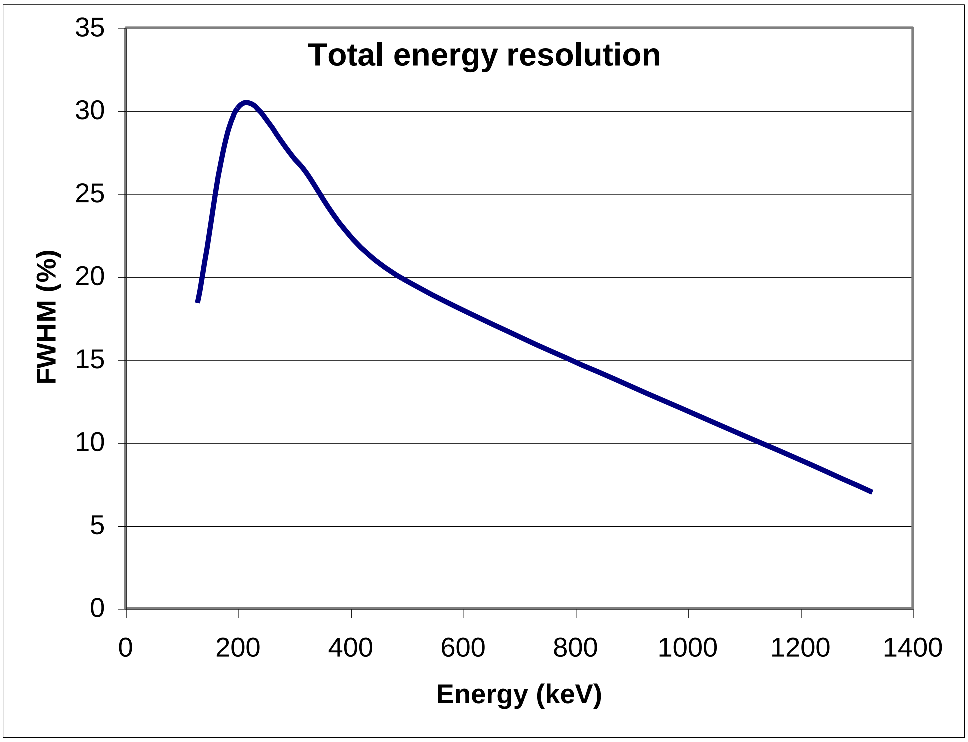

Figure 117: *Total Energy Resolution for27 GRBs.*

Bibliography

2014 CODATA recommended values.

Aartsen M.G. et al. (IceCube collaboration), 2016, ApJ, 824, 115.

Aartsen M.G. et al. (IceCube collaboration), 2017, Astropart. Phys., 92, 30-41.

Abadi, M., Barham, P., Chen, J., et al.: TensorFlow: a system for large-scale machine learning. 12th USENIX Symposium on Operating Systems Design and Implementation, volume 16, 265-283 (2016).

Abbasi R. et al. (IceCube collaboration), 2009, Nucl. Instrum. Meth. A, 601, 294.

Abbott B. P. et al. (LVC) 2016a, Physical Review Letters, 116, 061102.

Abbott B. P. et al. (LVC) 2016b, Physical Review Letters, 116, 241103.

Abbott B. P. et al. (LVC) 2017, Physical Review Letters, 118, 221101.

Abbott B. P. et al. (LVC), 2016c, Living Reviews in Relativity, 19, 1.

Abbott, B. P., Abbott, R., Abbott, T. D., et al. 2017, ApJL, 848, L12.

Abdalla H. and others, 2016, Phys. Rev. Lett., 117, 151302.

Abdo A.A. et al. (Fermi LAT Coll.), Science 325 (2009) 840.

Abdo A.A., et al. (Fermi-LAT collaboration) 2009b, ApJ, 707, L142.

Abdo, A. A. LAT: Fermi Large Area Telescope Observations of Markarian 421: The Missing Piece of its Spectral Energy Distribution.

Abdo, A. A., Ackermann, M., Ajello, M., et al. 2011a, ApJ, 727, 129.

Abdo, A. A., Ackermann, M., Ajello, M., et al. 2011b, ApJ, 736, 131.

Abdo, A. A., Ackermann, M., Ajello, M., et al. 2015, ApJ, 799, 143.

Abdo, A. A., et al. (Fermi-LAT collaboration) 2009a, ApJ, 699, 976.

Abdo, A.A. et al. 2009 Sci, 325, 845.

Abdo, A.A. et al. 2010 A&A 524, A75.

Accardo, L. et al. 2014, Phys. Rev. Letters, 113, 121101.

Acciari, V. A., Arlen, T., Aune, T., et al. 2011, ApJ, 729, 2.

Acero, F., Ackermann, M., Ajello, M., et al. 2016, ApJS, 223, 26.

Acero, F., Ackermann, M., Ajello, M., et al. 2016, ApJS, 223, 26.

Acharya, B. S., Actis, M., Aghajani, T., et al. 2013, APh, 43, 3.

Ackerman M., et al., 2015, ApJ, 810, 14.

Ackermann et al. 2015, APJ L, 813 (2), L 41.

Ackermann M. and others, 2015, Phys. Rev., D91, 122002.

Ackermann M. et al. [Fermi-LAT Collaboration], Astrophys. J. 793, no. 1, 64 (2014).

Ackermann M. et al., Science 334, 1103 (2011).

Ackermann, M., Ajello, M., Albert, A., et al. 2014, ApJ, 787, 18.

Ackermann, M., Ajello, M., Allafort, A. et al. 2013, Science, 339, 807-811 (A13).

Ackermann, M., Ajello, M., Allafort, A., et al. 2011, Science, 334, 1103.

Ackermann, M., Ajello, M., Allafort, A., et al. 2012a, ApJ, 755, 22.

Ackermann, M., Ajello, M., Allafort, A., et al. 2013, ApJ, 765, 54.

Ackermann, M., Ajello, M., Atwood, W. B., et al. 2012b, ApJ, 750, 3.

Ackermann, M., Ajello, M., Baldini, L., et al. 2011, ApJ, 726, 81.

Ackermann, M., Ajello, M., Baldini, L., et al. 2012, ApJ, 754, 121.

Ackermann, M., Ajello, M., Baldini, L., et al. 2017, ApJ Lett, 837, L5.

Ackermann, M., Albert, A., Atwood, W. B., et al. 2014, ApJ, 793, 64.

Ackermann, M., et al. 2015, ApJ, 799, 86.

Ageron M. et al. (ANTARES collaboration), 2011, Nucl. Instrum. Meth. A, 656, 11-38.

Ageron M. et al. (ANTARES collaboration), 2012, Astropart. Phys., 35, 530-536.

Aharonian F., et al. A&A, 475:L9{L13, 2007.

Ahlers M., Halzen F., 2015, Rep. Prog. Phys., 78, 126901.

Ahn, K., & Komatsu, E. 2005, Phys. Rev. D, 72, 061301.

Ahnen, M. L., Ansoldi, S., Antonelli, L. A., et al. 2016, A&A, 595, A98.

Ajello M., Costamante L., Sambruna R.M. et al., 2009, ApJ, 699, 603.

Ajello, M., Albert, A., Atwood, W. B., et al. 2016, ApJ, 819, 44.

Ajello, M., Costamante, L., Sambruna, R. M., et al. 2009, ApJ, 699, 603.

Ajello, M., Ghisellini, G., Paliya, V. S., et al., 2016, Astrophysical Journal, 826, 76.

Albert A. et al. (ANTARES Collaboration), 2017, JCAP, 04, 019.

Aleksić J. et al., 2014, JCAP, 1402, 008.

Anderhub et al. 2013, JINST, 8, P06008.

Andritschke, R., Zoglauer, A., Kanbach, G., et al.: The Compton and pair creation telescope MEGA. Experimental Astronomy 20(1-3), 395-403 (2005)

Antoja T., et al., Mon.Not.Roy.Astron.Soc., 453(2015)541560 [arXiv:1507.04353].

Atwood, W., Abdo, A.A., Ackermann, M., et al.: The large area telescope on the Fermi gamma-ray space telescope mission. The Astrophysical Journal 697(2), 1071 (2009).

Balbo, M. and Walter, R., ArXiv e-prints (2017).

Bambi C. and Dolgov A. D., NPB 784, 132 (2007).

Band, D., Matteson, J., Ford, L., et al. 1993, ApJ, 413, 281

Barkov, M. V., & Bosch-Ramon, V. 2014, A&A, 565, A65.

Barnacka, A., Geller, M. J., Dell'Antonio, I. P., & Benbow, W. 2015, ApJ, 809, 100.

Barnes J. et al. 2016, ApJ, 829, 110.

Bayer A. et al., Science 358 (2017) 79.

Bednarek, W., Sitarek, J. 2007 MNRAS 377, 920.

Begelmann, Blandford and Rees 1980, Reviews of modern Physics, 11, 288-291.

Beloborodov A. M., 2011, ApJ, 737, 68.

Beloborodov A. M., Hascoët R. and Vurm I., 2014, ApJ, 788, 36.

Beloborodov A.M., 2013, ApJ, 762, 13.

Benett G. W. et al. (The g-2 Collaboration), Phys. Rev. D73 (2006) 072003.

Benhabiles-Mezhoud,H.,Kiener,J.,Tatische, V., & Strong, A. W. 2013, ApJ, 763, 98. Erratum: ApJ, 766, 139.

Berger E. 2014, Annual Review of Astronomy and Astrophysics, 43, 52.

Bergstrom L. (2012), Annalen der Physik, vol 524 issue 9-10, pp479-496.

Berlato, F.: Design and optimization around 1 MeV of a calorimeter for a Cubesat mission. Master's thesis, Università degli Studi di Padova (2016).

Berton, M., Foschini, L., Caccianiga, A., et al., 2015, Proceedings of "The many facets of extragalactic radio surveys: towards new scientific challenges", arXiv:1601.05791.

Bertone G. (ed.) Particle Dark Matter. Cambridge University Press. Cambridge (2010).

Bertone G., Hooper D., and Silk J., Particle dark matter: Evidence, candidates and constraints, Phys.Rept. 405 (2005) 279-390, [hep-ph/0404175].

Bertoni B., Hooper D., andLinden T., Is The Gamma-Ray Source 3FGL J2212.5+0703 A Dark Matter Subhalo?, JCAP 1605 (2016) 049, [arXiv:1602.07303].

Bertram, E., et al.,. 2016, MNRAS, 455, 3763.

Bertram, E., et al.,. 2016, MNRAS, 455, 3763.

Beuhler, R. & Blandford, R. 2014, Rep. Prog. Phys., 77, 066901.

Binns, W. R., et al. APS April Meeting, abstract M4.009 (2017).

Blandford R.D. & Znajek R.L., 1977, MNRAS, 179, 433.

Blandford, R., & Eichler, D. 1987, Phys. Rep., 154, 1.

Blinnikov S. I., Dolgov A. D.and Postnov K. A., PRD 92, 023516 (2015).

Blinnikov S., Dolgov A., Porayko N. K. and Postnov K., JCAP 1611, 036 (2016).

Bloom, S. D. and Marscher, A. P., 1996, ApJ, 461, 657.

Bloser, P. F., Hunter, S. D., Ryan, J. M., et al. 2004, NewAR, 48, 299.

Boddy K. K. and Kumar J., Phys. Rev. D92 (2015) 023533, [1504.04024].

Boehm C. and Fayet P., 2004, Nucl. Phys., B683, 219-263.

Boggs S.E. et al., "Performance of the Nuclear Compton Telescope", Experimental Astronomy, vol. 20, no. 1-3, pp. 387-394, 2005.

Boggs S.E., "The Advanced Compton Telescope mission", New Astronomy Reviews, vol. 50, no. 7-8, pp. 604-607, 2006.

Boroson, T. A. 2002, ApJ, 565, 78.

Bosch-Ramon, V., Khangulyan, D., 2009, IJMPD, 18, 347.

Böttcher M., Reimer A., Sweeney K., and Prakash A. .ApJ, 768:54, 2013.

Breiman L. (2001). "Random Forests". Machine Learning. 45 (1): 5–32. doi:10.1023/A: 1010933404324.

Briggs M.S., Band D.L., Kippen R.M., Preece R.D., Kouveliotou C., van Paradijs J., Share G.H., Murphy R.J., Matz S.M., Connors A., Winkler C., McConnell M.L., Ryan J.M., Williams O.R., Young C.A., Dingus B., Catelli J.R., Wijers R.A.M.J., Observations of GRB 990123 by the Compton Gamma Ray Observatory, Astrophys. J. 524 (1999), p. 82.

Bringmann T. and Weniger C., 2012, Phys. Dark Univ., 1, 194-217.

Brunetti, G., & Jones, T. W. 2014, International Journal of Modern Physics D, 23, 1430007.

Bykov A. M., Astronomy Astrophys. Reviews, 22, 77 (2014).

Cao H., Bastieri D., Rando R. et al., "Machine Learning on Compton EventIdentification for a Nano-satellite Mission" Accepted for publication byExperimental Astronomy/

Cardillo M., Amato, E. & Blasi, P. 2016, A&A, 595, 58C.

Cardillo, M., Tavani, M., Giuliani, A. et al. 2014, A&A, 565, 74.

Carr B. J., in Inflating Horizons in Particle Astrophysics and Cosmology, edited by Susuki H. et al. (Universal Academy Press, Tokyo, Japan, 2005), p. 119.

Casandjian, J.-M. 2015, ApJ, 806, 240.

Cerruti M., Zech A., Boisson C., and Inoue S. .MNRAS, 448:910-927, 2015.

Cerutti B. et al., Mon. Not. R. Astron. Soc. (2016) 16.

Cerutti, B., Philippov, A., & Spitkovsky, A. 2016, MNRAS, 457, 2401.

Cesarsky C. J. and Montmerle T., Space Science Reviews 36, 173 (1983).

Chambers K. C., et al., The PAN-STARRS1 surveys, [arXiv:1612.05560].

Cheng K. S., Ho C. & Ruderman M., ApJ 300 (1986) 500.

Cheng K. S., Ruderman M., and Zhang L., ApJ 537 (2000) 964.

Cheng, K.-S., Chernyshov, D. O., Dogiel, V. A., et al. 2011, ApJ, 731, L17.

Cheng, K.S., Chernyshov, D.O., Dogiel, V.A., Hui, C.Y., Kong, A.K.H. 2010 ApJ 723, 1219.

Cheung, C. C., Larsson, S., Scargle, J. D., et al. 2014, ApJ Lett., 782, L14.

Clapson, A.-C., Jamrozy, M., Dyrda, M., Eger, P. 2011 A&A 532, A47.

Clayton, D. D., & Ward, R. A. 1975, ApJ, 198, 241.

Cline D. B. and Hong W., Astrophys. J. 401, L57 (1992).

Cohen A. G., De Rujula A. andGlashow S. L., ApJ 495, 539 (1998).

Collmar, W., 2006, ASP Conference Series, Vol. 350, 120.

Conrad, J., Cohen-Tanugi, J., & Strigari, L. E. 2015, Soviet Journal of Experimental and Theoretical Physics, 121, 1104.

Costamante L., et al.A&A, 371:512-526, 2001.

Cowsik, R., & Sarkar, S. 1980, MNRAS, 191, 855.

Crocker, R. M., & Aharonian, F. 2011, Physical Review Letters, 106, 101102.

De Angelis, A., Tatischeff, V., Tavani, M., et al.: The e-ASTROGAM mission. Experimental Astronomy 44(1), 25-82 (2017).

De Jager, O. C. & Harding, A. K. 1992, ApJ, 296, 161.

Deller, A. T. et al. 2015, ApJ, 809, 13.

Derishev, E. V., Aharonian, F. A. 2012, AIPC ,1505, 402.

Diemand J. and Moore B., The Structure and Evolution of Cold Dark Matter Halos, Advanced Science Letters 4 (Feb., 2011) 297{310, [arXiv:0906.4340].

Dolgov A. and Silk J., PRD 47, 4244 (1993).

Dolgov A. D., hep-ph/0211260.

Dolgov A. D., hep-ph/0511213.

Dolgov A. D., Kawasaki M. and Kevlishvili N., NPB 807, 229 (2009).

Donnarumma, I., De Rosa, A., Vittorini, V., et al. 2011, ApJ Lett., 736, L30.

Dorner et al. 2017, PoS(ICRC2017) 608.

Drlica-Wagner A., et al.,DES Collaboration, ApJ 813 109 (2015) [arXiv:1508.03622].

Dubus, G. 2006, A&A, 456, 801.

Dubus, G. 2013, A&A Rev, 21, 64.

Dubus, G. 2015, CRPhy, 16, 661.

Dubus, G., Cerutti, B., Henri, G., 2010, MNRAS, 404, L55.

Eger, P., Domainko, W., Clapson, A.-C. 2010 A&A 513, A66.

Einstein, A. 1936, Science, 84, 506.

Ellis S. C.and Bland-Hawthorn J., Phys. Rev. D 91 (2015) no.12, 123004.

F. Tavecchio and G. Bonnoli.ArXiv e-prints, 2015.

Fan Y. Z., Wei D. M., Zhang B., 2004, MNRAS, 354, 1031.

Fermi LAT Collaboration, 2009, Science, 326, 1512.

Ferrari, C., Govoni, F., Schindler, S., Bykov, A. M., & Rephaeli, Y. 2008, Space Sci. Rev., 134, 93.

Fichel C. E. et al. Astroph. J., 434 no. 2 557-559 (1994).

Finke J. D., et al.ApJ, 814:20, 2015.

Finke, J. D., Dermer, C. D., & B¨ottcher, M. 2008, ApJ, 686, 181.

Fishman, G.J., et al., 1989. In: GRO Science Workshop Proc. Johnson, W.N. (Ed.). NASA, Greenbelt, pp. 2–39.

Fong W et al. 2014, ApJ, 780, 118.

Foschini, L. 2013, Proceedings of the Conference Nuclei of Seyfert galaxies and QSOs - Central engine & conditions of star formation, arXiv: 1301.5785.

Foschini, L. 2014, in High-Energy Phenomena in Relativistic Outflows (HEPRO IV), eds. F. A. Aharonian, F.

Foschini, L. 2017, Proceedings of the Conference "Quasars at All Cosmic Epochs". Frontiers in Astronomy and Space Science., arXiv:1705.10166.

Foschini, L., Berton, M., Caccianiga, A., et all., 2015, A&A, 575, A13.

Fossati G., Maraschi L., Celotti A., Comastri A., and Ghisellini G..MNRAS, 299:433-448, 1998.

Fossati, G., Buckley, J. H., Bond, I. H., et al. 2008, ApJ, 677, 906.

Freire, P.C.C. et al. 2011 Science 334, 1107.

Freund, Y., Schapire, R.E.: A desicion-theoretic generalization of on-line learning and an application to boosting. European conference on computational learning theory, 23-37 (1995).

Frontera, F., Guidorzi, C., Montanari, E., et al. 2009, ApJS, 180, 192.

Garrison-Kimmel S., Boylan-Kolchin M., Bullock J., and Lee K., ELVIS: Exploring the Local Volume in Simulations, Mon. Not. Roy. Astron. Soc. 438 (2014), no. 3 2578-2596, [arXiv:1310.6746].

GCN IceCube EHE 50579430 130033.

Gehrels N., 2004, American Institute of Physics Conference Series, 727, 637.

Gehrels, N., Chincarini, G., Giommi, P., et al.: The Swift gamma-ray burst mission. The Astrophysical Journal 611(2), 1005 (2004).

Georg, W. 1999, PhD thesis, Technischen Universität München.

Géron, A.: Hands-on machine learning with Scikit-Learn and TensorFlow: concepts, tools, and techniques to build intelligent systems (2017).

Ghirlanda, G., Celotti, A., & Ghisellini, G. 2003, A&A, 406, 879.

Ghirlanda, G., Ghisellini, G., & Nava, L. 2010, A&A, 510, L7.

Ghirlanda, G., Nava, L., Ghisellini, G., et al. 2012, MNRAS, 420, 483.

Ghisellini G., Righi C., Costamante L., and Tavecchio F..MNRAS, 469:255{266, 2017.

Ghisellini G., Tavecchio F., Maraschi L., Celotti A., Sbarrato T., 2014, Nature 515, 376.

Ghisellini, G., Ghirlanda, G., Nava, L., & Celotti, A. 2010, MNRAS, 403, 926.

Ghisellini, G., Tavecchio, F., Maraschi, L., Celotti, A., & Sbarrato, T. 2014, Nature, 515, 376.

Ghisellini, G., Tavecchio, F., Sbarrato, T., Kauffman, S., & O. Tibolla 2017, this volume.

Ginzburg, V. L. & Syrovatsky, S.I. 1961, Prog. Theor. Phys. Suppl.,20, 1.

Giuliani, A., Cardillo, M., Tavani, M., et al. 2011, Astrophys. J. 742, 30-34.

Glorot, X., Bengio, Y.: Understanding the diffculty of training deep feedforward neural networks. Proceedings of the 13th International Conference on Artificial Intelligence and Statistics, 249-256 (2010).

Goldstein, A., Burgess, J. M., Preece, R. D., et al. 2012, ApJS, 199, 1.

Goldstein, A.,Veres, P., Burns, E., et al. (2017) An ordinary short gamma-ray burst with extraordinary implications: Fermi-GBM detection of GRB 170817A. Astrophys. J. 848, L14.

Gonzalez-Morales A. X., Profumo S., and Reynoso-Córdova J., Prospects for indirect MeV Dark Matter detection with Gamma Rays in light of Cosmic Microwave Background Constraints, arXiv:1705.00777.

GOMBOC, Andreja, 2012, Unveiling the secrets of gamma ray bursts. Contemporary Physics 2012. Vol. 4, no. let 53, p. 339–355.

Goodfellow, I., Pouget-Abadie, J., Mirza, M., et al.: Generative adversarial nets. Advances in neural information processing systems, 2672-2680 (2014).

Gotthelf, E.V., & Halpern, J.P. 2007, Ap&SS, 308, 79.

Granot J. 2002, ApJ, 570, 61.

Granot J., 2003, ApJ, 596, L17.

Grenier, I. A., A&A, 364, L93 (2000).

Grenier, I. A., Black, J. H., & Strong, A. W. 2015, ARA&A, 53, 199.

Grenier, I. A., Black, J., & Strong, A. 2015, ARAA, 53, 199.

Grenier, I. A., Casandjian, J. M., & Terrier, R. 2005, Science, 307, 1292.

Greiner J. et al., "Gamma-ray Burst Investigation via Polarimetry and Spectroscopy (GRIPS) ", Experimental Astronomy, vol. 23, no. 1, pp. 91-120, 2009.

Guo F. and Mathews W. G., Astrophys. J. 756, 181 (2012).

Guo, F., & Mathews, W. G. 2012, ApJ, 756, 181.

Guo, F., Mathews, W. G., Dobler, G., et al. 2012, ApJ, 756, 182.

Hanusch, A., Liseykina, T., & Malkov, M. 2017, arXiv:1707.02744.

Harding A. K., Stern J. V., Dyks J., & Frackowiak M., ApJ, 680 (2008) 1378.

Harding, A. & Kalapotharakos, C., 2015, ApJ, 811, 63.

Harrison F.A., "Development of the HEFT and NuSTAR focusing telescopes", Experimental Astronomy, vol. 20, no. 1-3, pp. 131-137, 2005.

Harrison, F.A., Craig, W.W., Christensen, F.E., et al.: The nuclear spectroscopic telescope array (NuSTAR) high-energy X-ray mission. The Astrophysical Journal 770(2), 103 (2013).

Hawking S.W., Nature (London) 248, 30 (1974).

Heinz, S., & Sunyaev, R. 2002, A&A, 390, 751.

Hewish, A., Bell, S., Pilkington, J., Scott, P., & Collins, R. 1968, Nature, 217, 709.

Hill, A. B., et al. 2011, MNRAS, 415, 235.

Hinton, J.: Ground-based gamma-ray astronomy with Cherenkov telescopes. New Journal of Physics 11(5), 055005 (2009).

Hjorth, J., & Bloom, J. S. 2012, The Gamma-Ray Burst – Supernova Connection, 169–190.

Hjorth, J., Sollerman, J., Møller, P., et al. 2003, Nature, 423, 847.

Ho, T. Kam: Random decision forest. Proceedings of the 3rd International Conference on Document Analysis and Recognition, 14-18 (1995).

Hochberg Y., Kuflik E., Volansky T. and Wacker J. G., 2014, Phys. Rev. Lett., 113, 171301.

Honma et al 1992, Publications of the Astronomical Society of Japan, 44, 529535.

Hotokezaka K. et al. 2016, MNRAS, 459, 35.

Indriolo, N., & McCall, B. J. 2012, ApJ, 745, 91.

Indriolo, N., Blake, G. A., Goto, M., et al. 2010, ApJ, 724, 1357.

Inoue T., Shimoda J., Ohira Y. and Yamazaki R., 2013, ApJ, 772, L20.

Inoue, Y., 2011, ApJ, 733, 66.

Inoue, Y., Totani, T., & Ueda, Y. 2008, ApJ, 672, 5.

Ioffe, S., Szegedy, C.: Batch normalization: accelerating deep network training by reducing internal covariate shift. International Conference on Machine Learning, 448-456 (2015).

Janocha, K., Czarnecki, W.M.: On loss functions for deep neural networks in classification. Schedae Informaticae 25, 49-59 (2016)

Japkowicz, N., Stephen, S.: The class imbalance problem: a systematic study. Intelligent data analysis 6(5), 429-449 (2002).

Johnson, T.J. et al. 2013 ApJ 778, 106.

Johnston, S., et al. 1992, ApJ, 387, L37.

Jourdain, E., Roques, J. P., Chauvin, M., Clark, D. J., 2012, ApJ, 761, 27.

Jurić M., et al., Proceedings of ADASS XXV [arXiv:1512.07914].

Kadler M. et al., 2016, Nature Physics, 12, 807-814.

Kalapotharakos, C., Brambilla, G, Timokhin, A., Harding, A. K., Kazanas, D., & . 2017, ApJ, submitted, ArXiv:1710.03170.

Kalapotharakos, C., Contopoulos, I., & Kazanas, D. 2012, MNRAS, 420, 2793.

Kalapotharakos, C., Kazanas, D., Harding, A., & Contopoulos, I. 2012, ApJ, 749, 2.

Kappadath, S. C. 1998, PhD thesis, Univ. New Hampshire.

Katsuta, J., Uchiyama, Y., & Funk, S. 2017, ApJ, 839, 129.

Kaufmann, S., Tibolla, O., Ciprini, S., et al. 2017, this volume.

Kino, M., Takahara, F. & Kusunose, M., 2002, ApJ, 564, 97.

Kinzer, R. L., Jung, G. V., Gruber, D. E., Matteson, J.-L., & Peterson, L. E. 1997, ApJ, 475, 361.

Klebesadel, R. W., Strong, I. B., & Olson, R. A. 1973, Observations of Gamma-Ray Bursts of Cosmic Origin, ApJ, 182, L85.

Komossa 2003, In Centrella, J. M., editor, AIP C, 686, 161174.

Komossa, S., Voges, W., Xu, D., et al. 2006, AJ, 132, 531.

Kong, A.K.H., Hui, C.Y., Cheng, K.S. 2010 ApJ 712, L36.

Kopp, A., Venter, C., Büsching, I., de Jager, O.C. 2013 ApJ 779, 126.

Kouveliotou, C., et al., 1993. Astrophys. J.413, L101.

Lacki, B., et al., 2014, ApJ, 786, 1.

Lange K., Carson R., EM Reconstruction Algorithms for Emission and Transmission Tomography, Journal of Computer Assisted Tomography 8 (1984) 306–316.

Lee, S., Patnaude, D. J., Raymond, J., C. et al. 2015, ApJ, 806, 71.

Li, J., Spitkovsky, A., & Tchekhovskoy, A. 2012, ApJ, 746, 60.

Liang, E.-W., Li, L., Gao, H., et al. 2013, ApJ, 774, 13.

Liang, E.-W., Yi, S.-X., Zhang, J., et al. 2010, ApJ, 725, 2209.

Liao, N.-H., Liang, Y.-F., Weng, S.-S., et al. 2015, arXiv:1510.05584.

Lichti, G. G., Bottacini, E., Ajello, M., et al. 2008, AAP, 486, 721.

Lisanti, M., Mishra-Sharma, S., Rodd, N. L., & Safdi, B. R. 2017, ArXiv e-prints, arXiv:1708.09385.

Loh, A., et al. 2016, MNRAS, 462, L111.

Lucchetta, G., Berlato, F., Rando, R., et al.: Scientific performance of a nanosatellite MeV telescope. The Astronomical Journal 153(5), 237 (2017).

Lyutikov M., Pariev V. I. and Blandford R. D., 2003, ApJ, 597, 998.

MacGibbon J. H. and Webber B. R., Phys. Rev. D 41, 3052 (1990).

MAGIC Collaboration, Nieto D. et al., The search for galactic dark matter clump candidates with Fermi and MAGIC, 32nd International Cosmic Ray Conference, Beijing (Aug., 2011) [arXiv:1109.5935].

Malkov, M. A., Diamond, P. H., & Sagdeev, R. Z. 2011, Nature Communications, 2, 194.

Mankuzhiyil N., et al., 2012, ApJ, 753, 2.

Marani G. F., Nemiro R. J., Norris J. and al., 1997 Bull. American Astron. Society, 29, 839.

Martí-Vidal, I., Muller, S., Combes, F., et al. 2013, A&A, 558, A123.

Mazets E.P., Golenetskij S.V., and Ilinskii V.N., Burst of cosmic gamma-emission from observations on Cosmos 461, Pis'ma v ZhurnEhTF, Tom 19 (1974), p. 126.

Mertsch P. and Sarkar S., Phys. Rev. Lett. 107, 091101 (2011).

Mészáros, P. & Rees, M. J. 1993, ApJL, 418, L59.

Mészáros P., 2006, Reports on Progress in Physics, 69, 2259.

Mészáros P. Theoretical models of gamma-ray bursts. In Meegan C. A., Preece R. D., and Koshut T. M., editors, Gamma-Ray Bursts, 4th Hunstville Symposium, volume 428 of American Institute of Physics Conference Series, pages 647–656, May 1998

Mészáros P., 2006, Reports on Progress in Physics, 69, 2259.

Metzger M. R., Djorgovski S. G., Kulkarni S. R. and al., 1997, Nature, 387, 878.

Mizumoto, T., Matsuoka, Y., Mizumura, Y., et al.: New readout and data acquisition system in an electron-tracking Compton camera for MeV gamma-ray astronomy (SMILE-II). Nuclear Instruments and Methods in Physics Research Section A: Accelerators, Spectrometers, Detectors and Associated Equipment 800, 40-50 (2015).

Montmerle, T. 1979, ApJ, 231, 95.

Mücke, A., & Protheroe, R. J. 2001, Astropart. Phys., 15, 121.

Mücke, A., Protheroe, R. J., Engel, R., Rachen, J. P., & Stanev, T. 2003, Astropart. Phys., 18, 593.

Murase K. et al., 2016, Phys. Rev. Lett., 116, 071101.

Murphy, R. P., Sasaki, M., Binns, W. R., et al., ApJ, 831, 148 (2016).

Nair, V., Hinton, G.E.: Rectified linear units improve restricted boltzmann machines. Proceedings of the 27th international conference on machine learning, 807-814 (2010).

Nakar E., Piran T. and Waxman E., 2003, J. Cosmology Astropart. Phys., 10, 005.

Nakar E. Short-hard gamma-ray bursts. Physics Reports 2007;442: 166-236.

Nava, L., Ghirlanda, G., Ghisellini, G., & Celotti, A. 2011, A&A, 530, A21.

Neronov, A., Vovk, I., & Malyshev, D. 2015, Nature Phys., 11, 664.

Neronov, A., Vovk, I., & Malyshev, D. 2015, Nature Phys., 11, 664.

Nissanke S. et al., 2013, ApJ, 767, 124.

Nobili, L., Turolla R., Zane S., 2008, MNRAS, 386, 1527.

Odaka, H., Ichinohe, Y., Takeda, S., et al. 2012, NIM A, 695, 179.

Ohm, S., Zabalza, V., Hinton, J. A., and Parkin, E. R., MNRAS449 (2015) L132.

Olive K.A. et al. (Particle Data Group), Chin. Phys. C38 (2014) 090001.

Orlando, E., et al. 2017, Proc. 35th International Cosmic Ray Conference, PoS(ICRC2017)692.

Pacini, F., 1967. Energy Emission from a Neutron Star. Nature 216, 567–568.

Padovani, P., 2017, Nature Astronomy, 1, 194.

Pakmor, R., Pfrommer, C., Simpson, C. M., & Springel, V. 2016, ApJ, 824, L30.

Pakmor, R., Pfrommer, C., Simpson, C. M., & Springel, V. 2016, ApJL, 824, L30.

Panaitescu, A. 2017, ApJ, 837, 13.

Papitto, A., Torres, D. F., & Li, J. 2014, MNRAS, 438, 2105.

Pappadopulo D., Ruderman J. T. and Trevisan G., 2016, Phys. Rev., D94, 035005.

Paredes, J. M., Bosch-Ramon, V., Romero, G. E. 2006, A&A, 451, 259.

Parizot, E., Marcowith, A., van der Swaluw, E., Bykov, A. M., & Tatische, V. 2004, A&A, 424, 747.

Parkin, E. R., Pittard, J. M., Corcoran, M. F., and Hamaguchi, K., ApJ726 (2011) 105.

Pedregosa, F., Varoquaux, G., Gramfort, A., et al.: Scikit-learn: machine learning in Python. Journal of Machine Learning Research 12, 2825-2830 (2011).

Philippov, A., & Spitkovsky, A. 2014, ApJL, 785, L33.

Pian, E., Tuerler, M., Fiocchi, M., et al. 2013, ArXiv e-prints.

Pineda, J. L., et al. 2013, A&A, 554, A103.

Planck Collaboration, Fermi Collaboration, 2015, A&A, 582, A31.

Pogge, R. W. 2000, New Astron. Rev., 44, 381.

Pohl, M., Wilhelm, A., & Telezhinsky, I. 2015, A&A, 574, A43.

Pons, J.A., Geppert, U., 2007, Magnetic field dissipation in neutron star crusts: from magnetars to isolated neutron stars. A&A 470, 303–315 [arXiv:astro-ph/0703267].

Pospelov M., Ritz A. and Voloshin M. B., 2008, Phys. Lett., B662, 53-61.

Preece, R. D., Briggs, M. S., Mallozzi, R. S., et al. 2000, ApJS, 126, 19.

Ramaty, R., Kozlovsky, B., & Lingenfelter, R. E. 1979, ApJS, 40, 487.

Rea, N., Zane, S., Turolla, R., & Lyutikov, M. 2008, ApJ, 686,1245.

Reach, W.T. & Rho, J. 2000, AJ, 544, 843-858.

Rees, M. J. & Gunn, J. E. 1974, MNRAS, 167, 1.

Remy, Q., Grenier, I. A., Marshall, D. J., & Casandjian, J. M. 2017, A&A, 601, A78.

Remy, Q., Grenier, I. A., Marshall, D. J., & Casandjian, J. M. 2017, submitted to A&A.

Rieger 2004, APJ, 615 (1), L5-L8.

Rodriguez J., et al., 2015, ApJ, 807, 17.

Ruderman M. A.et al., ApJ 196 (1975) 51.

Ruiz-Lapuente, P., et al., 2016, ApJ, 820.

Rumelhart, D.E., Hinton, G.E., Williams, R.J., et al.: Learning representations by back-propagating errors. Cognitive modeling 5(3), 1 (1988).

Rybicki G. B., Lightman A.P., 1979, Radiative processes in astrophysics.

Rygl K. L. J. et al., Astronomy Astrophys. 539, A79 (2012).

Sakamoto, T., Barthelmy, S. D., Baumgartner, W. H., et al. 2011, ApJS, 195, 2.

Sambruna, R. M., Markwardt, C. B., Mushotzky, R. F., et al., 2006, ApJ, 646, 23.

Samuel, Arthur (1959). "Some Studies in Machine Learning Using the Game of Checkers". IBM Journal of Research and Development. 3 (3): 210–229.

Santander M. et al., 2017, PoS, (ICRC2017), 618.

Sbarrato T., Ghisellini G., Tagliaferri G. et al., 2016, MNRAS, 462, 1542.

Sbarrato T., Ghisellini G., Tagliaferri G., Foschini L., Nardini M., Tavecchio F., Gehrels N., 2015, MNRAS, 446,2483.

Sbarrato, T., Tagliaferri, G., Ghisellini, G., et al., 2013, ApJ, 777, 147.

Scherer, K., Fichtner, H., Ferreira, S. E. S., Büsching, I., & Potgieter, M. S. 2008, ApJ, 680, L105.

Schlickeiser, R., Caglar, M., & Lazarian, A. 2016, ApJ, 824, 89.

Schneider, P., Ehlers, J., & Falco, E. E. 1992, Gravitational Lenses, XIV, 560 pp., Berlin: Springer-Verlag.

Schöenfelder, V., Aarts, H., Bennett, K., et al.: Instrument description and performance of the imaging gamma-ray telescope COMPTEL aboard the Compton gamma-ray observatory. The Astrophysical Journal Supplement Series 86, 657-692 (1993).

Schönfelder, V. 2004, NewAR, 48, 193.

Schönfelder, V., Bennett, K., Blom, J. J., et al. 2000, A&A, 143, 145.

Senno N. et al., 2016, Phys. Rev. D, 93, 083003.

Sharp R. G. and Bland-Hawthorn J., Astrophys. J. 711, 818 (2010).

Slane, P. O. 2017, arXiv:1703.09311v1.

Slatyer T. R.. Indirect dark matter signatures in the cosmic dark ages. I. Generalizing the bound on s-wave dark matter annihilation from Planck results. Phys. Rev. D 93 (2016) no.2, 023527.

Smith, R. J., et al. 2014, MNRAS, 441, 1628.

Sokol J., Science 356, 240 (2017)

Spanier, F. & Weidinger, M. 2012, Int. Journal of Modern Physics Conf. Series, 8, 293.

Springel V., Wang J., Vogelsberger M., Ludlow A., Jenkins A., Helmi A., Navarro J. F., C. S. Frenk, and White S. D. M., The Aquarius Project: the subhaloes of galactic haloes, MNRAS 391 (Dec., 2008) 1685-1711, [arXiv:0809.0898].

Srivastava, N., Hinton, G.E., Krizhevsky, A., et al.: Dropout: a simple way to prevent neural networks from overfitting. Journal of machine learning research 15(1), 1929-1958 (2014).

Steigman G., Dasgupta B., Beacom J. F., Phys. Rev. D86 (2012) 023506.

Steigman G., JCAP 0810, 001 (2008).

Stone, E., et al. 2013, Science, 341, 150.

Strong, A.W.,Orlando,E.,&Ja e, T. R. 2011, A&A, 534, A54.

Su M., Slatyer T. R. and Finkbeiner D. P., Astrophys. J. 724, 1044 (2010).

Su, M., Slatyer, T. R., & Finkbeiner, D. P. 2010, ApJ, 724, 1044.

Sutskever, I., Martens, J., Dahl, G., et al.: On the importance of initialization and momentum in deep learning. International conference on machine learning, 1139-1147 (2013).

Tagliaferri, G., Ghisellini, G., Perri, M., et al., 2015, ApJ, 807, 167.

Takami H., 2014, Physical Review D, 89, 063006.

Takata, J., Li, K. L., Leung, G. C. K., et al. 2014, ApJ, 785, 131.

Tam, P.H.T. et al. 2011 ApJ 729, 90.

Tanaka et al., 2017, Astronomer's Telegram, 10791.

Tatischeff, V., & Kiener, J. 2004, New Astronomy Reviews, 48, 99.

Tatischeff, V., & Kiener, J. 2011, MmSAI, 82, 903.

Tavani, M., Barbiellini, G., Argan, A., et al.: The AGILE mission. Astronomy & Astrophysics 502(3), 995-1013 (2009).

Tavecchio F. & Ghisellini G., 2016, MNRAS, 456, 3.

Taylor A. M., Vovk I., and Neronov A..A&A, 529:A144, 2011.

Telezhinsky, I., Dwarkadas, V. V., & Pohl, M. 2012, Astroparticle Physics, 35, 300.

Telezhinsky, I., Dwarkadas, V. V., & Pohl, M. 2013, A&A, 552, A102.

the MAGIC Collaboration, 2017, Astronomer's Telegram, 10817.

Thompson C., Lyutikov M., Kulkarni S.R., 2002, ApJ, 574, 332.

Thompson, C., & Duncan, R.C. 1993, ApJ, 408,194.

Tibolla, O., Kaufmann, S., Foschini, L., et al., 2013, ICRC 2013 proceedings paper, arXiv: 1306.4017.

Tiengo, A., Esposito, P., & Mereghetti, S. 2008, ApJ, 680, 133 [arXiv:0805.2294].

Toma K. and al., 2009, ApJ, 98, 1042.

Toma K., 2013, [arXiv:1308.5733v1].

Trombka, J. I., Dyer, C. S., Evans, L. G., et al. 1977, ApJ, 212, 925.

Uchiyama, Y., Blandford, R. D., Funk, S. et al. 2010, ApJ, 723, 122.

VERITAS Collaboration, Nieto D., Hunting for dark matter subhalos among the Fermi-LAT sources with VERITAS, in Proceedings, 34th International Cosmic Ray Conference (ICRC 2015), 2015. arXiv:1509.00085.

Vianello, G., Gill, R., Granot, J., et al. 2017, ArXiv:1706.01481.

Vianello, G., Götz, D., & Mereghetti, S. 2009, A&A, 495, 1005.

Walker M. G., Vol. 5 of the book 'Planets, Stars, and Stellar Systems', published by Springer, [arXiv:1205.0311].

Wang Y. et al, Mon Not R Astron Soc 445 (2014) 604.

Wang Y., Takata J., and K. S. Cheng, ApJ 764 (2013) 51.

Watanabe, K., Leising, M., Share, G., & Kinzer, R. 1999b, BAAS, 31, 702.

Weidenspointner, G., Varendor, M., Kappadath, S. C., et al. 2000, in AIP Conf. Proc. 510, The Fifth Compton Symposium, ed. M. L. McConnell, & J. M. Ryan (Melville, NY: AIP), 581.

Weymann, R. J., Chaffee, F. H., Jr., Carleton, N. P., et al. 1979, ApJ Lett., 233, L43.

Wiener J., Pfrommer C. and Oh P., Mon. Not. Roy. Astron. Soc. 467, no. 1, 906 (2017).

Wijers R. A. M. J., Rees M. J., and Meszaros P. Shocked by GRB 970228: the afterglow of a cosmological fireball. MNRAS, 288:L51–L56, July 1997.

Wijnands, R. & van der Klis, M. 1998, Nature 394, 344.

Willingale R., O'Brien P. T., Osborne J. P., Godet O., Page K. L., Goad M. R., Burrows D. N., Zhang B., Rol E., Gehrels N., and G. Chincarini. Testing the Standard Fireball Model of Gamma-Ray Bursts Using Late X-Ray Afterglows Measured by Swift. ApJ, 662:1093-1110, June 2007.

Wilson-Hodge, C. et al. 2016, American Astronomical Society, HEAD meeting, 15, id.118.09.

Winkler, C., Diehl, R., Ubertini, P., et al.: INTEGRAL: science highlights and future prospects. Space science reviews 161(1-4), 149-177 (2011).

Woosley, S. E., 1993, Ap. J., 405, 273.

Woosley, S. E., & Bloom, J. S. 2006, The Supernova Gamma-Ray Burst Connection. ARA&A, 44, 507.

Xia Z.-Q., Duan K.-K., Li S., Liang Y.-F., Shen Z.-Q., Yue C., Wang Y.-P., Yuan Q., Fan Y.-Z., Wu J., and Chang J., 3fgl j1924.8-1034: A spatially extended stable unidentified gev source?, Phys. Rev. D 95 (May, 2017)102001.

Yang H.-Y. K., Ruszkowski M., Ricker P. M., Zweibel E. and Lee D., Astrophys. J. 761, 185 (2012).

Zanin R., et al. 2016, A&A, 596, A55.

Zdziarski A. A., Malyshev D., Chernyakova M., Pooley G. G. 2017, MNRAS, 471, 3657.

Zdziarski, A. A., et al. 2012, MNRAS, 426, 1031.

Zdziarski, A. A., Pjanka, P., Sikora, M., Stawarz, L. 2014, MNRAS, 442, 3243.

Zhang B., Yan H., 2011, ApJ, 726, 90.

Zhou, H.-Y., Wang, T., Yuan, W., et al. 2006, ApJS, 166, 128.

Zoglauer, A. C. “First Light for the Next Generation of Compton and Pair Telescopes”. PhD Thesis. Max Planck Institut für Extraterrestrische Physik, 2005.

Zoglauer A., Andritschke R., Schopper F., "MEGAlib – the Medium Energy Gamma-ray Astronomy Library", New Astronomy Reviews, vol. 50, no. 7-8, pp. 629-632, 2006.

Zoglauer, A., Andritschke, R., Boggs, S.E., et al.: MEGAlib-simulation and data analysis for low-to-medium-energy gamma-ray telescopes. Proceedings of the International Society for Optical Engineering, volume 7011, 70113F (2008).

Zoglauer A. C. et al. “Cosima – the Cosmic Simulator of MEGAlib”. In: IEEE Nuclear Science Symposium conference record. Nuclear Science Symposium (2009).

Zoglauer A., Galloway M., Amman M., Boggs S.E., Lee J.S., Luke P.N., Mihailescu L., Vetter K., Wunderer C.B., "First Results of the High Efficiency Multi-mode Imager HEMI", Nuclear Science Symposium Conference Record, 2009 IEEE.

Zubovas, K., King, A. R., & Nayakshin, S. 2011, MNRAS, 415, L21.

Zweibel, E. G. 2013, Physics of plasma, 20, 055501.